THE FLORIDA STATE UNIVERSITY

COLLEGE OF ARTS AND SCIENCES

SEARCH FOR NEW AND UNUSUAL STRANGEONIA IN PHOTOPRODUCTION USING CLAS

By

MUKESH S. SAINI

A Dissertation submitted to the
Department of Physics
in partial fulfillment of the
requirements for the degree of
Doctor of Philosophy

Degree Awarded:
Spring Semester, 2013

Mukesh S. Saini defended this dissertation on March 12, 2012.

The members of the supervisory committee were:

Paul Eugenio
Professor Directing Dissertation

Tomasz Plewa
University Representative

Simon Capstick
Committee Member

Volker Crede
Committee Member

Horst Wahl
Committee Member

Dennis Weygand
Committee Member

The Graduate School has verified and approved the above-named committee members, and certifies that the dissertation has been approved in accordance with the university requirements.

To family, friends and teachers.

ACKNOWLEDGMENTS

I thank all the people who went before me and figured all this "stuff" out, enabling me to read, and ask, and learn, and understand bits and pieces of what goes on around me.

This thesis and my involvement in research would not have occurred but for the support and guidance of my very patient and generous thesis advisor, Dr. Paul Eugenio. He always did his best to imbue independence and free thought and initiative in me. I will try do justice to his efforts in whatever I do next. I have always harbored a hesitation in interacting with faculty; it is inbred in a kid where I come from. His demeanor and accessibility made a big difference. Small talk is under-rated in Physics. I thank him for his chats and guidance, and for the drives down to Virginia and the sailing trips and for keeping me motivated and seeing me through to the end of my thesis.

Tallahassee is a beautiful town and Florida State is my second home. I have met some of the nicest, politest and most helpful and joyful people here. Let me just reminisce and thank people in the chronological order I met them. Sherry Tointigh was the graduate secretary when I joined the physics department at FSU. As everyone else will testify, she was the best and took care of everything. As an international student, who had many hoops to jump through, she made all of the tasks a breeze. She made everyone who came in feel like FSU family and every student reached out to her to address whatever issues we had. The professors at FSU who taught me my courses; Dr. Nicholas Bonesteel, Dr. Jorge Piekarewicz, Dr. Pedro Schlottmann are great physics teachers. They did justice to physics as a subject to be taught, learnt and understood. Lunchtime with Dr. Piekarewicz and random discussions about everything defines a huge part of the FSU experience for me. Talking to Dr. Harrison Prosper about physics and statistics is just about as much motivation as a newly recruited graduate student can handle. Dr. Alexander Ostrovidov with his all-knowing superpowers has turned out to be the ultimate go-to guy. I am very

thankful to have known them and to have learnt from them.

A graduate thesis requires a supportive and collaborative cast of committee members. I thank Dr. Thomasz Plewa and Dr. Horst Wahl for overseeing this dissertation. I thank Dr. Simon Capstick for always guiding me to the answers of my queries. I thank Dr. Volker Crede for the physics discussions and his general support in my research and otherwise. I thank Dr. Dennis Weygand for his general guidance and myriad efforts at getting the physics right for this thesis.

I was able to make it to the graduate school at FSU due to the support of many teachers from my earlier alma maters. I thank Dr. Anuradha Misra, Dr. S.B. Patel, Dr. M.R. Press and Dr. D.C. Kothari for their tutelage at the University of Mumbai. At the K.C.College, Mrs. G.M. Kulkarni, Mrs. A.K Ravi and Mr. S.S. Singh provided me with direction and education and kept me on track and I am very grateful for that.

The experimental data for this dissertation was acquired at CEBAF using CLAS at Jefferson Lab through the planning and expertise of hundreds of people I know and many more whom I don't. I thank them for their tireless efforts for being at the forefront of Particle Physics and making this thesis possible. Jefferson lab and the surrounding towns in Virginia are beautiful places to spend summers working and learning. From my senior collaborators, I am especially grateful to Dr. Eugene Pasyuk and Dr. Franz Klein, who educated me on the small and the big details of the CLAS detector and its analysis. Their bestowed code and their patient guidance made a lot of my work as a calibrator and researcher possible. I thank Dr. Valeri Koubarovski and Dr. Carlos Salgado for their guidance with my research. When I started out with CLAS physics, Dr. Lei Guo directed me to where I needed to be then, and has since consistently guided me over the years. Dr. Dustin Keller gave me his time and patiently explained to me the intricacies of his kinematic fitter package and how to use it. A lot of calibration and analysis details were taught to me by Dr. Daria Sokhan, Dr. Julian Salamanca, Dr. Raffaella De Vita, Dr. Marco Battaglieri and Dr. Michael Paolone. I am grateful to each of them for devoting their time and effort to the completion of this work.

Starting out with CLAS analysis was not easy. The analysis framework is complex and very fragmented. No single expert could have guided me through. What got me

through was the team of go-getters assembled by the g12 group consisting of then students and now graduates, Johann Goetz, Craig BookWalter and Dianne Schott. We started out with detector calibrations and moved on to analysis as a team. The amount of code they bestowed upon me, with all the troubleshooting and debugging they did, helped me navigate the twisted ways of analysis. They are my true comrades and their hard work is reflected in this thesis. It is unimaginable for me to have been able to survive during the thesis work without their help and support and I cannot thank them enough.

When I started fresh, Lucasz Blaszczyk set me up with my linux terminal and CLAS framework and even initial toy analysis, which to me then was pretty much alien. My many old and new office mates - Sungkyun Park, Charles Hanretty, Ben Eakins, Wei Chia, Lonnie Mott, Farrukh Fattoyev who have slogged through the years alongside, providing me with conversations, interesting and mundane are already missed. Discussing physics, thesis and analysis with fellow students, Andrew Wilson and Nathan Sparks, in the hadronic physics group at FSU, was always productive. Newer students, Aristeidis Tsaris and Hussein Al Ghoul, have learned quickly and their questions illuminate the dark corners of my understanding. I am thankful to all of them for being the interesting, intelligent people and good friends that they are.

When I joined FSU in Fall-2005, I acquired an instant bunch of friends, provided by the FSU physics admissions committee. All of us bonded over physics and latenight homeworks and beers. Aaron McVeigh and Skylar Saucedo left early with their Masters and I still miss them. The long, and sometimes pointless, lunch conversations with Lam Nguyen, Alexander Silalahi and Kenshong Chen are also sorely missed and are a constant reminder that it is time to move on from Tallahassee. Peter Bender, Benjamin Sadler, Benjamin Conner, Jennifer Misuraca, Jennifer Kirchoff were always giving me a ride to one place or the other and watching random television shows and movies; Memorable times. Naureen Ahsan, Trang Hoang, Benjamin Thayer, Alexander Rojas, Hanna Terletska, Xiaoyan Shi and Yohanes Pramudya provided a complete rounded out international experience of comradeship, that I most appreciated about the graduate school. Just interacting with them, learning where all of us came from, how different and similar we all were, might just be the best lesson I learnt at FSU and I am grateful to all of them for that.

Life in Tallahassee was made much normal and possible by the presence of a some very good friends. Bodhana Dhole and Chandrima Mukherjee spoilt me with anytime tea and Bengali food along with my cousin, Swati Saini. Sambuddha Misra and Rajarshi Das were great fun roommates and comrades. Good times were spent and wasted with the aid of Girdhari Sharma, Aditya Joshi and Nithin Sathyamoorthy. Fatima Wajahat and Nastaren Abad proved themselves to be great company and amicable neighbors with high tolerance for my jokes. Komalavalli Thirunavukkuarasu hosted my family and was responsible for the bulwark of my wedding prep, aided and abetted by Avinash Saraon and Sudarshan Jagannathan. My wife and I have spent a lot of time in the company of these people and we are both very thankful to all of them for being kind to us. I am thankful to the All Saints Cafe and its people for providing abode and distractions for night-owls and insomniacs like me.

Moving to FSU also meant leaving behind people who were a big part of my life. Family, and Friends who are family. Bhavesh Ranka, Amit Patel, Bharat Rathi, Nitin Rana, Ranjodh Wilku, Aniruddha Joglekar, Zohar Reuben, Parag Jog and Sohanlal Purohit have provided great memories of my college days. Gaurav Vedpathak, Nireeshwari Rao, Sushil Pandey, Nitin Waghela, Naresh Deoli and Suman Dhayal have been great companions to me in my university years and beyond. Ganesh Shresta has been a great friend and a second son to my parents. I have missed everyone constantly and I thank you all for being great friends to me.

I have missed seeing my nieces, Pari and Alia, grow up. I have missed seeing all my cousins grow up. I have missed a lot of important stuff. I am fortunate though that my sister and brother-in-law live close to my parents and all my cousins have grown to make me proud. I feel guilty for not being able to visit my grandparents and spend time with them and my cousins as much as I should. I miss you and love you all.

In the end, everything was possible only due to my supportive and encouraging family. My father, Satyaprakash Saini, spoilt both his children with love and comfort and now continues to do the same with his grandchildren. My mother, Janakshri Saini, who would not let me rest or take it easy, motivating me to where I am. My sister, Sweta Kaushik, who kept me fed, out of trouble and on my toes. My brother-in-law, Brijesh Kaushik, who

is doing a great job of being the son in my absence. I owe you all everything.

I met my wife, Sanhita Ghosh, a fellow physicist at FSU and it was the best thing to have happened to me in Tallahassee. I am thankful to her for being patient and tolerant and for being such a great friend over the years.

TABLE OF CONTENTS

LIST OF TABLES

LIST OF FIGURES

GLOSSARY OF ACRONYMS

a1c	The program used for reconstructing event information in CLAS using the raw data acquired from the data acquisition or using the data created by the simulation program.
ADC	An analog/amplitude to digital converter.
BPM	The beam position monitor.
CC	The Cherenkov counter.
CEBAF	The continuous electron beam accelerating facility located at Jefferson lab, Newport News, Virginia.
CHL	The central helium liquifier used for cooling CEBAF.
CLAS	The CEBAF large acceptance spectrometer.
CM	The center of mass frame.
CODA	The CEBAF online data acquisition system.
CQM	The constituent quark model.
DAQ	The data acquisition system for CLAS.
DC	Drift Chambers.
DVCS	Deeply virtual compton scattering.
DOE	Department of Energy.
EC	Electromagnetic calorimeters.
FEL	The free electron laser at Jefferson Lab.
FPC	The fundamental power coupler used to deliver energy to a cavity.
FPGA	Field programmable gate array - logic control processors.
g6c	The third dataset from the CLAS experiment *g6*.
g11	A high beam current CLAS experiment.
g12	The run-period during which CLAS acquired the data used in this dissertation.
GEANT3	The third version of GEANT, which is a collection of simulation softwares designed to describe the passage of elementary particles through matter, using Monte Carlo methods.
genr8	An event generator used to generate event four-vectors describing specific physics.

GJ	The Gottried-Jackson frame is the resonance rest frame, with a specifically defined choice of axes.
GPD	Generalized parton distribution.
gpp	The utility used to smear the simulated signal information for CLAS and tagger, in order to provide resolutions and efficiencies that mimics data.
gsim	The utility used during simulations for creating raw electronic information from the detectors.
HOM	Higher order mode couplers.
HPA	High power amplifiers.
HQET	Heavy quark effective theory.
HyCLAS	One of the 2 initial experiments approved for the run-period g12 with focus on search for new hadronic states.
JLAB	Jefferson laboratory located in Newport News, Virginia.
linac	Linear accelerator.
LQCD	Quantum chromodynamics solved on a lattice.
MC	Monte Carlo simulations.
MCC	CEBAF's main control center responsible for beam delivery.
MINUIT	A coolection of numerical minimization routines provided by CERN.
MOR	Master OR gate for tagger.
MSS	The mass storage system used to store data at JLAB.
OZI	An empirical rule, named after Okubo-Zweig-Iizuka, deduced from observations of hadronic decays.
PART	A data structure used to store particle information for CLAS analysis.
PDG	The particle data group.
PID	Particle identification.
PMT	Photo multiplier tube.
PWA	Partial wave analysis.
ROC	Read-out crates.
QCD	Quantum chromodynamics.
QED	Quantum electrodynamics.
RF	Radio frequency.
SRF	Superconducting radio frequency technology.
ST	Start counter.
Super-G	One of the 2 initial experiments approved for the run-period g12 with focus on search for new hadronic states.
TAC	Total absorption counter.
TAGR	A data structure used to store particle information from the tagger.
TJNAF	Thomas Jefferson national accelerator facility.
TOF	Time of Flight detector.

TS	Trigger supervisor.
VMD	Vector meson dominance model.
VME	A high performance bus system with interrupt management and multiprocessor capability.

ABSTRACT

We perform a survey of the proton, K^+ , K^- - 3 charged track data, taken by the CLAS detector for the HyCLAS experiment [1] during the g12 run-period at Jefferson Lab. We aim to study the strong decay amplitudes, partial widths and production channels of strangeonia from the CLAS g12 dataset. HyCLAS was motivated by the experimental results for gluonic hybrid meson candidates, theoretical Lattice QCD, and Flux-tube Model calculations and predictions. The experiment was designed and conducted to search and observe new forms of hadronic matter through photoproduction.

Crucial among the various channels explored in HyCLAS are those for strangeonia, resonances such as $\phi(1680)$, $\phi_3(1850)$ and Y(2175) [2] decaying to $\phi\ \eta$. A meson decay via $\phi\ \eta$ is the signature that unequivocally identifies a strangeonium ($s\bar{s}$) state and is the main focus of this thesis. A strangeonium decay via $\phi\ \eta$ is considered the premier decay mode to cleanly establish the strangeonia spectrum [3]. This is due to negligible interference of the $\phi\ \eta$ decay mode with the non-strange $n\bar{n}$ ($n \in \{u, d\}$) meson decay modes, on account of the fact that $\phi(1020)$ is an almost pure $s\bar{s}$ vector meson and the η meson possesses a strong component of $s\bar{s}$ in it as well.

Another analysis explored was the $\phi\ \pi^o$ decay channel, which is an exotic decay mode for a meson. Decay of an initial $s\bar{s}$ meson via this channel is forbidden on account of the conservation of isotopic spin whereas the decay of a $n\bar{n}$ via the $\phi\ \pi^o$ decay mode is also forbidden by the Okubo - Zweig - Iizuka (OZI) rule. Thus, observation of a resonance decaying to $\phi\ \pi^o$ will provide strong evidence of mesons beyond $q\bar{q}$, probably of a gluonic excitation - $q\bar{q}g$ or a tetraquark state - $q\bar{q}q\bar{q}$ [4].

A final state of *proton*, K^+ and K^- is selected from the g12 dataset. An intermediate ϕ state is identified by its decay to $K^+\ K^-$. Using Energy-Momentum conservation, missing mass in an event is calculated. Depending on the analyses, suitable missing mass cuts for

the missing η mass or the π^o mass is implemented to identify the particular missing particle. Invariant mass for the ϕ and the missing η/π^o system is reconstructed to observe possible resonances.

$$\gamma\ p\ \rightarrow\ p\ X\ \rightarrow\ p\ \phi\ [\eta/\pi^o]\ \rightarrow\ p\ K^+\ K^-\ [\eta/\pi^o]$$

The yield and the cross section for the photoproduction of $\phi\ \eta$ mesons off of protons is calculated for $E_\gamma \in \{4.40, 5.45\}$ GeV/c^2 using elliptical sideband subtraction. Upper and lower limits on the photoproduction cross section for possible strangeonium resonances and their subsequent decay via the $\phi\ \eta$ intermediate state are calculated using the FeldMan-Cousins approach with a 90% confidence interval limit. A partial wave analysis is also performed on the $\phi\ \eta$ intermediate state to explore for discernable resonances.

The yield and the cross section for the photoproduction of ϕ mesons off of protons is calculated for $E_\gamma \in \{4.40, 5.45\}$ GeV/c^2 . Yield is estimated for the intermediate state $\phi\ \pi^o$ and its invariant mass distributions analyzed for possible resonances. The (proton K^+ K^-) final state is also explored for the rare $\phi\ \omega$ events and the yield for the channel is measured.

CHAPTER 1

PARTICLE PHYSICS

1.1 Introduction

"But I don't have to know an answer. I don't feel frightened by not knowing things, by being lost in a mysterious universe within any purpose, which is the way it really is, so far as I can tell. It doesn't frighten me." — Richard P. Feynman [5].

We have always tried to understand our world around us, to make sense of the structures and patterns we see everyday, everywhere. It is this curiosity, this quest to understand, that has been the driving force behind science. One of the foremost questions that people from Aristotle to Feynman, philosophers and physicists, have dealt with is 'What is the smallest, most fundamental object that we are made up of?', along with quite a few other existential conundrums.

Physics, for its part, has started answering many of these questions in a satisfactory manner, especially with regards to matter. There is a safe hypothesis that the world around us, which is made up of matter as we know it, constitutes only 4% of the observable universe. Rest is dark matter and dark energy, phenomena we do not understand and cannot interact with. As for the matter we can interact with, we have a very able and robust theory called 'The Standard Model', depicted in figure [1.1]. It can basically describe using mathematics and models, interactions between what we currently believe to be the most fundamental indivisible objects that constitute the matter, and its interactions around us.

We have a good understanding of the electromagnetic interactions between atoms and molecules and electrons and such in different environments. The field of 'Condensed Matter Physics' is dedicated to further this understanding and we learn something new every few

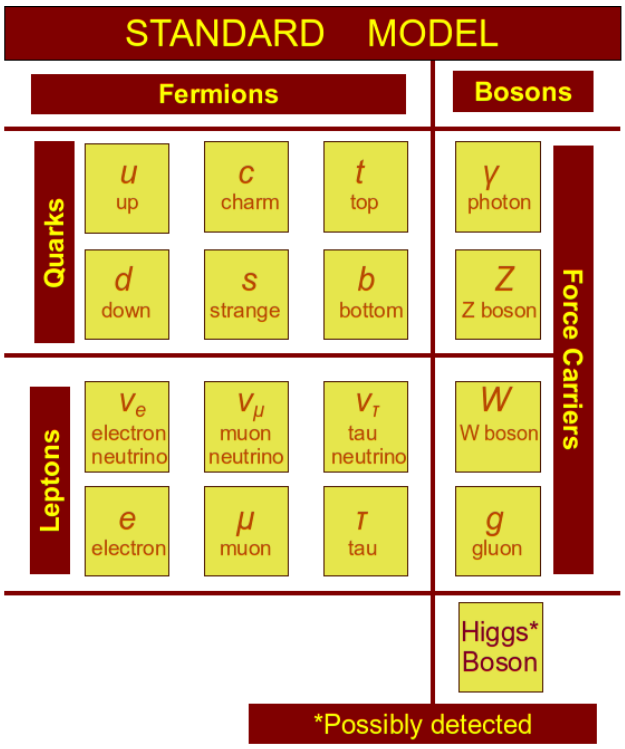

Figure 1.1: Standard Model of Particle Physics; all the known fundamental constituents of matter arranged according to their classification.

months. But when it comes to the interactions between the most fundamental constituents of matter, like the quarks within a nucleon, gaining new insights becomes an event on an entirely new timescale; much much longer timescale. To pursue a deeper understanding in the field of particle physics, we delve into how these basic constituents interact.

Our understanding of strong nuclear force has undergone major revisions over the last eight decades. Our present understanding is that the strong interaction is described by the non-abelian gauge field theory of Quantum ChromoDynamics(QCD) [6] [7] [8], which models the interactions of quarks and gluons, considered to be the most fundamental constituents of matter along with leptons and other gauge bosons.

The visible world around us is made up of hadrons and leptons. Hadrons have two identified subspecies, baryons and mesons, which are made up of Quarks and Gluons. Quarks and Gluons are considered to be among the fundamental building blocks of matter. Strong interactions are responsible for binding the quarks within a nucleon and the nucleons within

a nucleus. This interquark force is mediated by the fundamental particle called gluon. It is a massless vector boson and carries color charge, analogous to the electric charge. The color charge allows a gluon to self-interact making QCD much harder to solve compared to Quantum Electro-Dynamics(QED). Only colorless combinations of elementary particles are physically found to exist in nature. Free quarks and gluons, particles that carry color charge, are not observed in nature. This phenomena is referred to as 'color confinement' and it gives rise to our observed world of mesons and baryons.

In strong interactions, we observe no free quarks or gluons. The majority of the scientific community in the 60's believed quarks to be fictitious mathematical devices with almost no physical significance and hence unobserved. The status quo changed in 1968. In an electron-proton scattering experiment at SLAC, the electrons appeared to be bouncing off small dense objects inside the proton. Bjorken and Feynman analyzed this data in terms of a model where a proton was formed of constituent particles though they did not yet refer to the constituents as 'Quarks' but as 'Partons' [9] . This was the first experimental observation of quarks. Whereas in theory, with the discovery of asymptotically free gauge theory in the 70's the whole of theoretical nuclear physics was revolutionized. This laid the basis for "The Standard Model of Particle Physics". Asymptotic freedom also presented us with an interpretation for the observed phenomenon of confinement. Unlike QED, the force between colored charges does not decrease with increasing distance, leading us to believe that the quarks and gluons can never be liberated from an hadron.

Evolution of strong coupling constant as a function of momentum transfer is plotted in figure [1.2]. Currently we treat QCD in two extreme regimes. First being the perturbative regime where quark interactions have large momenta, hence they are high energy, small distance interactions where the quarks are treated as effectively free. The strong coupling constant (α_s) at short distances, high momentum transfer, becomes much smaller than 1 ($\alpha_s < 1$) and perturbative expansions in α_s of the QCD lagrangian becomes valid. QCD has been successful in predicting the hadronic mass spectrum and their dynamics in this region. Second is the non-perturbative regime where quarks and gluons are tightly bound within a hadron. In this region $\alpha_s \sim 1$ and perturbative expansions of the QCD Lagrangian become non-linear and we have to resort to specific hadronic models in order to predict the expected

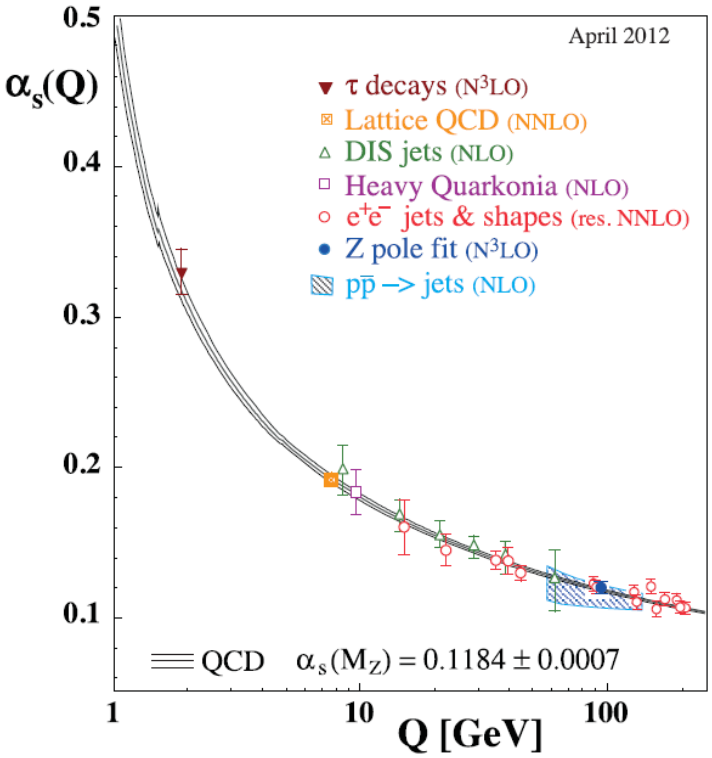

Figure 1.2: Evolution of strong coupling constant as a function of momentum transfer 'Q'. At smaller values of momentum transfer, the strong coupling constant '$\alpha_s' \sim 1$, which does not allow for perturbative treatment of QCD Lagrangian and theory has to resort to specific hadronic models to understand quark dynamics and make predictions. At higher momentum transfer, QCD Lagrangian can be treated perturbatively and this allows theory to make predictions which have already been tested in experiments successfully. Strangeonia spectrum occupies the transition region between these two extremes and can serve as a bridge for understanding the confinement potential in QCD. Image source [17].

hadronic mass spectrum as well as their dynamics. Since the strange quark bare mass is heavier than up and down quarks but is much lighter than the charm quark, strangeonia mass spectrum occupies the transition region between these two extremes and can serve as a bridge in understanding the confinement potential in QCD. Alternatively, the ongoing efforts to solve QCD on a lattice have yielded predictions that can now be validated in experiments [10] [11] [12] [13]. The latest available predictions from lattice QCD for isoscalar mesons are shown in figure [1.3] and the predictions for the states accessible to the analysis are presented in the table [1.1]. Many of these states labeled with their $J^{PC} = \{1^{--}, 2^{--}, 3^{--}, 1^{+-}\}$ are

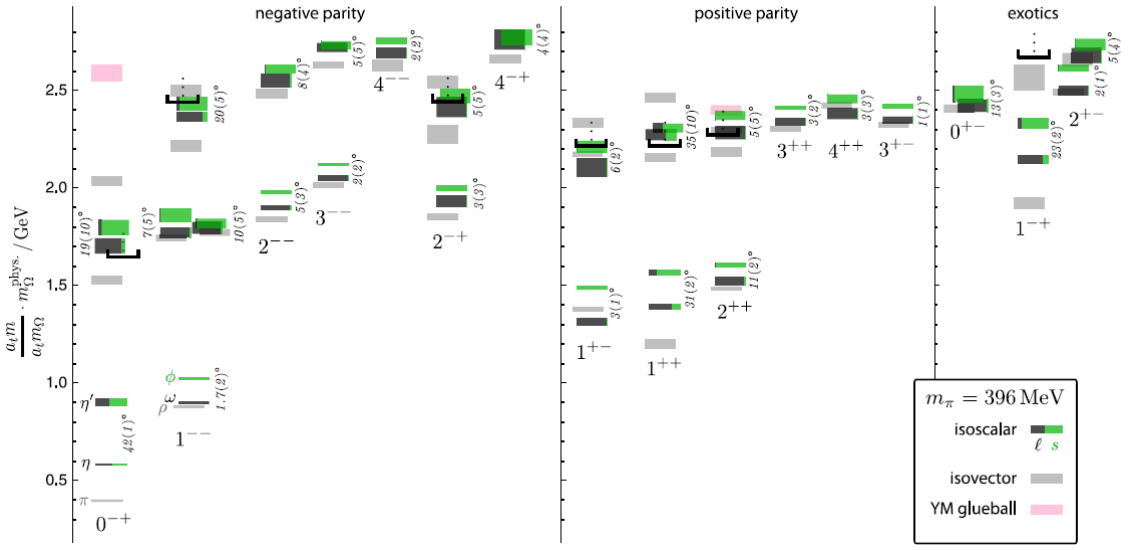

Figure 1.3: Lattice QCD predictions for the isoscalar meson's mass spectra labeled by their J^{PC}. The green boxes are the strangeonia mass with one sigma statistical uncertainty about their central values. The black boxes are for $n\bar{n}$ states, where $n \in \{u, d\}$. The boxes that are partially black as well as green represent the mixed states with their mixing angles stated beside the box and the black:green fraction of the colors representing the light:strange content of the state. Image source [10].

Table 1.1: Strangeonium states expected to be observed in the ϕ η invariant mass distribution, as predicted by Lattice QCD. These values are plotted as green boxes in the figure [1.3] extracted from the reference [10].

JPC	Mass (MeV/c^2)
$1--$	1023
	1819
	1862
$2--$	1979
$3--$	2123
$1+-$	1489

accessible to our strangeonium analysis.

Meson physics and strong interactions have been intricately connected since 1935, when Yukawa first introduced pions [14] to explain the internucleon force. Mesons make for ideal

studies of strong interactions in the strongly coupled non-perturbative regime in order to understand QCD [15] [16]. Every physical meson state spans over a basis of all the states allowed by QCD, like over $\{\ |q\bar{q}\rangle \quad |q\bar{q}g\rangle \quad |gg\rangle \quad |q\bar{q}\rangle^2 \quad . \ . \ .\}$. The amplitudes of the basis expansion for a meson are determined naturally by QCD interactions. We conveniently 'classify' a state as a meson, hybrid, glueball or something else depending on the most prominent state in the basis expansion for the resonance.

1.2 Meson Spectroscopy

Quarkonia are quark-antiquark ($q\bar{q}$ pair) meson states where the quark and the antiquark flavors are the same $\{u\bar{u}, d\bar{d}, s\bar{s}, ...\}$. These states are referred to as meson states with hidden flavors. Strangeonia are meson states for which the flavor wave function for the meson is primarily $s\bar{s}$. These are purely strange states with hidden strangeness. The strange quark has a higher bare mass than the up and the down quark, and hence strange meson states are expected to populate higher meson mass states as we see in the case of pions and kaons. Most mesons are not pure $q\bar{q}$ states but a linear superposition of a combination of allowed quark, antiquark and gluon $\{q\bar{q}, q\bar{q}g, q\bar{q}q\bar{q}, gg, ...\}$ basis vector states.

Meson spectroscopy is a broad field dedicated to the study of the mass spectrum and the quantum numbers of the observed and expected mesons and their decay channels, decay widths, production mechanism and other physical attributes, in order to gain an insight into QCD and its interactions. It assists to place the known physics on firmer experimental and theoretical grounds and acquire a handle on, as yet unknown, physics and phenomena in nature.

A principal goal of meson spectroscopy is to observe and identify states known as exotic mesons. These are states $\{q\bar{q}g, q\bar{q}q\bar{q}, gg, ...\}$ that are predicted by QCD to exist but are inaccessible to the regular quark model [17] states.

1.3 Motivation

Constituent Quark Models (CQMs) picture a nucleon as a color neutral set of three valence quarks. The flavors of these valence quarks determine the nature of the nucleon. Similarly, a meson's nature is determined by the flavor of its valence quark and antiquark

Table 1.2: Meson classification and their constituent structure.

Usual Mesons	EXOTICA			
Quark Model Mesons	Gluonic Hybrids	Tetra-quarks	Glue-Balls	...
$q\bar{q}$	$q\bar{q}g$	$q\bar{q}q\bar{q}$	gg	$\dots$

pair. An exotic meson is a resonance with J^{PC} or other quantum number forbidden to $|q\bar{q}\rangle$ states of the non-relativistic or the conventional quark model [3] [18] [19].

1.3.1 Quick overview of the quantum numbers

In the constituent quark model, conventional mesons are bound states of a spin $\frac{1}{2}$ quark and a spin $\frac{1}{2}$ antiquark. The quark and antiquark spins combine into a spin singlet or triplet state with total spin $S = 0$ or 1 respectively. S is coupled to the orbital angular momentum L to give total angular momentum $J = L$ for the singlet state and $J = L - 1,\ L,\ L + 1$ for the triplet states. In spectroscopic notation the resulting state is denoted by $n^{2S+1}L_J$ where n is analogous to Principal quantum number, with S for $L = 0$, P for $L = 1$, D for $L = 2$, and so on. For example, the lowest state for a vector meson with $J^{PC} = 1^{--}$ is the 1^3S_1 quark model state.

A parity operation on a system implies simultaneously inverting the direction of all of its cartesian coordinates, i.e. {x,y,z} $\Leftrightarrow$ {-x,-y,-z}. Hence, the parity for a meson is given by $P(q\bar{q}, L) = (-1)^{L+1}$, where '$-1^L$' contribution comes from the spherical harmonic function of the spatial part of the wave function of the meson and '-1^1' comes from the product of the intrinsic negative parity of the antiquark and the intrinsic positive parity of the quark in the meson.

A charge conjugation operation changes a particle into its antiparticle and vice versa. Hence the C-parity is only defined for the neutral self-conjugate mesons and is given by $C(q\bar{q}, L, S) = (-1)^{L+S}$. The '$-1^L$' contribution comes from the spherical harmonic function for the spatial part of the wave function of the meson, since the quark and the antiquark have, in effect, exchanged positions in space under charge conjugation. Since the quark and

the antiquark have in effect swapped positions, the spin quantum number for each must also change its sign. If the meson system was in an initial spin-0 configuration, charge conjugation produces no net effect. But if the meson system was initially in a spin-1 configuration, the charge conjugation operation, in effect, flips the spin projection. This behavior of the quark-antiquark spins is straightforwardly incorporated into the calculations of net effect of charge conjugation on the meson wavefunction by adding a contribution of -1^S.

For the members of an isospin triplet there is another quantum number, G-parity, which is defined as $G \equiv C_n(-1)^I = \pm 1$ and has the same value for all members of the triplet, where C_n is the C-parity of the neutral member. G-Parity, just like C-Parity, quantifies the behavior of a meson under charge conjugation. For an isospin triplet, $I = 1$ meson, a charge conjugation operation flips the charge of the meson. The charge conjugation changes the isospin projection $I_z = \pm 1$ meson into a $I_z = \mp 1$ meson. To transform the meson to its original isospin projection, a isospin flip is employed. To generalize this behavior of an isospin triplet under charge conjugation, along with the C-Parity an additional contribution of -1^I is added for the G-parity. G-parity is a near exact symmetry of strong interaction for light quarks because of the inherent approximate nature of isospin for the light quarks [18]. The approximate nature of isospin is due to the similar bare masses of the up and the down quark for the light mesons.

1.3.2 Exotic and hybrid mesons

An exotic meson is defined as a state orthogonal to $|q\bar{q}\rangle$ states of the non-relativistic quark model, i.e. a non-$q\bar{q}$ meson. An exotic can thus possess J^{PC} spin parity or other quantum numbers forbidden to quark model resonances [19]. A gluonic hybrid meson is a resonance for which the dominant component in the basis expansion is $|q\bar{q}g\rangle$. In principle, gluonic hybrid mesons are able to have all possible J^{PC} states including those which are not accessible to the conventional $|q\bar{q}\rangle$ meson state. If we are to observe and identify any exotica, hybrid meson spectra needs to be studied and documented carefully. This will help us distinguish between the two spectra. A certain amount of configuration mixing naturally occurs between these states. Mesons with J^{PC} quantum numbers inaccessible to $q\bar{q}$ states are called spin-parity exotics [20]. All states not allowed by the quark model, i.e. non-$q\bar{q}$ states, are exotic states, even though they might not possess the exotic quantum numbers.

$$\mathrm{J}^{PC}\Big|_{exotic} = 0^{--}, 0^{+-}, 1^{-+}, 2^{+-}, 3^{-+}, \ldots \ .$$

Since gluons carry color charge and hence self-interact, they are predicted to form quark-free color neutral states called glueballs. For baryons there are no J^P exotics and a hybrid baryon resonance would be observed by an overpopulation of experimental baryon states relative to the qqq spectrum. Two current popular models for Hybrids are the MIT bag model & Flux-tube Model. These models have a specific interpretation for their "excited glue" component [19] [20] [21] [22].

1.3.3 Constituent Quark Models

Bag Model: The MIT bag Model treats quarks and gluons as spherical cavity modes of Dirac and Maxwell quanta, confined within the cavity by the choice of color boundary conditions. The zeroth-order states are $\{\ |q\bar{q}\rangle \quad |q\bar{q}g\rangle \quad |gg\rangle \quad |q\bar{q}\rangle^2 \quad \ldots\}$. These bare basis states are mixed by quark-gluon and gluon self interactions to give physical states. In the bag model the lowest quark mode is a $J^P = 1/2^-$ mode while the lowest gluon mode is $J^P = 1^+$. Combining these lowest lying modes, we obtain hybrid basis states with the following spin-parity quantum numbers:

$$\mathrm{J}^{PC}\big|_{\text{bag model}} = (0^-, 1^-) \otimes 1^+ = 1^{--}, 0^{-+}, 1^{-+}, 2^{-+} \ .$$

Flux-tube Model: The flux-tube model is a Lattice QCD inspired description of combined gluonic degrees of freedom with quark degrees of freedom. In Lattice Gauge Theory simulations, a roughly cylindrical region of chaotic glue fields is observed between widely separated static color sources. This flux-tube can be excited contributing to the dynamics of the system. The flux-tube is the origin of the confining linear potential between the $q\bar{q}$ meson color singlet, familiar from the quark potential models. An excited flux-tube's orbital angular momentum when combined with the $q\bar{q}$ spin and angular momentum gives us the flux-tube hybrid spectra,

$$\mathrm{J}^{PC}\Big|_{\text{flux}-\text{tube hybrids}} = (0^{-+}, 1^{--}) \otimes (1^{+-}, 1^{-+}) = 0^{-+}, \underline{0^{+-}}, 1^{--}, \underline{1^{-+}}, 1^{+-}, 1^{++}, 2^{-+}, \underline{2^{+-}} \ .$$

The underlined J^{PC}'s are exotics and not allowed for conventional $q\bar{q}$ states. We are looking to identify the discrepancies between the observed meson spectrum and and the conventional quark model predictions which may signal new physics beyond conventional hadron spectroscopy.

Lattice QCD: In Lattice QCD (LQCD), space-time is treated as a 4-dimensional grid created of discrete points, like those of a 3-dimensional crystal lattice, which are connected to each other by lines. A quark can be located at any point whereas a gluon can only travel along the lines joining these points. So in LQCD, the space-time is in effect treated as a crystal lattice of a lattice spacing 'a'. As the lattice spacing is decreased, we move towards a more realistic description of QCD. LQCD is computationally very intensive and has been making progress towards giving a more realistic description consistent with the experiments [10] [11] [13] [12].

1.4 Strangeonia

Strangeonia are unflavored $s\bar{s}$ mesons primarily associated with the excited radial and orbital states of the ground state $s\bar{s}$. The study of strangeonium states can serve as a bridge between short and large distance behavior of the QCD confinement potential because of the intermediate mass of the strange quarks between light mesons and the charmonium sector. Excitations of $s\bar{s}$ provide a range of quark separations, where the confinement potential can be studied from the perturbative to the non-perturbative regime, i.e from high momentum q^2 to low momentum q^2 transfer. Understanding of the $s\bar{s}$ spectrum will help us bridge the gap between Heavy Quark Effective Theory (HQET) and the abundant light quarks around us. Of the 22 expected strangeonium resonances below 2.2 GeV, predicted by theory [3], only 7 probable resonances - $\eta\ \eta'$, $\phi(1020)$, $h_1(1386)$, $f_1(1426)$, $f_2'(1525)$, $\phi(1680)$ and $\phi_3(1854)$ are well identified where we count the maximally mixed $\eta\ \eta'$ as one resonance [3]. Of these, the $h_1(1386)$ still needs additional confirmation. Decay branching ratios for the golden decay mode $\phi\ \eta$ and the states accessible to it, as predicted by the '3P0' model calculations are listed in table [1.3], along with their current observational status.

Recent observations were made by the BaBar Collaboration of a stucture at 2175 MeV/c^2 in the $\phi f_o(980)$ recoil mass in $e^+e^- \to \gamma_{ISR}\ \phi\ f_o(980)$ [2]. If Y(2175) is a tetraquark state, due

Table 1.3: Theoretical predictions for the strangeonium states expected to be observed in the $\phi\ \eta$ invariant mass distribution from the reference [3].

State	Predicted Decay Width Theory MeV/c^2	Observed Decay Width Expt. MeV/c^2
$\phi(1680)$ 2S	$\Gamma_{theory} = 378$ $\Gamma_{\phi\eta} = 44$	$\Gamma_{expt} = 150 \pm 50$
$\phi(2050)$ 3S	$\Gamma_{theory} = 378$ $\Gamma_{\phi\eta} = 21$	Γ_{expt} = unknown
$h_1(1850)$ 2P	$\Gamma_{theory} = 193$ $\Gamma_{\phi\eta} = 33$	Γ_{expt} = unknown
$\phi_3(1854)$ 1D	$\Gamma_{theory} = 104$ $\Gamma_{\phi\eta} = 3$	$\Gamma_{expt} = 87^{+28}_{-23}$
$\phi_2(1850)$ 1D	$\Gamma_{theory} = 214$ $\Gamma_{\phi\eta} = 53$	Γ_{expt} = unknown
$\phi(1850)$ 1D	$\Gamma_{theory} = 652$ $\Gamma_{\phi\eta} = 29$	Γ_{expt} = unknown
$h_3(2200)$ 1F	$\Gamma_{theory} = 249$ $\Gamma_{\phi\eta} = 5$	Γ_{expt} = unknown

to C-parity and G-parity conservation the state would preferentially decay via $\phi\ \eta$ decay mode. This state also lends itself to the possibility of being the lightest strangeonium hybrid ($s\bar{s}g$) as hypothesized in reference [16]. This state has been tagged as a 1^{--} strangeonium hybrid [2] [24], and lies at the higher edge of the possible observational $\phi\ \eta$ invariant mass in g12.

Photoproduction of mesons occurs primarily through Vector Meson Dominance (VMD). During a hadronic interaction a photon oscillates into a $q\bar{q}$ pair conserving its spin parity $J^P = 1^-$. Hence we can now consider the vector photon as a vector meson (ρ, ω, ϕ) with a high content of $s\bar{s}$ and depending on the phasespace and dynamics, we expect to observe the radial excitation $\phi(1680)$ of the ground state $s\bar{s}$ vector meson $\phi(1020)$. This state has been observed in e^+e^- production and disputed in photoproduction [25] [17]. Past photoproduction experiments have observed the mass of a resonance near 1750 MeV/c^2 as an

enhancement in the mass of K^+K^- [26] [23]. The majority of experiments before FOCUS had low statistics with about a few hundred events at most. These experiments also assumed that any observed state was a diffractively photoproduced vector meson. Hence an observation near 1750 MeV/c^2 was identified with the $\phi(1680)$ from the e^+e^- experiments [17]. In e^+e^- production the $\phi(1680)$ mass averages nearer to 1680 MeV/c^2 , while in photoproduction the mass for the presumably same resonance is closer to 1750 MeV/c^2 . It was originally thought that these observations were of the same resonance with the mass shift due to interference effects with other decay channels. The FOCUS experiment at Fermilab has claimed that the structure in photoproduction at 1750 MeV/c^2 is a different resonance [25]. The $\phi(1680)$ resonance has been clearly established in e^+e^- production with the dominant decay channel being KK^* ($e^+e^- \rightarrow K_sK\pi$). Meanwhile, FOCUS has measured the $\phi(1750)/X(1750)$ mass to be 1753 MeV/c^2 with its dominant decay mode being K^+K^-. FOCUS found no photoproduced enhancement in its sample for KK^* corresponding to the 1750 MeV/c^2 state in K^+K^- and they place a strong upper limit for this branching ratio. They cite interference effects as a possible, but unlikely, reason for this resonance and they claim $X(1750)$ to be a new state, different from the radial $\phi(1680)$. Hence, the $\phi(1680)$ resonance either behaves differently because of its production mechanism, or its an altogether different resonance [25]. This issue is still an open question. The FOCUS observation is cited under and included with the $\phi(1680)$ in PDG and is not as of yet listed as a separate state [17]. Therefore, the $\phi(1680)/X(1750)$ meson state, possibly a strangeonium state, is a good obvious strangeonium candidate to search for in the $\phi\eta$ decay mode in the g12 experiment.

Another interesting decay mode accessible to g12 in the (proton K^+ K^-) final state is the $\phi\pi^o$, which is an exotic decay channel for a meson. Decay of an initial $s\bar{s}$ (I=0) meson via this channel is forbidden on account of the conservation of isotopic spin, since the $\phi\pi^o$ decay mode possesses the isospin (I=0+1=1). Another possibility is that the decay occurs from an initial $n\bar{n}$ state via the $\phi\pi^o$ decay mode of isotopic spin (I=1). This decay is then forbidden by the (empirical) Okubo-Zweig-Iizuka (OZI) rule and is strongly suppressed, and hence any observation we make of a meson decay via the $\phi\pi^o$ decay mode is of a rare nature. Another possibility is that the initial meson state is an exotic state like a gluonic excitation - $q\bar{q}g$ or a tetraquark state - $q\bar{q}q\bar{q}$. In any of these cases, observation of a meson resonance

decaying to $\phi\pi^o$ provides evidence of dynamics for mesons beyond $q\bar{q}$, probably of a gluonic excitation - $q\bar{q}g$ or a tetraquark state - $q\bar{q}q\bar{q}$ [4].

Physics is also a lot of bookkeeping and filling in the blanks exercise. To that end, we estimate the yield for the rare $\phi\omega$ events as well as cross section for the exclusive ϕ mesons in the g12 photoproduction data, since these states are accessible to our analysis.

1.5 Analyses presented in the thesis

We analyze the data obtained from our g12 runperiod to study the final state :

$$\gamma \;\; p \;\; \rightarrow \;\; p \;\; K^+ \;\; K^- \;\; [X] \tag{1.1}$$

In photoproduction reaction [1.1], an additional neutral particle such as a π^0, an η or an ω goes missing or undetected in CLAS. The missing particle is identified and selected using the energy-momentum conservation constraints placed on the missing mass for the event. Identifying an intermediate ϕ meson will allow access to study the $\phi\eta$, $\phi\pi^0$ and possible $\phi\omega$ states. Of these, the $\phi\eta$ channel can only arise from an initial $s\bar{s}$ state in accordance with the Zweig rule and thus will interfere negligibly with $n\bar{n}$ ($u\bar{u} \;\pm\; d\bar{d}$) states. This analysis should be able to help clarify the issue of $\phi(1680)/\phi(1750)$ further. For the $\phi\eta$ system, we will analyze the channel $\gamma p \rightarrow pK^+K^-[\eta]$, where we expect the proton to act as a spectator in a low momentum transfer, t-channel reaction. The final state of *proton*, K^+ and K^- will be selected and an intermediate ϕ state identified by selecting on the invariant mass of the K^+K^- system. Using energy-momentum conservation, a missing η will be identified and the invariant mass for the ϕ and the missing η system will be reconstructed to observe possible resonances. Similar techniques will also be used to look for other decays in various channels like the exotic $\gamma p \rightarrow pK^+K^-[\pi^0]$ and $\gamma p \rightarrow pK^+K^-[\omega]$. Both $\phi\pi^0$ & $\phi\omega$ channels are exotic as they are OZI suppressed decays for $q\bar{q}$ mesons [27] [4] as well as for the exclusive ϕ meson photoproduction.

CHAPTER 2

CLAS

Data analyzed for this thesis was acquired during the experimental runperiod 'g12' [1], by the CLAS detector [28], located at the Thomas Jefferson National Accelerator Facility (TJNAF, see figure [2.1]) in Newport News, Virginia, USA. The facility is popularly known as Jefferson Lab (JLAB). The experiment collected data from April 1, 2008 to June 9, 2009 over 70 calendar days and acquired 26.2 billion triggers (events of interest). This amounts to 68 pb^{-1} of physics data, spread over 63010 raw data files, each of $\sim$ 2 GB, occupying $\sim$ 126 TB of memory space on tape. After calibration and reconstruction, the g12 data available for final analysis had expanded by a factor of 3.

2.1 Jefferson lab

Jefferson Lab is one of 17 national laboratories funded by the U.S. Department of Energy. The lab also receives support from the City of Newport News and the Commonwealth of Virginia. The lab's primary mission is to conduct basic research of the atomic nucleus using the lab's unique particle accelerator, known as the Continuous Electron Beam Accelerator Facility (CEBAF) [29] [30] [31]. Jefferson Lab also conducts a variety of research using its Free-Electron Laser (FEL), which is based on the same electron-accelerating technology used in CEBAF. Jefferson lab engages in extensive outreach programs to engage the general public and educate students in science and technology, through organizing tours, seminars and simple experimental demonstrations for science education.

Fixed-target collision experiments for medium energy particle physics are carried out at JLAB. A particle beam comprising of either electrons or photons is incident on stationary

Figure 2.1: Aerial view of Jefferson Lab, outlining the not-visible injector, linacs, recirculation arcs and the various experimental halls. Image source [32].

targets in order to probe the structure of a nucleus. The resulting collisions and their outcome (various resonances produced) aid us in understanding the fundamental interactions and properties of the basic building blocks of our world. There are currently three operational experimental halls at JLAB - Hall-A, Hall-B, and Hall-C. Different experimental halls house different detectors, running separate experiments with varied physics objectives. This adds to the strength of the particle physics program at the JLAB, allowing it to investigate the physics through multiple-pronged experimental approaches. The facilities are used by researchers of 374 institutions from 42 countries, including 195 institutions from USA.

The most comprehensive resource to learn about CEBAF, CLAS and its components is its Nuclear Instrumentation paper [28]. Majority of the images and schematics related to CEBAF, CLAS, tagger and its components used in this thesis are sourced from the picture

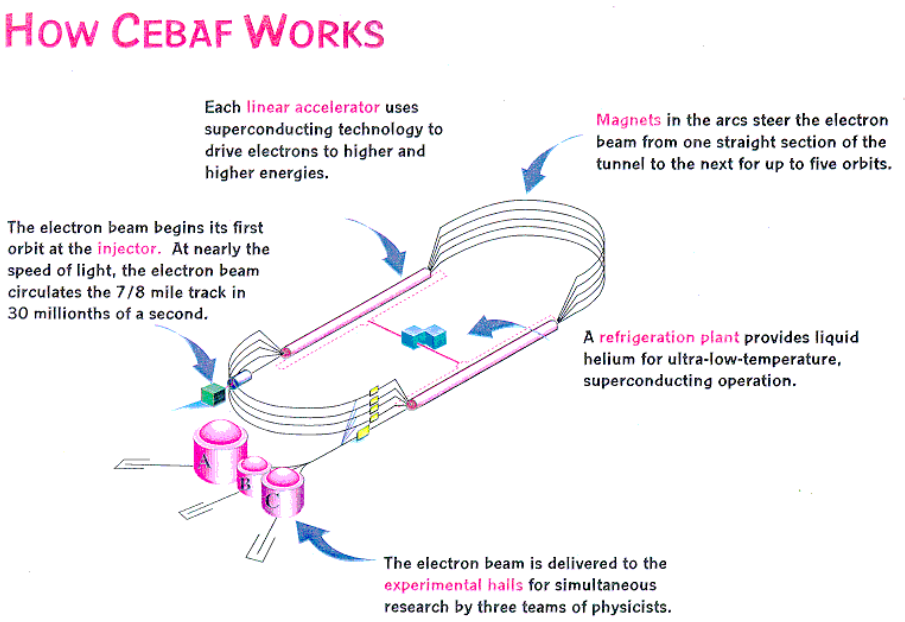

Figure 2.2: CEBAF's working schematic indicating its major components and their functioning. Image source [32].

exchange located at the JLAB website [32].

2.2 CEBAF

The 'Continuous Electron Beam Accelerator Facility' (CEBAF) 2.2 at the Jefferson Lab is an electron accelerator based on superconducting radio-frequency (SRF) technology dedicated to the investigation of the electromagnetic structure of mesons, nucleons, and nuclei. It produces high power electron beams with energies up to 6 GeV and and the derived bremsstrahlung photon beams with 100% duty cycle in its current configuration [28] [29] [30] [31].

CEBAF was the first large-scale application of SRF technology in the world, and it is the world's most advanced particle accelerator for investigating the quark structure of the atom's nucleus [33]. CEBAF accelerator consists of a polarized electron source, an injector, and a pair of superconducting RF linear accelerators (LINACs) connected to each other by two arc sections containing steering magnets in a horse race-track design, with a total track length of $7/8^{th}$ of a mile (1400 m). The accelerator is built 8 meters, or approximately

25 feet, below the earth's surface, and the walls of the accelerator tunnels are 2 feet thick. CEBAF uses liquid helium to cool niobium RF cavities to approximately 2K (-456^{o}F), which removes electrical resistance and allows for the most efficient transfer of energy to an electron. To this end, JLAB houses the world's largest liquid helium refrigerator. Jefferson lab's accelerator division is responsible for delivering high-quality electron beams for experiments and maintaining and operating CEBAF. They accomplish this with control over hundreds of thousands of hardware components, including complex cryogenic, microwave, vacuum and magnet systems that comprise the accelerator through advanced computer systems. They are responsible for steering an acceptable quality of beam into the experimental halls. The halls are, individually, in constant communication through various interfaces during the data-taking runperiod with the CEBAF Main Control Center (MCC) to ensure successful data acquisition for their experiments. The accelerator group at JLAB also pursues a broad program of theoretical and experimental research in accelerator and beam physics.

An electron's journey begins at the injector. Electrons are obtained by illuminating a GaAs photo-cathode with pulsed lasers. The laser pulses are fixed temporally such that each experimental hall is able to receive electron bunches every 2 ns. Injector provides beam to the main accelerator's two recirculating linacs connected by the beam transport arcs. CEBAF operates at 1497 MHz, delivering beam to each experimental hall at 499 MHz, one third of the linac frequency. This is to allow simultaneous operation of the three halls. Three beams are typically produced in the injector, each at 499 MHz with 120 degrees phase separation [31]. CEBAF design allows the electron beam to be 'continuous' rather than the 'pulsed' beam typical of ring shaped accelerators. There is a beam structure to the CEBAF beam but since the pulses are so short and close together - spatially as well as temporally, their delivery is considered as continuous for experimental purposes and detector operation. This translates to the presence of multiple temporally close beam bunches of extremely narrow spatial dimensions and of different energies and intensities present inside the linac at any given time.

2.2.1 Injector

Figure [2.3] shows the general layout of the injector. It shows the elements related to bunching and timing of the beam, starting with 100 KeV photo-cathodes located in the

electon gun. A single gun is in use at any given time, the other gun being a hot spare. The next element is the pre-buncher cavity, followed by emittance limiting apertures A1 and A2. The three-beam chopper system assures initial timing and longitudinal structure of the beam. This system operates at 499 MHz with three independently variable slits to define a phase acceptance from 0 to 110 ps for each beam. Any beam outside this window would not go correctly through the bunching and acceleration process, and therefore is stopped at the choppers. After this stage, the buncher starts the main bunching of the beams. The capture section provides beam acceleration to 500 KeV. The phase and amplitude of buncher and capture cavities are crucial to the beam bunch length and energy spread. A pillbox cavity after the capture section is part of a diagnostic system used to tune the beam bunch length by measuring the beam timing. In the next stage, the beams are further bunched and accelerated to 5 MeV by the first two SRF cavities. Finally, there are two accelerating modules, each containing 8 SRF cavities, which accelerate the beams to a final energy, typically 23 to 68 MeV. At the end, the beam passes through a chicane before joining the re-circulated beams in the main machine. There are 3 Faraday cups in the injector to measure the beam current at different stages. The machine setup from gun to 5 MeV is independent of the final energy of the injector. The magnetic elements in the injector provide transverse focusing and steering of the beam. MCC uses this to control the beam size through several apertures in the injector. Measurements with typical beam currents show a final bunch length of less than 1 ps and fractional energy spread of less than 0.1%, both well within the requirements of the main accelerator [31].

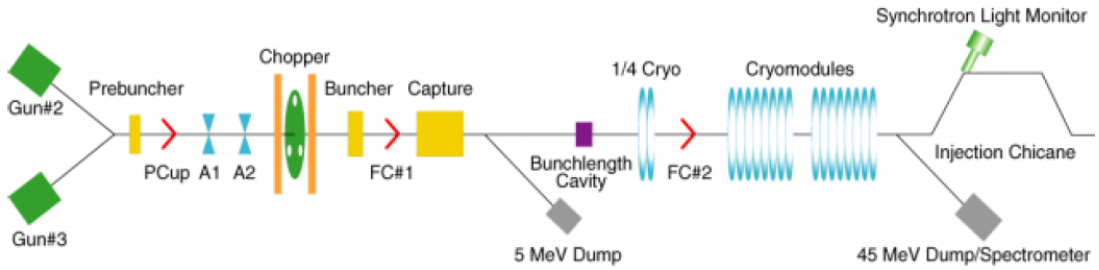

Figure 2.3: Injector's cartoon showing components for photo-producing, bunching and accelerating the beam electrons up to the point where they are ready to be injected into the linac. Image source [32].

2.2.2 Niobium RF Cavities

Each of the linacs consists of twenty cryomodules, with each module containing eight superconducting niobium cavities maintained at 2K using liquid Helium. A standing radio-frequency electromagnetic wave is induced inside the niobium cavities to provide the beam acceleration. These RF standing waves are kept in phase with the electron bunches, such that there is a continuous positive electric force on each bunch as it passes through the multi-cell cavity. To this end, the length of a cell is chosen such that the field direction is inverted when the relativistic electron bunch moves from one cell to the next. The microwave energy stored in the resonant mode of the cavity is transferred to the electron via this acceleration gradient. Accelerating gradient is the accelerator's ability to boost electrons' energy by a given amount within a given distance. This SRF operation generates a very large heat load which needs to be quickly and precisely dissipated. Niobium cavities maintained in 2K heat bath become superconducting, which causes their resistance to vanish for direct current (DC) but not for the alternating electromagnetic field of the applied RF. In the microwave cavity, the oscillating magnetic field of the RF wave penetrates into the superconductor to a depth of about 50 nm and induces forced oscillations of those electrons which are not bound in superconducting BCS pairs [34]. Even though the microwave surface resistance is many orders of magnitude smaller than that for a normal copper cavity, it is responsible for non-negligible Ohmic heat generation at the inner cavity surface. This heat is guided through the cavity wall into the liquid-helium bath and constitutes a significant heat load on the helium refrigeration handled by the Central Helium Liquefier (CHL), which is a large refrigerator located in the middle of Jefferson Lab's accelerator. CEBAF currently uses a mixture of 5-cell and 7-cell Niobium cavities operating at 1497 MHz where both the cavities have same-shaped cell. CEBAF recently completed the C50 cryomodule refurbishment project to increase the peak effective voltage of the refurbished cryomodules to a maximum of 50 MV. The project undertook removal, refurbishment and reinstallation of ten CEBAF cryomodules at a rate of three per year. The refurbishment process included reprocessing of SRF cavities to eliminate field emission and to increase the nominal gradient from the original 5 MV/m to 12.5 MV/m for these cavities. To increase these gradients, field emission and arc rates for the cavities needed to be reduced. Hence inner surfaces of the cells were polished to a

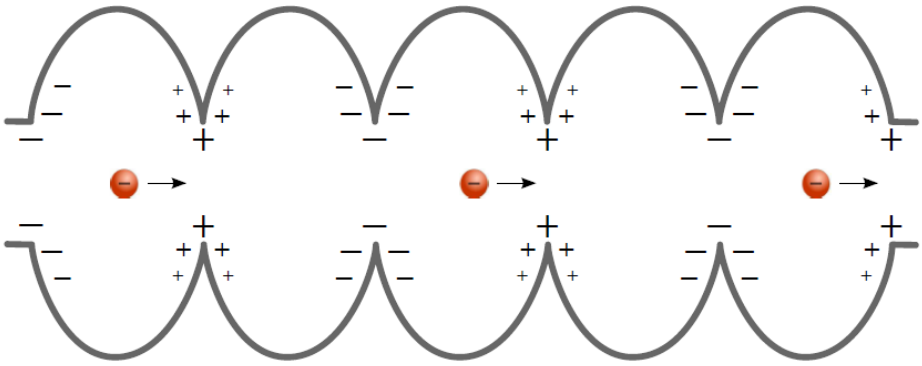

(a) RF-induced cavity charge accelerates the beam electrons through the cavity. As the electron traverses from one cell to the next, the RF-phase induces the appropriate charge distribution to maintain positive acceleration on the electrons. This is the mechanism for the transfer of RF microwave energy from the cavity to the beam electron.

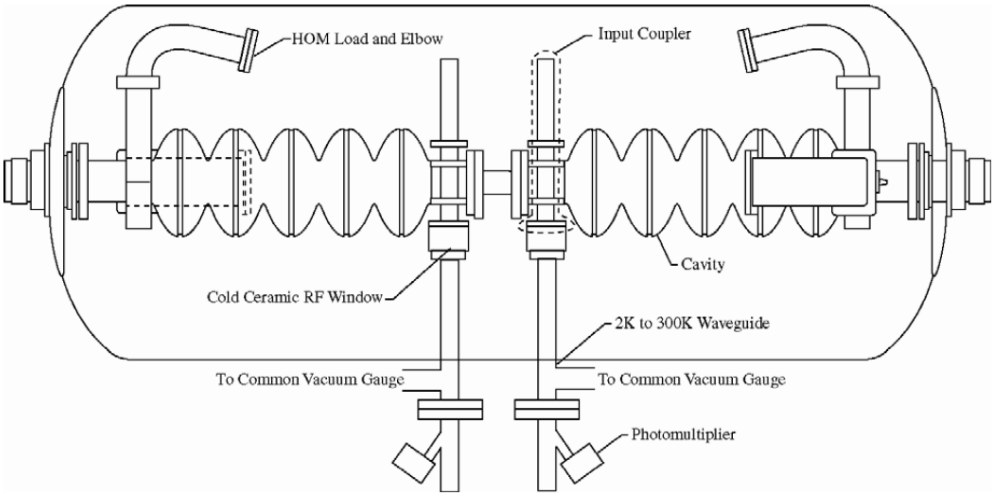

(b) Cavity Pair Diagram labeled with all its essential components.

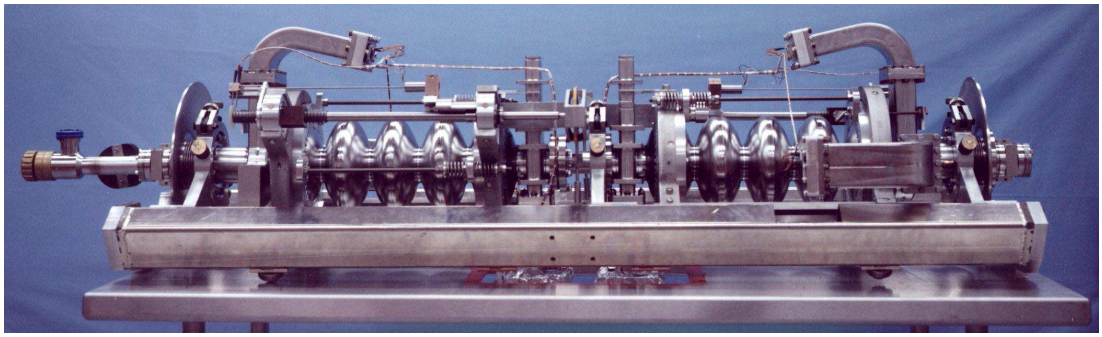

(c) Cavity Pair with its support hardware and beam-pipe before complete assembly and being transferred to the linac.

Figure 2.4: Design Concept of RF Cavities. Image source [32].

very high smoothness, and made free of impurities, as tiny surface blemishes or dust could cause cavities to lose the superconductivity, and prevent the cavities from sustaining the electric field needed for accelerating particles. In a cleanroom, cavities were subjected to an acid etch followed by high pressure rinsing with ultra pure water to eliminate particulate contamination from the surface of the cavities and as a result eliminate field emission. The RF window and waveguide attached to each cavity were replaced with a new "dog-leg" configuration that significantly reduces the risk of charging and trips from the field emissions [30].

Other changes included new ceramic RF windows for the air to vacuum interface of the fundamental power coupler and improvements to the mechanical tuner. Damaged or worn components were replaced as well. For almost all of the cavities, field-emission-induced radiation was eliminated in the operating range of interest, leading to a more robust 6 GeV CEBAF operation. To generate the standing microwave in these cavities that drive the electron beam in the linac, each cavity requires a separate klystron, with each providing a maximum drive power of 5 kW. To transfer energy from the klystrons to the cavity, RF couplers are used. In general, there are two types of RF power couplers for a given superconducting accelerator cavity. Fundamental Power Couplers (FPC) deliver energy to a cavity, and Higher Order Mode (HOM) couplers are used to extract or dissipate RF energy present in the cavity due to the radiative excitation of the cavity by the particle beam [30] [34] [35] [36]. The FPC is used to excite the resonant structure to build up stored energy in the fundamental acceleration mode of the cavity. HOMs are used to extract RF power from the cavity at frequencies above the fundamental, thereby damping the modes and decreasing their ability to degrade the beam quality and increase cryogenic load of the system. RF couplers are, in a most general sense, the assemblage of hardware and components needed to couple RF energy into or out of a resonant accelerating cavity.

CEBAF's RF system consists of a stable master oscillator, a phase distribution system, and the individual drive chains for the 320 superconducting cavities in the linacs and for the three drive lasers, two choppers, a buncher, a capture section, and 18 superconducting cavities in the injector. The drive chains, one per cavity, consist of the RF control module, the high-power amplifier (HPA) containing the klystron, and the waveguide feeding the

Figure 2.5: Linac's assembly with its cryomodules inside the beam tunnel. Image source [32].

cavities. A probe signal from each cavity is fed to its control module, thereby closing the feedback loop. The racks for RF controls are located in the service buildings at grade level above the tunnel [29] [30].

2.2.3 LINACs

After undergoing the 600 MeV linear acceleration in the Niobium SRF cavities of the LINAC 2.2, the electrons arrive at the bending arc. Magnetic recirculation arcs that bend and recirculate the beam are located at both ends of the linacs; four on the west side and five on the east side. A beam switch-yard separator allows MCC to extract the beam with a chicane from the appropriate recirculation arc after 1-5 passes to the target hall beamline. Separate recirculation arcs require differing magnetic field strength depending on the incoming beam electron energy. A chicane magnet at the end of each linac separates the beam into their different mono-energetic paths, which are then again merged back, at the entry to the other linac to form a single beam.

(a) North Linac Beam Spreader. The blue boxes on the beam-lines are powerful electromagnets required to split a multi-energy beam into its mono-energetic components.

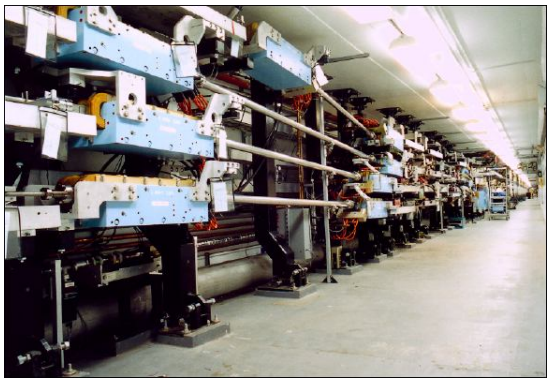

(b) North Linac Beam Recombiner. The blue boxes on the beam-lines are powerful electromagnets required to join the mono-energetic components of the electron beams into a single multi-energy electron beam.

Figure 2.6: Recirculating arcs of CEBAF. Image source [32].

When the beam passes through the large blue electromagnet, as seen in figure 2.6a, the electrons that are on their first trip (lowest energy) around the accelerator in the north linac, get bent a lot and end up near the ceiling. The electrons that are on their fifth pass (highest energy) are barely affected by the magnet and stay near the floor. This happens with the spreader magnet at the beginning of each recirculation arc and now each pipe has electrons with only one energy, so they will all bend the same when they are further bent by other magnets. After the beam makes a 180° turn, we recombine all the separate mono-energetic bunches into a single electron beam. This is done by the recombiner magnets. In figure 2.6b, you will see the blue boxes, that are electromagnets used to put all of the electrons back into one pipe to recreate the electron beam which now gets further accelerated by the other linac. Similar apparatus exists at the other end, which again separates, bends and recombines the beam to give us the recirculating electron beam bunches.

CEBAF is able to deliver this electron beam temporally separated in 2.004 or 3.006 ns bunches to the three experimental halls simultaneously at Jefferson Lab. The beam reaches the three end-stations called Hall-A, Hall-B, and Hall-C in up to 5 passes, where each pass adds in another 1.2 GeV of energy to the circulating electron beam bunch. It can deliver different beam energies as well as different beam currents to the different halls, making

Jefferson Lab a very versatile experimental facility. This beam can be circularly or linearly polarized, as per the requirements and the agreement of the individual halls taking data. Beam current intensities for Hall-A and Hall-C are generally in the range of 5-100 μA while for Hall-B it is generally 5-100 nA, primarily due to the different nature and capabilities of the detectors and the experiments conducted in the Halls. The electron beam makes up to five successive orbits, depending on each hall's experimental requirements and its energy is increased up to a maximum of 6 GeV. It gains $\sim$ 0.6 GeV in energy in every single pass through a linac. This number can be tweaked lower if one of the halls require a different even integral multiple of this energy, with an agreement between the different halls and the MCC. At its highest, each orbit currently allows the electron beam a gain of 1.2 GeV. During the ongoing 12 GeV upgrade, CEBAF is going to double this energy gain per pass to 2.4 GeV. This will be accomplished by - adding in 5 more higher voltage cryomodules to each linac, doubling the cryo-capacity for the accelerator, upgrading the magnets, and the power supplies.

2.3 Hall-B

Hall-B, as seen in figure 2.7, is capable of running both electroproduction as well as photoproduction experiments. The primary experimental programs undertaken at Hall-B span a broad range of interests in particle physics. Hall-B users perform Deeply Virtual Compton Scattering (DVCS) experiments to study and determine the Generalized Parton Distributions (GPD), which is the three-dimensional imaging of the nucleon's quark structure. They also perform electroproduction and photoproduction experiments to study the electromagnetic excitations of hadrons, to study the quark-gluon interactions in nuclei, and for characterizing nucleon-nucleon correlations in nuclei. Hall-B users are also involved in the search for existence of the heavy photons. To accomplish all these varied physics goals and experiments, it houses two very large detectors, tagger and CLAS. Hall-B, at a diameter of 65 feet and the height of 98 feet, is shaped like an elongated sphere and is the smallest of the 3 experimental Halls at Jefferson Lab. The dome of the hall protrudes to form one of the largest "hills" in Newport News. The hall houses JLAB's largest detector, 'CLAS', which serves as a spectrometer for the final state particles, and the 'tagger', used to measure

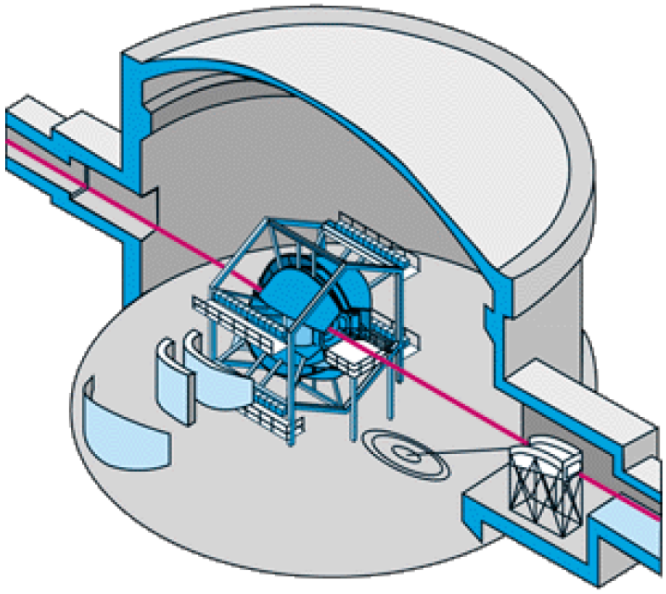

Figure 2.7: Hall-B cartoon (not-to-scale) indicating the layout of beamline, tagger and CLAS. In photoproduction experiments, electrons enter from the right, bremsstrahlung to produce photons on a thin radiator, get deflected by the tagger magnet into the tagger or the beamdump. Photons continue onwards to CLAS after passing through a collimator and ideally interact with the 'Target Nucleons' to produce hadronic events detected by CLAS. The non-interacting photons travel onward to the Faraday's Cup for some quality checks and then the beam-dump. Image source [32].

the event beam photon energy in photoproduction experiments. The electron beam enters the hall through the beamline, as seen in figure 2.8 from a recessed notch.

2.3.1 Beamline

Electron beam is separated from the CEBAF's linac for delivery to the hall at the beam switch-yard. It enters the hall through the beamline enclosure containing a multitude of devices to control and monitor the beam quality and positions. These devices are critical for proper beam transport and include beam-viewer, multiple beam position monitors, vacuum valves, vertical correctors, horizontal correctors, quadrupole magnets, vacuum ion pumps, harps, retractable beam stopper and so on (see figure [2.8]) [37] [29]. These help MCC control and manage the beam delivery to the detectors to the required experimental specifications.

In case of electroproduction experiments, the beam continues on to the target. In case of photoproduction experiments however, the beam is incident on the radiator where the

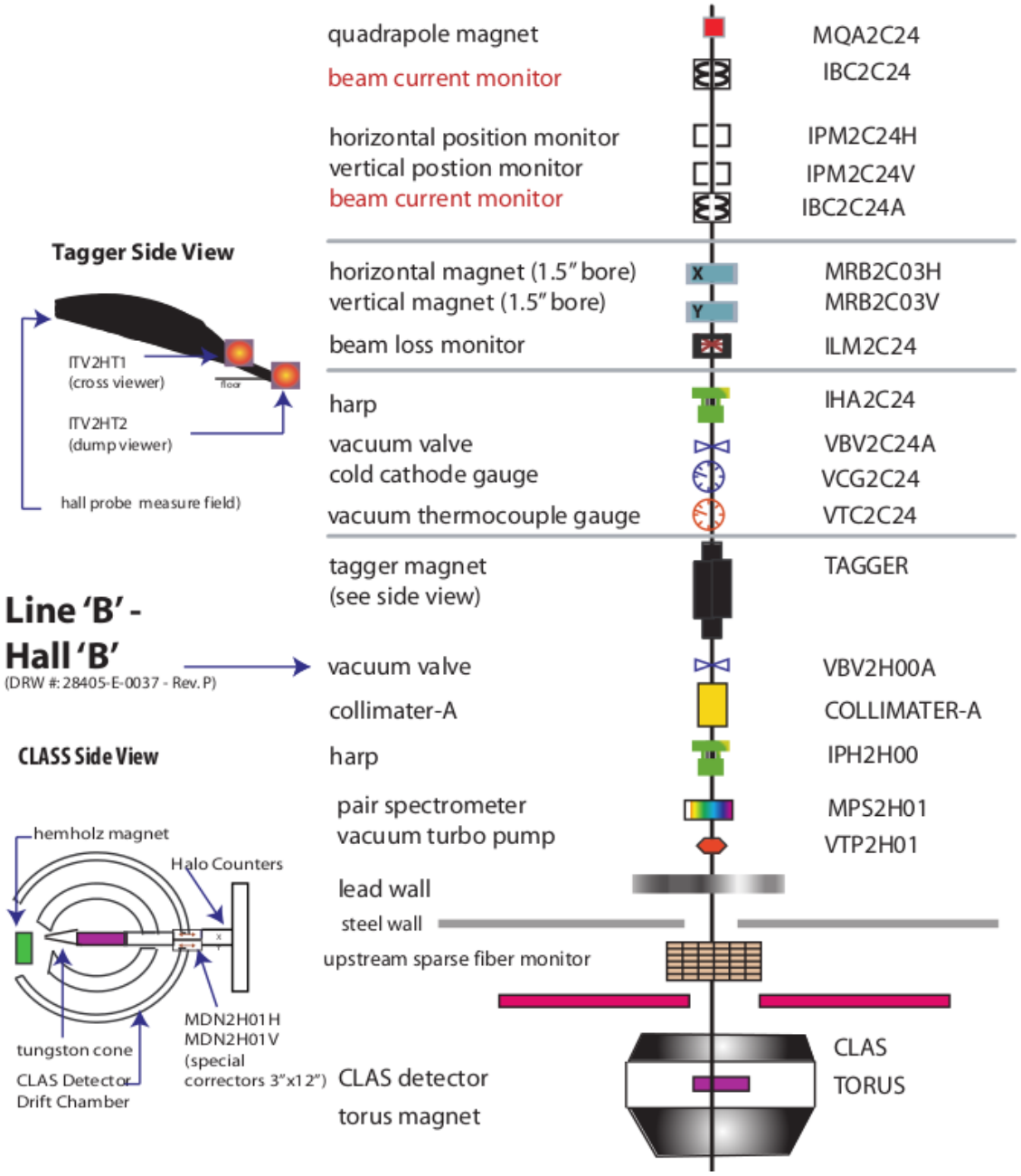

Figure 2.8: Schematic of Hall-B's beamline and its optics labeled with its various components. This provides us a reference for the beam-line optics as the beam enters the Hall-B and the various devices used to manage and analyze the quality of the beam as it travels onto the CLAS detector. Image source [32].

electrons bremsstrahlung, to give us a photon beam, which is then collimated before proceeding to the target. For photoproduction experiments, the electron beam from CEBAF is converted to a photon beam by scattering it off a gold foil radiator, with photons being produced via bremsstrahlung. Gold radiators are preferred because they reduce electron-electron scattering due to their high atomic number. After the electron beam interacts with the radiator, we have a medley of photons as well as scattered and unscattered electrons. We now need to remove these electrons, as well as collimate the bremsstrahlung photons to get a usable photon beam. A dipole magnet is used to bend and redirect the electrons towards the tagger, thereby removing these electrons from the mixed beam. The dipole field does not affect the beam photons, allowing them to advance towards the target through the collimator.

2.3.2 Tagger

Hall-B contains a photon beam tagging system, composed of a strong single dipole magnet combined with a hodoscope which uses two planar arrays of plastic scintillators to detect the energy-degraded electrons scattered by the thin bremsstrahlung radiator. Electrons are redirected by the dipole magnetic field towards the Hall-B tagger spectrometer [figure 2.9], where the scattered electron is tagged with the electron's energy as well as its time of arrival by the tagger spectrometer. The dipole field also redirects electrons with $E_e > 20\%$ and $E_e < 95\%$, of the CEBAF delivered electron beam energy, to the tagger beam dump.

2.3.2.1 Structure and functioning of Tagger. Tagger contains two layers of scintillator counters - E-counters and T-counters. A Scintillation Counter is generally a long piece of plastic scintillator, with Photo-Multiplier Tubes (PMTs) attached at one or both ends. PMTs are either directly attached to the ends of the scintillator or waveguides are used to transport light from the scintillator to the PMTs. Tagger E-counters have 1 TDC attached to their end whereas tagger T-counters have 2 TDCs attached to its two ends, referred to as the Right and the Left TDC for calibration purposes [38] [39].

The first layer of 384 small scintillators, along the flat focal plane, lie slanted to face the incoming electrons and hence partially overlap each other. The array is composed of 384 plastic scintillators, 20 cm long, and 4 mm thick. Their widths, along the dispersion direction,

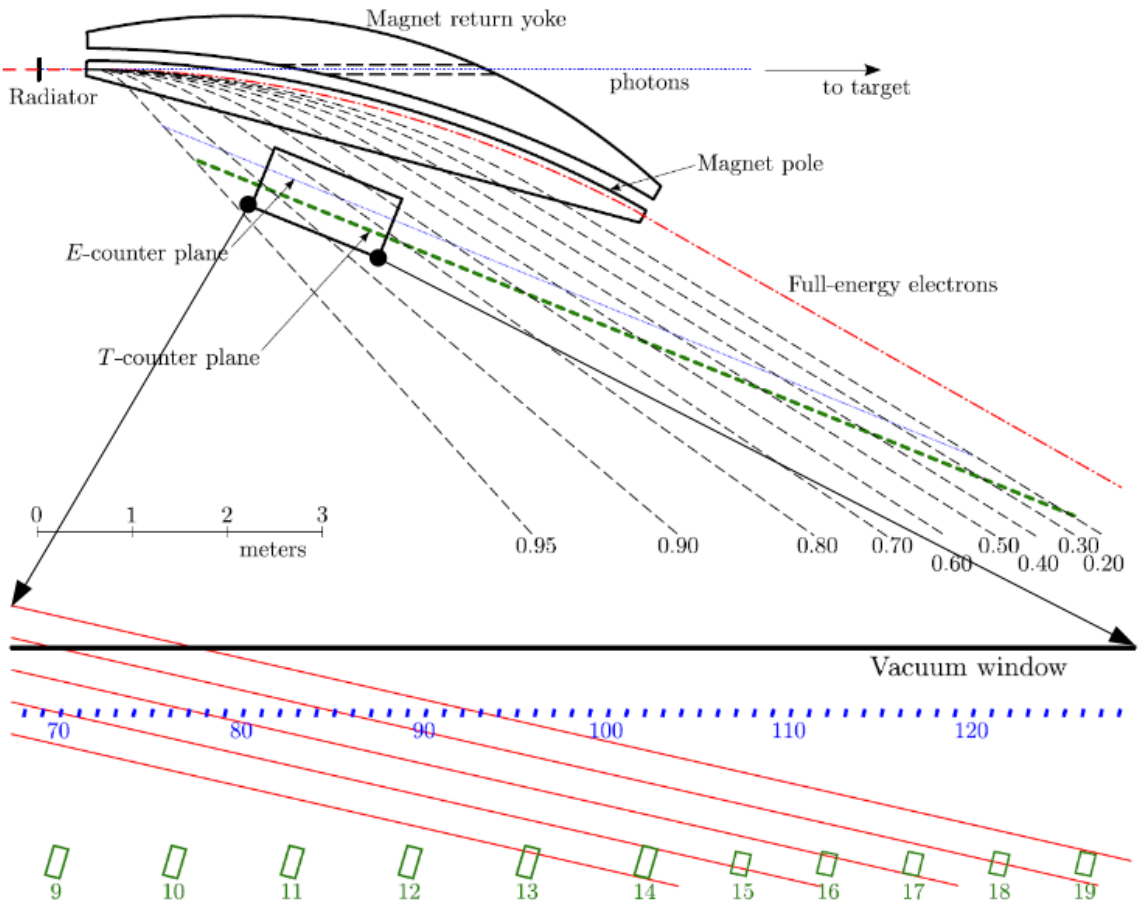

Figure 2.9: Tagger schematic with its E-T coincidence geometry. The blue dot-dashed lines are the E-counters whereas the green dashed lines are the T-counters. The dashed red lines are electrons that have not lost any energy, whereas the dashed black lines are scattered electrons that have ideally radiated a bremsstrahlung photon, and now carry the labeled fractional energies. The zoomed-in section allows for a closer look at the electrons traversing through the E-plane and the T-plane, and how we can use this E-T coincidence information to identify and measure the energy of the CLAS photon. Image source [32].

range from 6 to 18 mm, in order to subtend approximately constant momentum intervals of $0.003E_0$. This 'E-plane' is aligned along a flat surface coincident with the optical focal plane of the magnet. These E-counters record detected electron positions at the focal surface, and thus the momenta of the energy-degraded electrons. Each counter optically overlaps its adjacent neighbors by one-third of their respective widths, thus creating 767 separate photon energy bins through appropriate recording of coincidences and anti-coincidences, and pro-

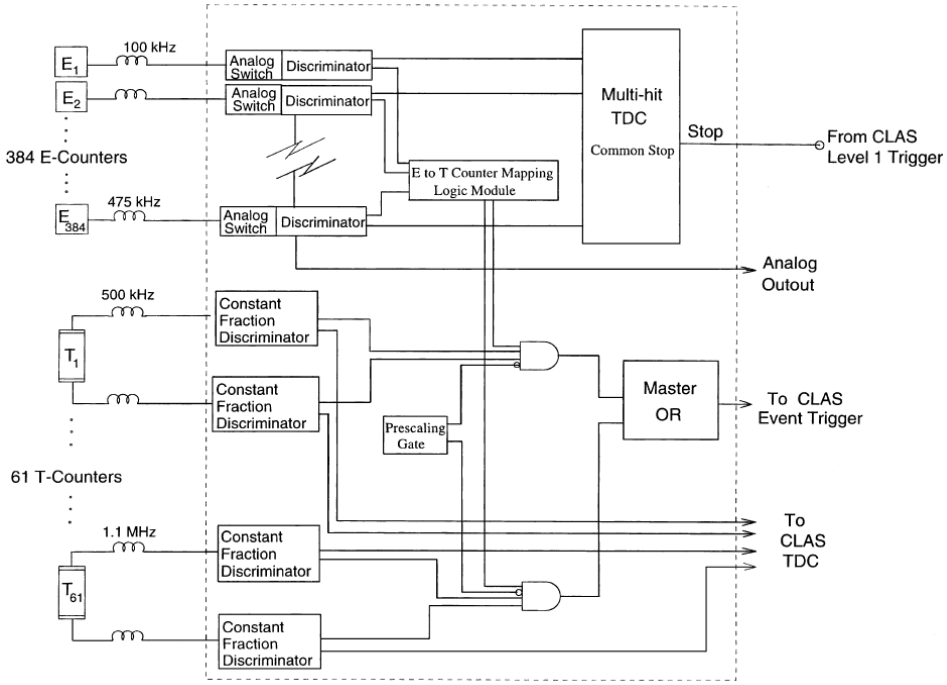

Figure 2.10: Tagger signal processing logic for identifying the energy and the interaction time of the scattered electron. Image source [32].

viding an energy resolution of $0.001E_0$. By using the case where the interaction is detected in a single scintillator or in the overlap region of a neighboring pair of these scintillators, we are able to extract more accurate information on the curvature geometry of the incoming electron, which translates to a finer electron and photon energy resolution. This technique instantly doubles our energy binning (E-bins) from 384 hypothetical single E-bins to 767 E-bins where every alternate (even) bin-number is the overlap region of the neighboring E-counters. Since we use the tagger to tag between 20-95% (75% range) of the incoming electron beam energy (E_0), this provides tagger with a $0.1\%E_0$ ($75\%E_0$ / $767bins$) average energy resolution in the tagging range. The field setting for the tagger magnet is matched to the incident beam energy so that the electrons which do not radiate follow a circular arc inside the curved edge of the pole face, and get directed into a shielded beam dump below the floor of the experimental hall.

A two-dimensional field map for the tagger dipole magnet using the tagger current is created. A ray tracing program uses these field values along with the incoming electron

beam energy and the design geometry of scintillation counter hodoscope to generate values for the energy of the radiated photon. The central value of each E-bin is considered to be the energy of the electron ($E_{e'}$) detected in that element. Energy conservation is then used to determine the corresponding tagged beam photon energy (E_γ) for the detected electron.

$$E_\gamma = E_0 - E_{e'}$$

The tagger dipole magnetic field redirects the electrons with energy over 95% of the incoming electron beam, straight into the tagger beam dump. Since these high-energy electrons must have photo-produced low energy photons, they are generally of no experimental interest and are discarded to the tagger beam dump. The tagger beam dump is designed to contain these electrons and their secondary radiations. The beam dump is located in the beam dump tunnel under the Hall-B floor and is surrounded by shielding. The shielding prevents the groundwater outside the dump-tunnel from becoming excessively radioactive as well as protects CLAS from secondary radiations from the beam-dump [37].

The second layer of 61 larger scintillators, downstream from the E-counters, provides us with the required timing resolution for the CLAS photon. This 'T-plane' contains 61 counters, 2 cm thick read out using phototubes attached by solid light guides at both ends (transverse to the momentum axis) of each scintillator giving tagger a timing resolution of about 110 ps [38] [39]. The T-counter scintillators are organized in two groups, with the first group of 19 narrower counters spanning the photon energy range from 75% to 95% of the incident electron energy, and the remaining group of 42 counters spanning the range from 20% to 75% of the incident electron energy. The T-counter widths (along the dispersion direction) are varied to compensate for the $1/E_\gamma$ behavior of the bremsstrahlung cross section, so that the counting rate in each detector remains approximately the same within each group. The rate in the first group is approximately $1/3^{rd}$ of that in the second group. This discontinuity in the width progression permits operation at considerably higher tagged-photon rates for experiments like g12 which are primarily interested in the highest-energy photons. T-counter width acceptances overlap their nearest neighbors by a few mm, just sufficient to ensure that there are no inter-counter gaps through which an electron could escape undetected. T-counter lengths (transverse to the momentum direction) are

also varied from 20 cm at the high electron momentum end to 9 cm at the low-momentum end, tracking the energy dependence of the bremsstrahlung characteristic angle distribution, in order to help suppress potential background from ambient radiation.

The same technique and design geometry is used to divide the 61 hypothetical T-bins into 121 finer T-bins. The ray-tracing program associates particular E-bins with their corresponding T-bins for a given field. This gives us information on the time of detection for the electron hit in the tagger, completing our quest for information about the energy and the time of the scattered electron in to the tagger. If the corresponding photon 'triggers' CLAS, we can use this information to calculate the energy and the timing of the triggering photon.

A resolution better than 210 ps is necessary to form a coincidence of the tagged beam photon with the corresponding nuclear interaction in the CLAS target (that triggered our data-collection process). This makes it possible for photoproduction experiments in Hall-B to investigate real photon induced reactions in conjunction with CLAS [39] [40]. Thus, the timing calculated for an event in CLAS is used to identify the closest electron beam bunch that could have created the event, and this timing is used to identify the corresponding tagger hits from that particular beam bunch, which are further used to calculate the possible energies for the event photon.

2.3.3 CLAS

CLAS is an acronym for 'CEBAF Large Acceptance Spectrometer'. For events occurring near the CLAS center, CLAS has an almost 4π angular coverage in solid angle. There are 'dead' regions in the coverage of the detector, where CLAS cannot measure due to presence of structures like its beamline, the toroidal magnets and others. CLAS is made of six identical, independent spectrometers (sectors). If we consider the sector co-ordinate system to have its z-axis along the beam-line, x-axis to pass through the center of the sector and the y-axis to be the resultant cross-product, the detector covers between $8^\circ < \theta < 145^\circ$ along its polar angle (altitude) and $-25^\circ < \phi < 25^\circ$ about its azimuth for each sector. Taking these regions into account reduces CLAS coverage to $\sim 3\pi$ in solid angle.

The physics done at CLAS is complementary to the other two halls at JLAB, since they must restrict their measurements to a narrow solid angle at a time and hence have

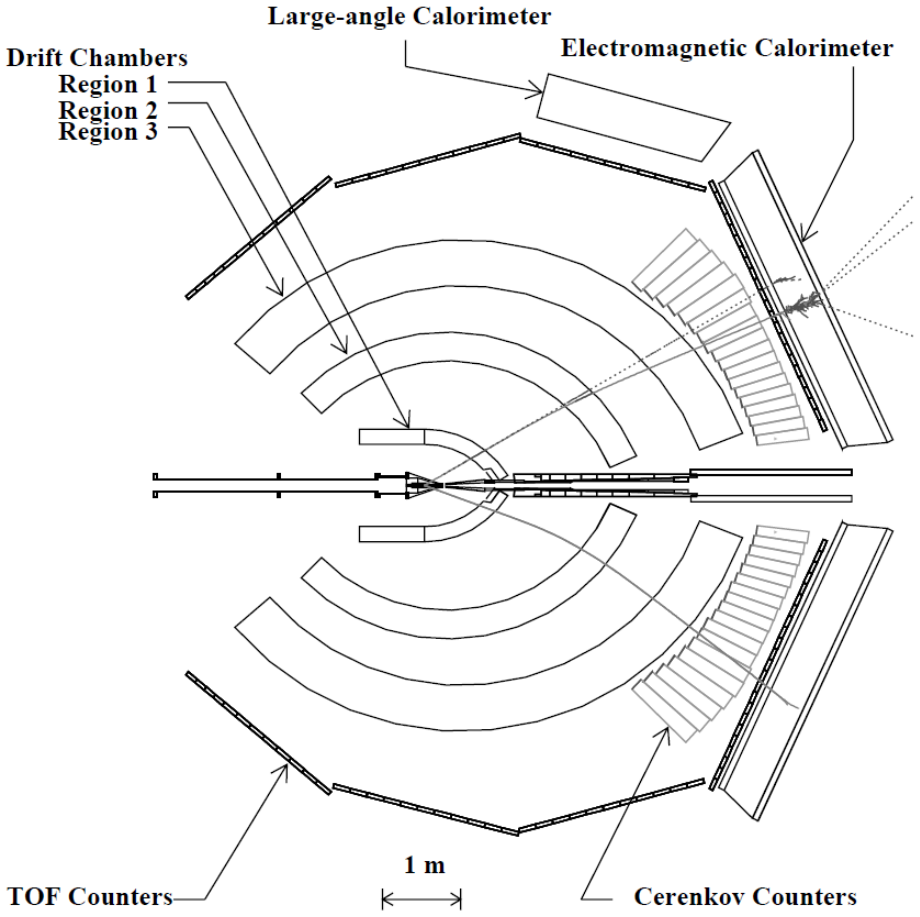

Figure 2.11: Cross section of CLAS cut along the beamline with typical examples of photon, electron and proton track (from top to bottom) superimposed on the figure. Image source [32].

to scan through the angles over time to compile data for a complete measurement. CLAS does not suffer from this limitation and is able to record data at all angles, all the time. The large acceptance also allows datataking for multiple simultaneous experiments with the help of a configurable trigger system, which was precisely the case with g12, which ran 3 parallel experimental proposals at the same time using special triggers [41] [42]. Due to its large acceptance, CLAS is well-suited for experiments that require the detection of multiple particles in the final state, like for the purpose of the analysis presented in this thesis ($X \rightarrow \phi\eta \rightarrow K^+K^-[\eta/\pi^0]$). Large-acceptance particle detection and high detection efficiency for final state particles, at a useful event-rate are big positives for CLAS in multiple experimental

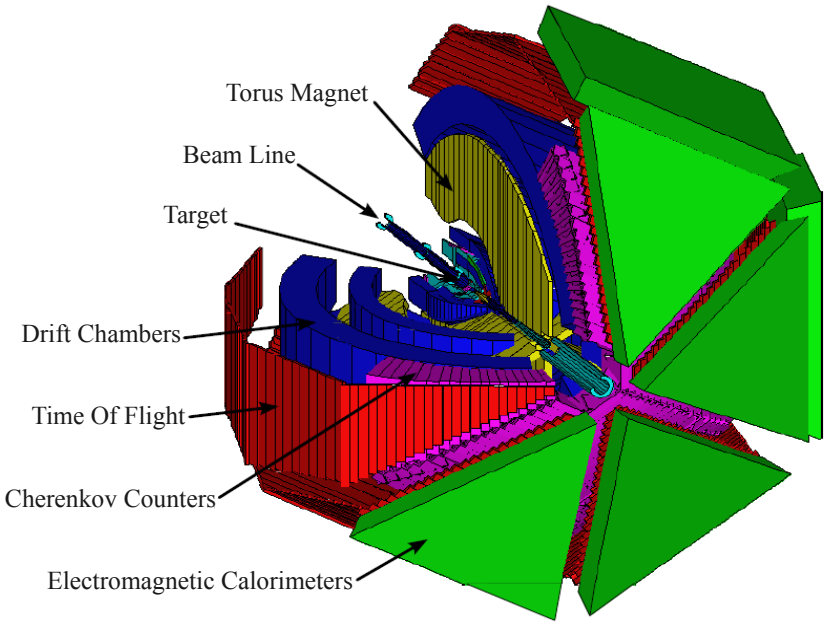

Figure 2.12: A 3-Dimensional look at the interiors of CLAS and the arrangement of its subdetector systems. Image source [32].

scenarios. For example, large acceptance is required for high-detection efficiency of multi-particle final states, typical in the nuclear break-up reactions and the decay of excited hadrons into multi-particle final states. It is also crucial in photoproduction experiments using tagged bremsstrahlung beam, where low luminosity is required to keep the accidental coincidences in the tagger low. In the case of polarized target experiments, low beam luminosity is a necessity to even operate, so that the experiment can run without quick degradation through thermalization of the target polarization. While Hall-A and Hall-C routinely receive electron beam current ($\sim 100\mu A$) sufficient to achieve luminosities of the order of $10^{38} cm^{-2} s^{-1}$, the maximum luminosity ably handled by CLAS is limited by detector occupancies to four orders of magnitude smaller than that for the other Halls. Delivering electron beam to different halls with such variations in beam-intensity between consecutive beam-bunches is another challenge that has been mastered by the MCC.

2.3.3.1 Mechanics of the detector. The design concept for 'CLAS' is based on using multiple layers of sub-detector systems to reconstruct the particle tracks, their mo-

menta and interaction times. This multi-layered design for CLAS was chosen for its ability to measure charged particles with good momentum resolution, to provide geometrical coverage of charged particles at large angles in the laboratory, and to keep a magnetic-field-free region around the target to allow the use of dynamically polarized targets like FROST and HD-ICE.

The electron or the collimated photon beam is analyzed and tuned in the beamline (see figure [2.8]) to generate information for instant quality checks and later analysis. The beam now strikes the CLAS target and interacts with the target nucleons to produce excited baryons and mesons. At CEBAF energies, the majority of charged particles detected are target protons, pions and kaons. Due to dominance of the pions in the data, they are used to calibrate the timing and the energy of most of the sub-detectors.

After a hadronic event with one or more charged final state particles occurs in the target, the particles usually have a range of momentum in all directions and can travel into the detector volume or the beam-line. For the particles entering the detector volume, CLAS uses toroidal magnetic field to bend the path traveled (track) of the individual charged particles through the drift chambers (DC). This helps map their trajectory and reconstruct their tracks, and hence measure their momentum and event vertex. CLAS measures the particles' time of flight from their event vertices in the target to the scintillation counters (ST, TOF) placed strategically along the way. This helps us perform the Particle-Identification (PID) later on during our reconstruction pass for further analysis. CLAS also uses various calorimeters and hodoscopes to help with neutral particle detection and uses Cherenkov counters to distinguish between charged particles like electrons and pions. To understand the mechanics further, we describe the individual detector subsystems and other components in some more detail.

2.3.3.2 Target. CLAS is designed with an approach where some detector components can be moved, removed and replaced to an experiments advantage. One of such primary component is the 'Target Cell'. There are multiple CLAS target cells of different sizes and they usually occupy the 'Center of CLAS'. FROST and HD-ICE experiments have had innovative, complicated target-polarization cells where they even put in a holding magnet for the FROST target-cell inside CLAS.

Figure 2.13: 40 cm long kapton target used during the g12 run, placed 90 cm upstream of the CLAS center, filled with liquid hydrogen (LH_2). Image source [32].

The 'g12' experiment used a cylindrical cell made of kapton, 4 cm in diameter and 40 cm in length. Even though the initial photon beam was collimated, due to scattering and diffusion the beam had a wider radial size as it traversed the target. This cell was previously used by other CLAS experiment like g6c and is a simple container design that does not allow for any polarization of the target material in the given setup. The experiment had a choice of using deuterium, helium or hydrogen as the target material contained in the cell, as they had all been used in earlier experiments. Liquid Hydrogen (LH_2) was chosen to be the best-suited target material for g12 physics.

A major component of g12 physics motivation required to investigate the peripheral production of mesons, which required the experiment to increase the forward angular coverage of the detector. To this end, g12 target cell was moved 90 cm upstream of CLAS center to increase the forward geometric (small angle) acceptance of the detector from the usual 8° to 6° in the polar angle. This led to a decreased acceptance at large angles, which was considered an acceptable trade-off for the g12 physics motivations.

2.3.3.3 Start Counter. Particle identification in CLAS is performed using the measurement of the time-of-flight of the scattered particle from the interaction vertex to the outer detectors (TOF or EC) in conjunction with its momentum measurement from the

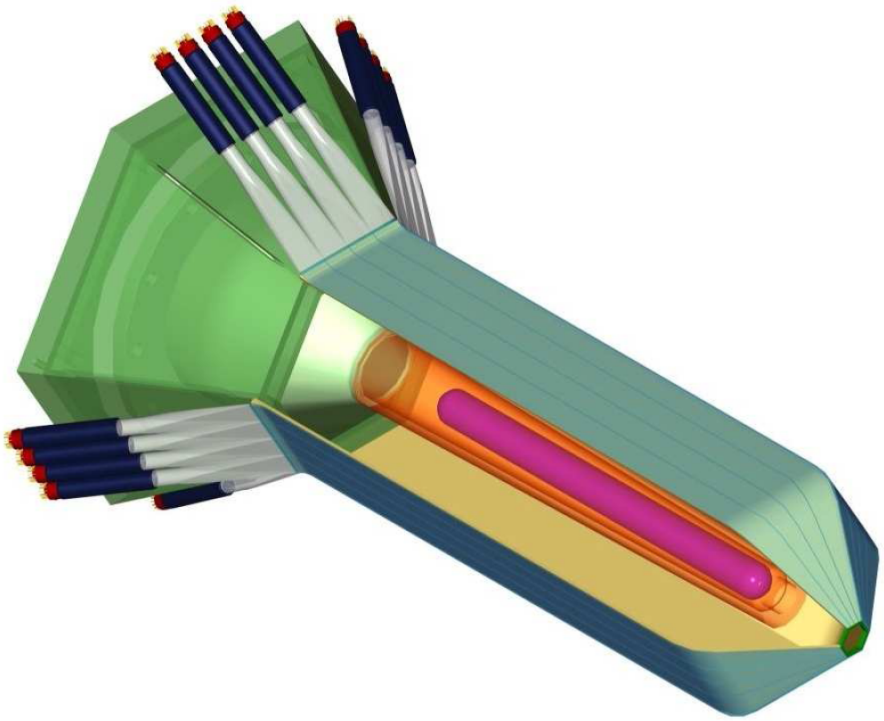

Figure 2.14: Diagram for start counter (ST) with target cell visible inside. It shows the 6 Planar surfaces with each plane dedicated to a CLAS sector. Each scintillator plane is made of 4 scintillation counters fused together where the forward tips of the scintillators are bent to form the nose-cone of ST. PMTs are attached at the other end using solid light-guides, to collect light from the scintillation produced on passage of a particle through it. Image source [32].

drift chambers [43]. To determine the time of hadronic interaction in the target, we first have to determine the photon beam bucket that produced the event. With a fresh bunch of photons coming in every $2.004ns$, a sub-nanosecond coincidence of the Hall-B tagging spectrometer with a sub-detector (start counter) close to the target region is required to pin down the photon beam bucket. Using this methodology, comparison to the nearest RF time gives the start time of the particle trajectory to better than 25 ps.

The start counter was designed to provide full acceptance coverage defined by the CLAS detector with a 40 cm long liquid hydrogen target [43]. The start counter [figure 2.14] is built of six identical sectors, surrounding the region earmarked for the target cell, mounted on a foam scattering chamber. Each sector consists of four scintillator paddles, each coupled

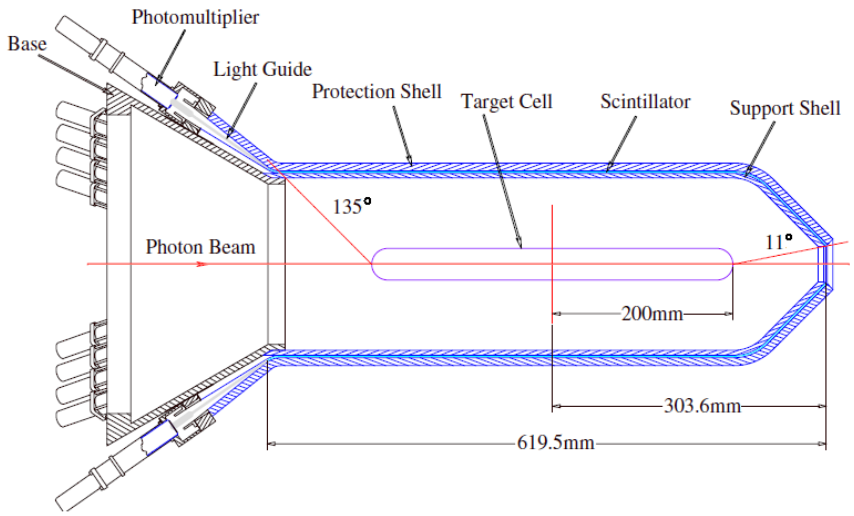

Figure 2.15: Diagram of cross section cut along the beamline, depicting the labeled components and its angular coverage when at the center of CLAS. Image source [32].

to an acrylic light guide. Each paddle is a continuous single piece of scintillator with a straight section 502 mm long, between two bends, and a tapered end referred to as the " nose". Each paddle is 29 mm wide and 2.15 mm thick, which along with the wrapping and the support material give a total thickness of about 0.26 g/cm^2 . The first bend, which couples to the light guide, is 35° with a radius of curvature of 25.4 mm. The second bend is 45° with a radius of curvature of 50.8 mm. The nose region of the middle paddles has a rectangular section 52 mm long and finishes off with a truncated triangular section 41 mm long. On the outer paddles, the nose section is a triangle about 30.0 mm long. The 127 mm long light guide tapers within a quasi-adiabatic cross section of the scintillator to the 15 mm diameter photomultiplier tube. The paddles and the light guides are wrapped in radiant mirror film. In addition, every other scintillator was wrapped in black Tedlar film. The hermeticity of the final assembly is estimated by direct measurements to be not less than 98%. It is mounted on a rigid hexagonal support shell with 5.3 mm thick walls made of high-strength foam with 110 mg/cm^2 density. The base with its flange, light guides, photomultiplier tubes, and various housing parts is completely out of the useful acceptance of CLAS.

A charged particle traversing the paddle causes light to be produced inside the scintillator. This light is reflected from the mirror film and makes its way to the light guide attached to the PMT. At the PMT the photo-signal is collected, converted, amplified and then the PMT's ADC and TDC values for that signal are recorded for later use in the analysis. The start counter also serves a crucial role in defining the trigger for photon runs. Addition of the start counter to Level 1 Trigger scheme reduces the trigger rate by about an order of magnitude [43].

2.3.3.4 Torus magnet. The CLAS toroidal magnet uses six iron-free superconducting coils to bend the charged particles towards or away from the beamline, while leaving their azimuthal angle practically unchanged. The six superconducting coils arranged in this toroidal geometry around the electron beam line generate an intergral magnetic field of up to 2.5 tesla-meters in the forward direction, reducing to 0.6 tesla-meters at a scattering angle of 90°. This is achieved at their maximum design current of 3860 Amperes, with the total number of amp-turns summed over all the torus loops being 5×10^6 [28] [44].

The magnet is approximately 5 m in diameter and 5 m in length. Each of the six coils has four layers of 54 turns of aluminum-stabilized NbTi/Cu conductor. The coils are cooled to 4.5 K by forcing super-critical helium through cooling tubes situated at the edge of the windings. Super-insulation and an intermediate liquid-nitrogen-cooled heat shield reduce the heat load. The coils are also designed to be self-protecting in case of a quench. Since the coils are not ferromagnetic, the magnetic field is calculated directly from the current in the coils. The magnetic field vectors are in a plane perpendicular to the torus axis at the target position. The main field component is in the ϕ direction with deviations from a pure ϕ-field close to the coils. The kidney-shape of the coils results in a high field integral for forward-going particles which are typically high momentum, and a lower field integral for particles emitted at larger angles. The coil geometry preserves a central field-free volume for the operation of polarized targets [28].

2.3.3.5 Drift Chambers. Tracking of a charged particle in CLAS is done primarily by using special wire-chambers known as Drift Chambers (DC). It occupies the most volume of any detector subsystem in CLAS. The chamber is filled with a gas mixture with which the charged particles interact via collisions or electromagnetic interactions, and lose energy

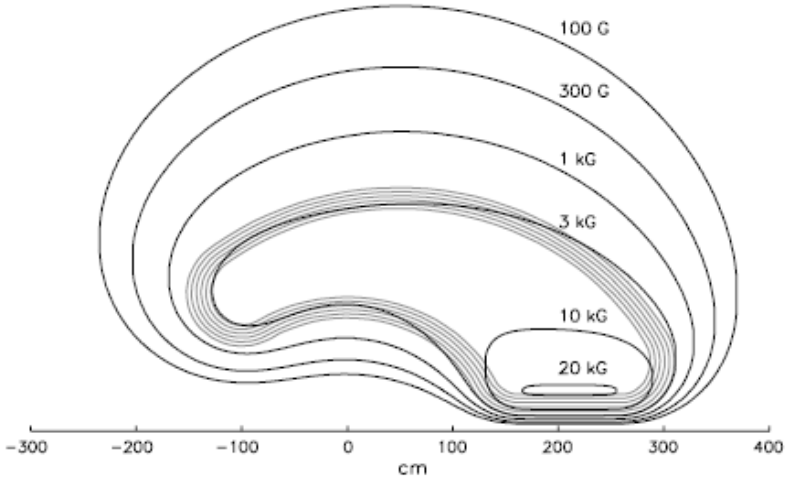

(a) Estimated Contours of constant absolute magnetic field for the CLAS toroid in the midplane between the two coils. The projection of the coils onto the sectors midplane is shown for reference.

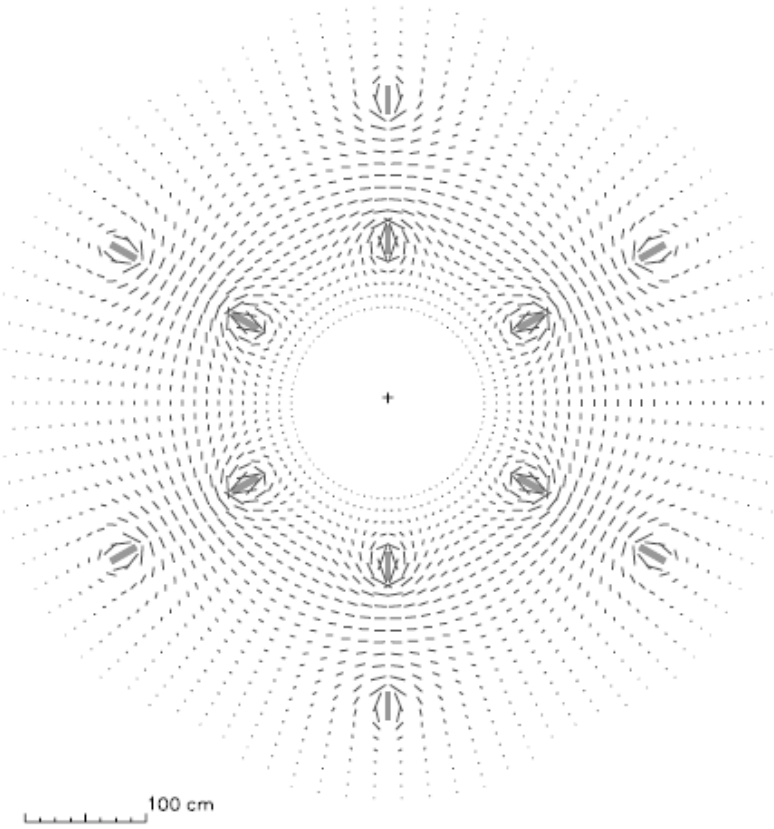

(b) Magnetic field vectors for the CLAS toroid in the plane transverse to the beam and centered on the target, with the length of each line segment proportional to the field strength at that point.

Figure 2.16: Drift Chamber Magnetic Field distribution. Image source [32].

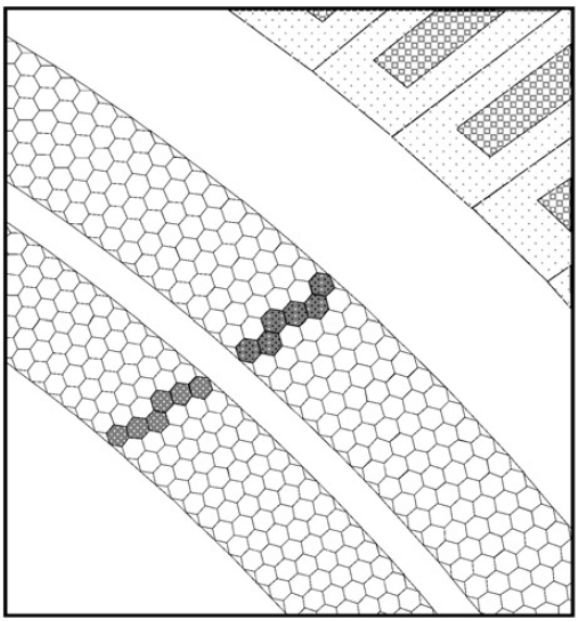

Figure 2.17: Figure depicts the layout of the sense wires and the guard wires in the Region 3 superlayers projected onto the midplane of the sector. The lines connecting the vertices of the hexagons are not real and drawn simply to convey a sense of design. Sense wires are at the center of each hexagon and the field wires are at the vertices. Guard wires that surround each superlayer are not shown. A charged particle is shown to have ionized the gas on its passage and fire the highlighted drift cells along its track. The edges of several Cherenkov modules are visible in the upper right corner. Image source [32].

and end up ionizing the chamber gas. The ionized particles get quickly collected by wires maintained at a potential difference close to the interaction region. This flow of current due to ionized gas particles generate current pulses in those particular wires, in effect telling us of the passage of a charged particle in the vicinity of those wires. When Drift times for these ionized particles are taken into account, along with other similar events throughout the volume of the chamber that occurred within a small time-period, we are able to predict the particle trajectory quite accurately. Drift Chambers are used in conjunction with strong magnets, that causes Lorentz force to bend the trajectory of highly energetic charged particles. This bending separates out the charged particles of different momenta, causing them to travel in different trajectories. This technique is analogous to the one widely used in laboratory mass spectrometers and is the basis for usage of the word 'spectrometer' in CLAS.

Building upon the philosophy of six equivalent, independent sector-based spectrometers, the drift chambers have identical components across all sectors. The toroidal magnet coils naturally separate the detector into six independent tracking areas or sectors [28] [44]. For simpler detector design and construction, 18 separate drift chambers were manufactured and installed at three radial positions in each of the six sectors. Each sector is further subdivided into three sections - Region 1, Region 2 and Region 3 - based on their radial locations. All the three regions have distinct purposes and characteristics. The six 'Region One' chambers (R1) surround the target in an area of low magnetic field, producing small deflections in the particle trajectory. The six 'Region Two' chambers (R2) are slightly larger and situated between the magnet coils in an area of high field near the point of maximum track sagitta. The six 'Region Three' chambers (R3) are the largest components and are radially located outside of the magnet coils in a region of zero field, causing almost no deflection in the particle trajectory.

The wedge-shaped volume between the torus coils, which surrounds the beamline, is bounded by endplates through which the drift chamber wires are drawn taut from one endplate to the other. In total, about 130,000 wires are strung through the cells of the drift chambers. The chamber bodies are designed to support wires running between these two endplates in each sector, each parallel to its neighboring coil plane, and thus tilted at 60° with respect to each other. This design provides maximum sensitivity to track momenta since the wire direction is approximately perpendicular to the bend plane of the curved trajectories. The wire midpoints are arranged in 'layers' of concentric circles. For pattern recognition and tracking redundancy, the wire layers are grouped into two 'superlayers', one axial (perpendicular) to the magnetic field, and the other tilted at a 6° stereo angle around the radius of each layer to provide azimuthal information. Each superlayer nominally consists of six layers of drift cells, with the exception of superlayer 1, which contains only 4 layers.

Cell material is minimized to present 1% or less of a radiation length to the charged particles traveling through it, to lower multiple scattering events. There are 1296, 2262, and 2304 individual hexagonal detection cells in each sector of the Region 1, 2, and 3 drift chambers, respectively. The sizes of the individual cells range from 15 mm in Region 1 to 45 mm in Region 3. Each individual hexagonal cell in the drift chamber contains a voltage wire

which is a 140 μm Gold-plated Aluminum and a detection wire which is 20 μm diameter Gold-plated Tungsten, surrounded by a Argon/CO_2 (90%/10%) mixture. This mixture of gas is optimized to produce a high ionization gain of induced charge on passage of charged particles through the cell. An active feedback system maintains constant pressure in the chamber regardless of atmospheric fluctuations by making small adjustments to the gas outflow. A high-voltage system maintains the sense-wires at a positive potential and the field wires at a negative potential whose absolute value is half that of the sense-wires. A layer of guard wires surrounds the perimeter of each superlayer, with the high-voltage potential adjusted to approximate the electric-field configuration of an infinite grid. This three-voltage scheme minimizes the effects of nearby grounded surfaces such as the endplate.

The charge generated due to ionization of the gas mixture, during the passage of an energetic charged particle, drifts toward the sense wire to produce a current. Such information provides initial hit-based tracking information about the particle trajectory, reconstructing the actual particle momenta with an accuracy of 3-5%. Induced charge in the gas drifts toward the sensor cell at a velocity of around 4 $cm/\mu s$. More accurate path information is provided after determination of the total time-of-flight of the particle by the scintillation counters. A reference time is then calculated and used to indicate when the particle passes through each cell, and this is compared to the TDC time of the signal generated in the sense wire. The distance of closest approach (DOCA) to the sensor wire in each cell can be thus calculated, improving the accuracy of the path through time-based tracking. Time-based tracking is capable of increasing the precision of track measurement to within 500 μm for the largest cells in Region 3. The radius of curvature for the 'fitted' trajectory due to the magnetic field is then used to determine the particle momentum to within a fraction of a percent accuracy.

2.3.3.6 Cherenkov Counters. Cherenkov radiation is emitted by charged particles that travel through a dielectric medium at speeds greater than the speed of light in that medium. The charged particles polarize the molecules of the medium along the trajectory they travel, which then decay rapidly back to their ground state, emitting prompt radiation. The emitted light forms a coherent wavefront if $c_{particle} > c_{medium}$ and is emitted under a constant Cherenkov angle with the particle trajectory. This Cherenkov radiation is

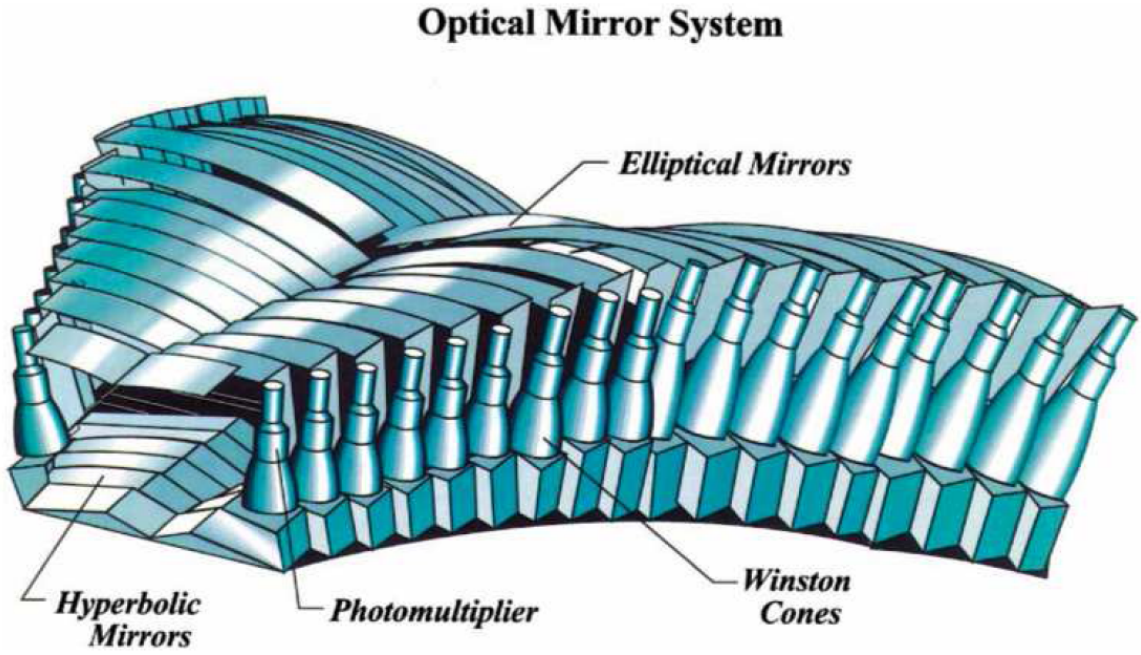

(a) 3D schematic of the 18 symmetrical, mirrored segments in one sector, about the sectors center, of the CLAS Cherenkov counter.

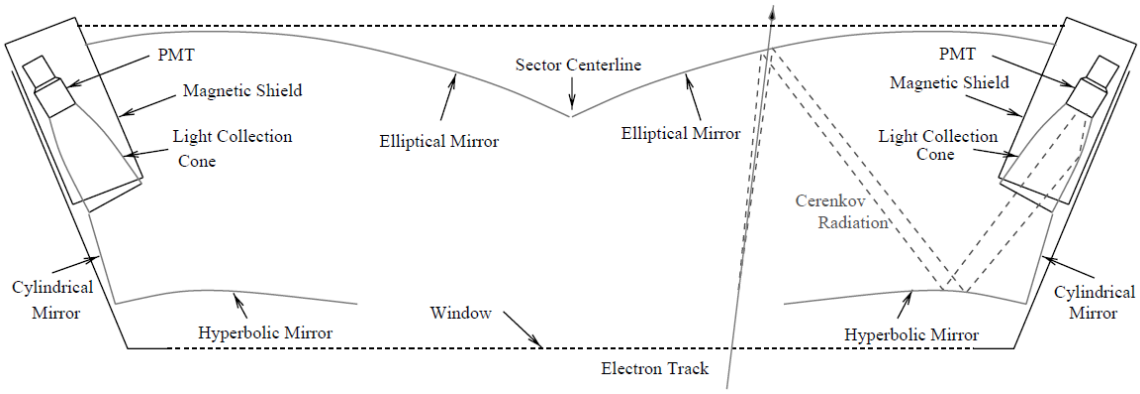

(b) Schematic diagram of a single Cherenkov segment, symmetric about the sector center. An electron track with Cherenkov light emissions along its trajectory and its collection by the PMT is shown. The PMTs, magnetic shields, and light-collecting Winston cones, lie in the region of the detector obscured by the CLAS magnet coils, and thus do not affect the electron acceptance.

Figure 2.18: Schematic views of Cherenkov counters. Image source [32].

continuous and has no spectral peaks. Higher frequencies have more intensity in Cherenkov radiation since the behavior of relative intensity per unit frequency is approximately proportional to the frequency around the region of visible light. Hence, Cherenkov radiation is usually observed to be blue; amongst the well-known example for Cherenkov radiation is the blue glow seen in underwater nuclear reactors. We use the phenomenon of Cherenkov emission, to simply differentiate between electrons and pions in CLAS data.

The Cherenkov Counter (CC) [45] serves the dual function of triggering on electrons and separating electrons from pions. Cherenkov detector has the solid angle coverage in each of the six sectors starting from the beamline out to the polar angle $\theta = 45^\circ$ from the center of CLAS, with the least possible amount of material that might interact with the charged particle to prevent degradation of the energy resolution. During g12 runperiod, since the target was placed 90 cm upstream of the CLAS center, the polar coverage was in the range from 6° to 35° in the lab frame. Most of the available space is covered with very high quality reflective mirrors while light collecting cones and photomultiplier tubes (PMTs) are placed in the regions of ϕ that are blocked by the magnet coils. Since charged-particle trajectories in CLAS lie approximately in planes of constant ϕ about the beamline, the placement of the PMTs in the shadows of the magnet coils does not affect the angular coverage. The light-collection optics was designed to focus the light only in the ϕ direction, thus preserving information on the electron polar angle θ. The full θ range ($\sim 8^\circ$ - 45°) of each of the six sectors is divided into 18 regions, and each of these 18 θ segments, is divided into two modules about the symmetry plane bisecting each sector into two distinct and equal ϕ regions as seen in figure [2.18]. This results in a total of 12 identical (accounting for an inversion symmetry for half of them) subsectors around the ϕ direction for each θ interval, leading to a total of 216 light-collection modules. The 5-inch diameter PMTs used in CC are equipped with high-permeability magnetic shields, since they are located in the fringe field region of the torus, where the highest transverse field can reach 70 Gauss at large scattering angles. The optical elements of each module consist of one elliptical and one hyperbolic mirror to provide the primary focusing for the Cherenkov light, a cylindrical mirror to compensate for imperfections in the focusing, and a light-collection (Winston) cone. The Cherenkov radiator gas used in the detector is perfluorobutane (C_4F_{10}) with

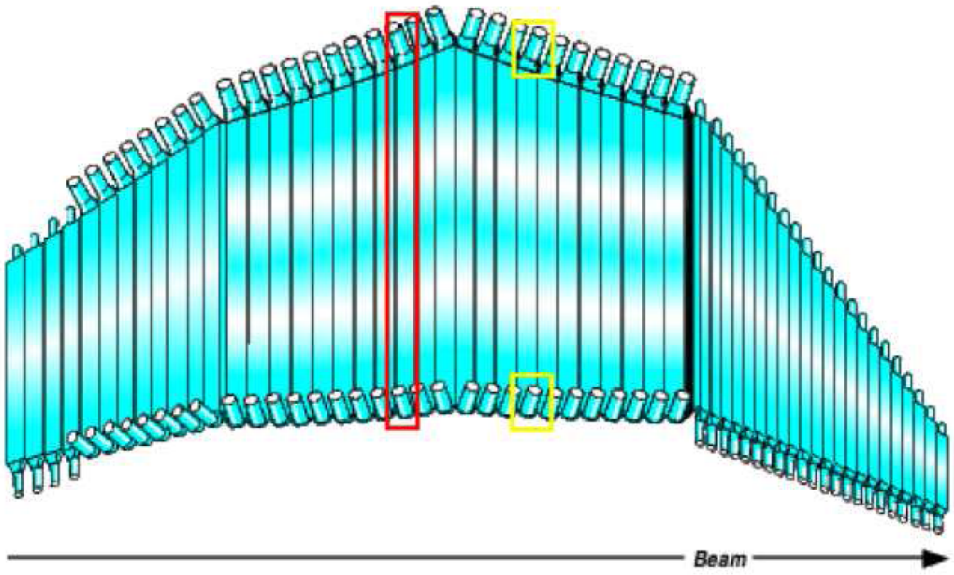

Figure 2.19: Arrangement of the TOF scintillation counters for a single sector, with PMTs boxed in yellow and a whole scintillator boxed in red. Image source [32].

an index of refraction of 1.00153, that results in a high photon yield and a pion momentum threshold of $2.5 GeV/c$. This gas also has excellent transmission properties for light at short wavelengths (high frequencies). Each sector of the detector holds approximately $6m^3$ of gas. The recirculating gas system maintains constant pressure in the gas volume, and removes impurities from the gas. The single-photoelectron response of the photomultiplier is used to equalize the gain of the PMTs, and to calibrate the response of the detector in terms of the number of photoelectrons initially produced due to the Cherenkov radiation collected by the PMT. An electron, traversing the active volume of the detector, typically results in 4-5 photoelectrons.

2.3.3.7 Time of Flight. Staying true to the six independent spectrometers design, the time of flight (TOF) subdetector of CLAS consists of six identical independent sections, one for each CLAS sector. Each section is composed entirely of plastic scintillators and their PMTs. The scintillators cover the entire active range in azimuthal angle ϕ and are located radially outside the tracking system and the Cherenkov counters, but in front of the electromagnetic calorimeters. They are located at a distance of about 5 meters from the center of CLAS. Their alignment and relative positioning with respect to other detector

subsystems is most clearly seen in figures [2.11], [2.12].

Each of the 6 TOF section consists of 57 plastic scintillators of uniform thickness of 5.08 cm but of variable length and width, with a pair of PMTs connected to the ends of each scintillator; see figure [2.19]. The scintillator thickness is chosen to have large energy deposition on passage of a minimum ionizing particle. Each scintillator is positioned such that it is perpendicular to the average local particle trajectory. The width of each counter subtends about 1.5° of scattering angle. The forward counters (1-23), covering the polar angles in the range $\sim 8°$ to 45°, are 15 cm wide and their light collected with 2-inch photomultiplier tubes. The large angle counters (24-53) cover the polar angles from $\sim 45°$ to 132°, are 22 cm wide and instrumented with 3-inch photomultiplier tubes. There are four more scintillators (54-57), covering the polar range between $\sim 132°$ to 142.0°, are 15 cm wide and instrumented with 2-inch photomultiplier tubes. After collecting photoelectrons and amplifying that signal, the signal output of the PMT is passed through leading-edge discriminators before being readout by its TDC and ADC [46]. TDC values enable us to calculate an accurate estimate of the time for an event and help with the Particle Identification (PID) whereas ADC helps us calculate the energy deposited by the particle in the scintillator and thus aid us further in PID. After extensive TOF calibrations, timing resolution of 0.218 ns has been achieved in g12.

2.3.3.8 Forward Calorimeter. Forward electromagnetic calorimeter operates on the principle of an incoming high energy particle creating a 'shower', cascades of secondary particles, by interacting with a dense material like lead (Pb) or iron (Fe). The high atomic number of these elements present high interaction cross sections to the incoming particles, leading to production of hadrons and photons in the sub-detector volume. These are high energy loss interactions since the initial particle is made to lose energy quickly and copiously by producing multiple secondary particles. Ideally, the whole energy of the incoming particles should get deposited into the sub-detector volume so as to have an additional handle on the incoming particles physics.

Design for CLAS forward electromagnetic calorimeter (EC) [47] is optimized to detect and also trigger on electrons with energies above 0.5 GeV; to detect photons at energies above 0.2 GeV and thus aid in reconstructing π^0's and η's through their 2γ decays; and

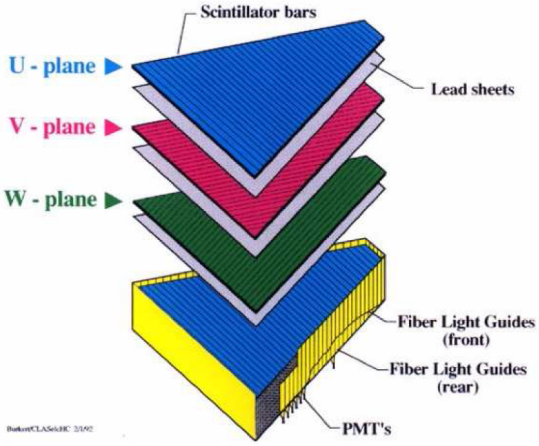

(a) A sector diagram of the CLAS forward electromagnetic calorimeter, showing the stacks of scintillator strips (blue, red, green). Each stack is at 120° with respect to its neighboring layers, alternating with lead sheets between the scintillator stacks. Fiber lightguides collect the light from the scintillator planes and transmit them to the PMTs.

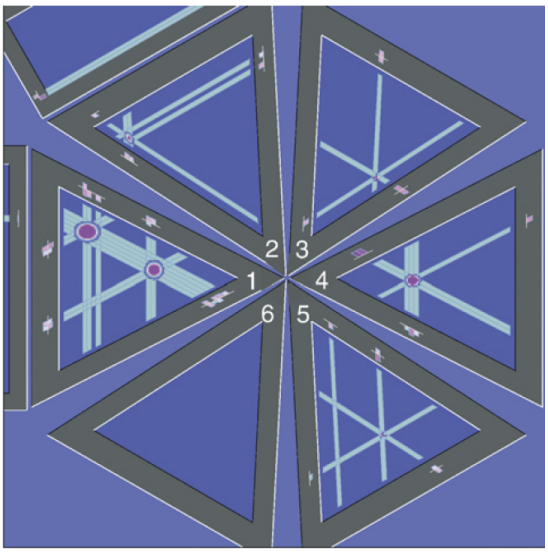

(b) Segment connecting 2 sides of a triangle represent a reconstructed hit in that scintillator segment. Intersection of peaks on each view (U, V, W) represent particles that have deposited energy in at least three different layers. The size of the oval at each intersection depicts the transverse energy deposited in the shower.

Figure 2.20: Design concept of EC in CLAS. Image source [32].

to detect neutrons, and hence being able to discriminate between neutrons and photons in conjunction with TOF measurements. EC covers the polar angle range (θ) from $\sim 8°$ to 45° measured from the CLAS center. Forward scattered particles in CLAS produced during photoproduction, travel outwards through ST, DC, CC, TOF and reach its outermost detector, the Forward Electromagnetic Calorimeter (EC). The EC absorbs energy from the scattered particles in about 16 radiation lengths of lead, interleaved with scintillation detector strips to provide energy, timing and location information of the scattered particle [47].

The independent electromagnetic calorimeters of each sector are composed of 39 dual alternating layers of 2.2 mm thick lead sheet and 10 mm thick sheet composed of 36 plastic scintillator strips (see figure [2.20a]), with their lengths optimized for maximum energy resolution and minimal transverse light attenuation. The cross section of EC is triangular

as seen in figures [2.12], [2.20]. A scintillator plane is constructed of 36 parallel strips of varying lengths, to form a scintillating layer. Orientation of the strips along their lengths, is rotated by 120° in the layers plane, to form the next scintillating layer. The orientations of the scintillator strips in the 3 planar arrangements - U-plane (blue), V-plane (red) and W-plane (green) strips are depicted in figure [2.20a]. All the scintillator layers are of the same color and material, and the different colors are used in the figure to specifically denote the directional component of the scintillator arrangement.

A lead:scintillator thickness ratio of 0.2 is used, giving CLAS a total thickness of 39 cm of scintillating material and 8.4 cm of lead. For each EC module, the lead-scintillator sandwich is contained within a volume whose cross section is nearly an equilateral triangle. There are 39 layers in the sandwich, consisting of alternating layers of 10 mm thick scintillator layer followed by a 2.2 mm thick lead sheet. The calorimeter possesses 'projective' geometry pointing to the nominal target position, i.e. the area of each successive layer increases linearly with distance to project the same angular coverage from the CLAS center. Each of the three views of the scintillator strips orientations (U, V and W), contain 13 layers, to provide stereo information on the location of the energy deposition by the shower. Each view is further subdivided into an inner (5 layers) and outer (8 layers) stack, to provide longitudinal sampling of the shower for improved electron/hadron separation. A fiber-optic light readout system transmits the scintillator light to their 1296 PMTs.

To reconstruct a hit in the EC, energy deposition is required in all the three views (U,V,W) of the inner or outer layers of a module. A pattern recognition algorithm first identifies groups of strips that collected the energy from the shower in each of the three views. Neighboring strips are grouped together if their PMT signals are above a certain threshold, and then the group's position centroid and root-mean-square is calculated. These grouped strips are referred to as 'peaks'. The intersection points of different peaks from each view are reconstructed and the intersection of all the three views corresponds to a hit. For examples of hit reconstructions in EC, see figure [2.20b] with hits reconstructed in five EC modules, including two hits in sector 1. The energy and the time of a hit is reconstructed by estimating the path length from the hit position to the readout edge, thus giving us information on the energy, position and the timing of the incoming particle in the EC.

2.3.4 CLAS and g12 Data Acquisition

Physics data collected during an experiment is initially a stream of numbers, generated from the signals observed in the multitude of electronics used in CLAS and CEBAF. These electronic signals are generated in the photomultiplier tubes (PMTs) connected to various scintillators in detectors like ST, TOF, EC, the PMTs installed in CC, the current carried by the DC wires, the beamline devices, magnets and other instrumentations in the Hall. All these electronic signals are converted into their numerical counterparts using appropriate readout devices like analog to digital converters (ADCs), time to digital converters (TDCs) and others. All the analog signals from the CLAS detector are digitized by FASTBUS and VME modules in read-out Crates (ROCs). In general, there are 24 ROCs but complicated experiments that install extra detector components like cryogenic polarized targets, install their own readout mechanisms alongside using extra ROCs. These ROCs and other data-taking components are controlled and managed by a central Data Acquisition system (DAQ) [28]. CLAS physics data acquisition, DAQ, is managed by the CODA (CEBAF Online Data Acquisition) software suite. CODA provides and manages the specified experimental configuration to the various DAQ components. The CODA software writes the generated experimental data stream from DAQ into 2 GB file blocks, which are then transferred and stored on tape silos for later data analysis and is henceforth referred to as 'raw data'. In the runperiod g12, DAQ collected an average of 50 million physics events per run of data collection, with an average event size of 4 kilobytes. After collecting the specified number of events, DAQ would generally be reset and the datataking restarted. Due to then newly employed Field Programmable Gate Array (FPGA) logic control processors, DAQ became capable of data collection at rates upwards of 10 KHz. However, g12 collected data at an average event rate of 8 KHz, which was high compared to any previous CLAS experiments then, due to limitations of the tracking efficiency that came about from the high occupancy of the Region 1 of the CLAS Drift Chambers. At this rate, each run lasted between 100-120 minutes depending on the stability of the CEBAF beam, producing between 130-140 files for a full run. These data files go through several stages of compression before finally being stored in a proprietary format called 'BOS' on magnetic tapes in a silo for later data reconstruction and analysis. For the g12 runperiod, 26 billion events were acquired, which

corresponds to 68 pb^{-1} of luminosity. Discarding runs with low number of events and other data quality issues, a total of 622 runs were found suitable for further analysis. The raw data from these 622 runs occupy 121 terabytes on the Jefferson Lab mass storage system (MSS) and their reconstructed counterparts occupy close to 300 terabytes.

During a runperiod, CEBAF delivers a beam with the requested parameters to Hall-B. In photoproduction experiment, the electron beam is scattered off of a radiator to produce photons and the electrons are bent by the tagger magnetic field to the tagger and the beam dump. The photons proceed onto the CLAS target and cause nuclear interactions. These generally produce excited states of mesons and baryons whose final products decay into the detector volume and get detected and measured by the various CLAS components and the data generated during this process is saved offline for later analysis as well as analyzed in real-time to determine if the datataking is progressing as expected. Generally an experiment is interested in certain physics and a lot of the incoming data is unsuitable, simply adding to the noise and the deadtime of an experiment. Deadtime is the time an experiment is unable to accept new data between events as the detector or the DAQ is unavailable. To keep a reasonable deadtime and only collect 'Events of Interest', an experiment defines a set of conditions referred to, in the physics parlance, as a 'trigger'. These trigger conditions needs to be satisfied before the data acquisition acquires and writes the data into the data stream. Triggers in particle physics experiments are usually defined to aid in making a quick judgment about the validity and the value of an event. This can be most easily accomplished by establishing the presence/absence of a signal (beyond a threshold if so needed) in certain associated detector components. In CLAS, most popular way of defining such triggers consists of a coincidence inside of a predefined time window (100 ns), in two or more associated CLAS subdetector components like ST * TOF or EC * CC of the same sectors. This coincidence raises the probability that the same particle has triggered the different subsystems of a sector and could be an event of interest with enough electronic information to be successfully reconstructed during offline analysis. If the experiment includes the condition for simultaneous triggering of multiple sectors, this raises the probability of acquiring events with multiple final states particles. Such simple triggering scheme involving just condition of coincidences or presence of signals constitutes the Level

1 (L1) triggering scheme. All PMT signals (i.e.ST, TOF, EC, CC) within $\tilde{1}00$ ns of the trigger are processed, alongside the drift chamber TDC signals [30]. The trigger supervisor (TS) electronics board processes these Level 1 trigger inputs to generate all the signals, busy gates and resets required to evaluate the event. If the event rate or the deadtime is too high, an experiment can employ a more advanced, albeit slower triggering scheme referred to as Level 2 (L2). For a Level 2 trigger, an experiment can require more stringent conditions like rudimentary reconstruction of tracks in DC.

In g12, both L1 and L2 trigger schemes were employed but even events that failed L2 were included into the CLAS datastream. The g12 runperiod was primarily interested in the high energy photoproduction regime. Since the bremsstrahlung photon beam delivered to CLAS creates a lot more lower energy photon interactions, the triggers allowed the experiment an additional handle to cut down the rate of these low energy photon events by placing conditions on data recording. CLAS was instructed through the trigger to accept events only when tagger counters corresponding to high photon beam energy recorded a hit in coincidence with satisfying the other trigger conditions. Majority of g12 data required a beam photon with energy $\geq$ 4.4 GeV to be present in the event. DAQ recorded data in an event based format. Whenever the L1 trigger conditions were satisfied, CLAS would stop taking additional data. All the incoming information about the triggering event from the different subdetectors, within a specified timerange referred to as a trigger window, was written to the disk. This constitutes the major contribution to the deadtime. This usually requires a simple hardware response constructed using a combinations of gates, see figure [2.10]. Some software analysis is quickly done to process the data through the L2 trigger. Real-time monitoring of this data is crucial to spot any malfunctioning of the CLAS or the tagger. This data is processed instantly with tracks reconstructed to display reconstructed track vertices, DC, ST, TOF, CC, EC hits, their statistics and occupancies in real time to the CLAS shift-takers. This assures the data quality of the CLAS dataset.

2.4 Data skims and their storage

The entire g12 dataset was processed and reconstructed using the computing resources at Jefferson lab. A parallel effort at FSU was also undertaken initially, and then dropped as

JLAB added more computing resources. The effort did give us an opportunity to test and confirm the robustness of the reconstruction process on different architectures and machine builds.

Each 50 Million event run has $\sim$ 130 files for the production triggers. Each of these files after the final reconstruction were skimmed for particular topologies and stored separately for further ease of analysis. This reconstructed skimmed data in their individual directories is available on the JLAB silos at '/mss/clas/g12/production/pass1/bos'. Out of the total 8 skims that exists on the silo, the first 5 skims (1-5) described are exclusive skims that contain each and every event from the g12 dataset and the other 3 (6-8) are special skims based on the specific needs of some analyses [41] [42]. The skims with their topologies are :

1. **1-1ckaon1ctrk -** Reconstructed events with at least 2 charged tracks, with one of the tracks identified by the reconstruction software as that of a kaon or that of a possible kaon. A possible kaon, for the sake of the skim, is defined as the one in which we have a high momentum track ($p_{\pi} \geq 2\ GeV$) identified as a pion or a high momentum track ($p_{proton} \geq 3\ GeV$) identified as a proton. The reasoning behind this lies in the way CLAS reconstruction software does its particle identification using a tracks β (see figure [3.3]).

2. **2-2pos1neg_not_1ckaon1ctrk -** Three prong data, with exactly 2 positively and 1 negatively charged particle tracks detected and reconstructed in CLAS. This skim does not include any kaon data.

3. **3-2ctrk_not_2pos1neg_1ckaon1ctrk -** Events with 2 or more charged tracks that did not pass either skim 1 or skim 2.

4. **4-not_2ctrk_2pos1neg_1ckaon1ctrk -** Physics events that did not pass the tests for skim 1, skim 2, or skim 3.

5. **5-other -** Scalers and Other non-physics events in the BOS files.

6. **6-1lepton -** A non-exclusive redundant set of events that may contain a possible lepton.

7. **7-4ctrk -** A non-exclusive redundant set of four-pronged events.

8. **8-ppbar -** A non-exclusive redundant set of events that contain at least a proton and an anti-proton.

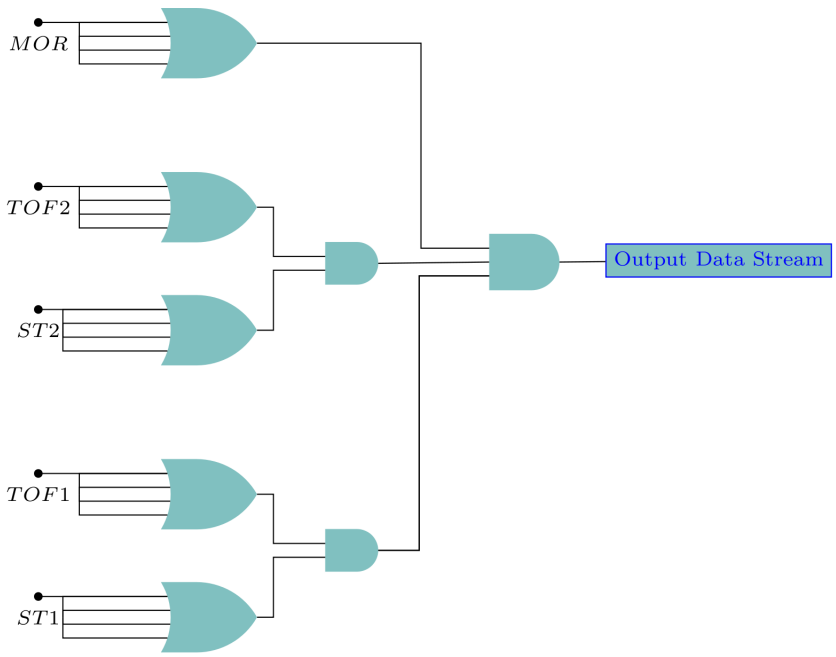

Figure 2.21: Primary trigger schematic, where ST × TOF hits are registered in 2 distinct CLAS sectors in a coincidence time window of ∼ 150 ns in conjunction with a hit in the 1^{st} 19 tagger paddles.

2.5 Trigger Configurations of g12

CLAS and its subsystem are constantly recording data to the tape during operation. Due to the limitations of the data acquisition, and to maintain quality control, 'triggers' are generally employed in particle physics experiments. When the conditions of the triggers are satisfied by an event, DAQ records the event data to the tape. Triggers require the hits to satisfy a predefined set of conditions for various CLAS systems within in a short window of time for the event.

The primary production trigger for g12 required tracks in two distinct sectors of CLAS in conjunction with a hit in the tagger where at least one of the tagged photons in the event period had an energy ≥ 4.4 GeV. The track condition was evaluated true when a hit was registered in the start counter and the time of flight scintillators (ST × TOF) of a CLAS sector within a short window of time ($\sim 150ns$). The photon energy ≥ 4.4 GeV requirement was enforced by requiring that at least one of the first 19 tagger counter recorded a hit

during the time window for the event, which would cause the tagger Master OR (MOR) boolean condition to be evaluated true (see figure [2.21]). Thus, the primary g12 trigger is represented as:

$$\text{Primary Trigger} \equiv 2 \times (\text{ST} \times \text{TOF}) \times \text{MOR}(1 \cup 2 \cup ... \cup 18 \cup 19) \tag{2.1}$$

Runperiod g12, consisted of 3 distinct CLAS experiments with distinct Physics goals. Two PAC-approved experiments called HyCLAS and Super-G were originally combined to form the g12 runperiod due to similar beam and detector configuration requirements for the experiments. Right before the start of datataking a third parasitic experiment was added to the schedule, which was accommodated alongside the other 2 main experimental components. The accommodation was made by adding a 'prescaled' trigger into the original g12 configuration as well as taking dedicated runs with a separate specified trigger at lower currents of 24 nA. Prescale of a 1000 implies that on average 1 out of every 1000 qualifying events that satisfies the trigger gets recorded. The main production trigger for the g12 experiment required the presence of at least two charged 'tracks' in two different CLAS sectors within a time window in coincidence with a hit in the tagger for a beam photon energy $\geq$ 4.4 GeV. These 'tracks' were identified at the trigger level by the existence of a hit signal in the ST and the TOF of the same sector within the trigger time window. These signals from tagger, ST and TOF are logically combined in an 'And' operation on a hardware level and when evaluated true, triggers a write of the data by the DAQ. Use of field programmable gate array (FPGA) as the trigger supervisor (TS) allowed the g12 experiment to run with a easily modifiable, very complex trigger configuration compared to any prior CLAS experiment. There were 12 concurrent, easily configurable, independent trigger definitions throughout the g12 runperiod.

In the presence of the L2 trigger requirement, the event gets evaluated by the L2 trigger using rudimentary software reconstruction. Majority of the g12 data was acquired with a beam current of 60-65 nA, at an average DAQ rate of 8 KHz. The g12 trigger definitions, their bit values and their prescaling factors are listed in the trigger table. Additional triggers (up to 12) were implemented alongside the main production trigger with a variety of experimental goals in mind. Additional extraneous information from CEBAF, beamline,

Table 2.1: Experimental running conditions for g12 and general statistics.

Electron beam energy	5.714 GeV
Electron beam intensity	65 nA
Electron beam polarization	Circular
Torus magnetic field/current	$\frac{1}{2}\ B_{max} \equiv 1930A$
Photon collimator radius	6.4 mm
Radiator thickness	10^{-4} radiation length (r.l.)
Radiator density	646 μgm/cm^2
Events / Run	50 M
Tagger counters used in primary trigger	T1-T19
Photon beam energy	1.1-5.45 GeV
Target	40 cm long Kapton cell, 4 cm in diameter
Target material	LH_2
Target position	-90 cm from the center of CLAS
Target polarization	None

beam monitors in the hall and other EPIC scalers were also written to the datastream every 2 and 10 seconds to ensure data quality. Throughout the runperiod, several calibration runs were taken to calibrate the voltage gains and determine the pedestals for PMTs and other components of CLAS. Normalization runs at lower beam current $\sim$ 5nA were taken for DC alignment corrections and the total photon flux determination. The aggregation of these 'extra' information was crucial for, and relied heavily upon for later offline calibration of the CLAS and the tagger.

2.5.1 Run conditions and list of runs and triggers

The runs listed in tables [2.2] and [2.3] are the 'good' runs that were reconstructed successfully and were available for full analysis. There are two sets of runs with different trigger configurations and beam currents - single sectors at 24 nA and production trigger ones at $\sim$ 65 nA distributed throughout the runperiod [42].

Table 2.2: Runs taken with the production trigger, available for g12 analysis

Run Number	Beam Current
56363	20
56365	30
56369	30
56384	5
56386	20
56401	50
56403	70
56404	60
56405	50
56406	40
56408	80
56410	90
56420-56422	5
56435	5
56436	15
56441	35
56442	30
56443	20
56445-56450	60
56453-56459	60
56460-56462	70
56465	70
56467-56472	70
56478-56483	70
56485-56487	70
56489-56490	70
56499	70
56501	60
56503	57
56504	56
56505-56506	40
56508-56510	60
56513-56517	60
56519	60
56521-56542	60
56545-56550	60
56555-56556	60
56561-56564	60
56573-56583	60
56586-56593	60
56605	60

Run Number	Beam Current
56608-56612	60
56660-56661	60
56665-56670	60
56673-56675	60
56679-56681	60
56683	60
56685-56696	60
56700-56708	60
56710-56724	60
56614-56618	60
56620-56628	60
56630-56636	60
56638-56644	60
56646	60
56653-56656	60
56726-56744	60
56748-56750	60
56751-56768	65
56770-56772	65
56774-56778	65
56780-56784	65
56787-56788	65
56791-56794	65
56798-56802	65
56805-56815	65
56821-56827	65
56831-56834	65
56838-56839	65
56841-56845	65
56849	65
56853-56862	65
56864	65
56865-56866	60
56870	65
56874-56875	60
56877	60
56879	60
56897-56898	60
56899	65
56900-56908	60
56914-56919	60

Table [2.2] - continued

Run Number	Beam Current
56921-56922	60
56923	65
56924	70
56925	80
56926-56930	60
56932	60
56935-56940	60
56948-56956	60
56958	60
56960-56975	60
56977-56980	60
56992-56994	60
56996-57006	60
57008-57017	60
57021-57023	60
57025-57027	60
57030-57032	60
57036-57039	60
57062-57069	60

Run Number	Beam Current
57071-57073	60
57075-57080	60
57095-57097	60
57100-57103	60
57106-57108	60
57114-57128	60
57130-57152	60
57159-57168	60
57170-57185	60
57189-57229	60
57233-57236	60
57249-57253	60
57255-57258	60
57260-57268	60
57270-57288	60
57290-57291	60
57293-57312	60
57317	60

Table 2.3: Runs taken with the single sector trigger, available for g12 analysis

Run Number	Beam Current
56476	24
56502	24
56520	24
56544	24
56559	24
56585	24
56619	24
56637	24
56663-56664	24
56697	24
56725	24
56747	24
56769	24
56804	24
56835	24
56869	5

Run Number	Beam Current
56910	35
56911	30
56912	25
56913	24
56933-56934	24
56981-56983	24
56985	15
56986	15
56989	25
57028	24
57061	24
57094	24
57129	24
57155-57156	24
57237-57238	24

CHAPTER 3

DATA REDUCTION AND SELECTION

3.1 Selection of proton K^+K^- final states

The analyses presented in this thesis explore data reconstructed from 95% of the g12 dataset. A total of 59694 files were skimmed and processed for 3 prong (charged tracks) events, where 2 tracks were identified to be of a positively charged particle and 1 track belonged to a negatively charged particle. These were further whittled down by creating files that only contained events where the particle identification routine used by the reconstruction software 'a1c' identified the event as containing a single proton, a K^+ and a K^- in its Particle ID data bank (PART).

The goal of this analysis is to identify the events which satisfy the basic criteria for being a good event with an identified proton, K^+ and K^- track. Once accomplished we will look at the missing mass of these events and establish whether there was a missing π° or an η in the event. 'Missing Mass' is defined to be the magnitude of the lorentz four-vector calculated by subtracting the four-vectors of the identified final state particles from the four vectors of the incoming beam photon and the target proton.

$$\mathrm{MM}_\mu = \gamma_\mu + \mathrm{proton}_\mu^{\mathrm{target}} - \mathrm{proton}_\mu^{\mathrm{recoil}} - \mathrm{K}_\mu^+ - \mathrm{K}_\mu^- \tag{3.1}$$

3.1.1 List of Applied Corrections

Corrections identified and applied to the g12 data set are :

1. **ELoss -** 'Eloss' refers to the correction implemented on each particle's momentum and energy. The correction accounts for the energy and the momentum loss that a charged particle incurs as it travels through and interacts with various components

and materials inside of CLAS. On its way to the TOF and the outer detectors [48], the particle interacts with the start counter, scattering chamber, target cell wall, and other materials. CLAS tracking code does not account for these material interactions of the particle along the track and simply returns the momentum as it calculates using the magnetic field between region 1 and region 3 of the Drift Chamber. These unaccounted energy losses can be substantial, especially for low momentum particles in photoproduction experiments with the start counter installed. The eloss correction takes all of these along with the geometry of the track into account and corrects the four-momentum for the particle track.

2. **Beam Energy Corrections -** 'BEC' refers to the beam energy corrections that g12 had to implement to correct the four-vectors of the beam photons to account for the errors introduced in their calculation due to suspected hysteresis displayed by the tagger magnet [41]. Tagger magnet hysteresis led to errors in the calculated bending magnetic field of the tagger for the incoming electron during reconstruction, propagating errors to the calculated four-vectors for the beam photons. Since the missing mass is calculated using the beam energy, these corrections play an important role for inclusive events, where we allow one of the particles to be missing.

3. **Momentum Corrections -** 'Pcor' refers to the corrections to the momentum of a particle introduced, due to the unknown deviations in the magnetic field map that was used, during the reconstruction of the particle's track [41], inside of CLAS. The small deviations of the real field from the provided mapped field to the reconstruction software arises due to our limited knowledge of the imperfections of the real field in CLAS as well as the misalignment of the drift chambers. This introduces small errors in the calculated momentum of the charged particles. The higher the multiplicity for the charged tracks in an event, the higher the error in the missing mass calculated for those events.

3.1.2 Selection Cuts for proton K^+ K^- events

After the preliminary selection of the events with a proton, a K^+ and a K^-, the analysis has a much reduced and cleaner set of the events of interest. The analysis further selects events using vertex, timing, beta and beam energy cuts as outlined below.

3.1.2.1 Vertex Cuts. Reconstruction estimates the event vertex by extrapolating all the tracks back to the target. Their average intersection location is referred to as the event vertex. The analysis requires all events to be within the stated target parameters. The

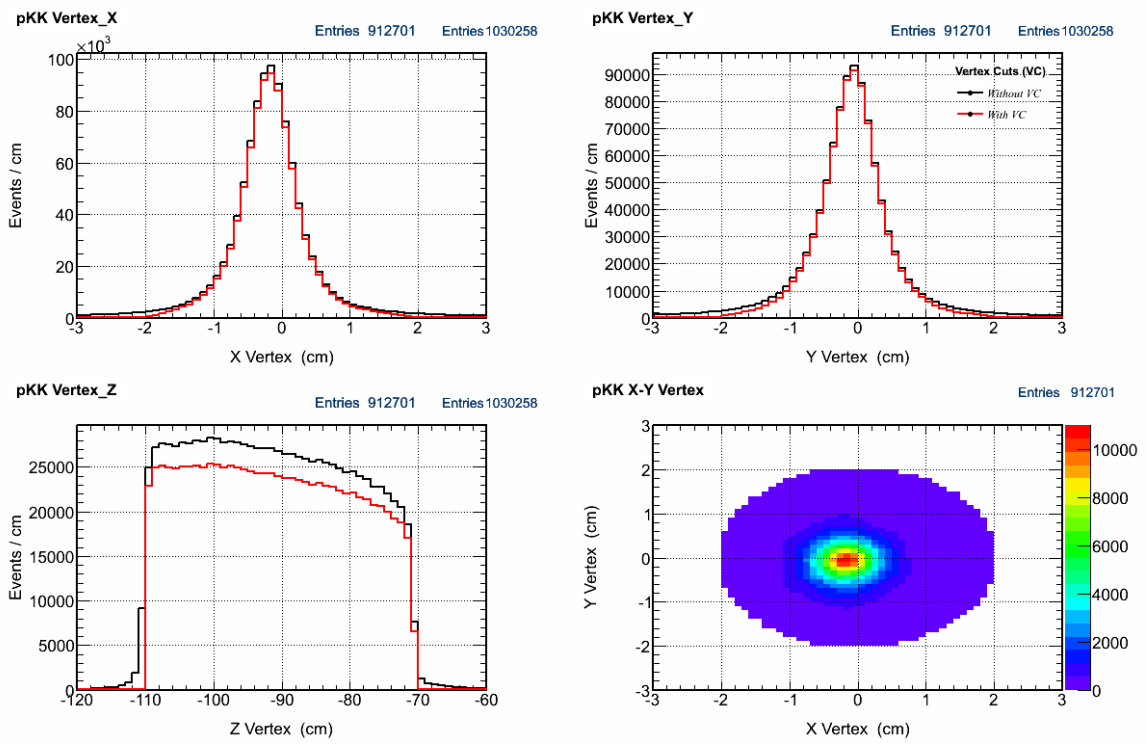

Figure 3.1: Selected proton K^+ K^- events before (black histogram) and after (red histogram) constraints to have the reconstructed vertex be inside the target volume were placed.

g12 experiment used a cylindrical cell made of Kapton, 4 cm in diameter and 40 cm in length centered at (0,0,-90-cm) in the CLAS lab frame. Hence, the reconstructed lab x-cordinate and the lab y-coordinate for a track should lie within a radius of 2 cm of the z-axis whereas the z-co-ordinate should lie between (-70 cm, -110 cm) in the CLAS lab frame as shown in figure [3.1].

3.1.2.2 Timing Cuts using Start Counter and Time of Flight. Event timing is calculated in CLAS in multiple ways. The timing of the incoming electron beam is the most accurate time known for an event in CLAS and is referred to as the RF time of the beam bucket. Once the timing of the scattered electron is measured, it is extrapolated to determine the RF beam bucket for that electron. The photon thus produced is one of the potential candidates to have had caused the event. The algorithm further extrapolates and propagates the RF time for the scattered electron/produced photon at the radiator to the event vertex. This timing for that particular photon is known as the 'RF vertex time' for

that photon. In a recorded event there are many photon candidates, but the requirement to be close in time to time-average of the measured tracks (event time), removes most of the extraneous photons in the event. In about 12% of events in g12, we have more than 2 photons in the same beam bucket. Most of these extra photons are of lower energy than the triggering photon. Hence selecting the photon with the highest energy, in conjunction with a selection cut on the missing meson, assures the selection of the correct photon in the analysis.

Since start counter is the closest sub-detector to the event vertex, its timing is the most reliable for any given track. The analysis iterates through the start counter times of each track to select tracks that are within 3-ns of the calculated event vertex time, and hence they are all very close to each other in time, increasing their probability of originating from the same event. This is crucial since CLAS records tracks for all the events that occur in $\sim$ 150-ns time interval about the triggering event.

The initial determination of the CLAS event time is performed by averaging over the event vertex time for each track in the event. Once this average event time is known, reconstruction software looks into the events TAGR bank which contains information about all the photons that were detected in the tagger during the event. The highest energy photon in the beam bucket closest to the average event time is chosen as the best match photon and is considered the photon causing the event for further analysis. The choice of the highest energy photon is an experimental bias for the analysis; since there is no physics handle to correctly identify the event photon in cases of multiple photons present in the event-causing beam bucket. As mentioned earlier, most extra photons have lower energy than the triggering photon and selecting the photon with the highest energy, in conjunction with a selection cut on the missing meson assures the selection of the correct photon for the analysis.

The analysis selects events where each of the detected track event time, as determined by their start counter hits, is within 3.006 ns of the event vertex time (tpho) as determined by extrapolation from the tagger. This allows us to select individual particles with their reconstructed event time in the neighboring bunches. Within this subset, events are selected where the tpho is within 1.002 ns of the average event vertex time as calculated from the

hits of the start counter. The distribution is shown in figure [3.2].

3.1.2.3 Beta Cuts. The time of flight (TOF) sub-detector system is crucial to the particle identification. It gives the stop time and the end-point for a track which is then used with the start-time and a hit-position from the start counter to calculate the distance traveled and the time taken to travel it, to obtain the speed and the 'β' of the particle. When combined with the momentum from the drift chambers, the algorithm is able to identify the mass and the charge of the particle that must have created the track.

A measure of how relativistic a particle is, can be obtained from the value of β for the particle.

$$\beta = \frac{\text{particle velocity } (v)}{\text{speed of light } (c)} = \frac{\text{Distance traveled by particle}}{(\text{Event vertex time - TOF hit time}) \times c} = \frac{p}{E} \tag{3.2}$$

CLAS maps the path and measures the distance traveled by the particle in its volume. Using the TDC/ADC hits it measures the position and the time of the hits of a track in its sub-detectors. With the information of the hit location, path traversed and the time taken to traverse, reconstruction software is able to calculate the β for the particle using equation[3.2]. Since there is a resolution spread in all these measurements, the final calculated β also has a resolution to it. One way to select good events and get rid of low quality events is to select tracks, whose β value resolve to within a certain margin of error to the expected β value for a given particle. These cuts work well for low momentum tracks. At higher momenta β curves for pions and kaons merge and the ability of this method for pion-kaon separation is compromised, as seen from figure [3.3].

3.1.2.4 Beam Energy Cuts. For g12, CLAS collected photoproduction data over the photon beam energy range of $1.1\ GeV - 5.45\ GeV$. The primary trigger biased the CLAS data collection towards accumulating events with $E_\gamma \geq 4.4\ GeV$. Taking into consideration the primary trigger and the minimum beam energy required to produce a $\phi\eta$ resonance kinematically through peripheral production is ~ 2.54 GeV, the analysis only looks at events produced with their best tagged photons with $E_\gamma \geq 4.4\ GeV$, i.e within the primary trigger range for g12. The plot has the photon beam energy corrections applied to it. These

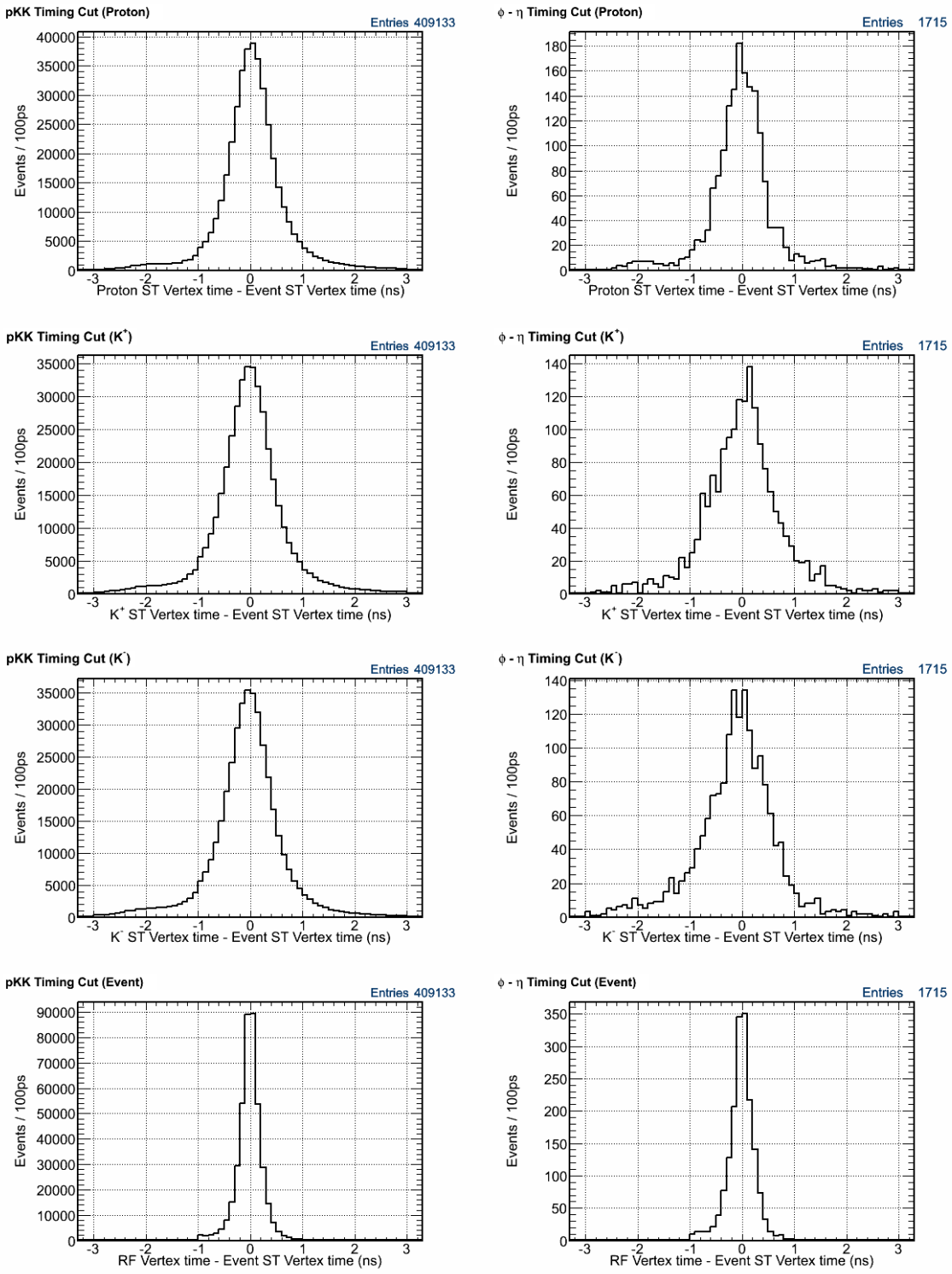

Figure 3.2: Selected proton, K^+ , K^- and the event time as averaged by CLAS reconstruction software 'a1c'. Left column depicts for all proton K^+ K^- events while the right column depicts the ones that were selected with nominal cuts placed for ϕ η event selection.

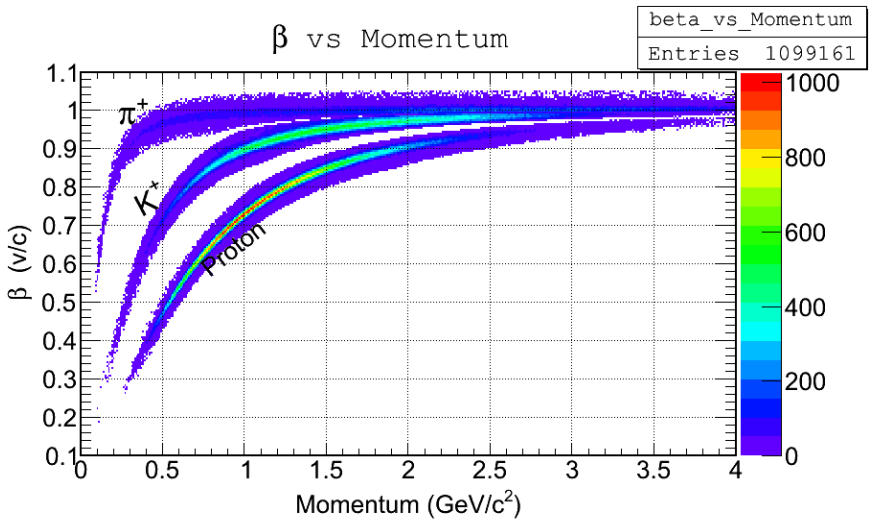

Figure 3.3: β (v/c) vs Momentum plot for positively charged particles

corrections were for a miscalculation during the reconstruction stage of the g12 data of the tagger magnetic field introduced due to the hysteresis of the tagger magnet [41].

3.2 Reconstruction and Particle Identification

The Particle Identification (PID) routine of the reconstruction software calculates the mass of a particle for a given track as :

$$\mathrm{m} = \frac{\mathrm{p}}{\gamma \times \beta} \tag{3.3}$$

where p is the momentum calculated for the track by the Drift Chamber and γ, β the relativistic variables that depend on velocity of the particle. The mass thus calculated is used to identify the closest matched known particle mass and the track is labeled as such.

For higher momentum π's and K's, the ability of CLAS reconstruction software, is severely compromised due to the CLAS resolutions of the momenta as well as the timings of the tracks. Since π's are generally produced in copious amounts and the K's are relatively rare, this reconstruction inefficiency affects analysis channels with kaons the most. The dataset has to be closely examined for the misidentified pions and these events are considered as one of the contributing backgrounds. Timing cuts, as observed in figure [3.2],

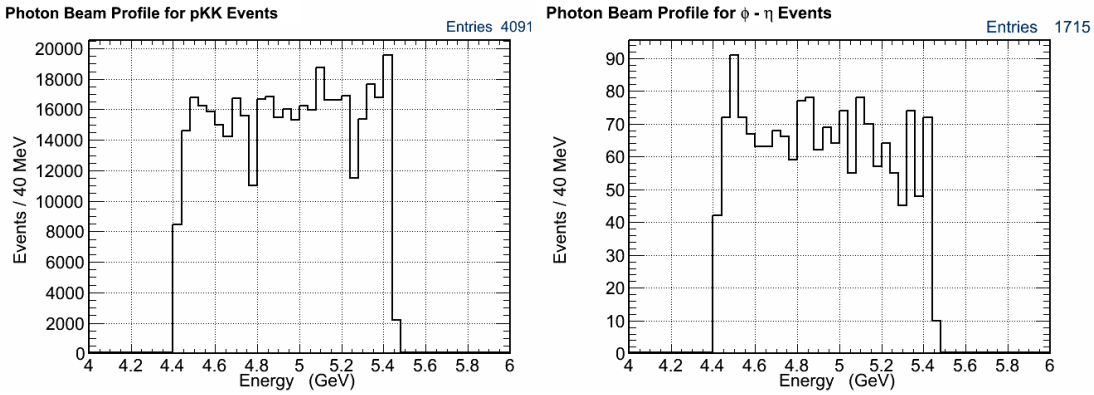

(a) Beam energy profile for events with detected proton, K^+, K^- with timing and vertex cuts.

(b) Beam energy profile for events with detected proton, K^+, K^- with timing cuts, vertex cuts and the elliptical $\phi - \eta$ cuts.

Figure 3.4: Beam energy profile for selected events

and β cuts, as observed in figure [3.3], help clean up the kaon data to a good extent and get rid of the pion contamination.

3.2.1 Synopsis of Data Quality Cuts

In table [3.1], all the cuts required to select well-reconstructed events are listed and are common to all the analyses presented in this thesis.

Table 3.1: Standard criteria for good proton, K^+, K^- event selection

abs(Timing cut on event vertex time)	1.002 ns
abs(Timing cut on protons, kaons vertex time)	3.006 ns
Event vertex z position cut	-110 $\leq$ z $\leq$ -70 cm
Event vertex x and y position cut	$x^2 + y^2 \leq 4$
Beta cut for each particle track	$\lvert\beta_{measured} - \beta_{calculated}\rvert \leq 0.07$
Beam energy cut	$E_\gamma \geq 4.4$ GeV

3.3 Kinematic Fitting

For any particular analysis, the measurements of the four-vectors of the detected final state particles made in CLAS have an associated resolution to them. This also makes the

calculated missing particle have an innate resolution to it, even when the missing particle might be a long-lived stable particle like a pion or a kaon and hence of a naturally occurring negligible width. This resolution comes due to convolutions of various uncertainties and the errors made during the reconstruction process, from measuring a track in the DC to the timing of various detector components. Once the particle identification of a given track is done, the energy-momentum conservation can be used to constrain the energy and the momentum of the particle such that the particle has its real (PDG stated) mass. To do this in a standard manner and not introduce unknown behavior, a standard procedure referred to as 'Kinematic Fitting' is used.

The kinematic fitting procedure used in the subsequent analysis uses the kinematic fitter routines developed by Dr. Dustin Keller. Reference [49] is the standard reference for the kinematic techniques developed and used for g12 and in this analysis. The fitter uses the 'Least Squares Fitting' techniques in conjunction with the method of 'Lagrange Multipliers' to enforce the energy-momentum conservation. It performs a χ^2 minimization using the provided measured values for a given event. The fitter has to be provided with the initial covariance matrix elements that contain the correlations between the kinematic variables of each track as determined during the reconstruction of the track. This covariance matrix is found to be inadequate for direct use by the kinematic fitter as it does not include multiple scattering errors and energy losses due to detector materials. This is addressed by using scaling parameters in the fitter routine. The covariance matrix elements are scaled appropriately by the kinematic fitter routine, and the individual kinematic variables are adjusted within the allowed constraints determined by the correlation matrix, to calculate the minimum χ^2 for the fit using the least squares fitting method.

The input values to the fitter include the corrections g12 obtained from the energy loss corrections, momentum corrections, and the beam energy corrections as mentioned and explained earlier in section [3.1.1].

After an event has gone through the fitter, the fitter creates a new covariance matrix to express the correlations between the kinematical variables and returns to us two quantities of interest along with the modified kinematic quantities. These quantities are the pull and the χ^2 for a given event. The pull value for an event is calculated using the pull distribution

as follows :

$$z = \frac{\eta_i - \eta_f}{\sqrt{\sigma_{\eta_i}^2 - \sigma_{\eta_f}^2}} \tag{3.4}$$

The pulls distribution of all the events is a good indicator of the quality of fits and serves as a calibrating tool to fine-tune the fitter. The pull distribution provides us with the correlations between the systematic errors of various kinematical variables.

A good quality fit from the kinematic fitter is statistically expected to yield a pull distribution for all the kinematical variables that were varied, to be a gaussian distribution centered (mean) at 0 with a gaussian width (variance) of 1. Significant deviations from this normal distribution indicates the presence of systematic errors or a huge amount of background in our data. To get a complete idea of tools, formalism employed and procedures involved in kinematic fitting, the following references [49], [50] are strongly recommended.

The other useful quantity obtained from the fitter is the χ^2/ν distribution of the events, where ν is the number of degrees of freedom of the problem/fit. This quantity is used to calculate the full confidence level distribution for the hypothesis used by the fitter to fit the data. In absence of any background, the confidence level distribution is expected to be a flat distribution of the data events with values between 0 and 1. In the presence of background, or badly reconstructed events, an overpopulation of events should be observed near 0; since background events do not satisfy the imposed kinematical constraints. Thus, the 'χ^2' for a fit can be converted into a probability test for our hypothesis, to give us an indication whether the event satisfies our hypothesized reaction or not. General approach after the kinematic fitting is to separate good events from bad events by tagging the events below a certain confidence level (1%-10%) as background and above that confidence level as the data events. Using the confidence level cuts discards a certain percentage of good events. The analyses have to explicitly account for that in all yield and cross-section calculations done using a confidence level cut.

Kinematical fit used for this analysis is an example of a '1C' fit. This categorization of the fit as '1C','4C' etc. depends on the number of variables and constraints involved for our fit hypothesis. For a set of 'k' known constraints and 'j' unmeasured variables, the effective number of constraining elements are (k-j) elements and such a fit is referred to as a '(k-j)C'

fit. For the subsequent analyses, the '1C' fit is used where the missing mass is hypothesized to be an 'η' or a 'π°'. The three momentum components of the missing particle are treated as the 3 unmeasured variable, while the energy-momentum conservation for the channel as a whole provides us with 4 constraints, categorizing the said fit as a '1C' fit.

The variables used by the kinematic fitter, to arrive at the right four-momentum for each particle, are the lab-frame momentum 'p' for a track, the angle 'ϕ' between the track and the beamline, and the angle 'λ' between the center-plane of the sector and the track plane. See figure[3.5] for the pulls distributions of these variables. Figure [3.6] shows the confidence level distribution for our fit hypothesis to a missing η meson. The flat distribution of confidence level plotted in the top row, along with the pulls from the fitter imply that the kinematic fitter is well-calibrated. Using a confidence level cut of 5%, a majority of the events, that the fitter finds compatible with a missing η, are selected. The bottom 3 rows of the figure [3.6] show the events that were discarded or selected based on our confidence level cut, to give us a clearer picture of the kinematics of the discarded events.

Figure [3.7] shows the fits for the selected events with a polynomial background and a ϕ meson with different lineshape functions - a gaussian (top-row), a lorentzian (middle-row) and a voigtian (bottom row). The masses plotted are for the kinematically improved four-momenta. It is thus observed that a lorentzian plus a polynomial gives a good representation of our K^+K^- invariant mass spectrum.

Kinematic fitting, with 1C fits to the missing mass, is subsequently used to obtain four-vectors from the g12 data, and the corresponding MC simulations, for performing PWA.

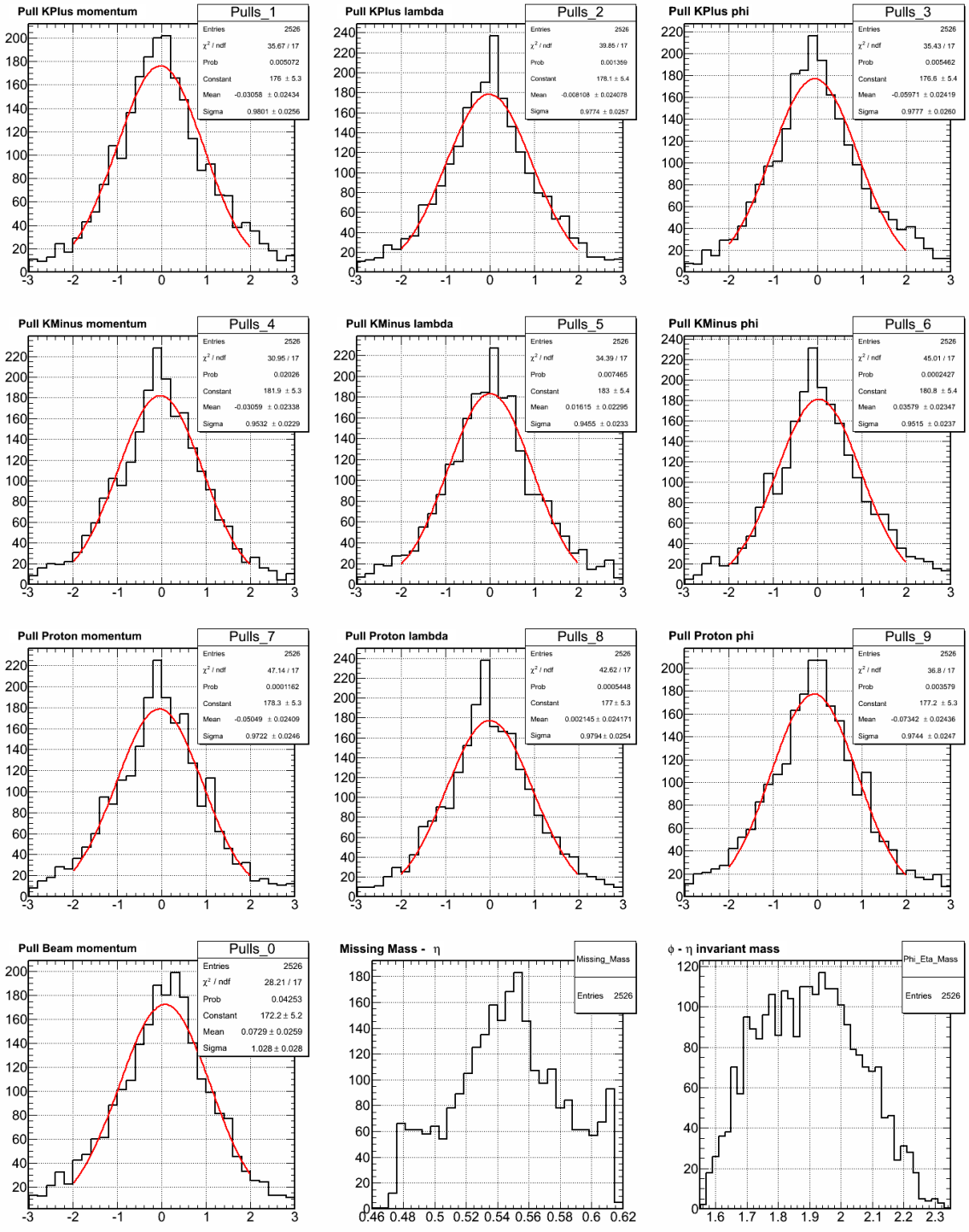

Figure 3.5: Pulls for the various variables returned by the kinematic fitter.

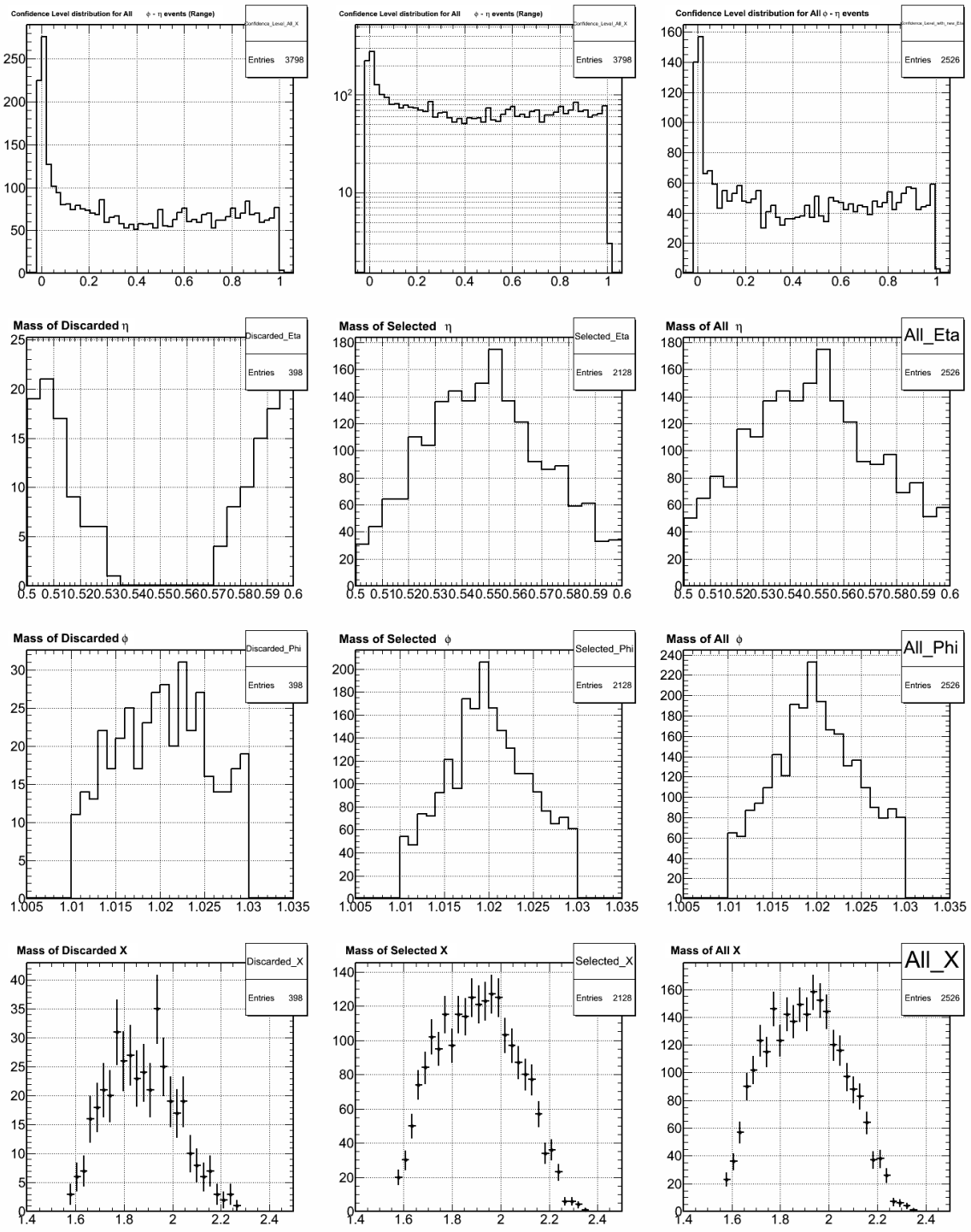

Figure 3.6: Plot for discarded and selected events for various invariant masses using the confidence level cut of 5% on the probability returned by the kinematic fitter.

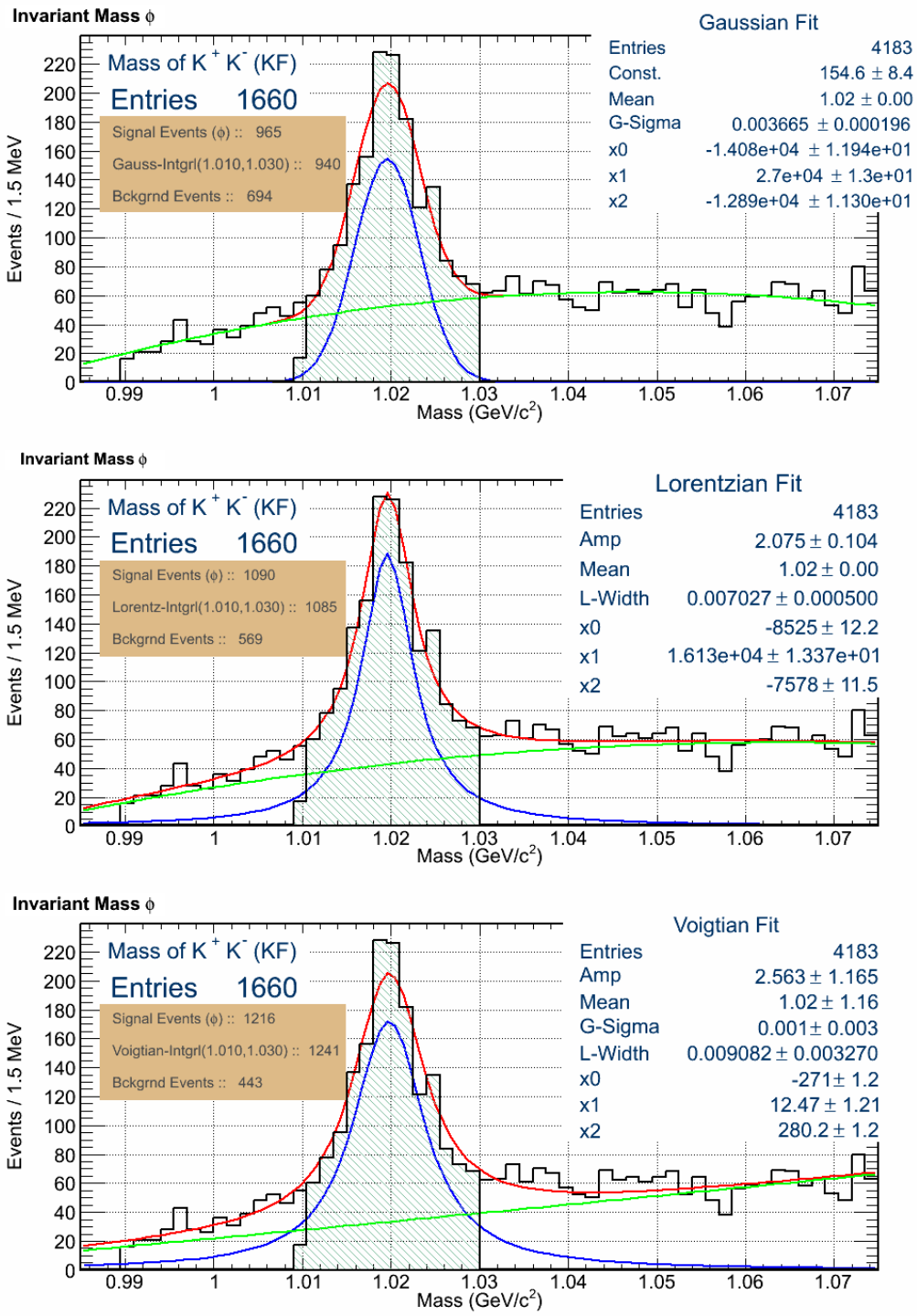

Figure 3.7: Estimate of the width and the yield of the ϕ meson as well as the background for the kinematically fitted events. Various lineshapes were assumed for the ϕ resonance and the yield calculated for them.

CHAPTER 4

STRANGEONIA ANALYSIS

4.1 Introduction

The majority of thesis work was performed by analyzing the 3-prong events from the g12 dataset, where 3 charged tracks were detected and successfully reconstructed in CLAS. The 3 reconstructed charged tracks were constrained to be a proton, a K^+, and a K^-. The particle identification was performed by the in-house reconstruction software for CLAS, 'a1c'. The thesis focuses mainly on the photoproduction of the strangeonium state, and its subsequent decay via reaction [4.1]. The initial goal of this analysis was to analyze the proton K^+ K^- [η] final state for observable resonances in the invariant mass spectrum of the ϕ η intermediate state, calculating the first cross sections for the ϕ η photoproduction, strangeonium production cross sections or alternatively determining upper limits on the strangeonium cross section, and performing a proper partial wave analysis (PWA) for isolating the strangeonia and their quantum numbers.

$$\gamma \;\; p \;\; \rightarrow \;\; p \;\; X \;\; \rightarrow \;\; p \;\; \phi \;\; \eta \;\; \rightarrow \;\; p \;\; K^+ \;\; K^- \;\; [\eta] \tag{4.1}$$

After applying the vertex and the timing cuts outlined in section [3.1], a subset of g12 data with well identified proton, K^+ , and K^- events is obtained. The primary decay mode in the search for strangeonium state is the decay of a meson to $\phi\eta$, as outlined in the figure [4.1]. The major background for this channel in the analysis comes from N^* production that decay via the proton η intermediate state, outlined in reaction [5.4] and observed in the analysis figure [4.2]. This background is also of interest in terms of exploring N^* physics, but the primary motivation of the analysis remains to obtain the strangeonium cross sections

and production amplitudes.

4.2 Cross section and yield

4.2.1 Concept

If two solid objects were to collide head-on, the overlap of the transverse solid area they present to each other is considered the 'collision cross section' for the event. Quantum mechanical cross section, similarly, represents the overlap of two objects, namely wavefunctions.

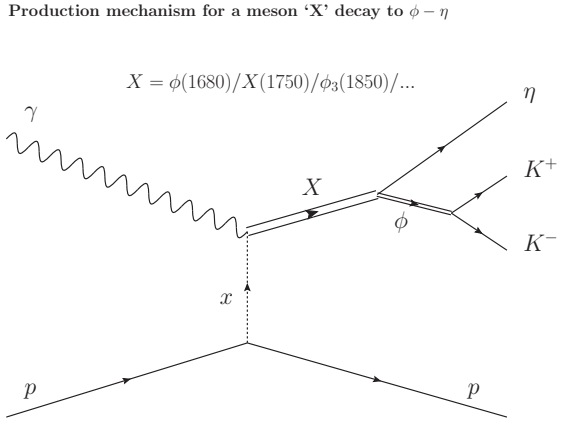

Figure 4.1: Feynman diagram for a meson 'X' decay via $\phi\eta$ is drawn for the photoproduction reaction [4.1]. A photon scatters off a proton to produce a resonance X via a virtual meson exchange.

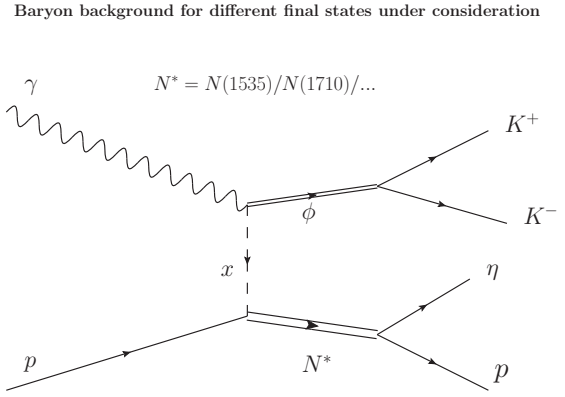

Figure 4.2: Feynman diagram for the background N^* to the photoproduction channel [4.1] is drawn. The incoming photon excites the proton into a N^* which then decays to proton η, while producing a scattered ϕ meson.

Overlap of these wavefunctions represent the probability of occurrence for the event. The newtonian concept is, thus, expanded to quantum mechanics in the form of cross sections for reactions.

Physical phenomena at microscopic scales are quantum mechanical in nature, and hence probabilistic by extension. They only allow us to measure their probability of occurrence, which is the cross section for the reaction. To measure observables such as the cross section in particle physics, the ensemble approach is chosen. In the ensemble approach to measure an observable, one repeats the same experiment under the same conditions, multiple times. The average value of the observable for a large number of measurements is the expectation value for the observable. By nature of quantum mechanics, it means that there is a real finite possibility of the event not occurring at all in multiple measurements. A large number of measurements are conducted to extract the average value of the observable. This is more or less how nuclear and hadronic cross sections are measured.

The experiment fixes an initial set of parameters and repeatedly measures the outcome. In case of g12, the event was incidence of a photon on a hydrogen nucleus (proton) in a LH_2 target. The number of such measurements taken and the occurrences of the events of interest (yield) are counted. This number, when corrected for the g12 experimental limitations, gives us an experiment independent value for the probability of occurrence of the event of interest; also referred to as the cross section for the event. Other examples of such cross sections are scattering of a pion off of a nucleus, transmission of a nucleon through a target, absorption of a photon by a nucleus.

4.2.2 Mathematical treatment for experimental cross section

For a nuclear or a hadronic reaction, the number of observed events is proportional to the number of target nuclei, number of incident particles, and the strength of the interaction 'σ' between the target nucleus and the incident particle. The interaction strength is determined by the physics between the two particles and the event of interest could be elastic scattering, inelastic scattering, absorption, etc. Luminosity 'L' is defined to be the number of incident particle that the target was exposed to per unit area per unit time. The analysis is not interested in the temporal evolution of luminosity, hence only the integrated luminosity is considered henceforth. The number of target nuclei, that the photon beam could interact

with, is calculated using the average density for a LH_2 target. Similarly, since the detector has a finite acceptance, not all events of interest that occur are observed. This is accounted by the 'Acceptance' calculated from the Monte Carlo (MC) simulations. Thus using the experimentally known parameters, measured yield and acceptance simulations, the analysis can calculate the cross section for a particular reaction. These definitions are mathematically expressed in equations [4.3-4.4], followed by a more detailed explanations of their parameters.

$$\frac{N_{target}}{V} = 2 \times N_{avogadro} \times \frac{\rho_{target}}{A_{H_2}} \tag{4.2}$$

$$\frac{N_{observed}}{Acceptance} = \sigma \times N_{incident} \times N_{target} \tag{4.3}$$

$$\sigma = \frac{N_{observed} \times A_{H_2}}{2 \times N_{incident} \times N_{avogadro} \times \rho_{target} \times L_{target} \times Acceptance} \tag{4.4}$$

where,

N_{target} *is* the number of target protons that on average lie in the path of the incoming beam photons,

$N_{observed}$ *is* the number of observed events in the experiment, aka the yield,

ρ_{target} *is* the density of the LH_2 used in the experiment,

$N_{incident}$ *is* the integrated flux (total number) of the incoming beam photons that were incident on the target to achieve the observed yield,

L_{target} *is* the length of the target cell,

Acceptance *is* derived from the simulations of the reaction phase space for the experiment and represents the corrections due to the finite acceptance of the detector.

4.2.2.1 Photon Flux Normalization. The analysis to measure a cross section requires the total amount of photon flux incident on the target during the entire experiment. The experiment is not always recording data, due to detector and data acquisition limitations. Thus the photon flux measured by the experiment has to account for the 'live time'

for the experiment and correct the measured photon flux. This correction of the measured flux to obtain the real photon flux for the experiment is referred to as the photon flux normalization. 'Live time' is the time that the data acquisition was ready to record events in conjunction with CLAS. For g12, the photon flux is recorded by the tagger and measured using gflux [51] as outlined in section [4.2.2.2].

4.2.2.2 gflux. A standard set of tools and techniques to calculate the photon flux normalization for the CLAS tagger are available through a CLAS software package called 'gflux' [51]. Using special calibration runs, gflux measures the number of good electrons that hit the tagger in a standard time window. It, then, compares it to the number of photons that make it to the 'Total Absorption Counter' (TAC) for low beam intensities and calculates a number called the 'tagging ratio' for the experimental setup.

The method of gflux normalization determines the photon flux at the target as a function of the photon beam energy (E_γ). The method utilizes the out-of-time electron hits in the tagger, that were not involved in the triggering physics event. It is assumed that these out-of-time hits follow poisson statistics and the event rate is measured for a given T-counter. CLAS tagger uses pipeline TDCs. It records a single hit for its scintillator during the trigger time-window. All the subsequent hits within that trigger window are ignored in flux calculations. The gflux method measures the minimum number of hits recorded in a tagger TDC for a given time-period 'τ'. The accelerator frequency for beam delivery is used to calculated the maximum numbers of trials that the experiment undertook in that given time-period. Thus the probability that at least one out-of-time hit occurred, in the given time interval 'τ' for a tagger T-counter, is calculated. This probability is the instantaneous rate for out-of-time hits. These instantaneous rates for a TDC are calculated every 10 seconds, which is the standard CLAS time-period between each scaler dump by the DAQ. The rates are then corrected for the live time of the DAQ/Detector. This final corrected number represents the average flux incident on that tagger scintillator. The software then calculates the corrected total number of electrons hitting the T-counter, and further corrects that flux for the tagging ratio using TAC. This is generally done for a given data-file by summing over all the recorded scaler intervals, to give us the final normalized photon flux for the data recorded in that file. Figure [4.3a] shows the total photon flux distribution for the

Table 4.1: Number of photons observed for every 100 MeV bin in E_γ, in the primary trigger range of g12.

E_γ Range (GeV)	Total Photons
4.4 - 4.5	2.0536×10^{12}
4.5 - 4.6	2.5412×10^{12}
4.6 - 4.7	2.3794×10^{12}
4.7 - 4.8	2.0871×10^{12}
4.8 - 4.9	2.3199×10^{12}
4.9 - 5.0	2.3638×10^{12}
5.0 - 5.1	2.2913×10^{12}
5.1 - 5.2	2.3103×10^{12}
5.2 - 5.3	1.9670×10^{12}
5.3 - 5.4	2.2492×10^{12}
5.4 - 5.5	1.1543×10^{12}
Total	2.1781×10^{13}

entire g12 runperiod whereas figures [4.3b], [4.3c], [4.3d] show the photon flux distribution as a function of beam energy for different periods of data-taking.

Table [4.1] contains the photon normalization statistics for the data presented in the thesis for various analyses. Another thing to note is that gflux has an ability to only use events from so-called 'good scaler intervals'. These are scaler intervals that have a live-time within a certain range of the average live-time. Since the statistics obtained for the analyses presented in this thesis are very low, the analyses do not use this ability of gflux. If this ability was implemented in the analyses, a minimum of 12% of the data would have to be discarded. This selection ability of good intervals is acceptable for high statistics decay mode, but not for the rare decays that the analyses are trying to observe. This leads to slightly larger errors on the photon flux determination, but at the same time the choice offsets this detrimental effect by allowing the analyses to retain higher statistics.

As a cross check for correct photon flux normalization, an analysis of the ρ meson cross section obtained from the g12 data was compared to that of the world data and was found to be in agreement [41]. Another g12 analysis for the photoproduction cross section of the Ξ Hyperon [41] was also found to be in agreement with previous CLAS analyses. This is further proof that the photon flux normalization in g12 is being performed correctly.

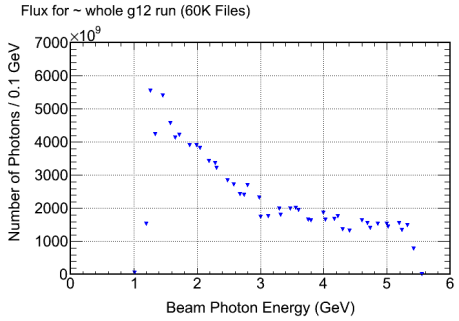

(a) Flux distribution as a function of E_γ for the runs used in the analyses.

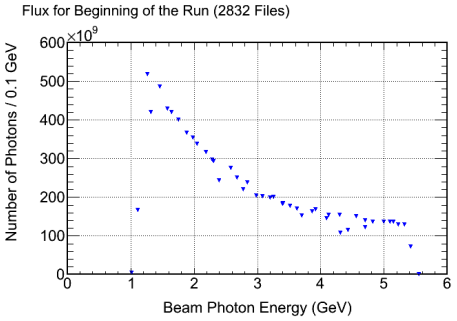

(b) Flux distribution as a function of E_γ for the runs in the early period of g12

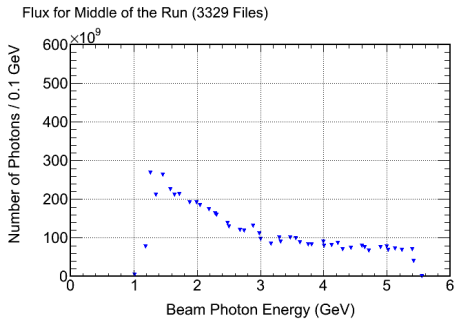

(c) Flux distribution as a function of E_γ for the runs in the middle period of g12.

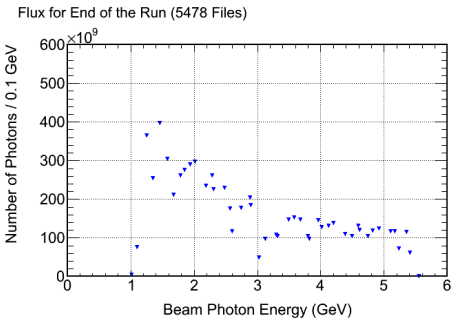

(d) Flux distribution as a function of E_γ for the runs near the end period of g12.

Figure 4.3: Flux distribution as a function of E_γ.

4.2.3 Corrections to the measured yield

Using specific physics motivated selection criteria, like observed ϕ and η meson widths and their sideband distributions, an initial number of signal events are identified as the yield observed by the experiment for a reaction. The observed yield is extrapolated to the physics yield that must have occurred but the experimental limitations did not allow to observe and record all of the occurrences. For example, the start counter used in the trigger for g12 has an estimated inefficiency of 6% per track. A detailed measurement of this and other inefficiencies were performed by the g11 experiment [52] [53], which had run-conditions and detector configurations very similar to g12. Another study was conducted to measure the general reconstruction efficiency for the g12 experiment as a function of the beam current [42]. The reconstruction inefficiency was found to linearly increase as a function of the beam

current, with the average inefficiency being 16% for the run-data at 60 nA. The analysis has to correct for these inefficiencies. The total fractional correction to the observed yield for a decay mode with 3 detected charged tracks in CLAS at the beam current of 60 nA is 1.4333.

$$\text{new yield} = \frac{\text{old yield}}{(1-0.06)^3 \times (1-0.16)} \tag{4.5}$$

4.3 Acceptance simulation for CLAS

CLAS detector is an hermetic detector, with near 4π coverage in solid angle, though due to detector frame and beam holes, practical acceptance is $\sim$ 3π in lab angle. Given the fact that CLAS is a fixed target experiment, the beam holes in the forward direction play a defining role in the acceptance of the physics events that occur in the collisions.

CLAS is unable to accept physics events in certain kinematical regions due to its construction. CLAS is not symmetric in accepting events in its detector volume, due to inefficient components, dead wires and other small deviations in geometry. When the data taken by CLAS is analysed, it reflects all these factors, which are due to CLAS and not due to any of the physics involved. Since a partial wave analysis or a cross section has to be independent of the characteristics of the detector involved, particle physics experiments usually use standard simulation packages and methods to estimate the effects of their detectors' acceptance on the physics data and hence be able to deconvolute the detector effects from the physics.

The standard software tools for performing simulations that are available for CLAS are genr8, ppgen, gsim, gpp along with the reconstruction software a1c. For a particular analysis channel, a set of phase space weighted events, that are generally isotropically distributed, is generated using genr8 or ppgen. This process generates a set of four-vectors for each event using phase space weighted Monte Carlo, that satisfy the kinematic constraints like the resonance mass, input beam energy and others as specified by the user. If the physics specified during this process was all the physics expected to be observed, then these set of four-vectors would be kinematically distributed just like the real data. In real data though, there is a convolution of physics as well the detector effects. To simulate the detector effects, these four-vectors are propagated through a virtual CLAS detector using a software package called 'gsim', based on GEANT [54]. Gsim takes each particle information and creates a

track for it through the detector. It generates hits in different detector elements according to the inefficiencies provided to it. This data is then post-processed with 'gpp', which takes the gsim generated TDC and ADC hits and smears them to provide resolutions similar to that of the real data, while removing detector hits due to dead and low efficiency wires. At the end of this cycle, if the process is properly calibrated at all steps, there is a final set of simulated data, which mimics the CLAS acceptance and resolutions, after it has been processed and reconstructed with 'a1c'.

These simulations are necessary for a proper partial wave analysis. Same selection criteria for the events are applied to both the observed data and the simulated data to arrive at experiment-independent quantities like cross sections, branching ratios and production amplitudes. The smearing factors, their calculations and more details for g12 simulations can be found in the g12 analysis note [41].

The analysis uses the acceptance corrected yield from the PWA to calculate the acceptance as a function of mass and the average acceptance for $\phi\ \eta$ decay mode, in addition to the phase space acceptance as an additional cross-check. This acceptance distribution is derived by dividing the $\phi\ \eta$ invariant mass distribution of the data events with the total accepted yield from the PWA.

4.3.1 Event Generation

In order to account for finite CLAS Acceptance, the simulated events are generated with kinematics as close as possible to the kinematics of the data distributions. To this end, for the $\phi\eta$ analysis, data was binned in a 2-dimensional histogram of beam energy and the $\phi\eta$ invariant mass. For each selected event in a bin, 10000 events were generated randomly distributed in the beam energy range (50-MeV binning) and the mass range (25-MeV binning) for that bin. This assures the simulation of acceptance for all the events observed in our data. The generated events were required to have a squared four-momentum transfer (t) distribution, such that after acceptance the simulated t-distribution had the same slope (within errors) as the observed data t-distribution. The decay of the $\phi\eta$ system occurs uniformly over the entire allowed phase-space. Since the analysis does not know of any particular resonance present in the data, the simulations are generated for phase-space to avoid an initial bias. The chosen bin size to generate events is smaller than the bin sizes

for the data analysis to reduce the effect of bin migrations due to the resolution of CLAS. Reconstruction introduces uncertainties and errors in the four-momentum of the tracks which is reflected as the resolution of the measured values. This sometimes causes events near the edge of a particular bin to 'migrate' to the neighboring bin. This effect hinders the correct normalization for these events and is addressed partially by making these bins narrower than the bin size selected for the analysis, so that when added together there is a smoother transition.

Events were generated where a photon interacted with a proton via a t-channel exchange process to produce a resonance 'X'. X decays to a ϕ and an η meson. The width for the ϕ meson was modified so as to achieve 7 MeV/c^2 resolution for the reconstructed ϕ meson, which is the width of the observed ϕ meson in the g12 data. The ϕ meson further decays to a K^+ and a K^- and is detected in CLAS along with the proton. The neutral η meson from the decay goes undetected in CLAS. Due to lack of real-world noise and track reconstruction issues in the simulations, the η meson has a width smaller than the data η meson, even after DC smearing by gpp. So the η width was modified in the simulation to achieve a width closer to the observed η meson width, as observed in figure [4.4]. Slope for data's t-distribution for ϕ η events is 0.897 $\pm$ 0.0528 GeV^2/c^2, as shown in figure [4.7b]. The input t-slope used to generate the simulated data was 0.7 GeV^2/c^2, and the t-slope for the accepted distribution was 0.921 GeV^2/c^2, which is within the errors calculated for the fit to the t-distribution of the ϕ η g12 data as shown in figure [4.7a].

The resonance 'X' is now made to decay uniformly over its accessible lorentz invariant phase space into a ϕ and an η meson. The η being neutral goes undetected in the main CLAS volume, since CLAS DC only tracks charged particles. The ϕ meson, which is also neutral, decays instantly into charged K$^+$ K$^-$ in our generated simulations, which are then tracked through the CLAS DC. The generated phase space kinematical distributions and invariant masses are compared to the accepted simulation as well as the experimental data to ensure that the simulation is in general agreement to the observed data distributions. The acceptance for the simulated kinematics is now calculated as the ratio of the accepted events to the generated events. These MC distributions is also used for the PWA normalization to account for the detector/experiments acceptance. Figure [4.5] shows the generated (top) and

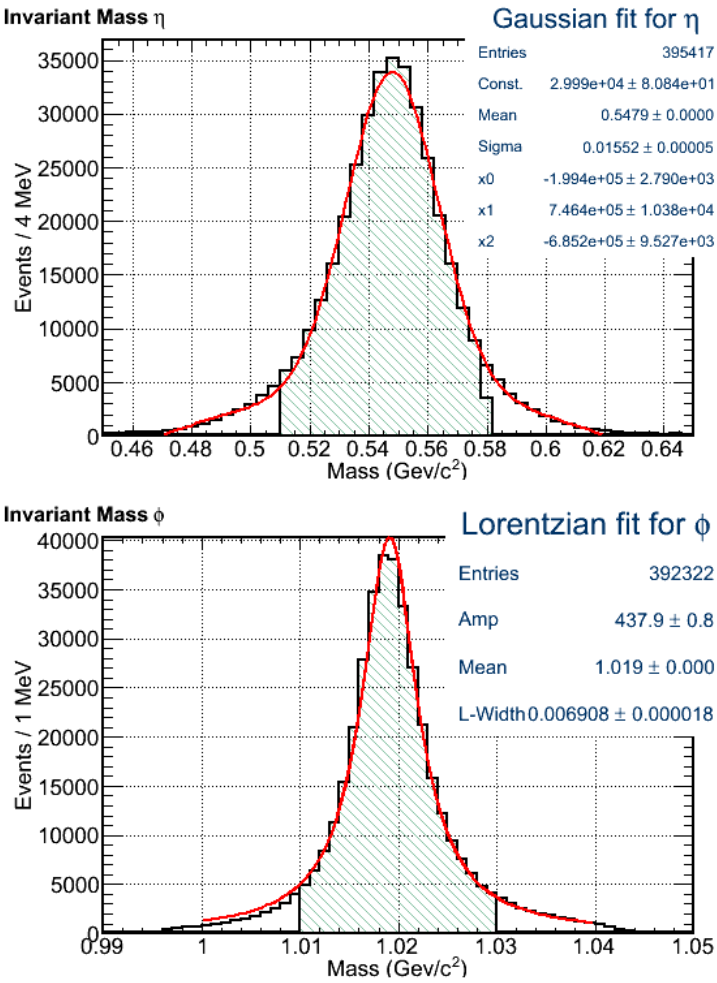

Figure 4.4: Means and widths for the accepted ϕ and η mesons in the simulation.

the accepted invariant mass distributions for the ϕ η phase space simulation. The bottom plot consists of the values of acceptance that are used in the analysis for calculating the cross section for each mass bin in the strangeonium spectrum. The average value shown is used to calculated the overall ϕ η photoproduction cross section.

For calculation of the systematic errors on the acceptance of the decay channel, many iterations were performed with minor variations in the input kinematics like t-slope, resonance widths, etc. The deviations in the acceptance were calculated and used to estimate the systematics on the overall acceptance for the decay channel.

CLAS detector is geared towards baryon spectroscopy, where the baryon resonances

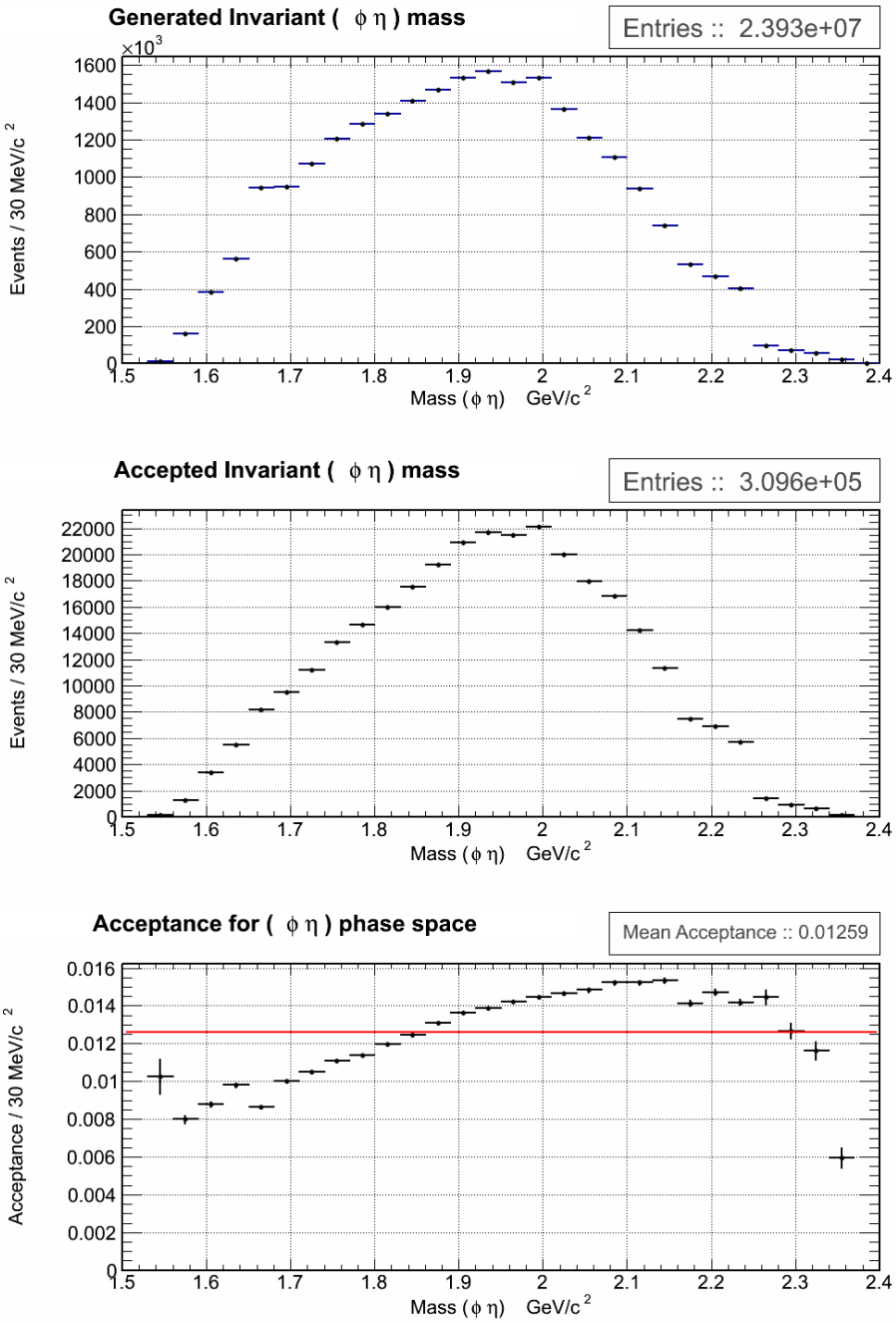

Figure 4.5: Topmost histogram is the generated distribution, using the 2-Dimensional binning of the observed data. Middle histogram is the CLAS accepted invariant mass distribution. Bottom plot is the acceptance plot for the phase space generated $\phi\ \eta$ invariant mass distribution. The plotted values are used for calculating bin by bin acceptance (table [4.2]) and cross section.

produced, decay at large angles in general and are observed with good acceptance in the detector. Engaging in meson spectroscopy while fruitful, comes with a host of issues related to the acceptance for the low-t region where peripheral production of meson dominates and are the prime motivators for meson spectroscopy. This is due to the beam exit hole in the forward direction, which from the boosted resonance's center of momentum frame becomes substantially large, leading to a great loss of the events of interest. Even though the analysis tries and accounts for all these issues in simulations, the matter of fact remains that the analysis does not have data in the region where the most and the best statistics is expected. Substantial systematic errors are introduced in the simulated data due to the differences in DC efficiency and the reconstruction efficiency between the CLAS data and the simulations in the edge regions of the beam hole and due to DC noise as a function of beam current.

Large acceptance effects in the low-t region, where majority of the peripheral photo-production occur, are observed in the g12 data. These is a largest source of the calculated systematic error that comes from the acceptance. It is observed from figures [4.7b], [4.7a] that the analysis is missing a large amount of low-t events and only has events in the high-t region due to acceptance. The t-slope, used to generate simulated data, is fit to the higher momentum transfer region of the distribution and the fit values might not be representative of the complete physics that is observed. In fact, multiple iterations with various t-slope for the generated simulations were performed, and depending on the choice of the fit-range for the data t-distribution, the analysis is able to find agreeable results for t-slope values in the range (0.63-1.47) GeV^2/c^2. This uncertainty in choosing a particular t-slope leads to high systematic errors for the acceptance.

The analysis finds the overall acceptance calculated using phase space events of 1.26% to be the consistent within errors with the acceptance of 1.23% calculated using the PWA performed in section [A.5]. The respective fits are shown for comparison in figures [4.5] and [4.6]. The analysis uses the acceptance calculated using the PWA as the primary acceptance for the ϕ η decay mode, as it better describes the kinematical correlations of the data and effects of the CLAS detector, as discussed in the section [4.3.2].

4.3.2 Using PWA to calculate acceptance

Using the simulations presented here, a partial wave analysis of the data decay distribution was performed with a large basis consisting of 49 waves listed in table [A.1]. The purpose of this 95 parameter fit was not to find the contributions of those basis states to the $\phi\ \eta$ data. The purpose is to expressly describe the data decay angular distribution in the most accurate possible way, along with the kinematical correlations therein. The acceptance corrected yield obtained from this fit describes the data decay angular distribution and the kinematical correlations in the data quite well due to the large number of parameters used, and can be used for describing the acceptance of the CLAS detector. This acceptance is evaluated in 30 MeV/c^2 bins, as shown in figure [4.6] and can be compared to the phase space simulated acceptance shown in figure [4.5].

4.3.3 Acceptance kinematical distributions

Distributions of various kinematical variables with cuts identical to those placed on the g12 data for the $\phi\ \eta$ decay mode are presented for comparison. All the invariant masses and decay angular distributions were compared with the data and found to be in good agreement, as can be seen from the comparison of the simulated data in figures [4.9], [4.10] with the observed data in figures [4.25], [4.26]. These simulations are also used for performing the PWA presented in chapter [A]. Average acceptance of 1.26% is observed for the $\phi\ \eta$ data. Bin-wise acceptance with the respective errors is presented in table [4.2].

4.4 Strangeonium Survey

A general survey of the $\gamma\ p\ \rightarrow\ p\ K^+\ K^-\ [X]$ inclusive data landscape is initially performed. Various kinematical and physics motivated selection cuts are implemented on the data to observe their effect on different invariant masses and other kinematical variables. This exercise assists the analysis to optimize the selection criteria for various channels. Thus, the cuts are adjusted to provide a final data sample that possesses a good signal to background ratio. The effects of various corrections on the data are also observed and any improvement/degradation is quantified. The progression of the analysis, with its incremental choices to arrive at the final selection of $\phi\ \eta$ events, is presented.

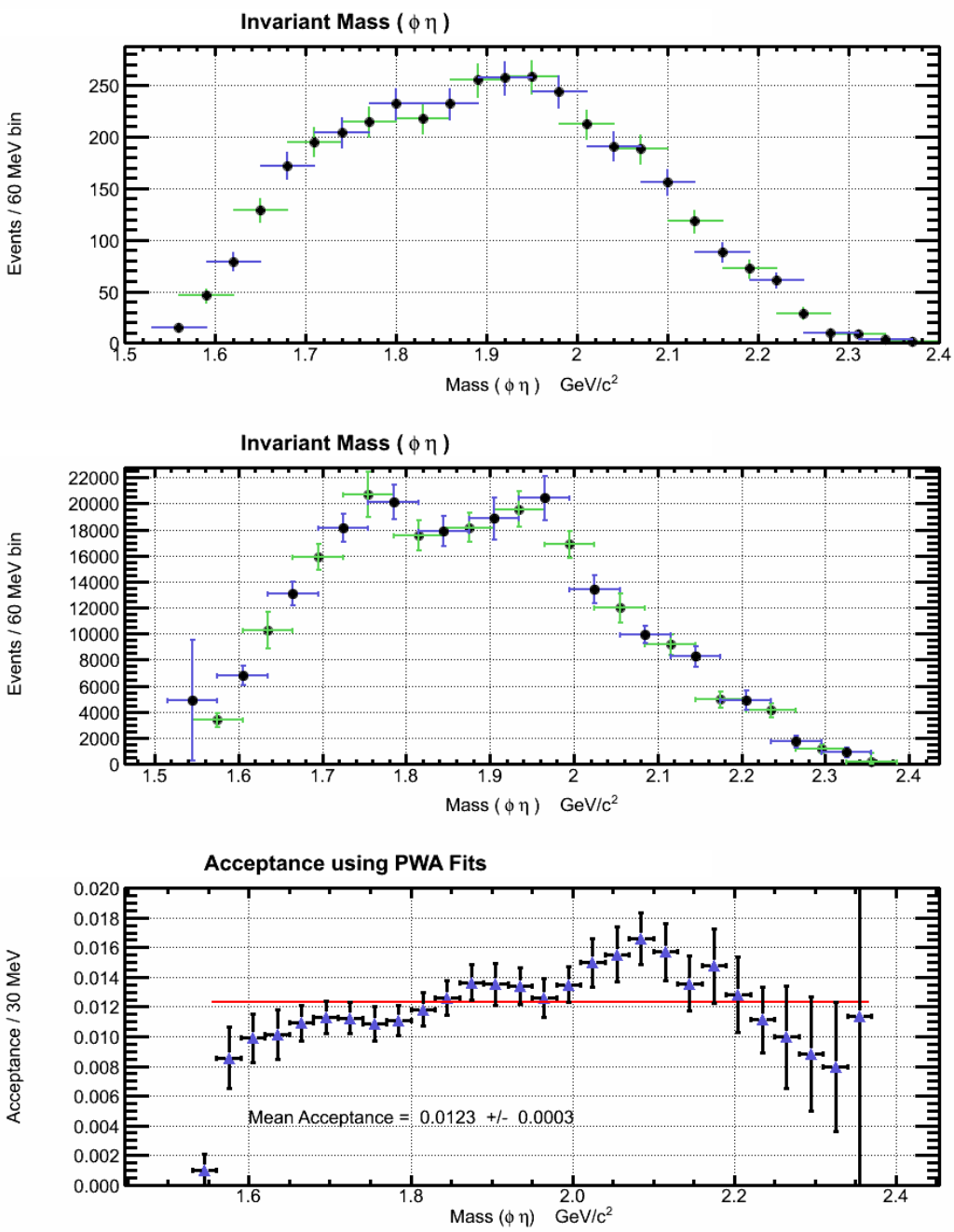

Figure 4.6: PWA techniques presented in section [A.5] was used to calculate acceptance as a function of the $\phi\ \eta$ invariant mass and to estimate the average acceptance for the $\phi\ \eta$ decay mode. The acceptance distribution shown in the bottom plot is derived by dividing the $\phi\ \eta$ invariant mass distribution of the data events shown in the top plot with the total accepted yield obtained from the PWA shown in the middle plot. The larger error bars, compared to the phase space acceptance displayed in the bottom plot of figure [4.5], are due to big contributions from the statistical errors on the $\phi\ \eta$ data in individual mass bins.

Table 4.2: Calculated acceptance from ϕ η phase space simulation, for 30 MeV/c^2 bins in the ϕ η invariant mass spectrum.

Mass MeV/c^2	% Acceptance	% Error
1575	0.84	0.19
1605	1.05	0.17
1635	1.05	0.13
1665	1.07	0.11
1695	1.11	0.11
1725	1.09	0.10
1755	1.11	0.10
1785	1.17	0.11
1815	1.20	0.12
1845	1.32	0.12
1875	1.33	0.12
1905	1.34	0.13
1935	1.38	0.12
1965	1.37	0.12
1995	1.45	0.13
2025	1.47	0.50
2055	1.56	0.31
2085	1.54	0.17
2115	1.52	0.19
2145	1.54	0.24
2175	1.33	0.22
2205	1.29	0.23

In figure [4.11a], the inclusive invariant mass of the K^+ K^- is plotted. The distribution is obtained by adding the K^+ K^- four-momenta and taking its four-vector magnitude. This method postulates that the K^+ and the K^- mesons were initially bound into a resonance and hence the magnitude of their four-vector sum is the mass of the initial resonance. This assumption is only partially true, as observed in the figure [4.11a]. There is the very visible ϕ meson, shaded blue, in that mass distribution, sitting over a background of non-resonant K^+ K^- event. The limitation of this method is the ever-present non-resonant background. Analyses that intend to extract the yield for resonant events generally assume that the background has a simple functional form, ideally possessing simple phase space characteristics. In figure [4.11a], a clear ϕ meson peak (highlighted in blue) is observed as expected. Features of

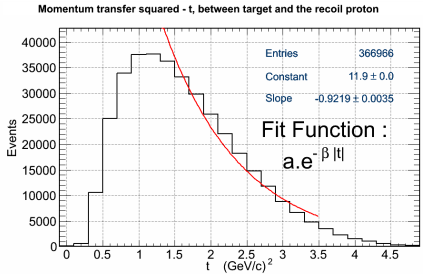

(a) Momentum transfer squared - t, between the target and the recoil proton for the generated MC simulation. The lack of events at low values of t is due to the CLAS acceptance for the very forward going events which end up in the beam hole and are hence lost to CLAS tracking and reconstruction, which mimics what we observe in the g12 data.

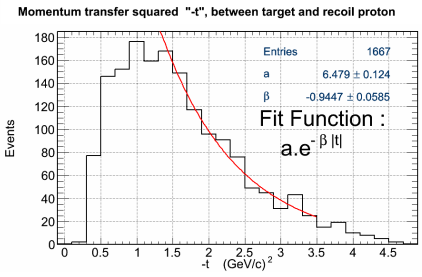

(b) Momentum transfer squared - t, between the target and the recoil proton for the g12 ϕ η data. The lack of events at low values of t is due to the CLAS acceptance for the very forward going events which end up in the beam hole and are hence lost to CLAS tracking and reconstruction.

Figure 4.7: Mandelstam's 't' distribution profile comparison for the selected MC and data for ϕ η events.

other possible resonances that decay via K^+ K^-, like $f_2(1270), a_2(1320), f_0(1500), f_2^{'}(1525)$, are also visible. This thesis does not address all these physical states, but the distribution does provide a picture of the rich physics that the g12 dataset contains in this channel.

In figure [4.11b], the missing mass off of the proton K^+ K^- events is plotted. As observed, the tail of the distribution extends into the negative missing mass region. This gives the impression that quite a few seemingly unphysical events were reconstructed. This is not the case though. The peak near zero consists a majority of real events. These real events are mostly the exclusive events for the final state, where there is no missing particle in CLAS. The secondary contribution is from the tail of the missing π^o events in CLAS. This apparent unphysical nature of the mass of the missing particle, comes from the innate resolutions in the timing and momentum reconstruction. Small errors and spreads in these measurements are propagated through the detection and reconstruction process. This errors are mathematically able to resolve the distribution into negative missing masses as observed. A small fraction of these events are also due to the selection of the wrong beam photon. This happens when there are 2 or more beam photon in the same beam bucket and the reconstruction algorithm ends up choosing the wrong one. Tagger has no physics handle to

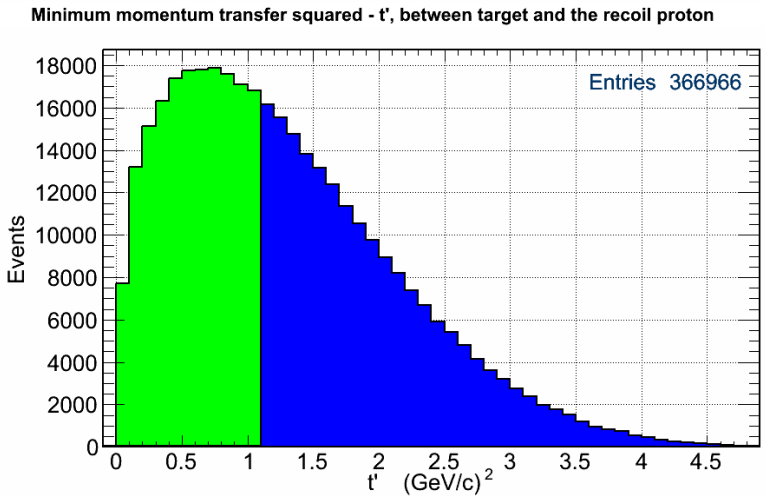

Figure 4.8: Plot of t′, which is the difference between the momentum transfer squared 't' and 'tmin'. t′ is the excess of momentum transfer squared, left over after the production of the resonance of a particular mass, that determines the kinematics of the reaction. The green and the blue selection for events denote the cuts used to approximately divide the data into regions with equal number of events.

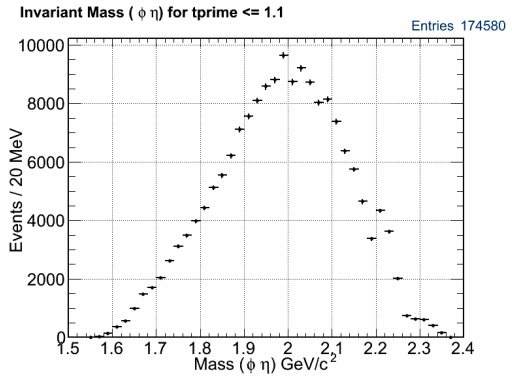

(a) Event distribution for (ϕ η) invariant mass for low-t′ MC events.

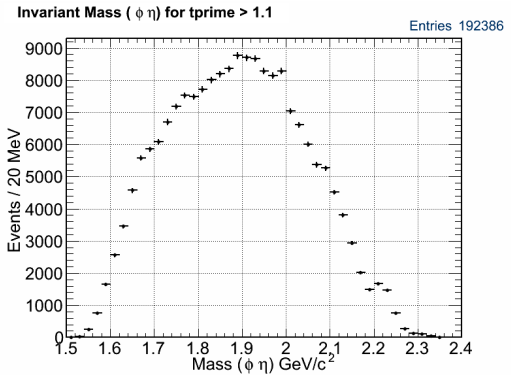

(b) Event distribution for (ϕ η) invariant mass for high-t′ MC events.

Figure 4.9: Event distribution for (ϕ η) invariant mass divided in approximately equal distributions for the simulation on the basis of a t′-cut as highlighted in figure [4.8].

select the right one, so the choices available to the analysis is either random selection or using the experimentalists bias. The algorithm is designed with a bias for photons with higher energy; as those events are most sought-after experimentally. This behavior was investigated and accounts for a portion of the experimental systematic errors. Other contributors are the

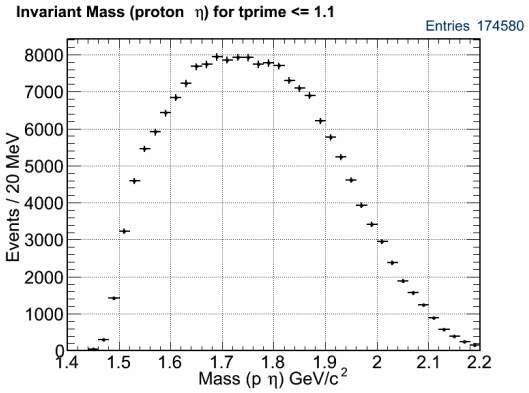

(a) Event distribution for proton η invariant mass for low-t′ MC events.

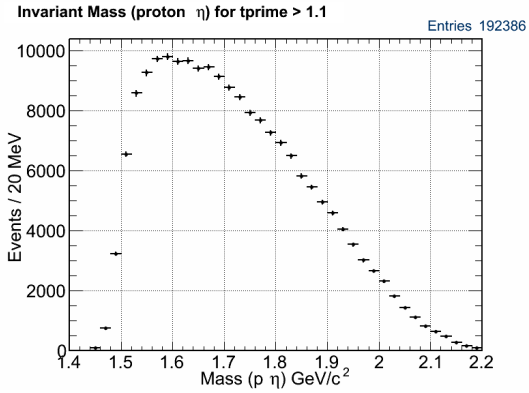

(b) Event distribution for proton η invariant mass for high-t′ MC events.

Figure 4.10: Event distribution for proton η invariant mass divided in approximately equal distributions for the simulation on the basis of a t′-cut as highlighted in figure [4.8].

momentum and energy resolution of the experiment. These are tackled with the kinematic fitting procedure, as explained in the kinematic fitting section [3.3] of this thesis. The events in the near-zero peak are hence considered to be physical events and used in subsequent analyses. Peaks at the meson masses for π^o, η and ω are also observed.

The analyses goals are to observe a ϕ meson in the intermediate state. Therefore a rudimentary selection criterion on the invariant mass of K^+ K^- to be a ϕ meson is implemented. The blue shaded areas in the figures [4.11a], [4.11b], [4.11c] are the events left in the distribution after this cut is applied. As the analysis progresses through these selection cuts, the resonance peaks for π^o, η, ω mesons off of the ϕ meson and a proton become clearer.

All the plots highlighted in green have a selection criterion placed on their missing transverse and longitudinal momentum. If the transverse and longitudinal missing momentum component is less than a certain value ($P_z \leq 100$ MeV *and* $P_t \leq 50$ MeV), the event is considered to be from the exclusive $\gamma p \to pK^+K^-$ channel (channel [5.3]). This event is then removed from the analysis for missing mesons (channel [4.1], [5.1], [5.2]) in the final state. As can be seen from figure [4.11e], this selection cut does not affect the mesons of higher masses and resonance peaks for η, π^o *and* ω meson off of a proton and a ϕ meson is still clearly visible. Also see figure [4.11f] for a closer look at these events. Figures [4.12a], [4.12b] shows the incoming beam photon energy distribution for the various event selections.

As observed, the selected events are distributed across the measured/triggered beam photon energy range in an almost flat, slowly decreasing, manner.

4.4.1 Analysis of the proton, ϕ, η final state

The analysis initially selects the proton, K^+ , K^- g12 data with selection cuts on the K^+ K^- invariant mass to be within the observed ϕ mass range, as in figure [4.13], and the missing mass for these events to be within the observed η mass range, as in figure [4.14]. The analysis selects the ϕ meson from the data to have the mean of 1020 MeV/c^2 and a lorentzian width of 10 MeV/c^2 and the η meson to have the mean of 545 MeV/c^2 and a width of 35 MeV/c^2 . As observed in figures [4.13], [4.14], the selection includes and preserves most of the events of interest for this analysis.

These selection criteria along with the other standard cuts listed in table [3.1] are applied to obtain a set of events, where a ϕ meson and an η meson are expected in the dataset. In the missing mass spectrum plotted in figure [4.14], it is observed that there is approximately 50% background non-η events, beneath the signal η events. Hence the analysis employs a more stringent selection criterion to obtain a ϕ η yield estimate from a cleaner sample. The analysis now implements an elliptical selection criterion for ϕ η events. For the elliptical selection of events, the equation [4.6] is used.

$$\left(\frac{\mathrm{x} \;-\; \phi_{\mathrm{mass}}}{\frac{\phi \;\; \mathrm{mass} \;\; \mathrm{range}}{2}}\right)^2 + \left(\frac{\mathrm{y} \;-\; \eta_{\mathrm{mass}}}{\frac{\eta \;\; \mathrm{mass} \;\; \mathrm{range}}{2}}\right)^2 \;=\; 1 \tag{4.6}$$

After obtaining a cleaner sample with application of an elliptical cut on the ϕ η invariant mass, shown in figures [4.16]-[4.19], the event sample still contains background beneath the η and the ϕ meson. The analysis then resorts to the standard technique of sideband subtraction. A sideband here is defined as a region in the resonance's invariant mass spectrum, where the probability of the event being the resonance is extremely low, but the event still lies close to the resonance region. The acceptance for the events is generally smooth, as is the physics and the kinematics for the events involved. Thus the sidebands of a resonance have similar kinematics to the background beneath the resonance. Under these assumptions, when the smoothly varying sidebands are subtracted from the resonance region, the analysis is left with the approximate yield and structure for the resonances present in the data. This

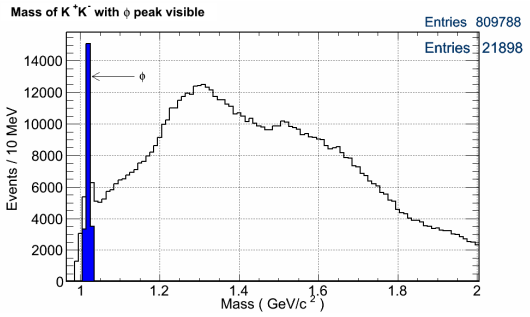

(a) Invariant mass of K^+ K^- that pass the basic standard selection criteria with the ϕ peak highlighted. The ϕ events are selected with a rudimentary cut on the ϕ mass range. The distribution has non-ϕ, K^+ K^- background beneath the ϕ peak.

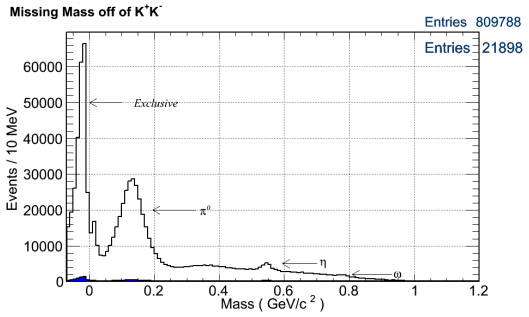

(b) Missing mass off of proton K^+ K^-, that pass the basic standard selection criteria. Observable resonance peaks in the missing mass spectrum are labeled.

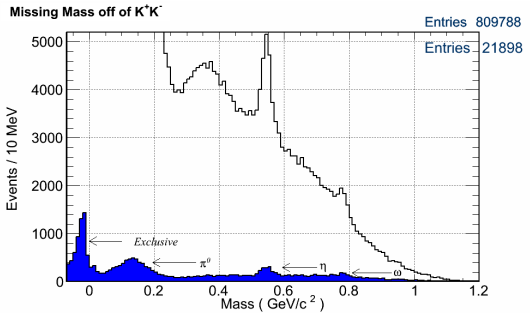

(c) Missing mass off of proton K^+ K^- with the basic standard selection cuts. The missing mass off of the selected ϕ mass range is highlighted in blue. The reduction in number of events is due to the ϕ selection cut.

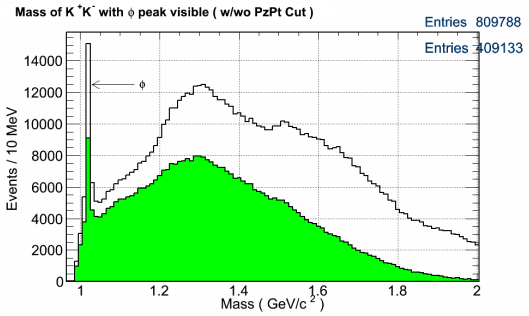

(d) Invariant mass of K^+ K^- that pass the standard selection cuts. Events in the green shaded region have transverse and longitudinal momentum cut applied to isolate exclusive events from the events with a missing particle.

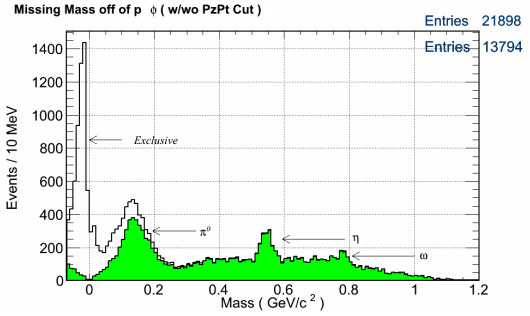

(e) Missing mass off of a proton and the selected ϕ, with and without transverse and longitudinal momentum cut. The cut is most useful to identify exclusive events, and has barely any effect for higher missing resonances.

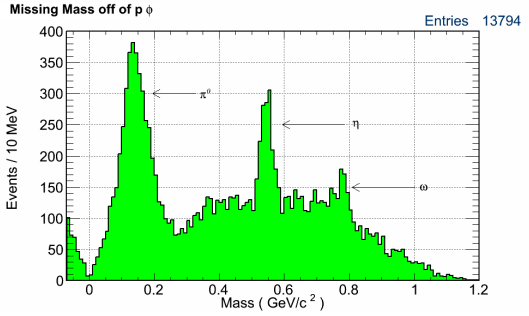

(f) Missing mass off of proton ϕ) with the transverse and longitudinal momentum cut. Peaks for π^o, η, ω are clearly identifiable.

Figure 4.11: Standard selection plots and features for proton, K^+, K^- events in g12 data.

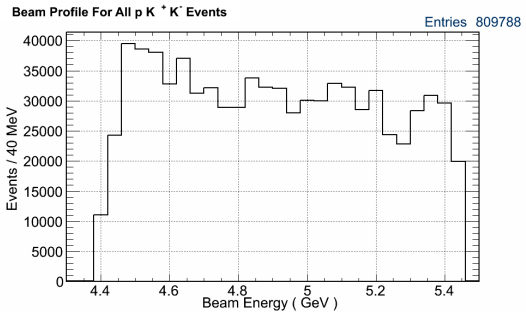

(a) Beam Profile for proton K^+ K^- that passed the basic standard selection criteria.

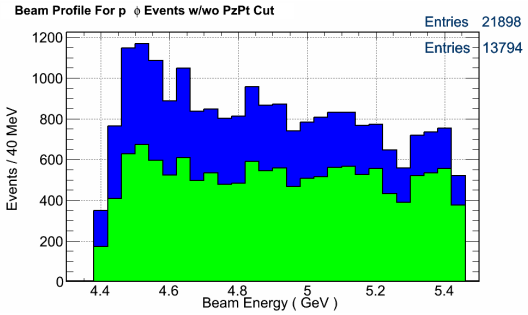

(b) Beam Profile for proton ϕ events that passed the basic standard selection criteria, with and without the transverse and longitudinal momentum cuts.

Figure 4.12: Beam energy distribution profile for selected events.

technique, in principle, also works for all the kinematical variables. The analysis thus gets a cleaner look at the kinematics of the resonance after sideband subtraction. Care is taken for the normalization of the sideband events to the background events, to obtain the correct yield.

To ensure minimal leakage of signal into the sideband, the sideband is chosen outside the tails of the signal distribution. A 'gap region' is left between the signal and the sideband. The gap region expectedly has a higher signal to background ratio than the selected sideband. In figure [4.16], the analysis observes the overpopulation of events in the mass-bins at the intersection of the ϕ meson mass distribution and the η meson mass distribution. This leads to the conclusion that there are correlated ϕ η events in the data sample as expected.

The analysis further chooses the sideband for the ϕ η events in the figure [4.17]. The parameters are carefully chosen such that the area of the sideband is equal to the area of the ϕ η signal region and are listed in the table [4.3]. In figure [4.17], the carefully chosen sideband for the ϕ η events is visible. The analysis has postulated a smoothly varying background, which is justified from the observations of figures [4.16], [4.17]. The number of the sideband events are approximately equal to the background events. These numbers are also in agreement with the number of ϕ's and η's the analysis estimated in the figures [4.13], [4.14] from the fit functions.

The analysis cannot label an individual event to be a definite ϕ η event. The event

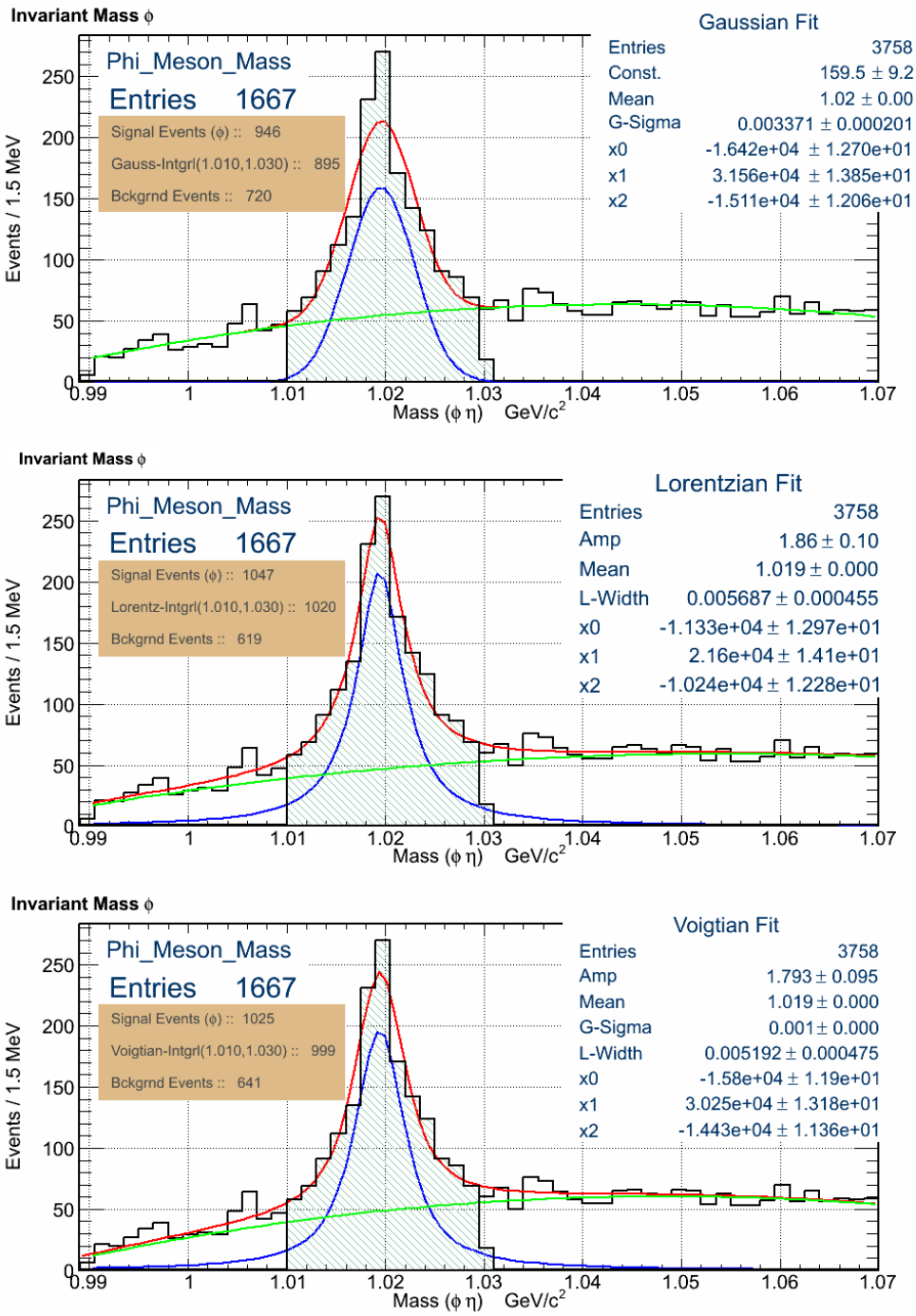

Figure 4.13: Invariant Mass of K^+ K^- with the ϕ mass range shaded in green, where a selection cut has been imposed on the missing mass to be within the η meson mass range. For ϕ meson highlighted selection (mean,width) $\equiv$ (1020,10) and for η meson highlighted selection (mean,width) $\equiv$ (545,35) is used. All the 3 plots have the same data, but the fit functions used are different. The background function used in all the fits is a 2^{nd} order polynomial. Top plot fit uses a gaussian to fit the signal, middle plot fit uses a lorentzian and the bottom plot is fitted using a voigtian. Estimated count of the signal and background events, using the fits, is printed in the brown box.

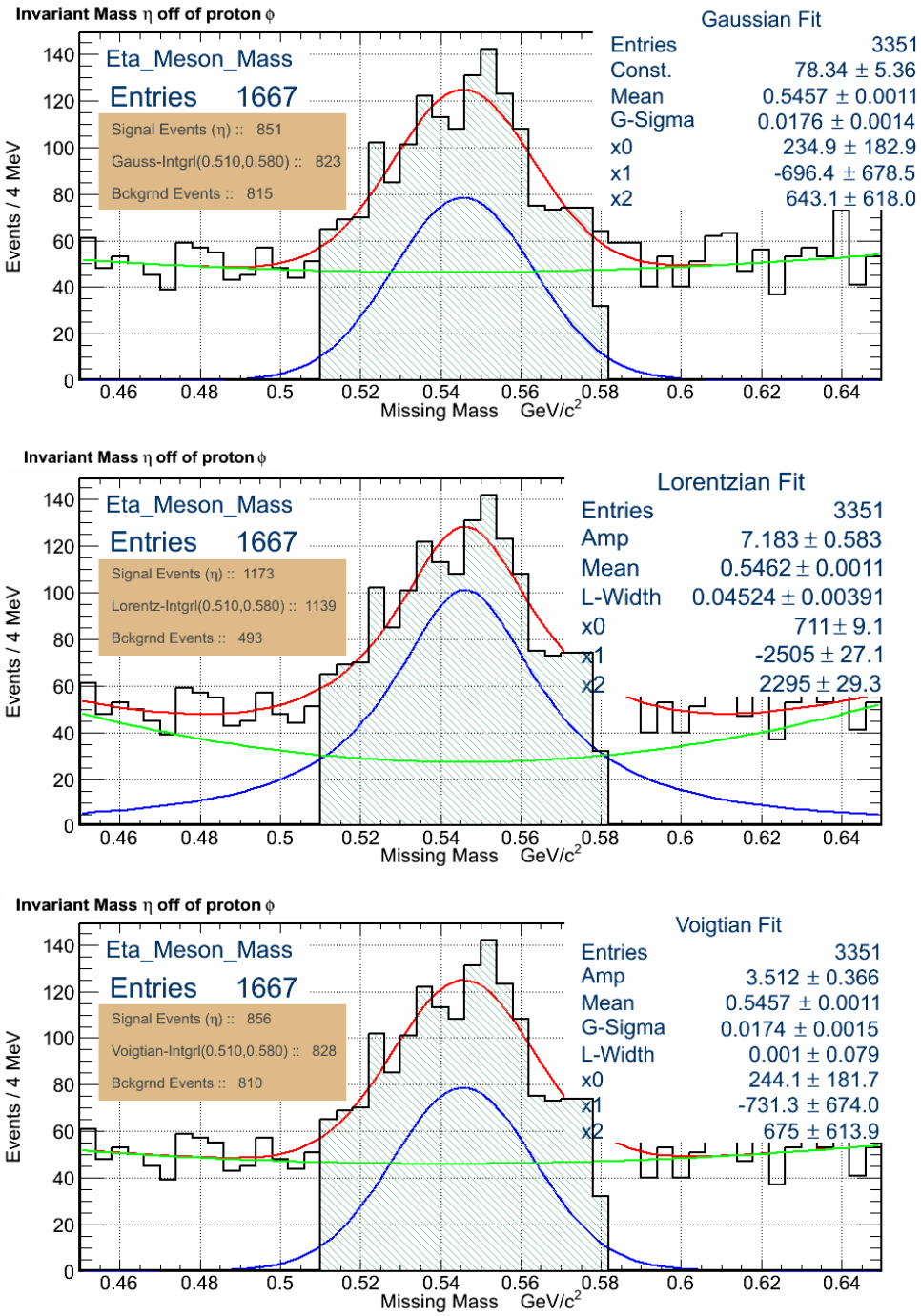

Figure 4.14: Missing mass off of proton ϕ, with the η mass range shaded in green. For ϕ meson highlighted selection (mean,width) $\equiv$ (1.020,0.010) and for η meson highlighted selection (mean,width) $\equiv$ (0.545,0.035) is used. All the 3 plots have the same data, but the fit functions used are different. The background function used in all the fits is a 2^{nd} order polynomial. Top plot fit uses a gaussian to fit the signal, middle plot fit uses a lorentzian and the bottom plot is fitted using a voigtian. Estimated count of the signal and background events, using the fits, is printed in the brown box.

could very well be a background event. The analysis can only make a statistical claim about the distribution as a whole. The events in the sideband are only used to estimate the background beneath the signal for the $\phi\ \eta$ events. The analysis can thus extract the signal yield by using the sideband subtraction. The technique of sideband subtraction is a good method to understand the kinematics and the invariant mass distributions for the whole analysis. The $\phi\ \eta$ sideband chosen by the elliptical selection are shown in figures [4.17], [4.20]. The invariant mass distributions of the signal region selected by the elliptical cuts are shown in the figures [4.18], [4.21]. The sideband subtracted distributions are shown in figures [4.19], [4.22]. From the invariant mass distributions displayed in these figures, the analysis estimates the yield of the $\phi\ \eta$ events in the g12 dataset.

After the sideband subtraction, the analysis expected the strangeonium states $X \rightarrow \phi\ \eta$, if present, to become more discernable. Around the $\phi\ \eta$ mass region of 1960 MeV, a possible structure does emerge in figure [4.22]. The distribution, though, does not have the statistical significance to identify the possible structure as an observed resonance.

A separate analysis was conducted on $\phi\ \eta$ invariant mass using simple sideband subtraction on the ϕ mass alone, then just the η mass, and then a rectangular selection on the ϕ

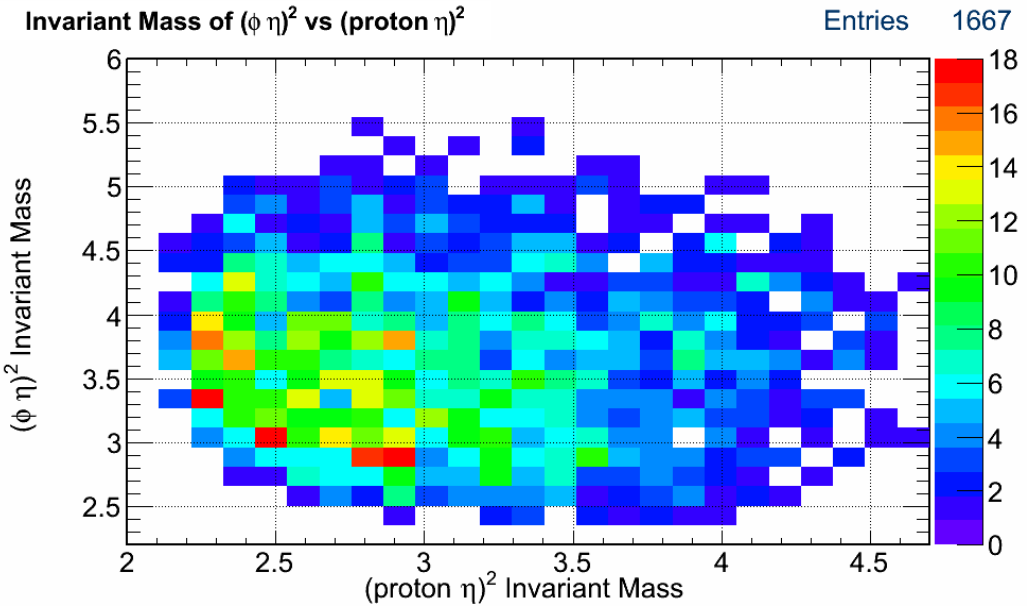

Figure 4.15: Dalitz analysis plot for $\phi\ \eta$ invariant mass against proton η invariant mass.

Table 4.3: Parameters used for the elliptical sideband subtraction. These were chosen such that the elliptical area beneath the signal ϕ η events is equal to the area beneath the background region. Background region is the region between the stated sideband mass range and the sideband mass gap in the table.

ϕ mass	1.0195 GeV/c^2
ϕ mass range selected	0.0019 GeV/c^2
ϕ sideband mass gap selected	$\sqrt{3}\times$ 0.0019 GeV/c^2
ϕ sideband mass range selected	$2\times$ 0.0019 GeV/c^2
η mass	0.5478 GeV/c^2
η mass range selected	0.070 GeV/c^2
η sideband mass gap selected	$\sqrt{3}\times$ 0.070 GeV/c^2
η sideband mass range selected	$2\times$ 0.070 GeV/c^2

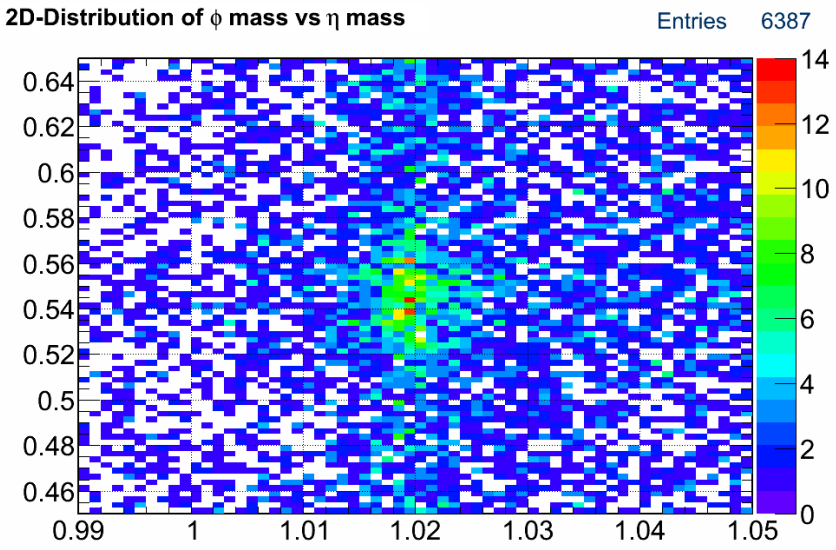

Figure 4.16: Two-Dimensional plot of the invariant mass of K^+ K^- versus the missing mass in the extended region of interest around the ϕ and the η mass. Correlation between the ϕ mesons and the η mesons is observable.

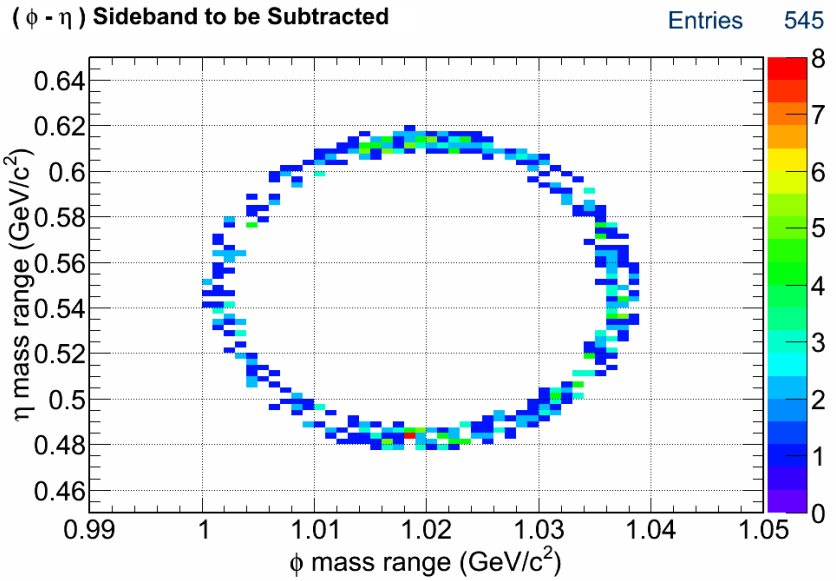

Figure 4.17: Two-Dimensional plot of the invariant mass of K^+ K^- versus the missing mass for the selected sideband region. The elliptical area of this region is equal to the area beneath the signal ϕ η region.

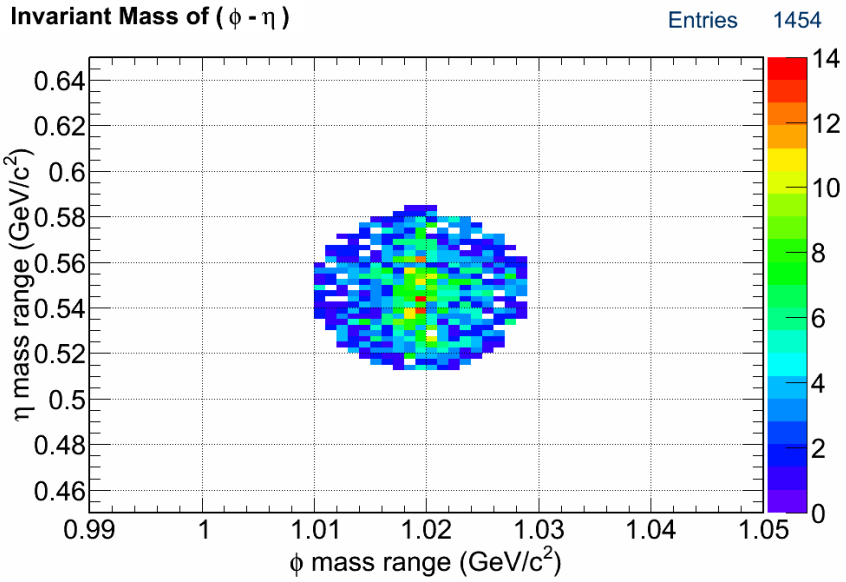

Figure 4.18: Two-Dimensional plot of the invariant mass of K^+ K^- versus the missing mass for the region considered to contain the signal for ϕ η events.

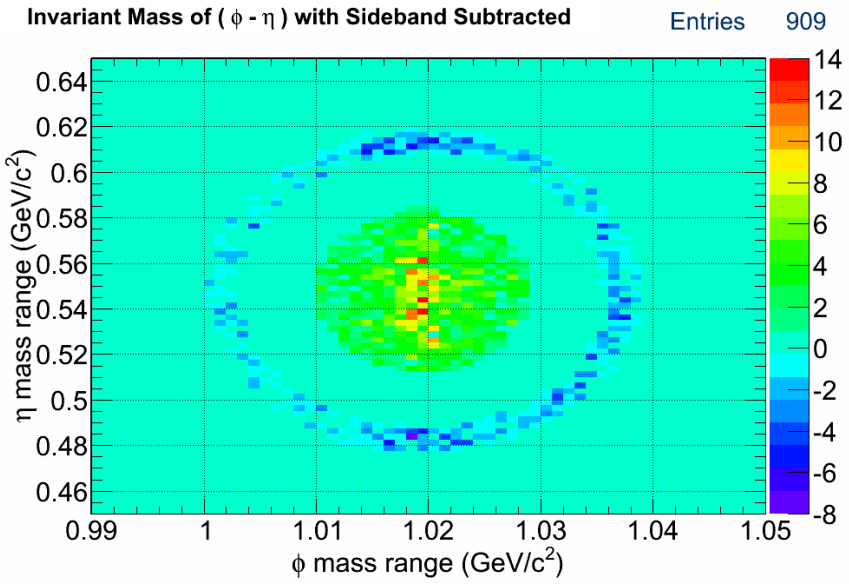

Figure 4.19: Two-Dimensional plot of the invariant mass of K^+ K^- versus the missing mass after the sideband subtraction. The ring is the sideband that was subtracted from beneath the ϕ η region, to give us the sideband subtracted region, visible as the disc here.

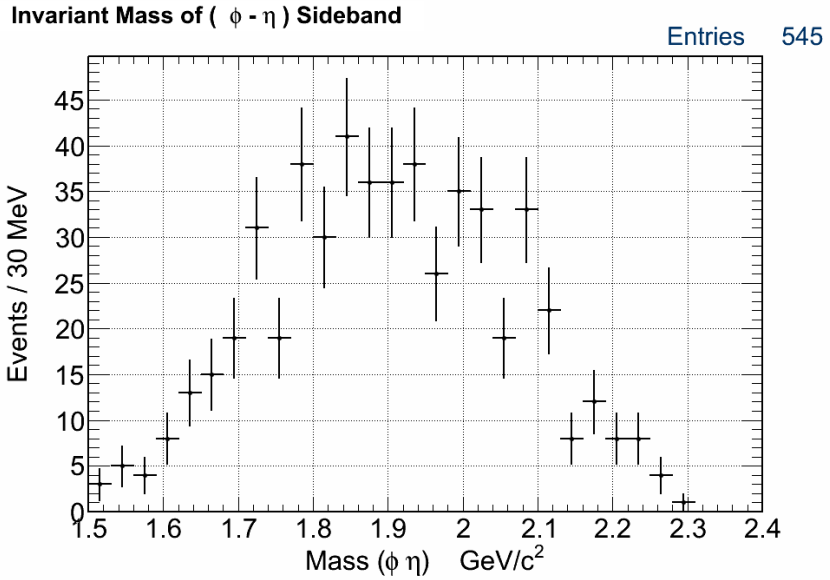

Figure 4.20: Invariant mass distribution for the events of the sideband.

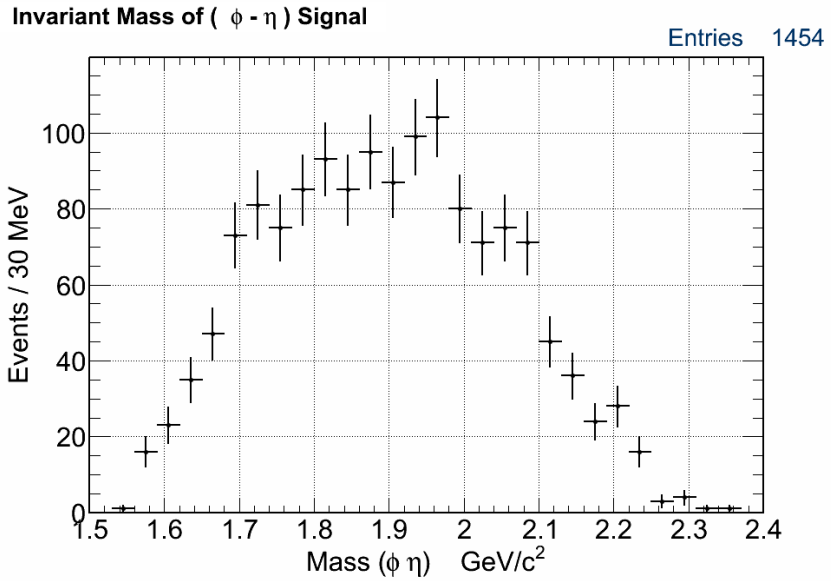

Figure 4.21: Invariant mass distribution for events in the region considered to be the $\phi\ \eta$ signal region.

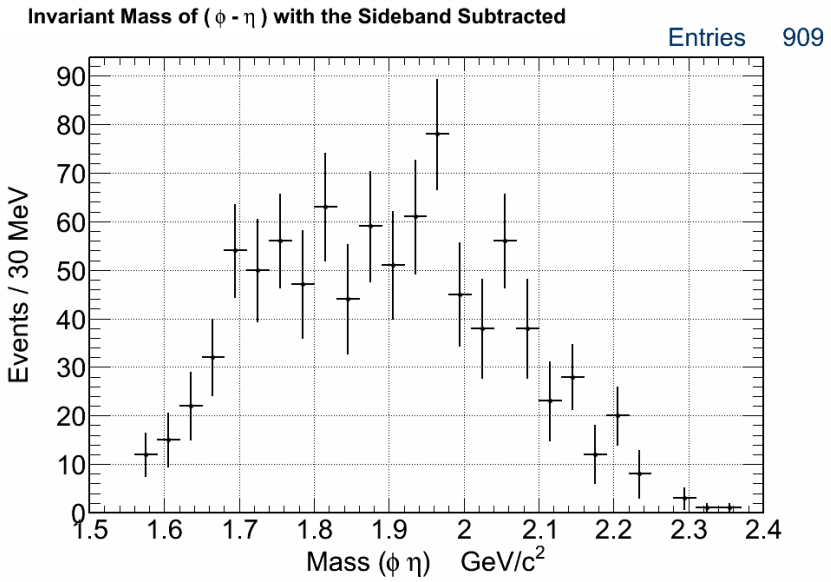

Figure 4.22: Invariant mass distribution for events in the $\phi\ \eta$ signal region after the sideband subtraction. This distribution is the closest to the true $\phi\ \eta$ distribution in the absence of any background.

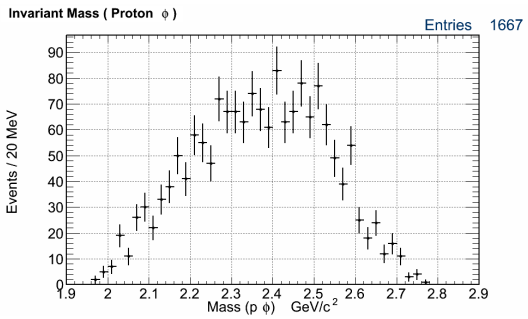

(a) Invariant mass of proton ϕ for the final state - proton ϕ η. No statistically significant resonant structure is observed.

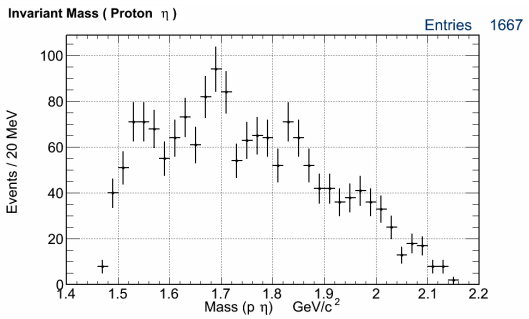

(b) Invariant mass of (proton η) for the final state proton ϕ η. A peak for a N^* decay to proton η is clearly identifiable. The N^* is probably the N(1710) expected in proton η decay mode.

Figure 4.23: Invariant mass distributions for baryonic decays for the final state proton ϕ η.

mass as well as the η mass. The results were in general agreement to the ones presented here except that the elliptical sideband subtraction was found to give enhanced structures with lower background. Hence the other analysis is not presented here. The errors displayed in these plots are purely statistical.

For the final state of $\gamma p \rightarrow p\phi\eta$, it is quite possible that the ϕ meson and the η meson are not correlated to each other but to the proton. Therefore the analysis looks at the different invariant mass combinations for the proton ϕ η events in figures [4.23a], [4.23b]. The analysis observes that in the invariant mass distribution of the proton η events in figure [4.23b], there is an overpopulation of events around 1.7 GeV/c^2 . This hints at the presence of $N^* \rightarrow$ proton η events in the channel of interest.

A quantity often found useful in meson spectroscopy is the lorentz invariant 'Mandelstam t'. It is the magnitude square of the four-momentum transfer between the incoming beam and the outgoing peripheral resonance. Being lorentz invariant, this quantity is the same in all frames of references. In photoproduction, like in g12, for cases of peripheral meson production, this equation can be stated as:

$$t \;=\; \mid P^{\mu}_{\gamma} \;-\; P^{\mu}_{X} \mid^2 \;=\; \mid P^{\mu}_{target} \;-\; P^{\mu}_{recoil} \mid^2 \tag{4.7}$$

where P^{μ}_{γ}, P^{μ}_{X}, P^{μ}_{target} and P^{μ}_{recoil} are the four-momentum of the incoming beam photon, outgoing peripheral resonance, target proton and the recoil proton in any frame of reference.

This four-momentum transfer gives an idea of how deep the probing particle (γ) probed the nucleon, or the structure inside the nucleon it was able to interact with, or whether it just scattered peripherally off the edge of the nucleon and carried most of the energy-momentum with it. This quantity, thus, indicates and helps isolate the kind of physics observed in the data.

Another related useful quantity is the 't′', which is defined to be the difference between t and t_{min} in the center of mass frame, where t_{min} is the value of t in center of mass when the scattering angle for the produced resonance is zero. Hence, t′indicates the excess of the momentum transfer squared, available to a resonance, and now determines the kinematics for the event. A peaking of the t′ distribution at low value, is a consistent indicator that the production mechanism for the channel proceeded via peripheral meson production.

$$t' \quad = \quad t \; - \; t_{min} \tag{4.8}$$

The analysis observes the behavior of the ϕ η data, with selection cuts based on the kinematical variables 't′' in figure [4.24].

The general approach for analyses looking at peripheral production is to put a hard cut by selecting low t′ events from their data. This removes the baryon background, as meson production events generally possess lower t′ values than their baryonic counterparts. Due to the limited statistics as well as the observed acceptance for the decay channel under consideration, a complete treatment of the data using this technique is not possible. As a workaround, to observe the effects of momentum-transfer, the t′-cut is selected so as to divide the data into two approximately equal subsets. The green color represents the low-t′values whereas the blue represents the high-t′values for the selected events. Invariant ϕ η mass distribution for low-t′ and high-t′events are shown in the figures [4.25a], [4.25b]. Corresponding invariant mass distributions for the proton η events are shown in the figures [4.26a], [4.26b]. The analysis also compares these distributions with their simulated counterparts in figures [4.10a], [4.10b] and finds general agreement between these distributions, which indicates the robustness of the simulation.

It is observed that there are hints of possible strangeonium states in the invariant ϕ η mass distribution as well as possible baryonic states in the proton η invariant mass

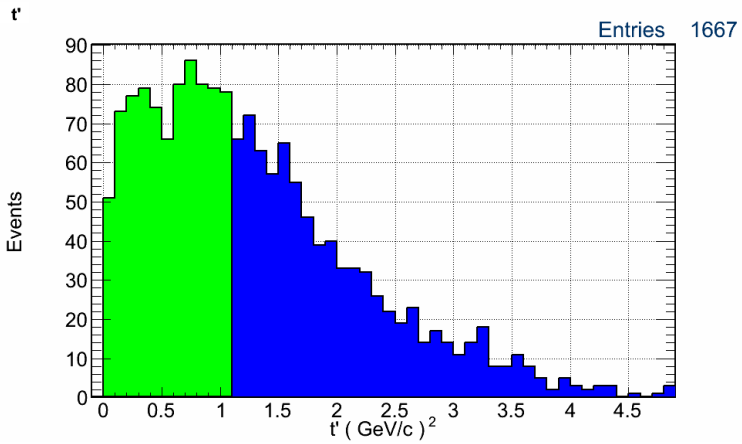

Figure 4.24: Plot of t′, which is the difference between the momentum transfer squared 't' and 'tmin'. t′ is the excess of momentum transfer squared, left over after the production of the resonance of a particular mass, that determines the kinematics of the reaction. The green and the blue selection for events denote the approximately equal number of events used in the figure [4.25b].

distributions. Analyses with tighter low-t′ cuts were also performed, but due to the limited statistics for the final state, the results were inconclusive with regards to the presence of any resonant structure. A probable $N^*(1710)$ resonance decay to proton η is observed in the proton ϕ η invariant mass, shown in figure [4.23b]. Enhancements in certain regions for strangeonium states that decay via ϕ η around the masses of 1.695 GeV/c^2 , 1.960 GeV/c^2 and 2.050 GeV/c^2 are observed in figure [4.22]. These enhancements are not statistically significant, hence the analysis further determines upper and lower limits on the strangeonium cross sections using the Feldman-Cousins method.

4.4.2 Cross section for ϕ η Events

The analysis observes an accepted yield of 909 ϕ η events in the g12 dataset after sideband subtraction over the entire g12 primary trigger range. Acceptance is calculated for the channel by simulating CLAS using the procedure outlined in section [4.3.1]. Identical selection criteria are implemented on the reconstructed events in the simulations as they were on the g12 data. Acceptance over the entire beam energy range is calculated in sections [4.3.1], [4.3.2] and is used to estimate the overall cross section for the ϕ η decay mode. The analysis also accounts for the ϕ meson branching ratio of 48.5% to K^+ K^- . Systematics and

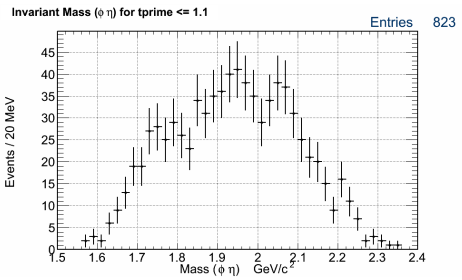

(a) Event distribution for ϕ η invariant mass for low-t$'$ events.

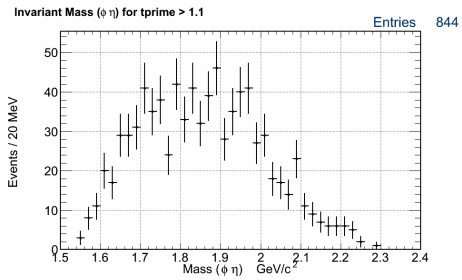

(b) Event distribution for ϕ η invariant mass for high-t$'$ events.

Figure 4.25: Event distribution for ϕ η invariant mass divided in approximately equal distributions on the basis of a t$'$-cut as highlighted in figure[4.24].

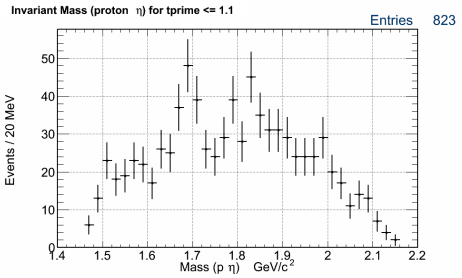

(a) Event distribution for proton η invariant mass for low-t$'$ events.

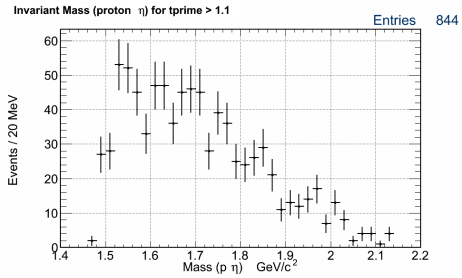

(b) Event distribution for proton η invariant mass for high-t$'$ events.

Figure 4.26: Event distribution for proton η invariant mass divided in approximately equal distributions on the basis of a t-cut as highlighted in figure[4.24].

statistical errors on these calculation are listed in tables [4.5], [4.6]. The estimated yield, cross section, and the associated corrections are listed in table [4.4].

Photoproduction cross section of ϕ η intermediate state is calculated to be 5.8 $\pm$ 0.3 (statistical error) $\pm$ 0.7 (systematic error) nanobarns for $E_\gamma \in \{4.40, 5.45\}$ GeV.

4.4.3 Error Calculations

Major sources of error in the measured quantities for the analyses shown are the statistical errors and the systematic errors. The statistical errors arise due to the limited statistics for any measurement. To reduce these, the experiment needs to collect more statistics and hence acquire more precision. For measurements of parameters with fixed values and events

Table 4.4: Parameters used in cross section calculation for $\phi\ \eta$ events.

Yield of $\phi\ \eta$ events	909
Reconstruction inefficiency at 60 nA	16%
ST inefficiency per charged track	6%
Scale factor for the branching ratio	2.0619 (48.5%)
Branching Ratio Corrected Yield of $\phi\ \eta$ events	2686 $\pm$ 133
E_γ Flux (10^{13})	2.18 $\pm$ 0.17
ρ_{target}	0.0708 $\frac{gm}{cm^3}$
A_{H_2}	2.016
$N_{Avogadro}$	6.022 $\times 10^{23}$
L_{target}	40 cm
Mean acceptance from $\phi\ \eta$ phase space simulation	1.26%
Mean acceptance for $\phi\ \eta$ using PWA	1.23% $\pm$ 0.03%
Systematic error - $\phi\ \eta$ simulations	7.9%
Systematic error - Sideband Subtraction	0.8%
Systematic error - PID	1.3%
Systematic error - Photon Flux Normalization	7.9 %
Systematic error - Miscellaneous	0.26%
Conservative total systematic error	12.5%
$\sigma_{X\to\phi\eta}$	5.8 nanobarns
Statistical error on $\sigma_{X\to\phi\eta}$	0.3 nanobarns
Systematic error on $\sigma_{X\to\phi\eta}$	0.7 nanobarns

that occur at a steady rate, the measurements are expected to be of the poisson nature and the errors on the measurement 'N' would simply be '$\sqrt{N}$'. The uncorrelated errors for different parameters are then added in quadrature. On the other hand, the systematic errors reflect the understanding and controls of the experiment, and the limitations of the analytical tools used. As a case in point, the major source of systematic error in the calculation for cross section is the imperfect simulation of the real-time CLAS response.

The measurement error causing factors are simulated by smearing the detector response [41]. DC efficiency map was created from analyzing the g12 data and those efficiencies are applied to the drift chamber wires during the simulations. The width for the missing η in the $\phi\ \eta$ simulations is still much narrower than the one observed in the data. Thus the biggest source of systematic error justifiably comes from the simulation of CLAS acceptance.

Multiple simulations were performed by tweaking the physics model used. This was done

Table 4.5: Systematic error parameters estimated for the g12 experiment, using the g11 experiment [52][53] as references.

PID	1.3%
Total Normalization	7.9%
Photon Attenuation	0.2%
LH_2 Density	0.11%
Target Length	0.125%
Total estimated g11 systematic error	8%

Table 4.6: Statistical and systematic errors for the photoproduction of $\phi\ \eta$ intermediate state.

Statistical error on the measured yield ($\sqrt{Y+2B}$)	45
Scale factor for the detector yield error	1.4333
Scale factor for the statistical yield error accounting for the $\phi \rightarrow K^+\ K^-$ branching ratio of 48.5%	2.9553
Error for the $\phi \rightarrow K^+\ K^-$ branching ratio	0.5%
Systematic error from $\phi\ \eta$ acceptance simulations	7.9%
Systematic error from $\phi\ \eta$ sideband subtraction	0.8%
Systematic error estimate from g11	8%
Conservatively estimated total minimum systematic error experiment for the photoproduction of $\phi\ \eta$	12.5%

by changing the model's t-slope parameter for the exchange interaction. Since the statistics for the $\phi\ \eta$ decay mode is very low, the error on the t-slope is high. The systematic error for the acceptance simulation, thus estimated, is 7.9%.

There were a high number of similarities in the run-conditions and the detector configurations between the runperiods, g11 and g12. Detailed studies were performed for the g11 experiment to estimate various sources of systematics, like the target length, LH_2 density, etc. These systematics are considered replicable for the calculations in the analyses presented, when used in the conservative limit and are reproduced in the table [4.5] from the references [52], [53]. All the systematic and the statistical error estimates for the g12 experiment and the $\phi\ \eta$ final state are listed in table [4.6].

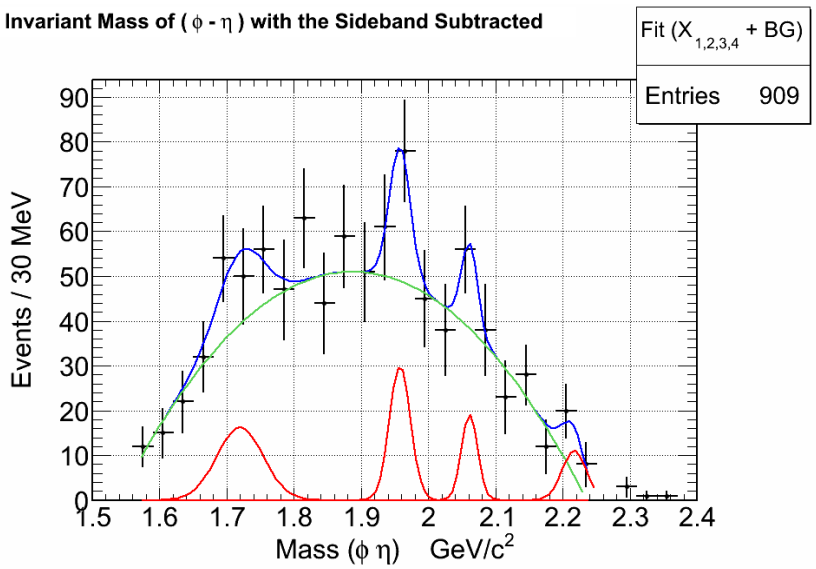

Figure 4.27: Sideband subtracted $\phi\ \eta$ mass plot, fitted to best estimate the background for the process $X \rightarrow \phi\ \eta$. The blue fit is the final sum fit of the gaussians fitted to assumed resonances with loosely constrained width and mean and a quadratic background. The green fit is the final fitted background that is used in the calculations of the upper and the lower limit. It is observed that the fit mimics the background very well. The various red gaussians are fits to perceived resonances, that are chosen to either check for an expected resonance, like in the case of the ϕ_{1680}, or the one visible around 1960 MeV.

4.5 Upper limits on Strangeonia Cross sections

The analysis of the sideband subtracted invariant mass distribution of $\phi\ \eta$ events does not find any resonant structure of statistical significance in the data. This can observed from the figure [4.22] and its derivative figure [4.27]. Hence, most of the observed $\phi\ \eta$ events are attributed to the background $\phi\ \eta$ production instead of the expected strangeonia. The approach of Feldman and Cousins [64], preferred for placing confidence intervals on detection of small signals, is used to calculate the upper limit to the cross sections for the expected strangeonia. The Feldman-Cousins method [64] calculates a stated confidence interval, 90% for this analysis, using the number of total observed counts and the estimated background for the events.

4.5.1 Techniques

The analysis calculates the background two different ways. This gives the analysis two different description of the background, and a better handle on the systematics for these decays. The first approach is to use multiple loosely restrained gaussians to fit many possible signal peaks and a polynomial to describe the background in a single fit for the whole distribution, as shown in figure [4.27]. This approach gives the analysis the best real-world description for the background. The second approach, which is found in most standard Feldman-Cousins analysis, is to perform one fit for each mass bin. A gaussian with a fixed mean and width is used in conjunction with a polynomial background to fit the distribution for each mass-bin. One particular fit is shown in figure [4.29] for the 1965 MeV/c^2 bin.

4.5.2 First approach

In first approach, multiple gaussian functions for the possible resonances, and a smooth second order polynomial for the background, is used to describe the observed data, in order to estimate the signal and the background yield. Other fit-functions (e.g. polynomials of orders 3,4,5,6) were tested and the polynomial of order 2 was judged to be the most straightforward and viable fit-function. The analysis accepts fractional numbers for the background estimate even though that is not a physical possibility. The polynomial fit is unconstrained, whereas the gaussian fits used to estimate the resonance signal are very loosely constrained for its mean and sigma values. This allows the fit function to find optimum fit values to fit the perceived resonance.

Note that the primary goal for this fit here is to get the least estimate of the background, not to get good fits for the signal. As observed in figure [4.27], the background fit is satisfactory. This analysis calculates the confidence limits two different ways. One where it uses multiple loosely constrained gaussians for signal fit with a quadratic background, which gives the least estimate for the background events in any given bin. The other where it uses a single gaussian of a fixed mean and width to fit each bin, with a quadratic background function, which gives the greatest estimate of the background for a bin. If a correlation does exist between the background and the signal events, it is not possible for the analysis to extract that correlation due to low statistics; hence uncorrelated signal and background

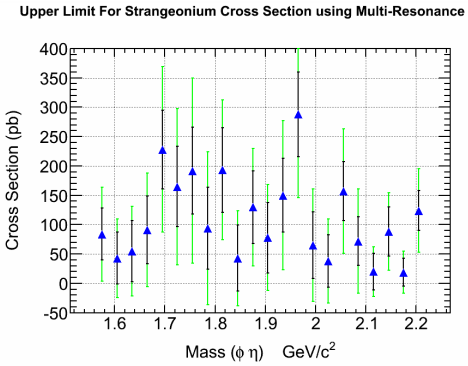

(a) Plot of upper limit for strangeonium cross section, with a confidence limit of 90%, using Feldman-Cousins Method. This plot is a representation of the values presented in table [4.8]. The background was estimated for each bin from a fit using multiple gaussians to fit possible resonances, with a quadratic background.

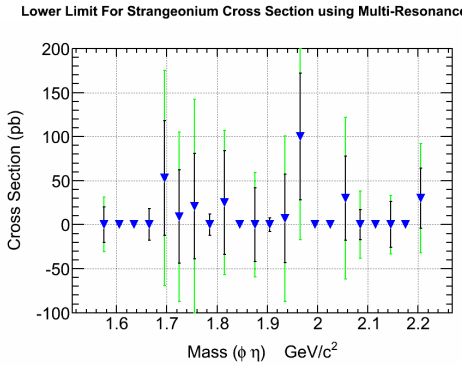

(b) Plot of lower limit for strangeonium cross section, with a confidence limit of 90%, using Feldman-Cousins Method. This plot is a representation of the values presented in table [4.8]. The background was estimated for each bin from a fit using multiple gaussians to fit possible resonances, with a quadratic background.

Figure 4.28: Plots of upper and lower limits for strangeonium photoproduction cross section with 90% confidence limit, using Feldman-Cousins method and using multiple gaussians to fit possible resonances.

events are assumed.

Based on the values presented in the table [4.7], the upper and the lower limits on the photoproduction cross section of the strangeonium X via $\phi\,\eta$ decay mode are calculated and tabulated in table [4.8] and plotted in figure [4.28]. The experimental parameters used for the calculations are referenced in table [4.4]. These 90% confidence intervals are tabulated in 30 MeV/c^2 wide mass bins, where a quadratic function has been chosen to fit the background $\phi\,\eta$ events.

4.5.3 Second approach

In the second approach, each bin of the $\phi\,\eta$ mass distribution is fitted with a quadratic background function and a gaussian of a fixed decay width of 15 MeV/c^2 . This fit is used to estimate the background content of that particular bin. The counts for the background as well as the observed events are then used to calculate the 90% confidence interval on the photoproduction cross section for a strangeonium resonance 'X' to have decayed via $\phi\,\eta$. The calculated limits are listed in tables [4.9], [4.10]. Figure [4.29] demonstrates an example fit

Table 4.7: Expected signal events estimated using the Feldman-Cousins method, for the 90% confidence interval, corresponding to the upper and the lower limits on the photoproduction cross section, for a resonance centered at the particular mass bins. First approach with multiple gaussians used to fit possible resonances is used to estimate the background. Calculations are presented in the format: Value ± statistical error ± systematic error.

Mass GeV/c^2	Obs. Count	Est. Bkg Count	Upper Limit Signal Count	Lower Limit Signal Count
1.575	12	10.01 ± 3.44	9.00 ± 4.70 ± 3.88	0.00 ± 2.18 ± 1.21
1.605	15	17.49 ± 2.89	5.30 ± 5.44 ± 2.83	0.00 ± 0.00 ± 0.00
1.635	22	24.21 ± 2.80	6.98 ± 6.63 ± 2.98	0.00 ± 0.00 ± 0.00
1.665	32	30.18 ± 4.69	12.35 ± 7.88 ± 5.30	0.00 ± 2.43 ± 0.00
1.695	54	35.40 ± 8.19	32.12 ± 9.46 ± 10.40	7.46 ± 9.13 ± 8.00
1.725	50	39.86 ± 7.87	23.16 ± 9.48 ± 9.13	1.32 ± 7.39 ± 6.00
1.755	56	43.57 ± 10.12	25.96 ± 9.98 ± 11.37	2.81 ± 8.15 ± 8.30
1.785	47	46.52 ± 7.84	13.01 ± 9.67 ± 8.26	0.00 ± 1.60 ± 0.00
1.815	63	48.72 ± 3.89	28.44 ± 10.57 ± 6.89	3.72 ± 8.65 ± 3.35
1.845	44	50.17 ± 4.44	6.76 ± 8.81 ± 3.86	0.00 ± 0.00 ± 0.00
1.875	59	50.86 ± 4.63	22.16 ± 10.48 ± 6.41	0.00 ± 7.16 ± 2.92
1.905	51	50.80 ± 4.22	13.22 ± 10.09 ± 4.98	0.00 ± 1.38 ± 0.00
1.935	61	49.99 ± 9.39	25.05 ± 10.54 ± 10.65	1.25 ± 8.41 ± 7.29
1.965	78	48.42 ± 6.33	45.12 ± 11.25 ± 11.02	15.61 ± 11.24 ± 7.05
1.995	45	46.10 ± 6.13	11.01 ± 9.54 ± 6.51	0.00 ± 0.10 ± 0.00
2.025	38	43.02 ± 5.45	7.13 ± 8.37 ± 5.03	0.00 ± 0.00 ± 0.00
2.055	56	39.19 ± 8.99	30.34 ± 9.76 ± 10.85	5.81 ± 9.30 ± 8.61
2.085	38	34.61 ± 9.54	14.91 ± 8.52 ± 10.00	0.00 ± 3.48 ± 4.34
2.115	23	29.27 ± 2.92	4.01 ± 5.99 ± 2.20	0.00 ± 0.00 ± 0.00
2.145	28	23.17 ± 2.88	14.85 ± 7.15 ± 4.14	0.00 ± 4.42 ± 1.18
2.175	12	16.33 ± 2.87	3.50 ± 4.50 ± 2.27	0.00 ± 0.00 ± 0.00
2.205	20	8.73 ± 4.30	19.80 ± 5.37 ± 5.85	4.83 ± 5.36 ± 4.41

used to estimate the background count required for the using the Feldman-Cousins method. A quadratic distribution function for the background was used in conjunction with a gaussian of fixed width of 15 MeV/c^2 and with a mean fixed to the central value of each of the 30 MeV/c^2 bin. The resulting fit was used to estimate the background by integrating the quadratic background function over the bin-width. The error to this integration was treated

Table 4.8: Upper and lower limits with a 90% confidence limit on the interval, for the decay cross section of X $\rightarrow \phi\ \eta$ for the g12 trigger range, using the first approach to estimate the background.

Mass (GeV/c^2)	Cross Section Upper Limit (pb)	Cross Section Lower Limit (pb)
1.575	84 ± 44 ± 36	0 ± 20 ± 11
1.605	43 ± 44 ± 23	0 ± 0 ± 0
1.635	55 ± 52 ± 24	0 ± 0 ± 0
1.665	91 ± 58 ± 39	0 ± 18 ± 0
1.695	228 ± 67 ± 74	53 ± 65 ± 57
1.725	165 ± 68 ± 65	9 ± 53 ± 43
1.755	192 ± 74 ± 84	21 ± 60 ± 61
1.785	94 ± 70 ± 60	0 ± 12 ± 0
1.815	193 ± 72 ± 47	25 ± 59 ± 23
1.845	43 ± 56 ± 25	0 ± 0 ± 0
1.875	130 ± 62 ± 38	0 ± 42 ± 17
1.905	78 ± 60 ± 30	0 ± 8 ± 0
1.935	150 ± 63 ± 64	7 ± 50 ± 44
1.965	288 ± 72 ± 70	100 ± 72 ± 45
1.995	65 ± 57 ± 39	0 ± 1 ± 0
2.025	38 ± 45 ± 27	0 ± 0 ± 0
2.055	157 ± 50 ± 56	30 ± 48 ± 44
2.085	72 ± 41 ± 48	0 ± 17 ± 21
2.115	20 ± 31 ± 11	0 ± 0 ± 0
2.145	88 ± 42 ± 24	0 ± 26 ± 7
2.175	19 ± 24 ± 12	0 ± 0 ± 0
2.205	124 ± 34 ± 37	30 ± 34 ± 28

as the error to the estimated background. This gives symmetric errors on the background count. When propagated to the confidence limit calculations, the Feldman-Cousins method does not yield symmetric errors. In that case, to obtain a conservative estimate, the error with the larger magnitude is chosen as the error on the confidence limits. This error is treated as a systematic error emanating from the fit and is added to the other systematic errors listed in table [4.6], using the root-mean-square method. The errors are then scaled by the appropriate scaling factors presented in the tables [4.6], [4.5].

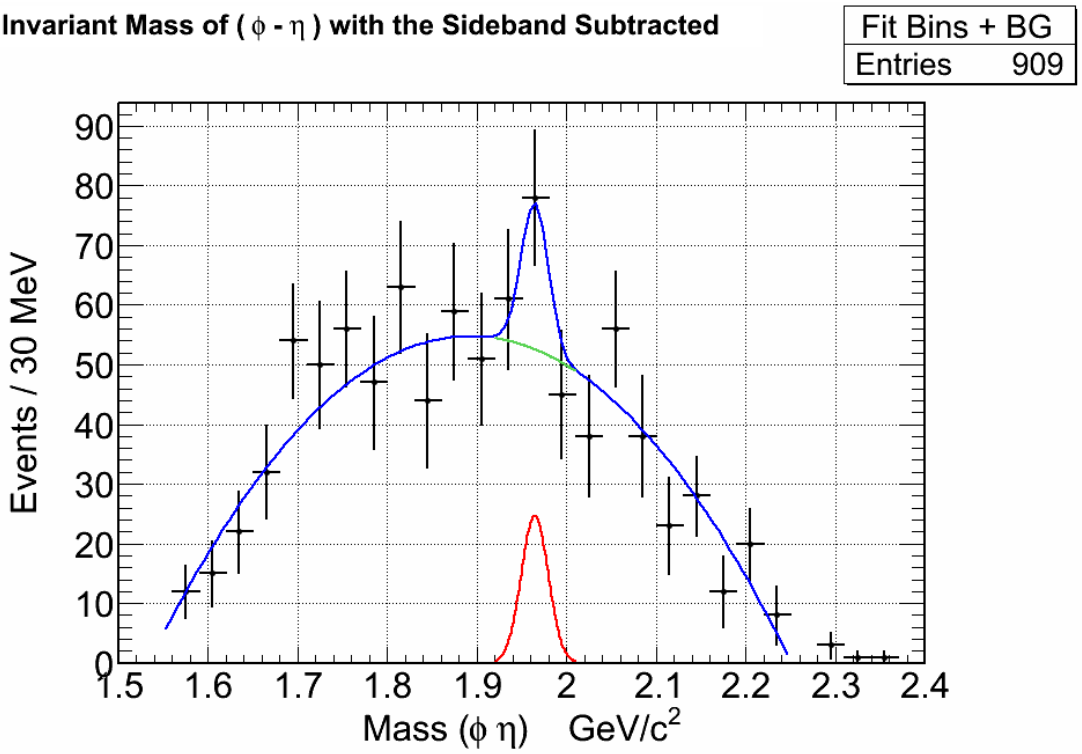

Figure 4.29: Sideband subtracted $\phi\ \eta$ mass plot, fitted to best estimate the background for the process $X \rightarrow \phi\ \eta$ for the X resonance mass of 1965 MeV/c^2 , using the second approach.

The bin-wise estimate, for the confidence interval and the background, along with the appropriately scaled errors, using the stated method is tabulated in tables [4.9], [4.10].

4.6 Partial Wave Analysis of the $\phi\ \eta$

A full partial wave analysis for the γ p $\rightarrow \phi\ \eta \rightarrow$ p K$^+$ K$^-$ decay mode was performed. The analysis, initially, considered a large number of states that could have decayed via the stated channel. A background wave to accommodate non-resonant $\phi\ \eta$ was usually added to the list of waves, referred to as a waveset for a given PWA fit. Multiple wave combinations were formed and PWA fits were performed. The number of observed events available for the fit were small, hence smaller wavesets were identified, that included waves most likely in the observed data from perusing multiple fits as well as physics motivations.

No clear resonant structure was observed in any of partial waves for the multiple fits

Table 4.9: Expected signal events estimated using the Feldman-Cousins method, for the 90% confidence interval, corresponding to upper and the lower limits on the production cross section, for a resonance centered at the particular mass bins. Second approach is used to estimate the background.

Mass GeV/c^2	Obs. Count	Est. Bkg Count	Upper Limit Signal Count	Lower Limit Signal Count
1.575	12	10.06 ± 3.82	8.95 ± 4.71 ± 4.21	0.00 ± 2.16 ± 1.45
1.605	15	19.21 ± 2.75	4.03 ± 5.14 ± 2.27	0.00 ± 0.00 ± 0.00
1.635	22	26.64 ± 2.42	5.08 ± 6.27 ± 2.14	0.00 ± 0.00 ± 0.00
1.665	32	33.26 ± 2.27	9.31 ± 8.03 ± 2.90	0.00 ± 0.00 ± 0.00
1.695	54	37.85 ± 8.04	29.67 ± 9.59 ± 10.00	5.61 ± 8.65 ± 7.20
1.725	50	43.36 ± 10.33	19.66 ± 9.66 ± 11.06	0.00 ± 5.98 ± 6.49
1.755	56	47.49 ± 9.76	22.05 ± 10.17 ± 10.71	0.00 ± 7.54 ± 7.14
1.785	47	51.61 ± 2.80	8.40 ± 9.45 ± 2.92	0.00 ± 0.00 ± 0.00
1.815	63	53.52 ± 9.32	23.64 ± 10.80 ± 10.45	0.00 ± 8.15 ± 7.00
1.845	44	55.90 ± 3.07	4.03 ± 6.20 ± 1.59	0.00 ± 0.00 ± 0.00
1.875	59	56.83 ± 3.10	16.19 ± 10.77 ± 4.49	0.00 ± 3.05 ± 0.00
1.905	51	56.94 ± 3.16	7.85 ± 9.62 ± 3.01	0.00 ± 0.00 ± 0.00
1.935	61	55.53 ± 9.76	19.50 ± 10.80 ± 10.51	0.00 ± 5.23 ± 4.54
1.965	78	52.50 ± 11.64	41.05 ± 11.43 ± 14.24	11.58 ± 11.38 ± 11.81
1.995	45	52.40 ± 2.92	6.33 ± 8.23 ± 2.22	0.00 ± 0.00 ± 0.00
2.025	38	49.26 ± 2.73	3.59 ± 6.10 ± 1.35	0.00 ± 0.00 ± 0.00
2.055	56	44.49 ± 9.74	25.05 ± 10.03 ± 10.95	2.14 ± 7.96 ± 7.69
2.085	38	40.55 ± 2.47	9.14 ± 8.70 ± 2.94	0.00 ± 0.00 ± 0.00
2.115	23	34.97 ± 2.24	2.17 ± 3.13 ± 0.81	0.00 ± 0.00 ± 0.00
2.145	28	28.57 ± 2.26	9.46 ± 7.51 ± 2.94	0.00 ± 0.42 ± 0.00
2.175	12	21.37 ± 2.43	1.60 ± 2.40 ± 0.84	0.00 ± 0.00 ± 0.00
2.205	20	10.53 ± 9.06	18.00 ± 5.53 ± 9.75	3.11 ± 5.45 ± 9.00

performed. This is primarily due to low statistics, as well as high background for the decay mode. A brief overview of the partial wave analysis along with the techniques implemented and detailed results with fits are presented in appendix [A]. The PWA using all the waves mentioned in table [A.1] was also used to calculate the acceptance for the $\phi\ \eta$ analysis.

Table 4.10: Upper and lower limits with a 90% confidence limit on the interval, for the decay cross section of X $\rightarrow \phi\ \eta$ for the g12 trigger range, using the second approach to estimate the background.

Mass (GeV/c^2)	Cross Section Upper Limit (pb)	Cross Section Lower Limit (pb)
1.575	84 ± 44 ± 39	0 ± 20 ± 14
1.605	33 ± 42 ± 18	0 ± 0 ± 0
1.635	40 ± 50 ± 17	0 ± 0 ± 0
1.665	68 ± 59 ± 21	0 ± 0 ± 0
1.695	210 ± 68 ± 71	40 ± 61 ± 51
1.725	140 ± 69 ± 79	0 ± 43 ± 46
1.755	163 ± 75 ± 79	0 ± 56 ± 53
1.785	61 ± 68 ± 21	0 ± 0 ± 0
1.815	160 ± 73 ± 71	0 ± 55 ± 47
1.845	26 ± 39 ± 10	0 ± 0 ± 0
1.875	95 ± 63 ± 26	0 ± 18 ± 0
1.905	47 ± 57 ± 18	0 ± 0 ± 0
1.935	117 ± 65 ± 63	0 ± 31 ± 27
1.965	262 ± 73 ± 91	74 ± 73 ± 75
1.995	38 ± 49 ± 13	0 ± 0 ± 0
2.025	19 ± 33 ± 7	0 ± 0 ± 0
2.055	129 ± 52 ± 57	11 ± 41 ± 40
2.085	44 ± 42 ± 14	0 ± 0 ± 0
2.115	11 ± 16 ± 4	0 ± 0 ± 0
2.145	56 ± 44 ± 17	0 ± 2 ± 0
2.175	9 ± 13 ± 5	0 ± 0 ± 0
2.205	112 ± 35 ± 61	19 ± 34 ± 56

4.7 Analysis of X(1750) in photoproduction

The $\phi\ \eta$ analysis is further able to comment on the status of the $\phi(1680)$ and X(1750) mesons. As stated previously, the FOCUS experiment at Fermilab claimed that the structure in photoproduction at 1750 MeV/c^2 is a different resonance [25] than the $\phi(1680)$ resonance that has been clearly established in e^+e^- production. The dominant decay channel for $\phi(1680)$ in e^+e^- is KK^* ($e^+e^- \rightarrow K_sK\pi$), whereas in photoproduction FOCUS found no enhancement in its sample for KK^* for the $X(1750)/\phi(1680)$ MeV/c^2 state. They observed

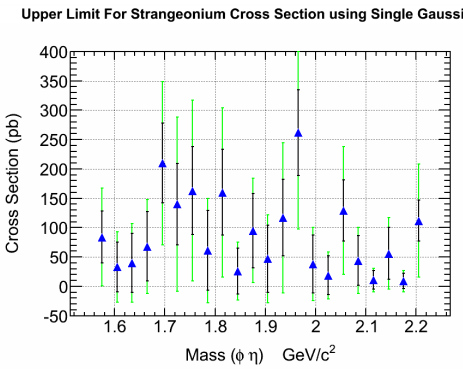

(a) Plot of upper limit for strangeonium cross section, with a confidence limit of 90%, using Feldman-Cousins Method. This plot is a representation of the values presented in table [4.10]. The background was estimated for each bin from a fit using a single gaussian of fixed mean and width, with a quadratic background.

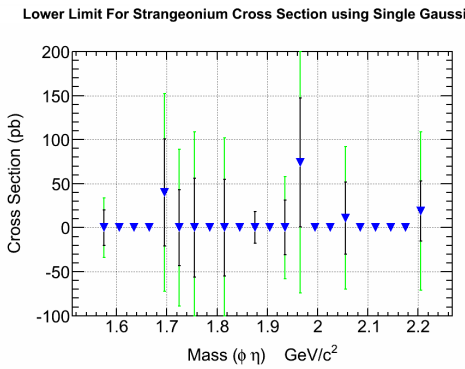

(b) Plot of lower limit for strangeonium cross section, with a confidence limit of 90%, using Feldman-Cousins Method. This plot is a representation of the values presented in table [4.10]. The background was estimated for each bin from a fit using a single gaussian of fixed mean and width, with a quadratic background.

Figure 4.30: Plots of upper and lower limits for strangeonium photoproduction cross section with 90% confidence limit, using Feldman-Cousins method and using a single gaussian to fit the signal in a mass bin.

$X(1750)$ in the K^+K^- spectrum and placed a strong upper limit on the KK^*/K^+K^- branching ratio. They cite interference effects as a possible , but unlikely, reason for this discrepancy and they claim $X(1750)$ to be a new state, different from the radial $\phi(1680)$.

The cross section for the $X(1750) \rightarrow \mathrm{K}^+\ \mathrm{K}^-$ was measured to be 8 $\pm$ 3 nb at a beam energy of 45 GeV at the Omega spectrometer at SLAC [23]. The theoretical model for strangeonium decay referred for this thesis [3] uses the 3P0 model to predict a branching ratio for $\phi\ \eta$:$\mathrm{K}^+\ \mathrm{K}^-$ of 1:2. An estimate for the photoproduction cross section of the $X(1750) \rightarrow \phi\ \eta$ is thus obtained for $\mathrm{E}_\gamma \sim 5$ GeV using the following set of observations:

- From figure [4.31] extracted from reference [65], it is observed that the asymptotic behavior of the photoproduction cross sections of the light vector mesons ρ, ω and ϕ evolve as $\mathrm{W}^{0.22}$, where 'W' is the center of mass energy of the photon-proton system.
- The photoproduction cross section at lower energies is observed to be greater or at least equal to that predicted by the $\mathrm{W}^{0.22}$ behavior.
- This behavior of at least equal or greater cross section at lower energies than that predicted by the asymptotic behavior is observed to be true even for heavier mesons.

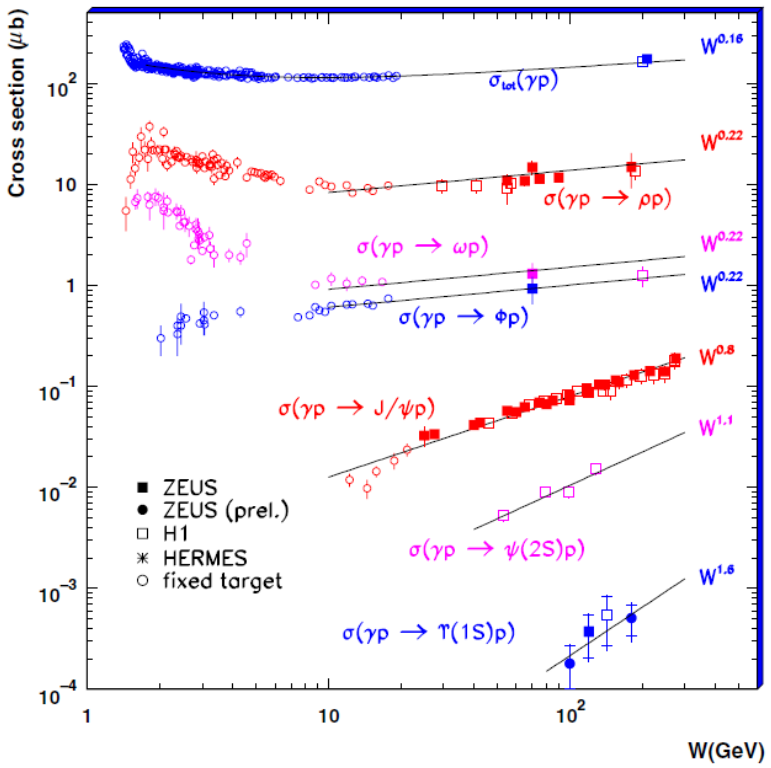

Figure 4.31: Plot of photoproduction cross section of vector mesons from threshold to high center of mass energies (W), off of a proton, extracted from the reference [65].

- In light of the above observations, it is postulated that the cross section for the excited vector meson $\phi(1680)/X(1750)$ should also follow the same behavior and hence should at least have a cross section of 3.14 $\pm$ 1.18 nb for $E_\gamma \sim 5$ GeV.

Hence the $X(1750)$ vector meson photoproduction cross section should be observed at a level of $\sim$ 2 nb or greater in the $\phi\,\eta$ decay mode. The highest upper limit for the production cross section for a strangeonium resonance in the $\phi\,\eta$ invariant mass region of 1650-1800 MeV/c^2 is 250 pb, for a mass around 1695 MeV/c^2 . This big difference in the calculated cross section for a strangeonium state from the $\phi\,\eta$ analysis with that expected for the $X(1750)$ vector meson in photoproduction, suggests strongly that the $X(1750)$ observed in $K^+\,K^-$ is not a strangeonium vector resonance and is different from the strangeonium vector meson $\phi(1680)$.

4.8 Summary of strangeonia analysis

The photoproduction reaction, $\gamma\ \mathrm{p} \rightarrow \mathrm{p}\ \phi\ \eta \rightarrow \mathrm{p}\ \mathrm{K}^{+}\ \mathrm{K}^{-}\ [\eta]$, was analyzed for observable resonances in the invariant mass spectrum of the $\phi\ \eta$ intermediate state. First measurement of the $\phi\ \eta$ photoproduction cross section was carried out. It is calculated to be 5.8 ± 0.3 (statistical error) $\pm$ 0.7 (systematic error) nanobarns for $\mathrm{E}_{\gamma} \in \{4.40, 5.45\}$ GeV. Search for resonant strangeonium structures in the $\phi\ \eta$ invariant mass was performed. The search was unable to isolate any strangeonium states with the statistical significance required to claim discovery. Thus the upper limits on the photoproduction cross sections for the expected strangeonium states via their $\phi\ \eta$ decay mode was calculated and presented as a guide for future experiments. The lower limits were all consistent with zero. The largest cross section upper limits of $\sim$ 250 pb were observed for strangeonia masses of 1695 MeV/c^2 and 1965 MeV/c^2 . A full partial wave analysis was performed for the $\phi\ \eta$ decay mode using kinematically fitted four-vectors and no resonant features were observed.

The analysis is able to use the calculated upper limits for photoproduction of the strangeonium resonance in conjunction with the observed behavior of vector meson photoproduction cross section to make the obervation that the vector strangeonium state $\phi(1680)$ $\not\equiv X(1750)$. It should have been observed with a cross section of 2 nb or greater but is in fact not observed even at a level of 250 pb in the $\phi\ \eta$ analysis.

CHAPTER 5

OTHER EXPLORATORY ANALYSIS FOR $\gamma P \rightarrow PK^+K^-[X]$

The detected final state of proton K^+ K^- in the g12 dataset contains immense amount of interesting physics. Therefore, this thesis also explores other production and decay modes accessible to this final state. Photoproduction reactions - [5.1, 5.2] were also analyzed for exotic and hybrid signatures and the short exploratory analysis done on these channels is presented. Exclusive photoproduction of the ϕ meson [5.3] was also analyzed to calculate the yield as well as the cross section and is also presented in this chapter.

$$\gamma \quad p \quad \rightarrow \quad p \quad \phi \quad [\pi^o] \tag{5.1}$$

$$\gamma \quad p \quad \rightarrow \quad p \quad \phi \quad [\omega] \tag{5.2}$$

$$\gamma \quad p \quad \rightarrow \quad p \quad \phi \tag{5.3}$$

$$\gamma \quad p \quad \rightarrow \quad N^* \quad \phi \tag{5.4}$$

5.1 Analysis of proton ϕ π^o final state

Analysis of the proton, K^+, K^- g12 data, where the K^+ K^- invariant mass is constrained to be within the observed ϕ mass range and the missing mass for the events is constrained to be within the observed π^o mass range is performed. After applying these selection criteria and the standard cuts, the analysis has a set of events for $\gamma p \rightarrow p\phi\pi^o$ decay. The resulting invariant mass distributions are shown in figures [5.1a], [5.1b].

This sample of ϕ π^o is relatively clean when compared to the sample for the ϕ η data. Most of the background for this decay mode lies beneath the ϕ meson. To obtain a cleaner

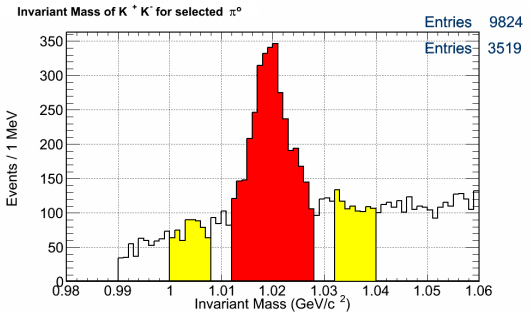

(a) Selection of ϕ mesons and its sidebands to be used for sideband subtraction. A gap is left between the sidebands and the ϕ events to minimize the ϕ leakage into the sidebands.

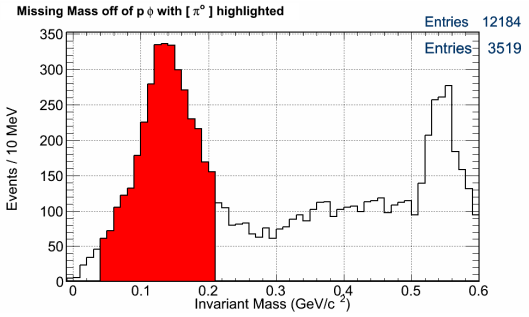

(b) Distribution of missing mass off of proton ϕ with the selected π^o highlighted.

Figure 5.1: Selection of the ϕ meson and its sidebands as well as the selection of π^o meson from the missing mass distribution.

Table 5.1: Values for the selection of the ϕ sidebands and the π^o events.

π^o mass range	(40,210) MeV/c^2
ϕ mass range	(1008,1028) MeV/c^2
Left ϕ sideband	(1000,1008) MeV/c^2
Right ϕ sideband	(1032,1040) MeV/c^2

sample of ϕ π^o events, a traditional sideband subtraction is performed on the ϕ meson. The justification is that for the background beneath ϕ, kinematics should be roughly the same as those of the events in the sideband. Therefore, normalized sideband subtraction from the signal region should leave the analysis with the majority of the expected signal. The background beneath the π^o mass distribution is negligible in the π^o mass range selected. Hence no sideband subtraction is performed on π^o mass distribution. The values for making the sideband and the π^o selection are listed in table [5.1].

An interesting overpopulation in the region of 1.85 GeV and 2.05 GeV in the invariant mass ϕ π^o spectrum is observed in figure [5.2a]. The overpopulation around the 1.5 GeV/c^2 is partially due to the KK^* reflection as discussed later.

The ϕ π^o invariant mass plots for the left ϕ sideband, the right ϕ sideband, and their

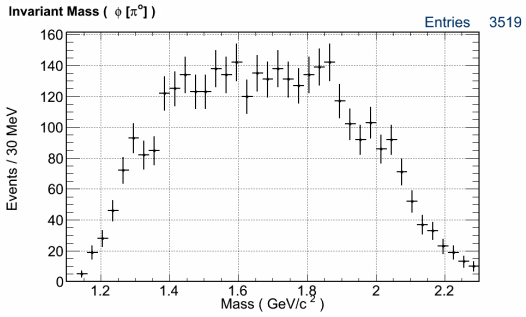

(a) Invariant mass of $\phi\ \pi^o$ mesons using the red highlighted region for ϕ mass range, as observed in figures [5.1a]), [5.1b].

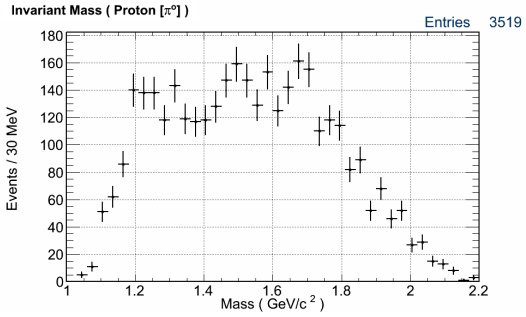

(b) Invariant mass of proton π^o using the red highlighted region for selected $\phi\ \pi^o$ events, as observed in figures [5.1a], [5.1b].

Figure 5.2: Invariant mass distributions for $\phi\ \pi^o$ and proton π^o.

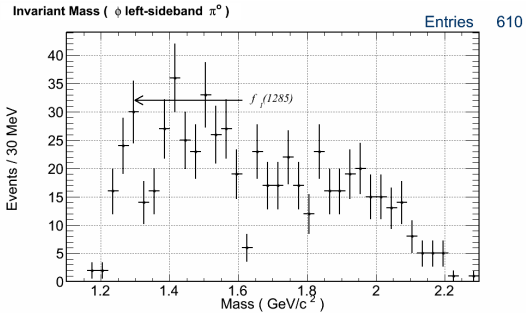

(a) Invariant mass distributions of the $K^+\ K^-$, using event in the π^o mass range and the left sideband of the ϕ.

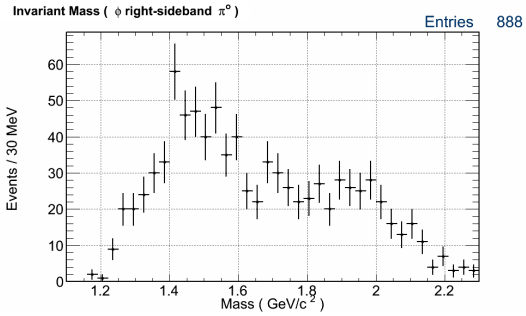

(b) Invariant mass of the $K^+\ K^-$ events from the 'right sideband of the ϕ and the π^o' events.

Figure 5.3: Invariant mass of the left and the right sidebands with the π^o.

sum are shown in figures [5.3a], [5.3b], [5.4b] respectively. The analysis does not observe a clear overpopulation at 1.85 GeV/c^2 or at 2.05 GeV/c^2 of the $\phi\ \pi^o$ invariant mass spectrum plotted for the sidebands of ϕ meson. The analysis does observe the overpopulation around 1.85 GeV/c^2 as well as 2.05 GeV/c^2 in the sideband subtracted distribution shown in the figure [5.4a]. However, the overpopulations are not statistically significant.

There is a $K^+\ K^-\ \pi^o$ contribution in the $\phi\ \pi^o$ invariant mass distribution. This contamination can come from the KK^* events. Therefore the analysis looks at the invariant mass of $K^+\ \pi^o$ in figure [5.5a] as well as $K^-\ \pi^o$ invariant mass in figure [5.5b] for the selected $\phi\ \pi^o$ events displayed in figure [5.2a] for hint of contamination from these KK^* events.

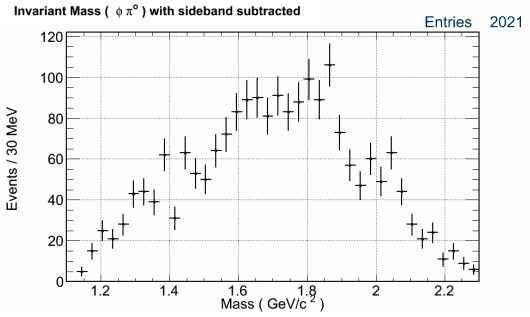

(a) Invariant mass of the $\phi\ \pi^o$ after the invariant mass distributions of the events from the left and the right sideband of ϕ meson have been subtracted from the distribution aka the sideband subtracted $\phi\ \pi^o$ distribution.

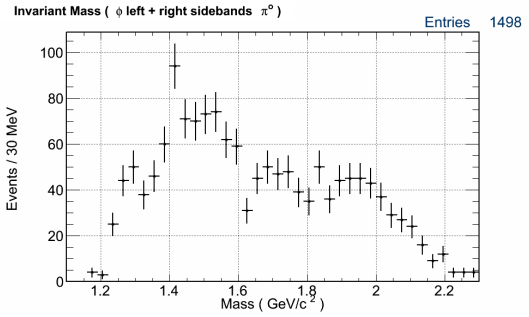

(b) Invariant mass distribution of the left and the right sideband of the ϕ meson added together. This is the sideband distribution that was subtracted from the signal distribution, figure[5.2a], to arrive at the sideband-subtracted distribution, figure[5.4a].

Figure 5.4: Sideband subtracted invariant mass of $\phi\ \pi^o$ distribution and the sideband distribution.

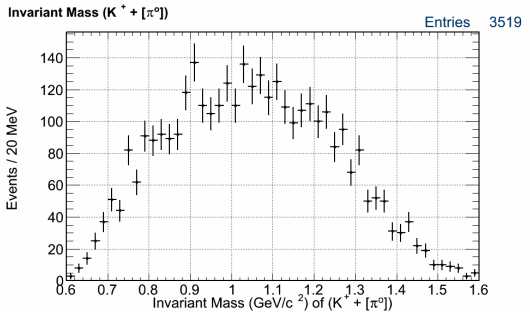

(a) Invariant mass of $K^+\ \pi^o$

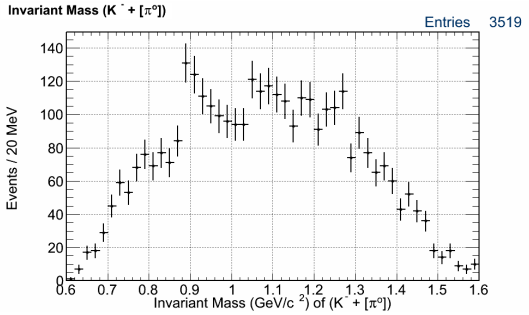

(b) Invariant mass of $K^-\ \pi^o$.

Figure 5.5: Contribution of KK^* to the plotted $\phi\ \pi^o$ invariant mass spectrum. We estimate somewhere between 5%-8% of KK^* events as the background for $\phi\ \pi^o$ distribution.

The analysis estimates the number of $K^*(892)$ events of both charge configurations to contribute somewhere between 5%-8% of KK^* events in the $\phi\ \pi^o$ mass spectrum. From the two-dimensional plots of the K^* vs $\phi\ \pi^o$ invariant mass in figures [5.6a], [5.6b], it is observed that those K^* events reflect into the $\phi\pi^o$ invariant mass spectra around 1.5 GeV, primarily due to lack of phase space.

In order to discern the presence of a $X \rightarrow \phi\ \pi^o$ state in the data, an analysis using t$'$, similar to the one performed earlier on the $\phi\ \eta$ data, is performed. The $\phi\ \pi^o$ invariant mass

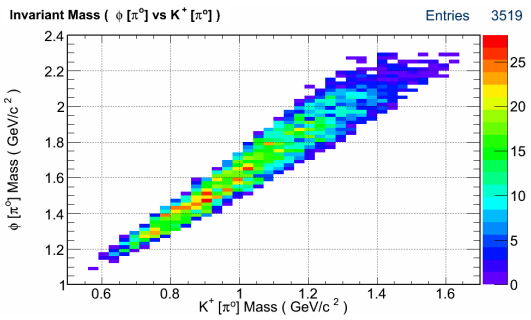

(a) Invariant mass of K^+ π^o vs ϕ π^o.

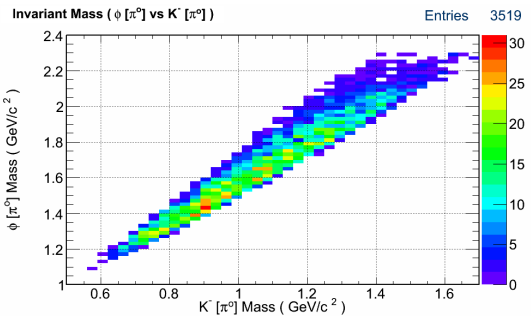

(b) Invariant mass of K^- π^o vs ϕ π^o.

Figure 5.6: Contribution of KK^* to the plotted ϕ π^o invariant mass spectrum. Estimating a simple count, disregarding the errors, we have somewhere between 5%-8% of KK^* events.

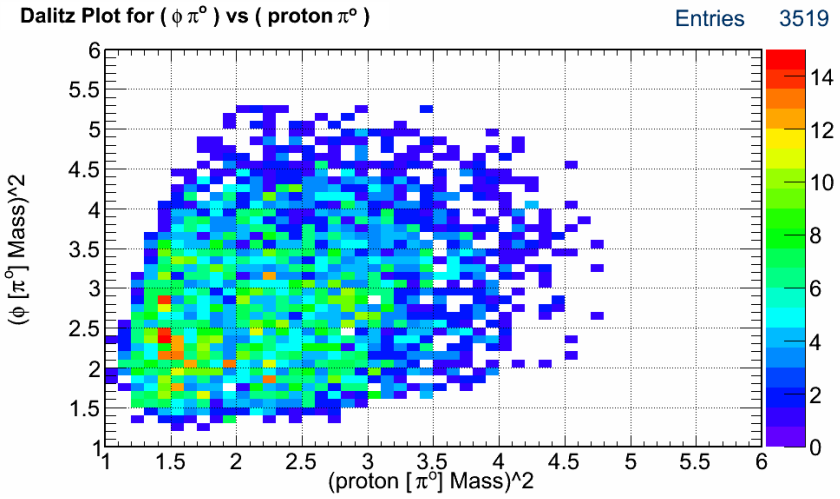

Figure 5.7: Dalitz analysis plot for ϕ π^o invariant mass against proton π^o invariant mass.

distribution is divided into two approximately equal sets with a cut on its t′value and any resulting features that the data exhibits are analyzed.

This approach provides quite a few insights about the ϕ π^o decay channel. In figure [5.9b], a broad overpopulation in the invariant mass ϕ π^o spectrum for high-t′values is observed. The t′-cut now clearly chooses two different regions of the associated kinematics for the decay channel. This does not serve as a baryon cut for this analysis as can be observed from the proton π^o invariant mass spectrum shown in figure [5.10]. Even though this cut makes the physics of the data more accessible, it does not aid us with separating the

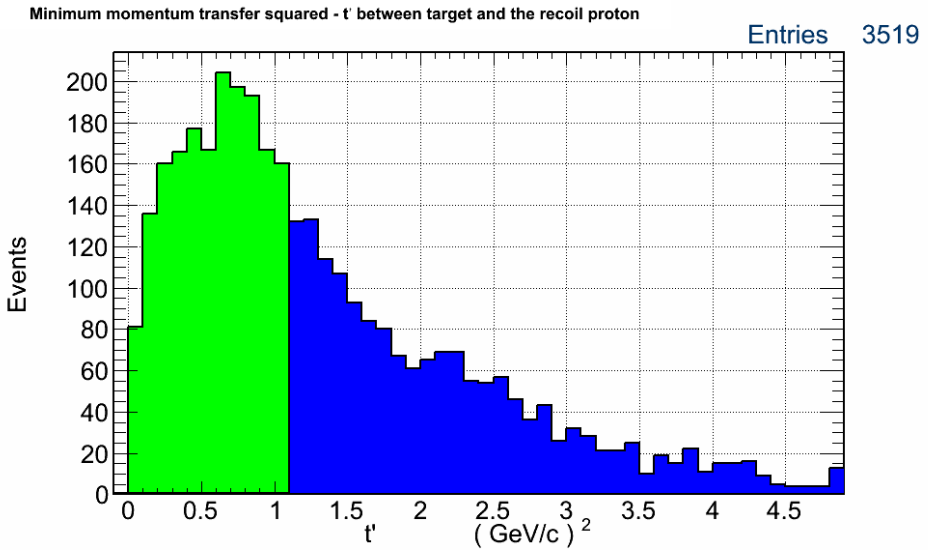

Figure 5.8: Plot of t′, which is the difference between the momentum transfer squared 't' and 'tmin'. t′ is the excess of momentum transfer squared, left over after the production of the resonance of a particular mass, that determines the kinematics of the reaction. The green and the blue selection for events denote the approximately equal number of events used in the figure [5.9b].

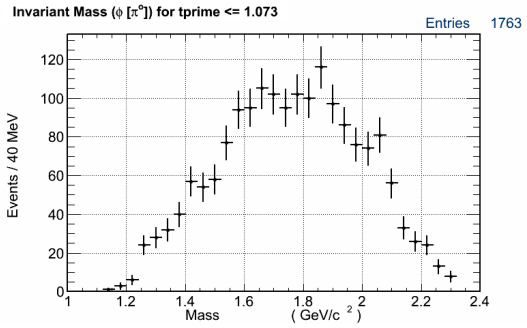

(a) Event distribution for $\phi\ \pi^o$ invariant mass for low-t′ events.

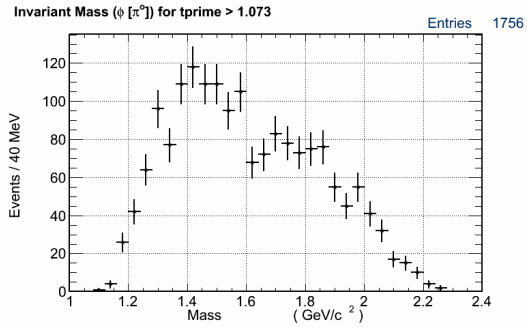

(b) Event distribution for $\phi\ \pi^o$ invariant mass for high-t′ events.

Figure 5.9: Event distribution for $\phi\ \pi^o$ invariant mass divided in approximately equal distributions on the basis of a t′-cut as highlighted in figure[5.8].

meson resonances. The analysis thus does not observe any statistically significant resonant structure in the $\phi\ \pi^o$ decay mode for the g12 data.

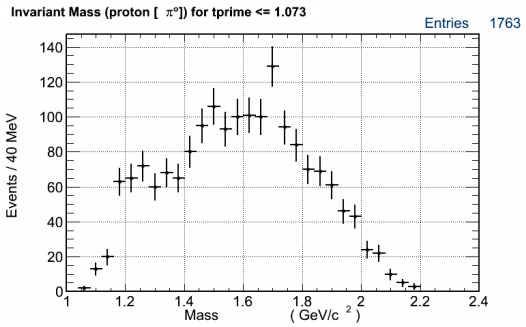

(a) Event distribution for proton π^o invariant mass for low-t′ events.

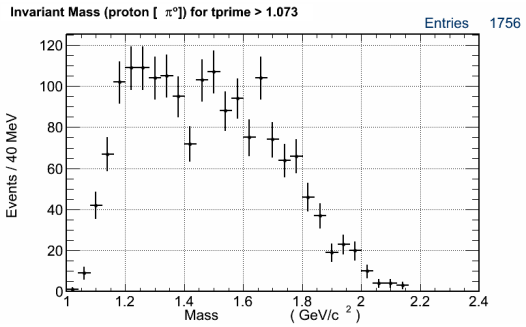

(b) Event distribution for proton π^o invariant mass for high-t′ events.

Figure 5.10: Event distribution for proton π^o invariant mass divided in approximately equal distributions on the basis of a t-cut as highlighted in figure[5.8].

5.2 Analysis of proton ϕ ω final state

Analysis of the proton, K^+, K^- g12 data, where the K^+ K^- invariant mass is constrained to be within the observed ϕ mass range and the missing mass for the events is constrained to be within the observed ω mass range is performed. After applying these selection criteria and the standard cuts, the analysis has a set of events for $\gamma p \rightarrow p\phi\omega$ decay. The resulting invariant mass distributions are shown in figures [4.13], [5.11]. A large amount of background non-ω events beneath the ω is observed in the missing mass spectrum shown in the figure [5.11]. In this scenario the analysis can only estimate the yield of the ω meson in the final data sample for detected proton, K^+ , K^- data in g12 off of a ϕ meson. These numbers provide guidance for the expected yield and required sensitivity for the future photoproduction experiments interested in this channel.

5.3 Analysis of proton ϕ exclusive final state

For the final state of proton ϕ, the analysis is able to achieve a very clean sample of ϕ mesons by constraining the linear and transverse missing momentum as well as the missing energy. The yield of the final selected events is estimated variously by using a gaussian, lorentzian and voigtian fit function with a quadratic background distribution for the background K^+ K^- , non-ϕ events. The fits and the yield are shown in the figure [5.12].

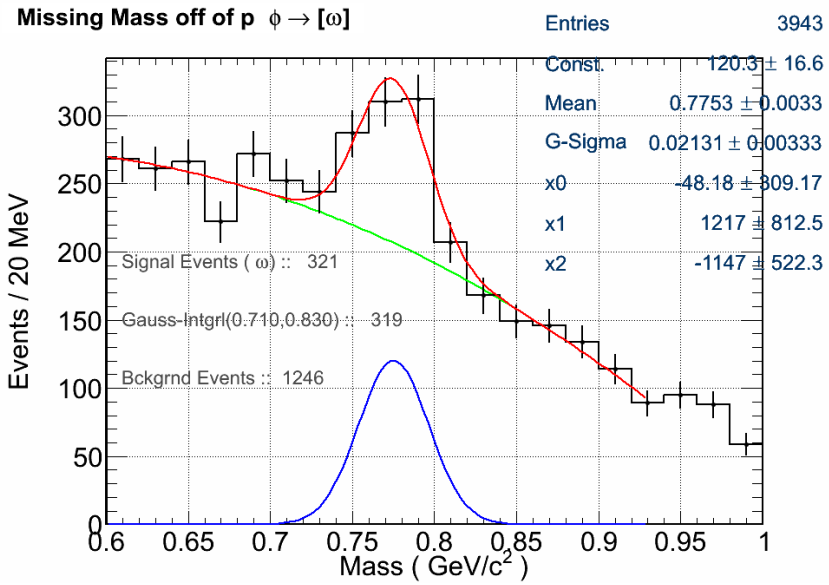

Figure 5.11: Yield estimate for ω events in the decay channel proton ϕ ω.

The results for the ϕ yield from these fits are tabulated in table [5.2].

5.3.1 Cross section for ϕ Events

The accepted yield of ϕ events in the g12 dataset over the entire g12 primary trigger range is listed in table [5.2]. Acceptance is calculated for the channel by simulating CLAS tracking and reconstruction using the procedure outlined in section [4.3.1]. Same selection criteria are implemented on the reconstructed events in the simulations as they were on the g12 data. Acceptance over the entire beam energy range as well as in binning of 150 MeV/c^2 is calculated and listed in table [5.2]. These are used to estimate the overall and binned cross section for the ϕ photoproduction. The analysis also accounts for the ϕ meson branching ratio of 48.5% to K^+ K^- . Systematics and statistical errors for these calculation are listed in tables [4.5], [4.6]. The estimated yield, cross section, and the associated corrections are presented in tables [5.2], [5.3].

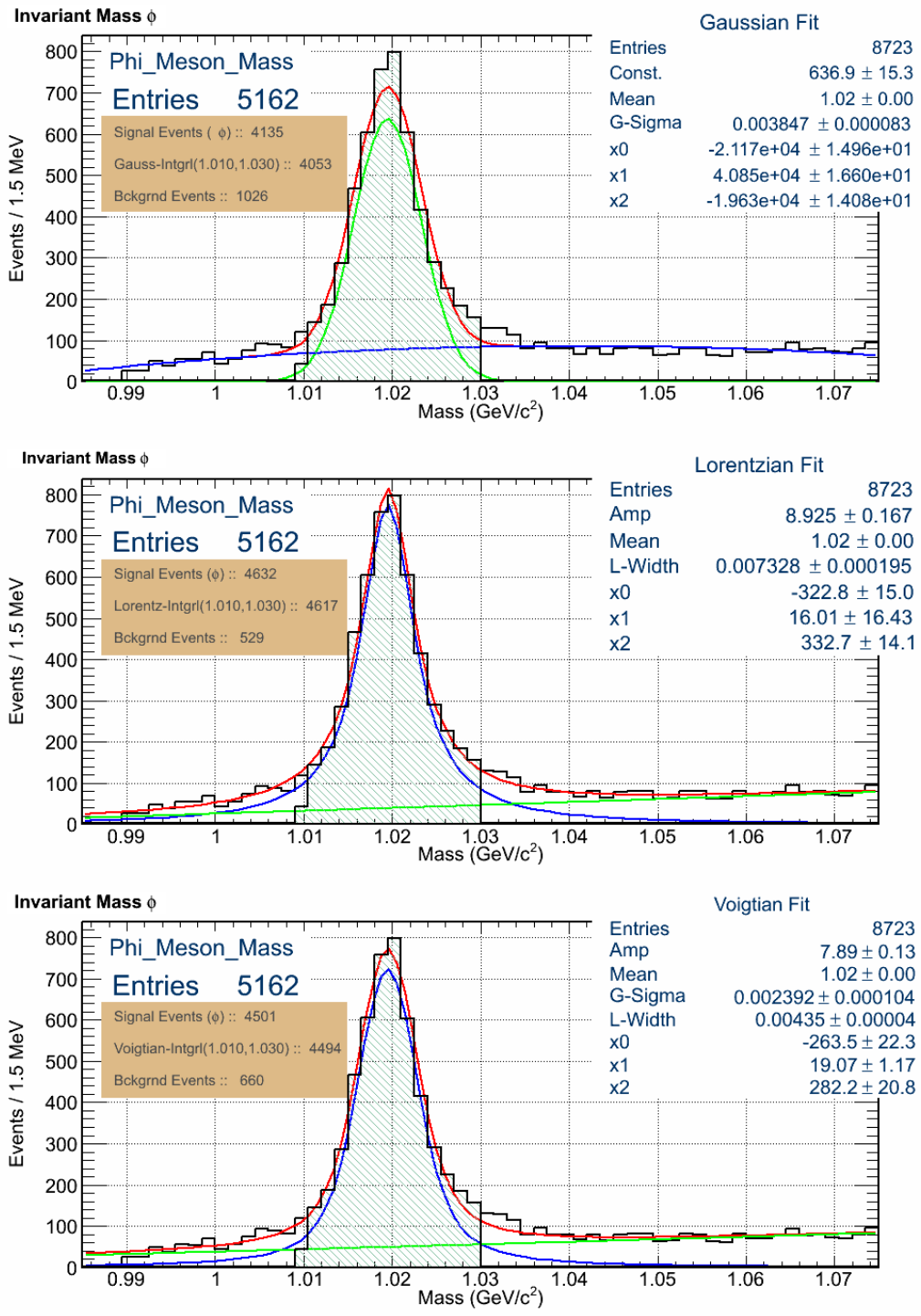

Figure 5.12: Various estimates for the yield of ϕ meson for proton K^+ K^- exclusive decay channel, using different fit functions. The 'Lorentzian Fit' best serves to describe the signal line-shape with a quadratic background. These fits are also performed for E_γ binning of 150 MeV/c^2 and are shown in figures [5.13]-[5.26].

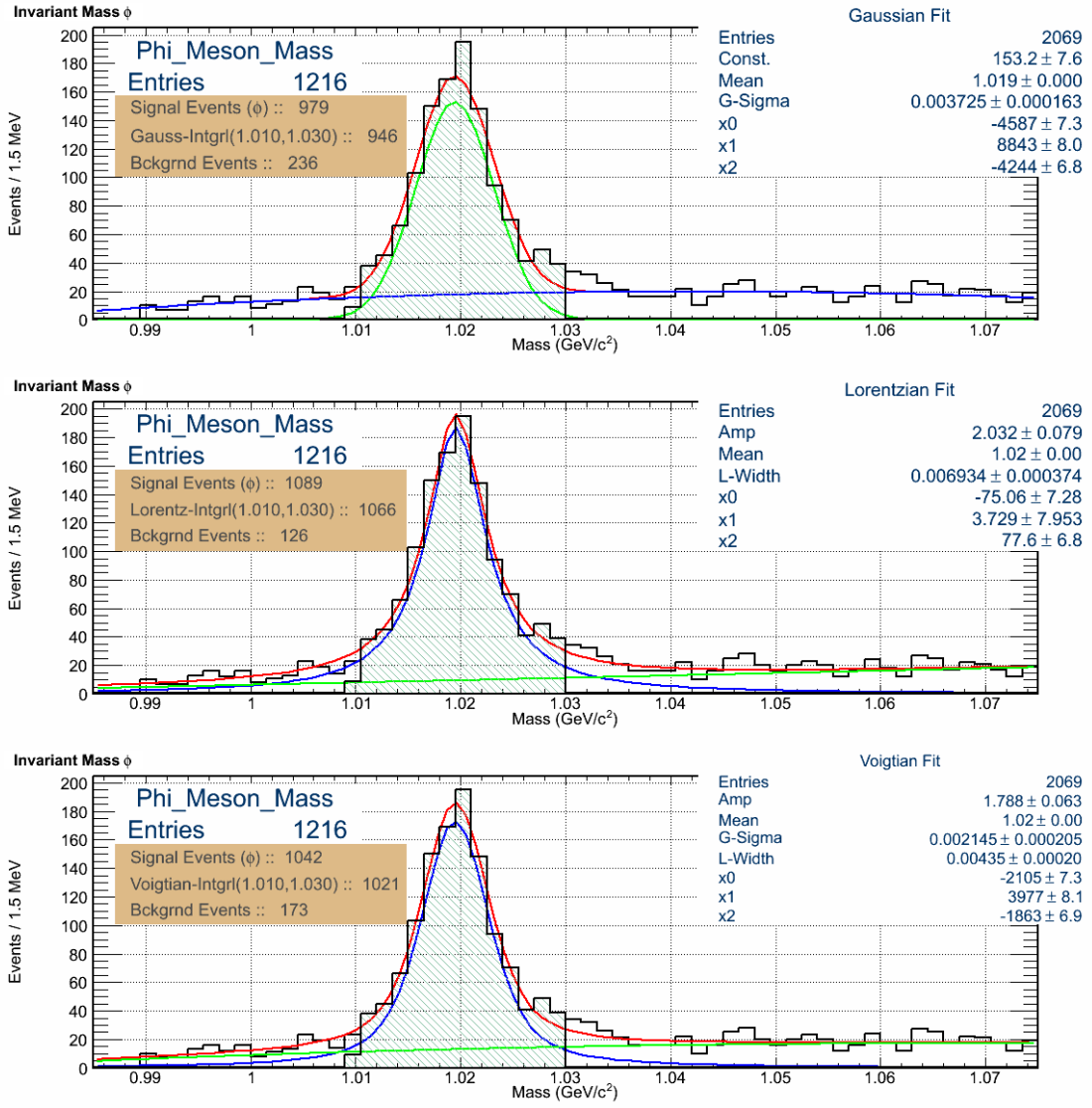

Figure 5.13: ϕ yield of g12 data for E_γ range: 4.40 - 4.55 GeV.

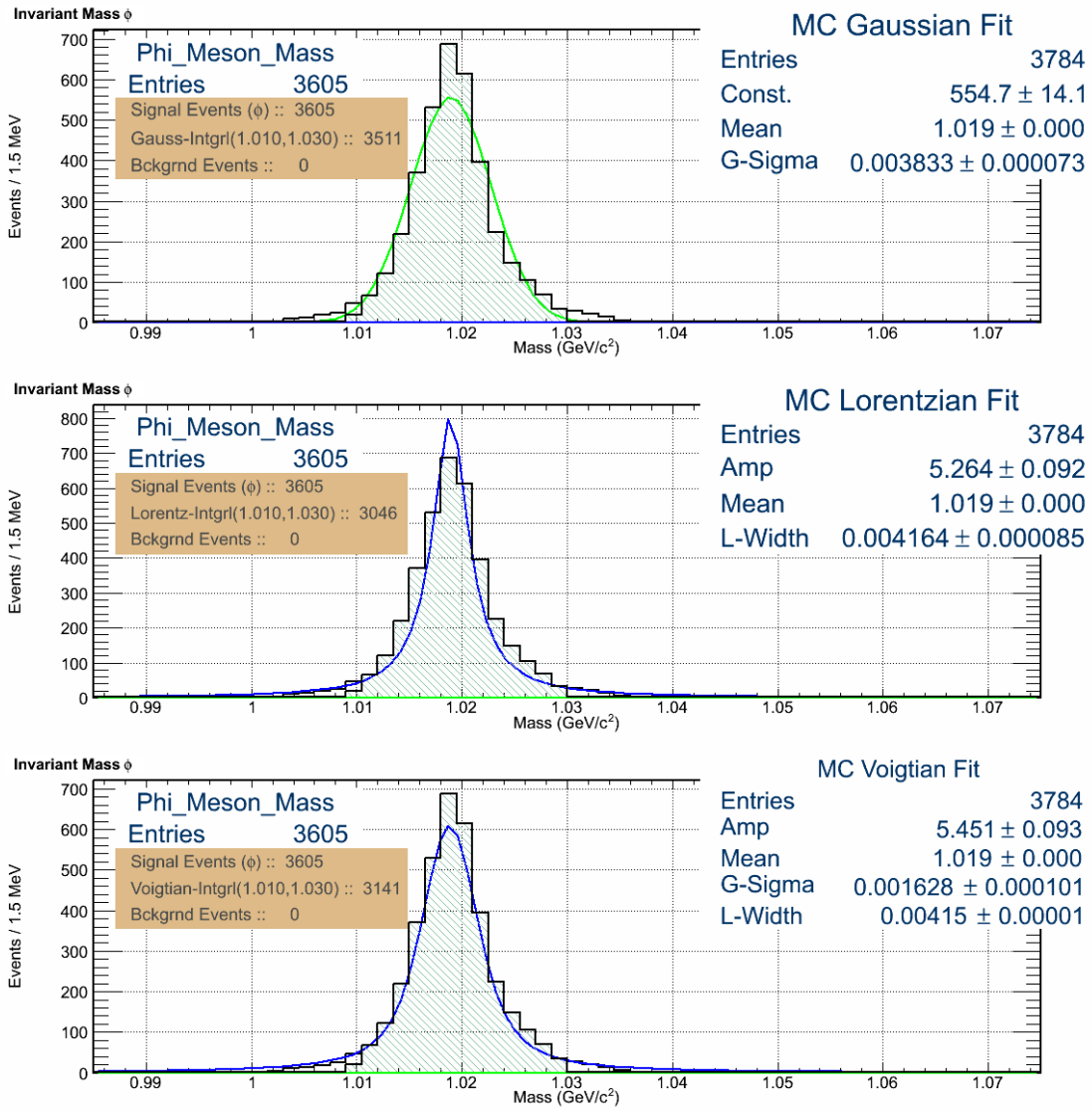

Figure 5.14: ϕ yield of MC E_γ range: 4.40 - 4.55 GeV.

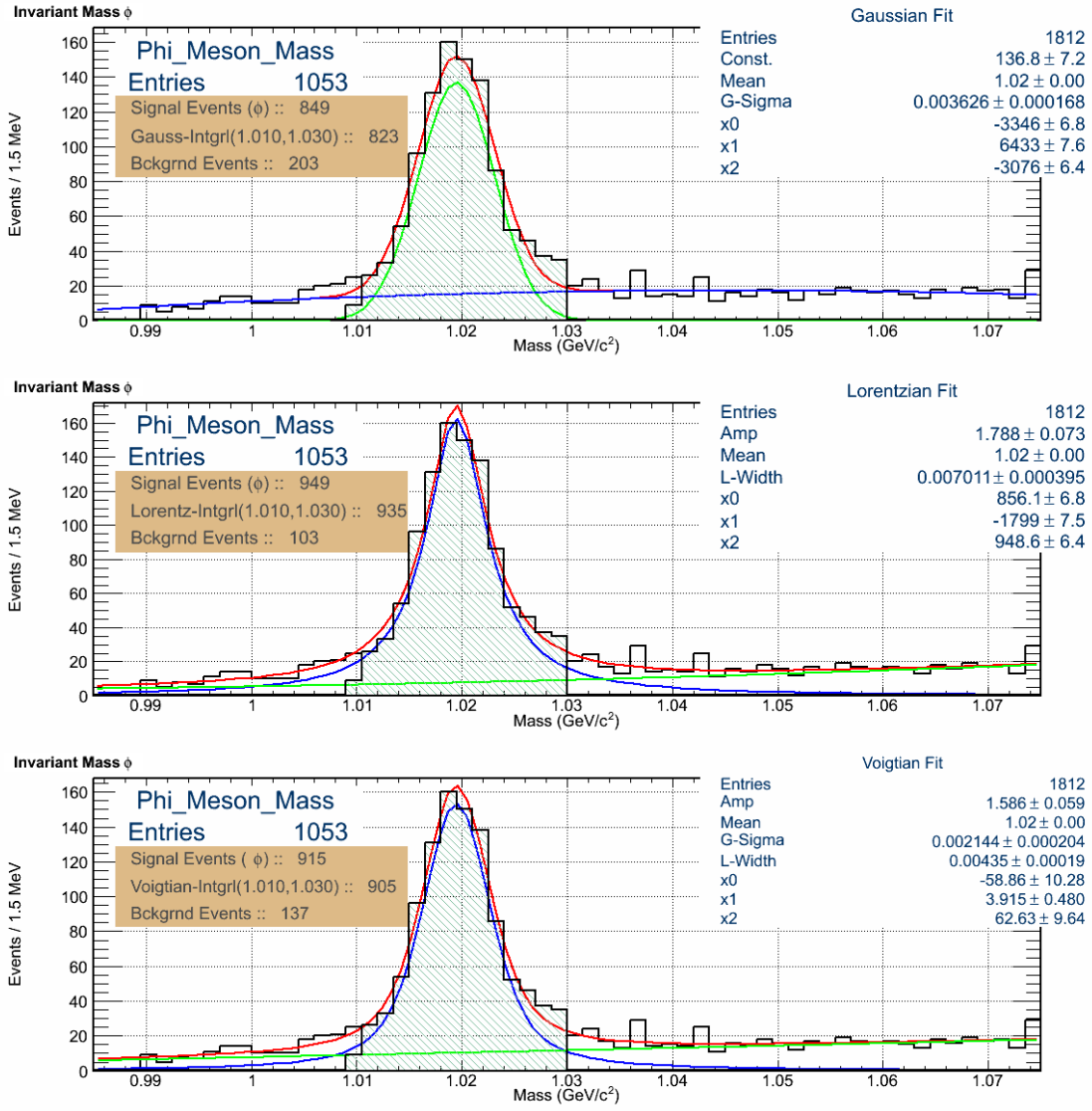

Figure 5.15: ϕ yield of g12 data for E_γ range: 4.55 - 4.70 GeV.

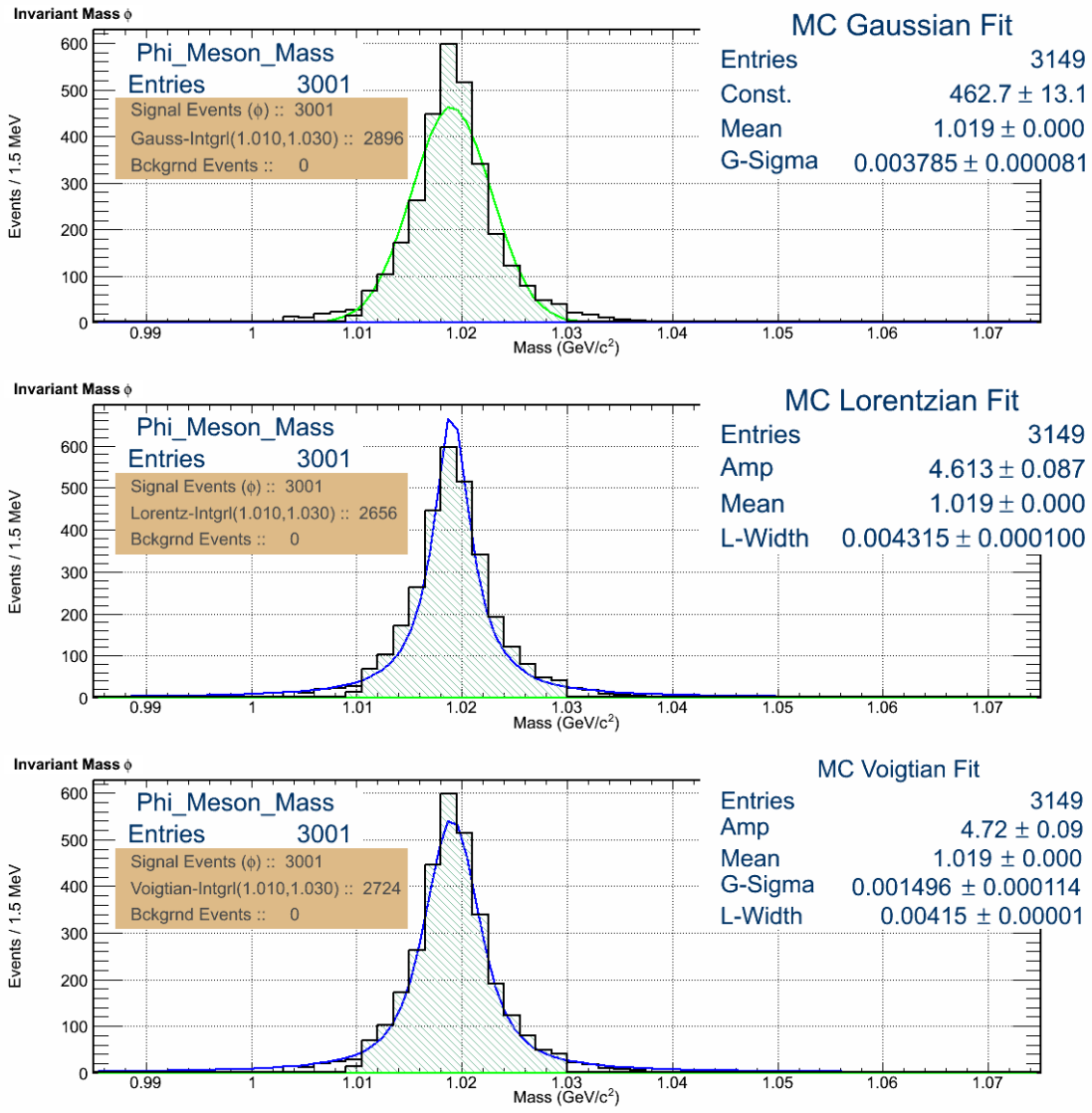

Figure 5.16: ϕ yield of MC E_γ range: 4.55 - 4.70 GeV.

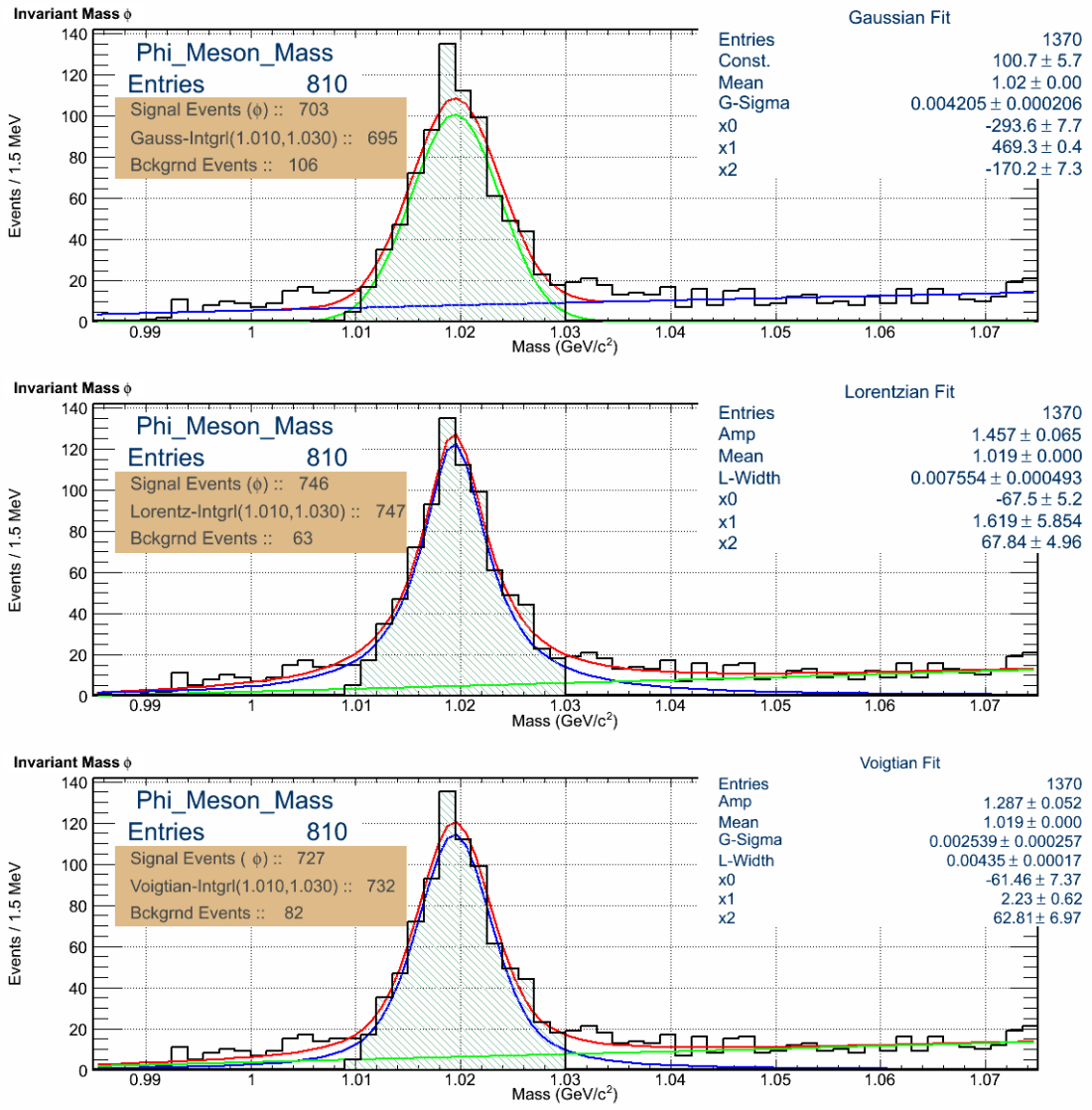

Figure 5.17: ϕ yield of g12 data for E_γ range: 4.70 - 4.85 GeV.

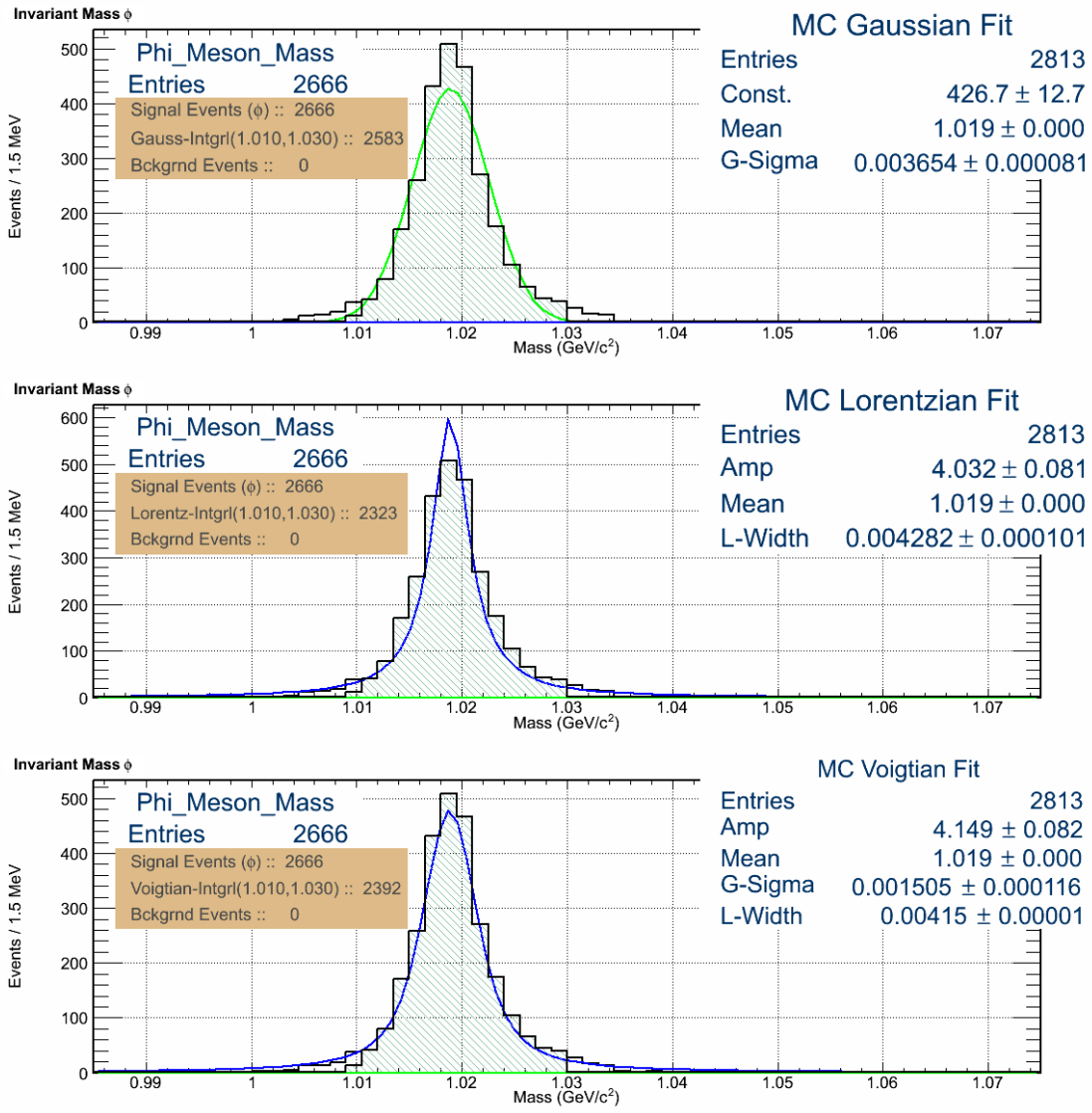

Figure 5.18: ϕ yield of MC E_γ range: 4.70 - 4.85 GeV.

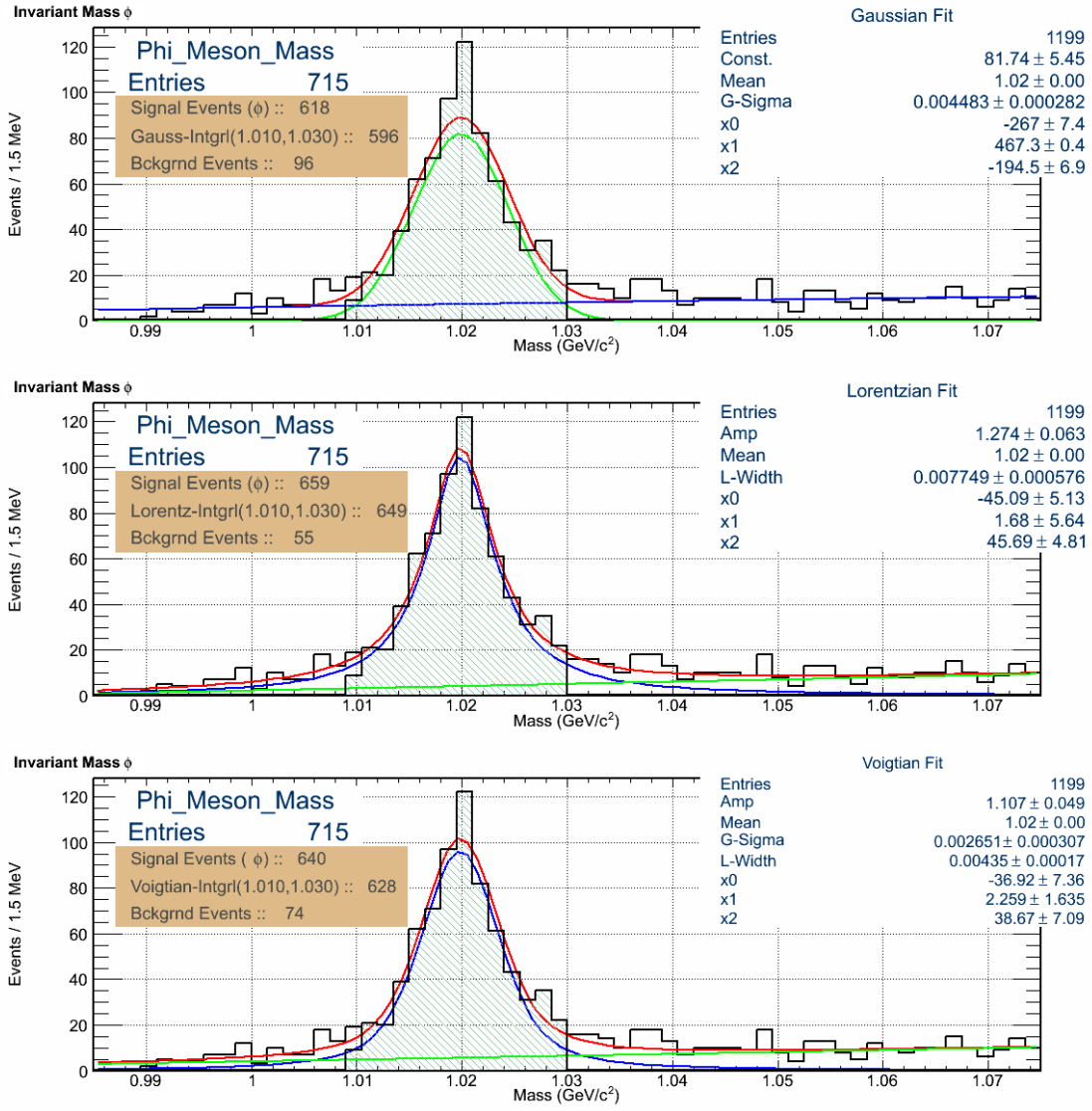

Figure 5.19: ϕ yield of g12 data for E_γ range: 4.85 - 5.00 GeV.

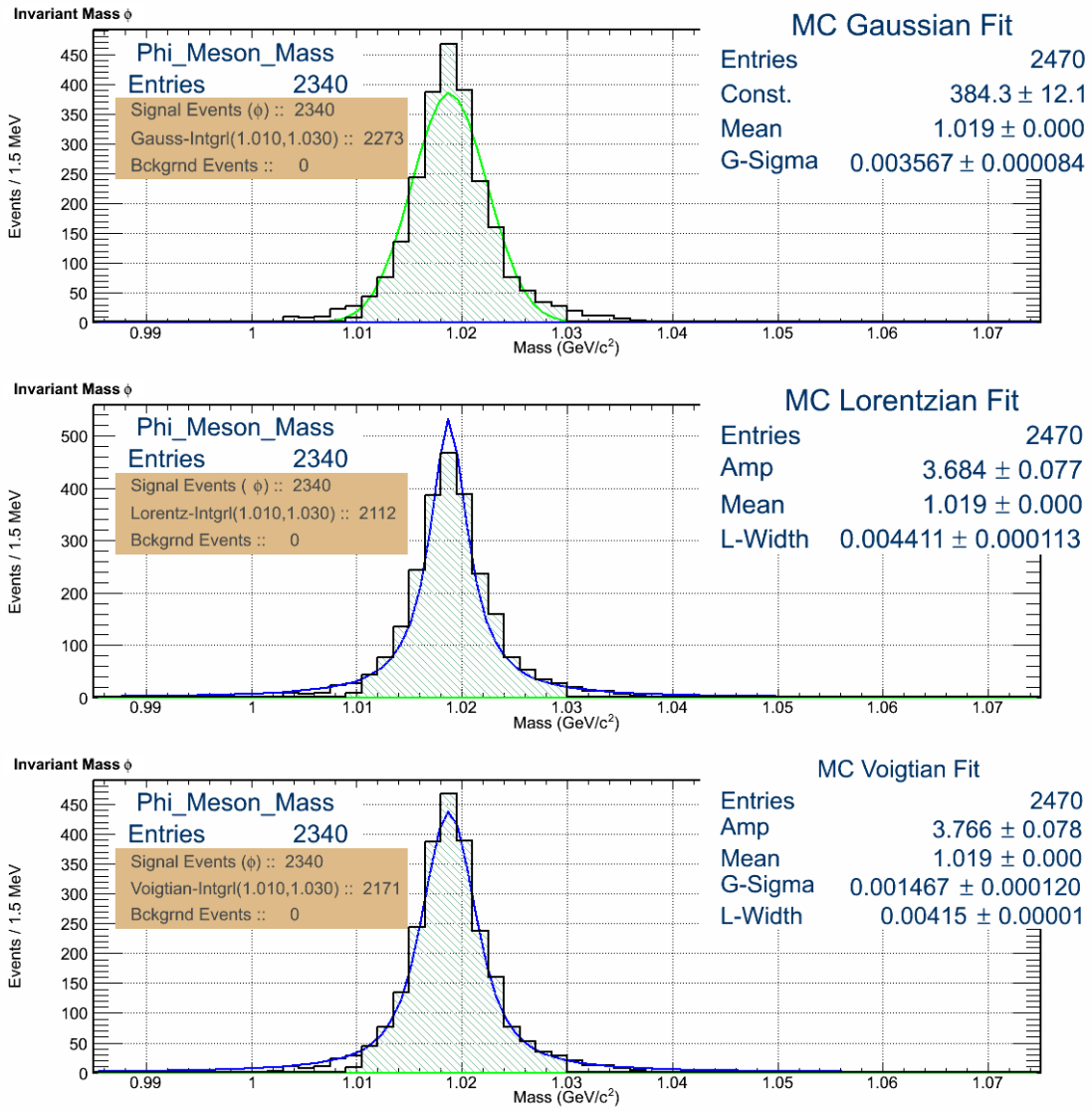

Figure 5.20: ϕ yield of MC E_γ range: 4.85 - 5.00 GeV.

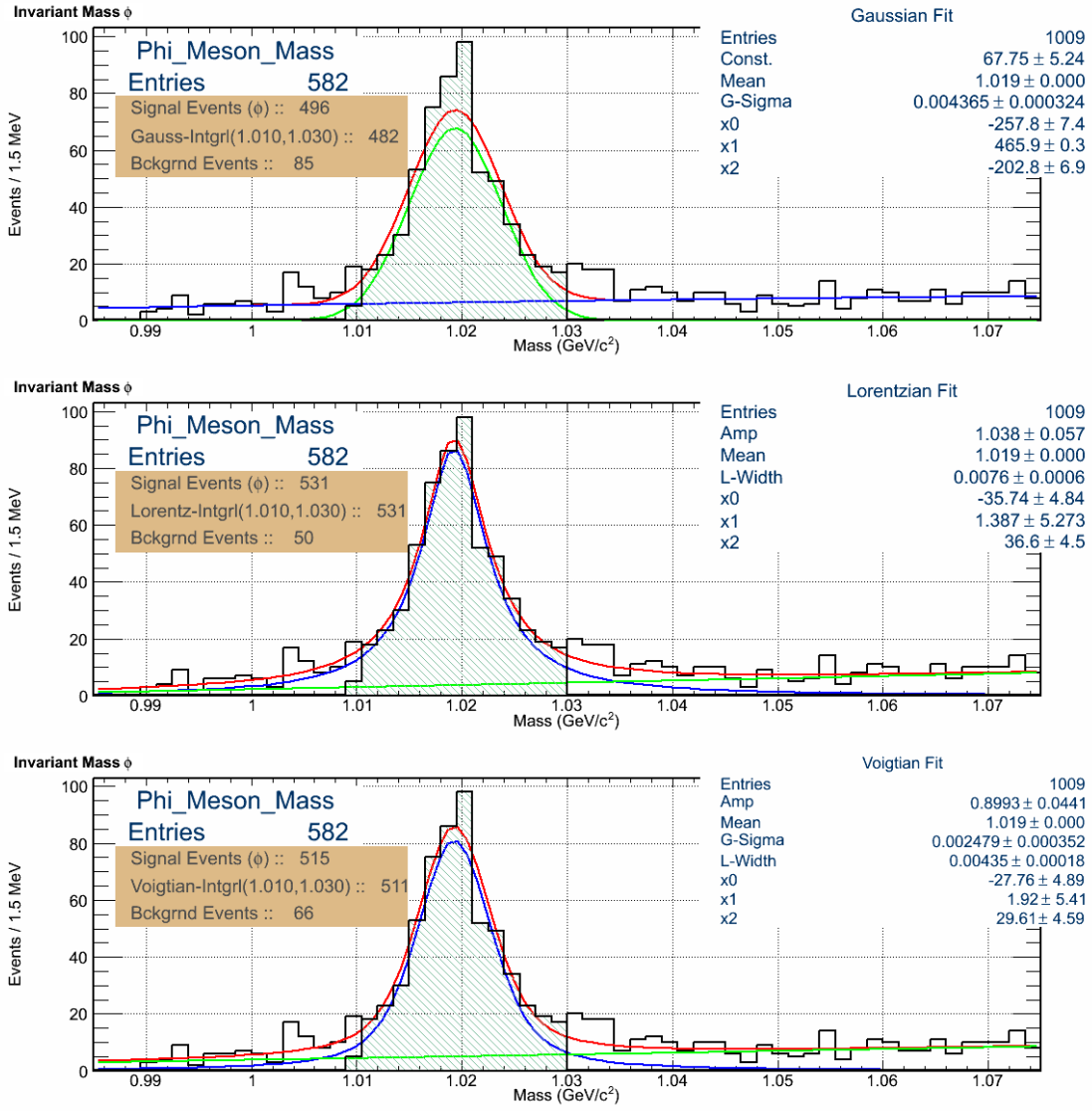

Figure 5.21: ϕ yield of g12 data for E_γ range: 5.00 - 5.15 GeV.

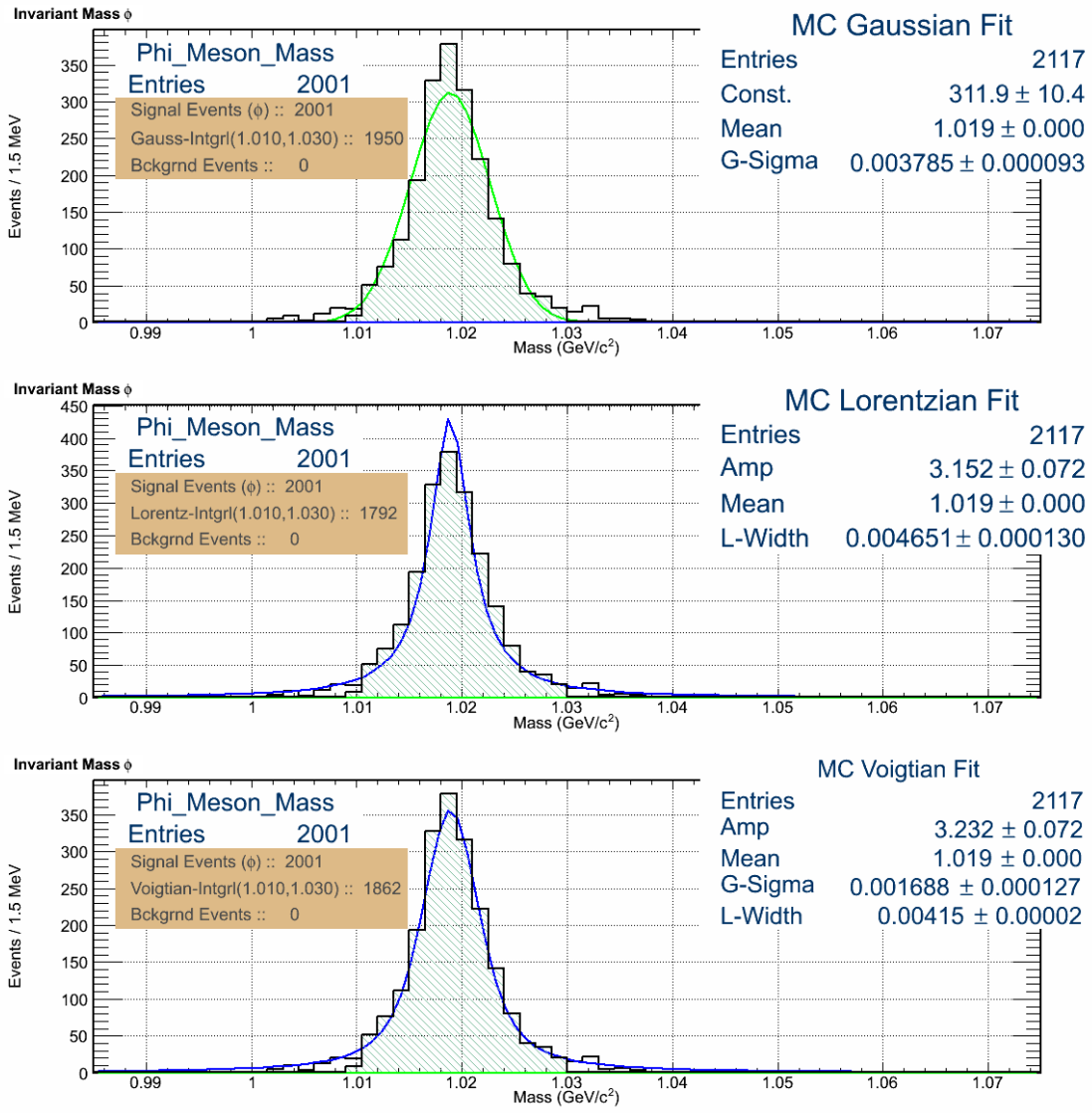

Figure 5.22: ϕ yield of MC E_γ range: 5.00 - 5.15 GeV.

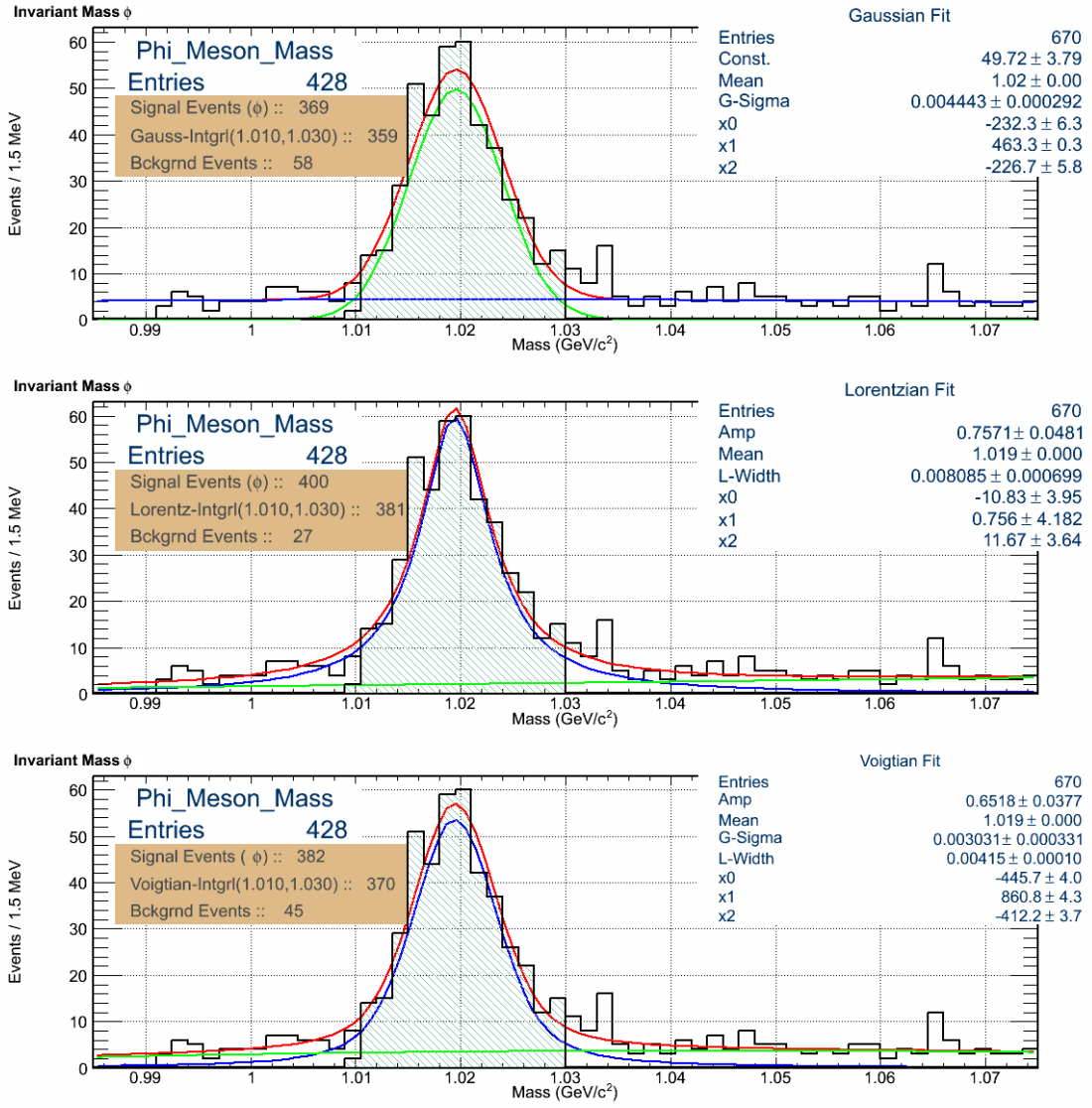

Figure 5.23: ϕ yield of g12 data for E_γ range: 5.15 - 5.30 GeV.

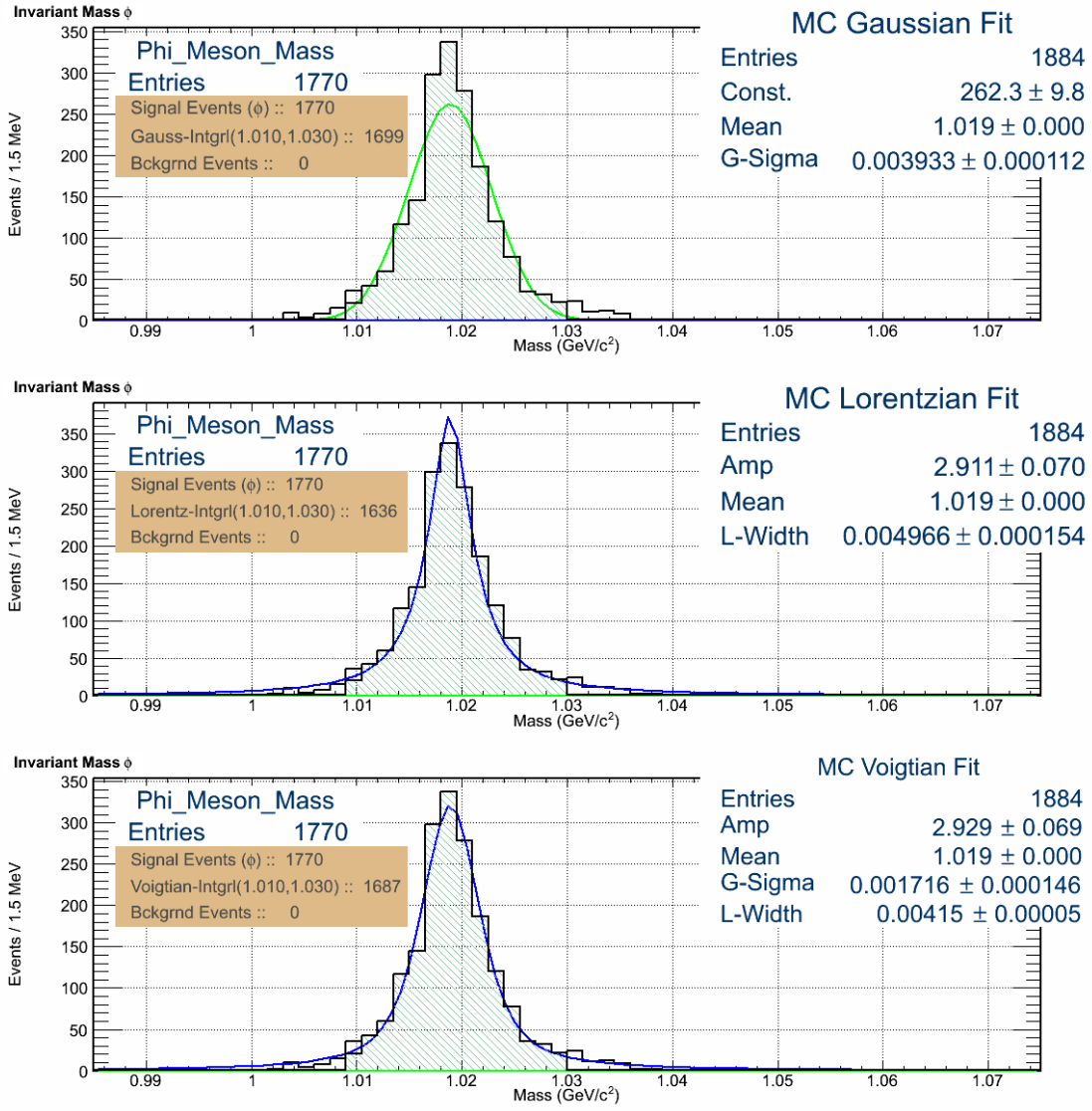

Figure 5.24: ϕ yield of MC E_γ range: 5.15 - 5.30 GeV.

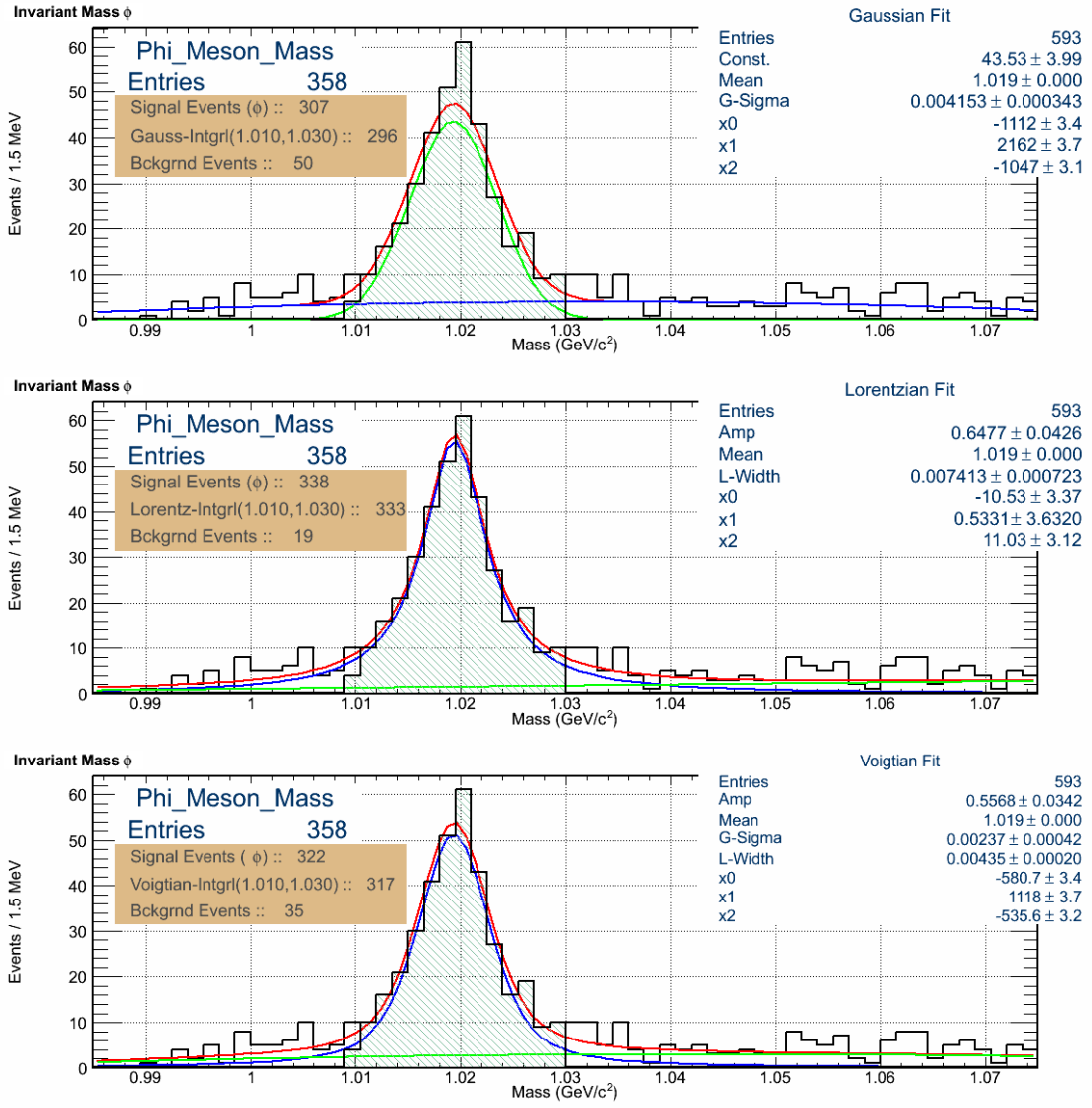

Figure 5.25: ϕ yield of g12 data for E_γ range: 5.30 - 5.45 GeV.

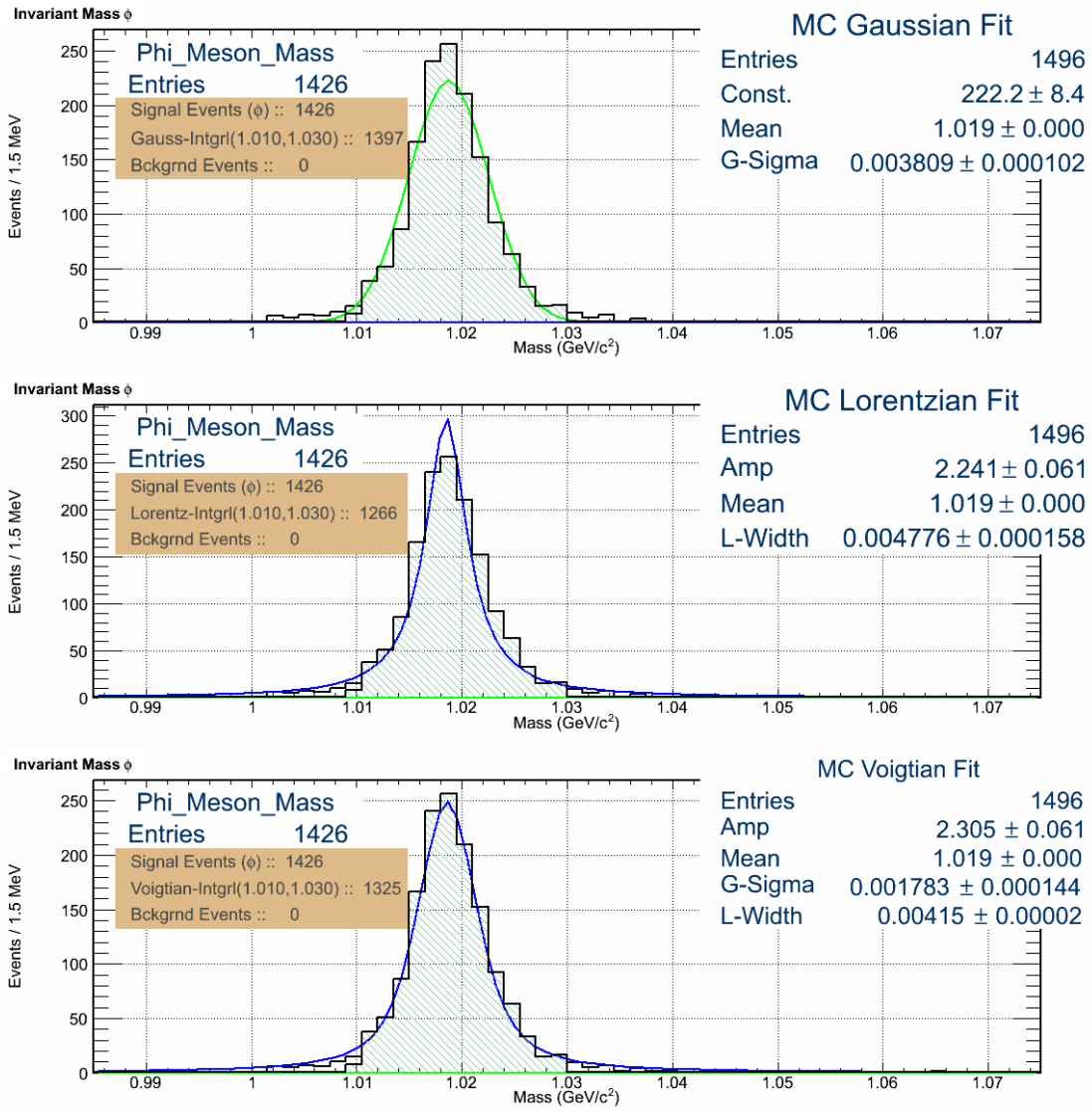

Figure 5.26: ϕ yield of MC E_γ range: 5.30 - 5.45 GeV.

Table 5.2: Data and model parameters used in cross section calculations for $\phi \rightarrow K^+K^-$ events.

E_γ Range (GeV)	E_γ flux	g12 yield	MC Accptd	MC Gnrtd	Acceptance
4.40 - 4.55	3.4224×10^{12}	1089	3605	749099	0.004812
4.55 - 4.70	3.5517×10^{12}	949	3001	750908	0.003996
4.70 - 4.85	3.1619×10^{12}	746	2666	748572	0.003561
4.85 - 5.00	3.6088×10^{12}	659	2340	751419	0.003114
5.00 - 5.15	3.4943×10^{12}	531	2001	749166	0.002671
5.15 - 5.30	3.0743×10^{12}	400	1770	750836	0.002357
5.30 - 5.45	3.4035×10^{12}	338	1426	749716	0.001902
g12 trigger range	2.1781×10^{13}	4632	16809	5249716	0.003202

Table 5.3: Cross sections, binned and total, for the g12 trigger range for $\phi \rightarrow K^+K^-$ events.

E_γ Range (GeV)	$\sigma_{\phi \rightarrow K^+K^-}$ (nb)	Corrected $\sigma_{\phi \rightarrow K^+K^-}$ (nb)	Corrected $\sigma_{\gamma p \rightarrow p\phi}$ (nb)
4.40 - 4.55	38.2040	54.7578	112.90236
4.55 - 4.70	39.0472	55.9663	115.39411
4.70 - 4.85	38.9257	55.7922	115.03514
4.85 - 5.00	33.8138	48.4653	99.92817
5.00 - 5.15	32.9633	47.2463	97.41478
5.15 - 5.30	32.2859	46.2754	95.41293
5.30 - 5.45	30.7383	44.0572	90.83933
g12 trigger range	36.7480	52.6709	108.59949

CHAPTER 6

SUMMARY

An analysis of the largest photoproduction dataset available for $E_\gamma \in \{4.40, 5.45\}$ was performed for the reaction $\gamma p \to p K^+ K^- [X]$. The main objective of this thesis was to identify strangeonium states, through an analysis of their golden decay channel - $\phi\ \eta$. No published data for the decay mode $\gamma p \to p \phi \eta$ exists. Hence, the analysis makes the first measurement of the $\phi\ \eta$ photoproduction cross section, which is calculated to be 5.8 $\pm$ 0.3 (statistical error) $\pm$ 0.7 (systematic error) nb for $E_\gamma \in \{4.40, 5.45\}$ GeV. Various invariant masses and kinematical variables were analyzed in conjunction with techniques like sideband subtraction and partial wave analysis to search for the presence of strangeonium resonances. The analysis did not observe strangeonia in the invariant $\phi\ \eta$ mass spectrum. Therefore, an upper limit to the cross section for strangeonium resonances was calculated with 90% confidence limit using Feldman-Cousins method, with two different approaches, and are presented in tables [4.8] and [4.10]. The plots [4.30] and [4.28] show the upper and the lower confidence limits of 90% for strangeonium photoproduction cross section as a function of mass for $E_\gamma \in \{4.40, 5.45\}$ GeV. The largest upper limit to the cross sections for strangeonium photoproduction of about 250 pb is observed at masses 1695 and 1965 MeV/c^2 .

The analysis is further able to comment on the status of the $\phi(1680)$ and X(1750) mesons. The $\phi(1680)$ is primarily observed in e^+e^- production in the KK^* decay mode, whereas the $X(1750)$ is primarily observed strongly in K^+K^- decay mode in photoproduction. FOCUS has claimed these to be different states but PDG still has it listed under the same state with a disclaimer. The cross section for the $X(1750) \to K^+\ K^-$ has been measured to be 8 nb at a beam energy of 45 GeV at the Omega spectrometer at SLAC [23]. The 3P0 theoretical model [3] predicts a branching ratio for $\phi\ \eta$:$K^+\ K^-$ of 1:2. As summarized in section [4.7],

the $X(1750)$ vector meson photoproduction cross section should be observed at a level of $\sim$ 2 nb or greater in the $\phi\ \eta$ decay mode. The $\phi\ \eta$ analysis, though, places the highest upper limit on the production cross section for a strangeonium resonance in the $\phi\ \eta$ decay mode in the region of 1650-1800 MeV/c^2 at 250 pb at a mass around 1695 MeV/c^2 . This is at least an order of magnitude different than the estimated cross section for the $X(1750)$, if it were the vector meson $\phi(1680)$, in the $\phi\ \eta$ decay mode. This strongly suggests that the $X(1750)$ observed in $K^+\ K^-$ is not a strangeonium resonance and is different from the strangeonium $\phi(1680)$.

Other interesting decays modes accessible to the reaction $\gamma p \rightarrow pK^+K^-[X]$ were also explored. The $X \rightarrow \phi\ \pi^o$ final state analysis is presented in section [5.1] and the $X \rightarrow \phi\ \omega$ final state in presented in section [5.2]. The analyses searched for the presence of resonances in their respective invariant masses and did not observe any resonant structure. Estimated yield for these final states for the g12 luminosity is provided to serve as a reference for future photoproduction experiments interested in these decay modes. Photoproduction cross section for ϕ meson off of proton nuclei, as a function of the incoming photon beam energy, was also calculated and is presented in chapter [5].

APPENDIX A

PARTIAL WAVE ANALYSIS OF PROTON K^+ K^- η FINAL STATE

When a decay channel like $\phi\ \eta$ is analyzed, the invariant mass spectrum observed is almost always a sum of many resonances which interfere with each other. To disentangle and extract the spin-parity of these resonances, a standard set of techniques called 'Partial Wave Analysis' (PWA) is employed.

A.1 Partial Waves

The final decay distribution of a dataset consists of multiple partial waves in general. In the rest frame of the resonance, the decomposed amplitudes for these waves can be written as:

$$U_k(\Omega) = \sum_{lm} V_{lmk} A_{lm}(\Omega) \tag{A.1}$$

where V_{lmk} stands for the production amplitude for a state $|lm\rangle$ and k represents the spin degrees of freedom for the initial and the final nucleons i.e $k = 1$ for spin-nonflip and $k = 2$ for spin-flip amplitude. $A_{lm}(\Omega)$ is the decay amplitude described in terms of Wigner D-functions and equivalent spherical harmonics as:

$$A_{lm}(\Omega) = \sqrt{\frac{2l+1}{4\pi}} {D^l_{m0}}^*(\phi, \theta, 0) = Y^m_l(\Omega) \tag{A.2}$$

where the solid angle $\Omega = (\theta, \phi)$ refers to the direction of the decay particle used as the analyzer for the decay in the rest frame of the resonance (Gottfried-Jackson frame).

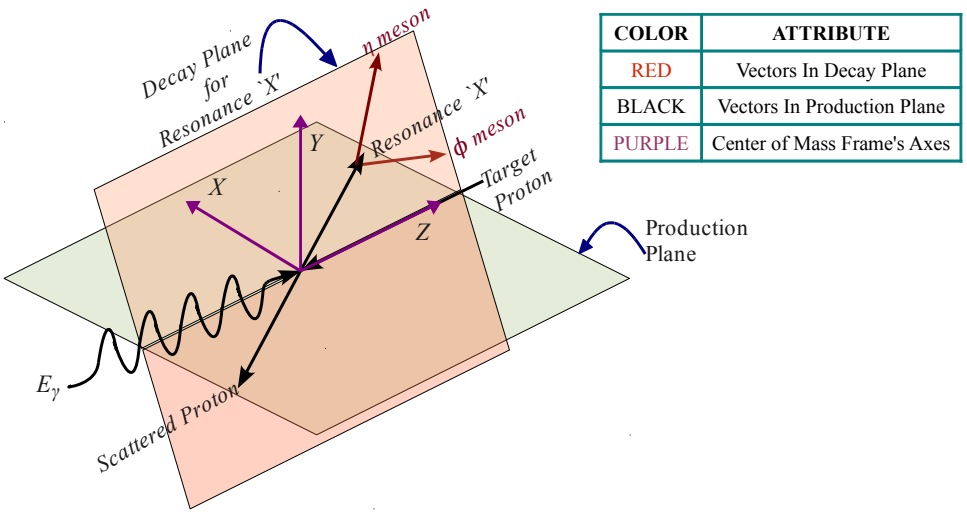

Figure A.1: Schematic of the production and the decay of a resonance 'X' into its observed final decay products K^+ K^- η via the intermediate isobar ϕ meson in the center of mass (CM) frame. The axes for CM frame are plotted. Gottfried-Jackson (GJ) frame orientation is obtained by boosting all the relevant particles to the GJ aka 'X' rest frame, keeping the direction of the boosted beam still as the z-axis, the y-axis is kept the same as the the production-normal (y-axis of the CM frame) and x-axis is simply the $y \times z$.

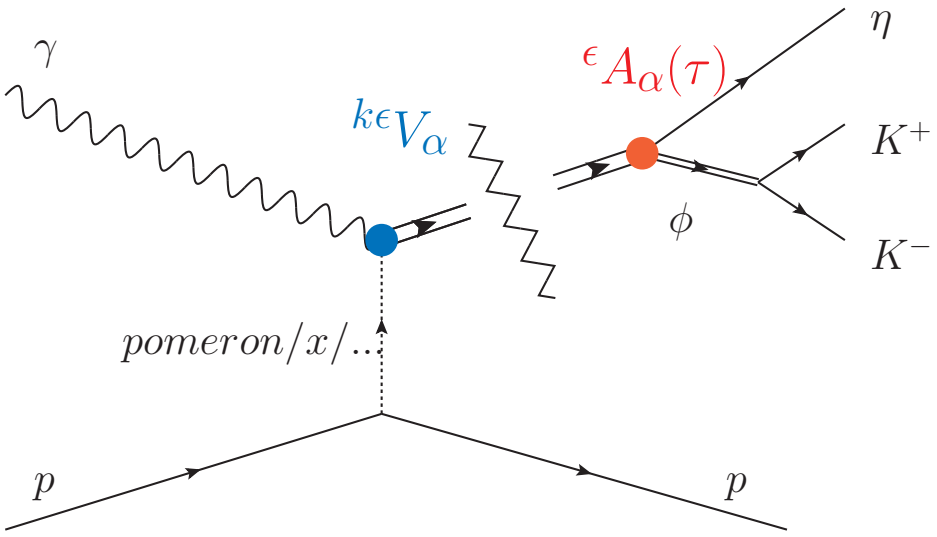

Figure A.2: Schematic of the production and the decay of a resonance 'X' in to observed final decay products K^+ K^- η via the intermediate isobar ϕ meson.

Thus the angular decay distribution (Intensity) for the resonance in the resonance rest frame (GJ) can be decomposed into its partial can be described in the form:

$$I(\Omega) = \sum_{k} \left| U_k(\Omega) \right|^2 \tag{A.3}$$

A.2 PWA Formalism

The formalism for the partial wave analysis used in the analysis is developed in detail in the reference [57]. The paper on (K K π) [56] specifically deals with the cases presented in this thesis. References [55], [58], [59], [61] and [62] provide a closer, comprehensive look at the application and the results of this approach.

Approach to a Partial Wave Analysis for a dataset can be developed using spin formalisms in a few consistent way like:

- tensor formalisms, in non-relativistic (Zemach) or covariant form
- spin-projection formalism
- Rarita-Schwinger method, where the whole formalism is based on using lorentz invariants. As a rule, operators are constructed using Mandelstam variables only.

The two popular way of performing PWA is using helicity formalism or using canonical (orbital) formalism, both are examples of tensor formalism. For this analysis, helicity formalism is employed. More detailed information about the helicity formalism and its application can be perused in "An Experimenter's Guide to the Helicity Formalism"[63].

Spin-orbit formalism is not preferred even though the total angular momentum is conserved, because the spin and the angular momentum operators are defined in their respective rest frames. For multi-particle and sequential decays, the analysis has to track it through to different frames. This gets complicated very quickly. Whereas in Helicity formalism, the helicity operator ($\bar{h} = \bar{S}.\hat{p}$) is invariant under rotations, as well as boosts for relativistic baryonic systems. Consequently relativistically lorentz invariant eigenstates of helicity (h), with either total angular momentum (J) or momentum (p), can be constructed.

Helicity is a good quantum number in strong interaction for a resonant state, however, it does not play well with the parity operator (P). Pure helicity eigenstates are found to not

conserve parity. And since all strong interactions conserve parity, even for sequential decay, the resonant state is described in terms of a linear combination of pure helicity eigenstates such that they conserve parity and order is restored.

The following conventions is used to restore parity. Reflectivity Operator is defined as:

$$\hat{\epsilon} = \hat{P} e^{i\pi J_y} \tag{A.4}$$

where J_y is the usual rotation operator about the y-axis. The $\hat{\epsilon}$ operator reflects a vector about the defined production plane x-z.

Using this operator the reflectivity basis is constructed as:

$$|\bar{p}\epsilon PJM\rangle = \theta(m) \left\{ |\bar{p}PJM\rangle + \epsilon P(-1)^{J\text{-}M} |\bar{p}PJ - M\rangle \right\} \tag{A.5}$$

where,

$$\begin{aligned} \theta(m) &= \frac{1}{\sqrt{2}} \; for \; m > 0; \\ \theta(m) &= \frac{1}{2} \; for \; m = 0; \\ \theta(m) &= 0 \; for \; m < 0. \end{aligned}$$

Observe that for positive reflectivities, m=0 states are not allowed. To get rid of arbitrary selection of the reflectivity for a state, the reflectivity quantum number is chosen such that it coincides with the naturality (N) of the exchanged particle. Reflectivity (ϵ) / Naturality (N) for a particle, in this case, by definition is:

$$\epsilon = N = P(-1^J) \tag{A.6}$$

hence the following holds true,

$$\begin{aligned} \text{Natural parity exchange } \epsilon = 1; \qquad J^P &= 0^+, 1^-, 2^+, \ldots \\ \text{Unnatural parity exchange } \epsilon = \text{-1}; \qquad J^P &= 0^-, 1^+, 2^-, \ldots \end{aligned}$$

As an added advantage, states of different reflectivities/naturalities do not interfere. Therefore, equation [A.1] can be rewritten and expanded in terms of the helicity basis, while enforcing parity conservation, as:

$$^{\epsilon}U_k(\Omega) = \sum_{lm} \epsilon V_{lmk} \sqrt{\frac{2l+1}{4\pi}}\, ^{\epsilon}D^{l}_{m0}{}^{*}(\phi, \theta, 0) \tag{A.7}$$

$$I(\Omega) = \sum_{\epsilon k} \left|^{\epsilon}U_k(\Omega)\right|^2 = \left|^{+}U_1(\Omega)\right|^2 + \left|^{-}U_1(\Omega)\right|^2 + \left|^{+}U_2(\Omega)\right|^2 + \left|^{-}U_2(\Omega)\right|^2 \tag{A.8}$$

Thus separating out the observed decay distribution in terms of the helicities (+,-) and the rank($k = 1, 2$) in the helicity basis.

The thesis analysis assumes that the produced state ($X \rightarrow \phi\ \eta$) recoils off of the target proton diffractively, where the ϕ as the intermediate isobar decays to ($K^+\ K^-$) as depicted in figures [A.2], [A.1].

Hence the sequential production and decay of 'X' gives us:

$$X \quad \rightarrow \quad \phi\ \eta \quad \rightarrow \quad K^+\ K^-\ \eta \tag{A.9}$$

where the scattering/transition matrix for the reaction can be expressed in terms of the kinematical variables (τ), decay(A_α) and production (V_α) amplitudes as:

$$\mathcal{M} = \sum_{\alpha,\phi} \underbrace{\langle K^+K^-\ \eta\ p|\, \hat{T}_d^{\phi \rightarrow K^+K^-}\, |\phi\ \eta\ p\rangle\, \langle \phi\ \eta\ p|\, \hat{T}_d^{X \rightarrow \phi\eta}\, |X_\alpha\ p\rangle}_{Decay - A_\alpha(\tau)} \underbrace{\langle X_\alpha\ p|\, \hat{T}_p\, |\gamma p\rangle}_{Production - V_\alpha} \tag{A.10}$$

The decay waveset 'α' should include in theory all possible decay mechanisms (a complete set), but this requires an infinite number of waves. Practically only states of lower angular momentum is accessible due to the energy cost of the angular momentum barrier. Hence the description for the observed intensity distribution is expressed only in terms of a reduced set. Table [A.1]) is optimized to describe the observed data. The intensity distribution is now expressed as:

$$I(\tau) \propto \sum_k \left| \sum_\alpha V_{k\alpha} A_\alpha(\tau) \right|^2 \tag{A.11}$$

where k is referred to as the rank of the interaction , the number of possible external spin-flip configurations for the baryon-meson interaction. The sum over k is a incoherent sum while the sum over α is a coherent sum over the partial waves and hence includes the interference between these waves. Each partial wave of the waveset 'α' represents the following set of kinematical parameters:

$$\alpha \ \forall \ \{J, P, C, M, L, l, (w, \Gamma)\} \tag{A.12}$$

where,

J	=	Total angular momentum of resonance 'X'
P	=	Parity of the resonance 'X'
C	=	Charge conjugation parity for the resonance 'X'
M	=	Z-projection of the total angular momentum
L	=	Angular momentum between the ϕ and the η meson
l	=	Angular momentum between the decay products of ϕ
(w, Γ)	=	Mass and width parameter for the Breit-Wigner

The decay amplitude A_α for a partial wave is calculated using the information provided in the form of the four-vectors for all the final state particles, and the dynamics specified (τ) in the wave file of the partial wave. This is calculated by a utility called 'gamp' and uses Wigner D-functions to form and follow the physics specified in the wave file, through various frames, to arrive at a value for the amplitude for that event, to have been decomposed into that wave.

The production amplitude V_α for a partial wave is the strength that the particular partial wave must have had, to give the observed distribution, in conjunction with the other waves of the waveset. This is the physics the analysis is looking for, the production strength for particular waves (J^{PC}). This is what the analysis seeks to obtain from a partial wave analysis, the decomposition of the observed decay distribution into the partial waves (and their relative strengths) that produced that distribution.

To obtain the true production amplitudes for a distribution correctly, the analysis has to account for the acceptance of the experiment. This is done by including the acceptance

effects into the fit function that is minimized to estimate these production amplitudes. This fit function is called the 'Likelihood Function' and and as the name suggests calculates the likelihood for a scenario on an event by event basis. The technique used is the 'Extended Maximum Likelihood Method'.

A.2.1 Extended Maximum Likelihood Method

The likelihood function uses the information from the decay products, for a given set of events, to parametrize the physics/dynamics of the input model as follows:

$$\mathcal{L} \propto \left[\frac{\bar{n}^n}{n!}e^{-n}\right] \prod_i^n \left[\frac{I(\tau_i)}{\int I(\tau)\eta(\tau)pqd\tau}\right] \tag{A.13}$$

where,

$\mathcal{L}$ *is* the likelihood function,

n *is* the number of events observed,

$\bar{n}$ *is* the average number of events observed if the experiment was ran multiple times,

$\eta(\tau)$ *is* the finite experimental acceptance as determined by the Monte Carlo simulations,

$pqd\tau$ *is* the lorentz invariant phase space element for the involved kinematics.

The term in the 1^{st} square bracket represents the 'Poisson probability' for finding n events for the described kinematics (mass bin in this case), and the average/expectation value '$\bar{n}$' is defined as:

$$\bar{n} \propto \int I(\tau)\eta(\tau)pq(d\tau) \tag{A.14}$$

The denominator of the product term (2^{nd} bracket) of the likelihood function (equation [A.13]) is the normalization term over the resonance mass bin and the $\eta(\tau)$ is the acceptance determined by the simulation, which have the same selection criteria as the data applied to it. Once the acceptance is accounted for in this manner, the yield/strength for a partial wave obtained is the acceptance corrected strength.

The likelihood function in the form of equation [A.13], when iterated over a large number of events grows quickly to very large values. A standard way of tacking is to simply use a

logarithmic version of the equation [A.13], which increases in value logarithmically slower. Another thing to consider is that the function described in equation [A.13] is a positive quantity, and MINUIT is a minimizer. This is dealt with by minimizing the likelihood function in its negative logarithmic form (-ln($\mathcal{L}$)) so that the largest likelihood value gives the least value for the fit function when minimized by MINUIT. Equation [A.13] is rewritten as:

$$ln\mathcal{L} \propto \sum_{i}^{n} ln(I(\tau_i)) - \int I(\tau)\eta(\tau)pqd\tau \tag{A.15}$$

$$\propto \sum_{k\epsilon\alpha\alpha'} ln\big({}^{\epsilon}V_{\alpha k}\, {}^{\epsilon}V^{*}_{\alpha' k}\, {}^{\epsilon}A_{\alpha}(\tau_i)\, {}^{\epsilon}A^{*}_{\alpha'}(\tau_i)\big) - \eta_x\Big(\sum_{k\epsilon\alpha\alpha'} {}^{\epsilon}V_{\alpha k}\, {}^{\epsilon}V^{*}_{\alpha' k}\, {}^{\epsilon}\psi^{a}_{\alpha\alpha'}\Big) \tag{A.16}$$

Where η_x is the detector/experiments acceptance function calculated using a straightforward ratio as:

$$\eta_x = \frac{\text{MC Events Accepted}}{\text{Raw MC Events Generated}} \tag{A.17}$$

And ${}^{\epsilon}\psi^{a}_{\alpha\alpha'}$ represents the normalization integral calculated from phase space MC simulation for N_a accepted events as:

$${}^{\epsilon}\psi^{a}_{\alpha\alpha'} = \frac{1}{N_a}\sum_{i}^{N_a} {}^{\epsilon}A_{\alpha}(\tau_i)\, {}^{\epsilon}A^{*}_{\alpha'}(\tau_i) \tag{A.18}$$

And using these statistics, the number of events (acceptance corrected yield) as predicted by the PWA fit is:

$$N = \sum_{k\epsilon\alpha\alpha'} {}^{\epsilon}V_{\alpha k}\, {}^{\epsilon}V^{*}_{\alpha' k}\, {}^{\epsilon}\psi^{r}_{\alpha\alpha'} \tag{A.19}$$

Where, ${}^{\epsilon}\psi^{r}_{\alpha\alpha'}$ is the normalization integral calculated using the generated raw Monte Carlo events for the given resonance mass bin under consideration.

To arrive at these production amplitudes, a combination of tools is used. Some of them have been mentioned and will now reiterate for completeness, along with a short step by step guide to performing a PWA.

A.3 Technique

For this analysis, majority of the PWA tools were developed by Dr. Paul Eugenio at FSU. They have a lot in common with the 'E852' experiments' approach to partial wave analysis. Additional software tools were developed for consistency checks performed on simulated results to verify the effectiveness of the analysis. The PWA toolkit uses the information from the angular distributions of the final decay products in the rest frame of the resonance, referred to as the Gottfried-Jackson (GJ) frame with a predefined prescription for determining the GJ frame axes. The toolkit requires as input an optimal set of waves that the user assumes, with physics justifications, to have contributed to the observed invariant mass distribution. These waves use the intermediate isobar model, to model the decay of the resonance to the observed final decay products, decaying through the intermediate isobars ($\phi \rightarrow K^+ K^-$, in the case of $\phi\ \eta$) in all possible quantum mechanically allowed states. These decay mechanisms are encoded into input wave files, which describe the relative angular momentum between the decay products, their intermediate isobars, the decay chain and the associated quantum number at every step of the chain. A wave with a particular set of quantum numbers has a preferential decay distribution in space. For example, S wave decay is isotropic, while a decay in an L wave with M=0 projection is azimuthally uniform in space, and so on. These decay distributions are dealt with, in our PWA, using Wigner D-functions, which helps translate a decay distribution from one frame of reference to another in a consistent, useful manner. This redefines the problem of finding the quantum numbers of the resonances in our distribution, to a problem of identifying the right set and production amplitudes for the individual waves into their final decay products, such that the angular distributions for the assumed waves is the same as that observed in the experimental distributions. Strictly speaking, since the waves under consideration are all orthogonal, the angular distributions for a particular set of waves and amplitude should be unique. But given the experimental acceptance as well as resolution, it is completely possible to arrive at ambiguous solutions for the waveset and production amplitudes. To achieve the quantum numbers for the resonances in the decay distributions, the analysis parametrizes the production amplitudes for the waves and then fits the input data decay distribution, to the supplied wavesets' expected decay distribution using 'MINUIT'. The

best fit would be achieved when the production amplitudes for all the waves in the waveset best describe the observed distribution. This best description is achieved by using the method of 'extended maximum likelihood' discussed in section [A.2.1]. Minuit is a versatile numerical minimization program provided by CERN, that handles the fitting as well as the error calculation for the fits, in a comprehensive manner.

The invariant mass spectrum observed is assumed to be constructed of multiple resonances that satisfy the quantum mechanical relationships governing the hadronic states due to the nature of strong interaction like conservation of angular momentum (J), Parity (P) and charge conjugation (C). The analysis builds all the possible states from the final decay products that could have contributed to the decay channel with all possible allowed permutations of J,P, and C. An infinite number of such permutations are theoretically possible, hence the analysis takes into account the energy cost for creating such states, for very high angular momentum on account of the angular momentum barrier factor, and only consider the low values of 'J' as contributing to our observed decay spectrum. In this analysis, keeping in mind the energy available to our ϕ η system, the analysis can safely consider the J-value=4, as being the highest accessible momentum for the resonance.

The analysis considers the states listed in table [A.1] to be accessible to our experiment. The states for the PWA are referred to in the format (JPCMRL), where 'J' is the angular momentum for the resonance, 'P' is the parity of the resonance, 'C' is the charge conjugation parity of the resonance, 'M' is the projection of J for that resonance, 'R' is the reflectivity of the resonance and is the result of way the wavefunction is formulated for the resonance and 'L' is the orbital angular momentum between the decay products/isobars.

A.4 PWA procedure

1. Decide on the selection criteria and obtain a list of events that contribute to the observed decay distribution you want to decompose.
2. Obtain the final state four-vectors for all the selected events.
3. Create a model waveset that contains the physics and the dynamics expected in the observed decay distribution. This is a highly iterative, trial and error process.
4. Divide the events according to their resonance 'X' mass and calculate the decay amplitudes for these events using the model waveset.

Table A.1: Waves considered to have contributed to the observed ($\phi\ \eta$) invariant mass distribution in our analysis.

Waves of $+^{ve}$ reflectivity
$0-\,-0+P$
$1+\,-0+D$
$1+\,-0+S$
$1+\,-1+D$
$1-\,-1+P$
$1+\,-1+S$
$2-\,-0+F$
$2-\,-0+P$
$2+\,-1+D$
$2-\,-1+F$
$2-\,-1+P$
$2+\,-2+D$
$2-\,-2+F$
$2-\,-2+P$
$3+\,-0+D$
$3+\,-1+D$
$3-\,-1+F$
$3+\,-2+D$
$3-\,-2+F$
$3+\,-3+D$
$3-\,-3+F$
$4-\,-0+F$
$4-\,-1+F$
$4-\,-2+F$
$4-\,-3+F$
$4-\,-4+F$

Waves of $-^{ve}$ reflectivity
$1-\,-0-P$
$1+\,-1-D$
$1-\,-1-P$
$1+\,-1-S$
$2+\,-0-D$
$2+\,-1-D$
$2-\,-1-F$
$2-\,-1-P$
$2+\,-2-D$
$2-\,-2-F$
$2-\,-2-P$
$3-\,-0-F$
$3+\,-1-D$
$3-\,-1-F$
$3+\,-2-D$
$3-\,-2-F$
$3+\,-3-D$
$3-\,-3-F$
$4-\,-2-F$
$4-\,-1-F$
$4-\,-3-F$
$4-\,-4-F$

5. Decide on the likelihood function, parametrized in terms of the production amplitudes to be found, that is to be used to calculate the production strengths for the waves of the input waveset. Incorporate the simulations in your likelihood function to model for the acceptance of your detector/experiment.

6. Minimizer the likelihood function, using tools like 'MINUIT' to arrive at the most probable set of production amplitudes for your particular model. Check for inconsistencies, ambiguities and in general perform quality checks.

7. Validate the model used, by weighing simulations with the estimated production amplitudes. Verify that the kinematics thus generated are similar to the observed kinematics within reasonable errors and assumptions.

A.5 PWA Fits

The Partial wave analysis performed here was done keeping in consideration the low statistics and abundance of background in the selected decay distribution. Due to these limitations, the analysis initially divided the entire $\phi\ \eta$ data in 100 MeV bins starting at 1500 MeV. The said data was again rebinned in 100 MeV bins; this time starting at 1550 MeV, thus shifting the bin edges 50 MeV from the edges of the previous binning. This technique counts most of the events twice (except for the edge bins). The method gives us a smoothened, higher statistic, binned data in 50 MeV bins, increasing the probability of getting better fit results.

The analysis also included a flat background wave to simulate and absorb the abundant background beneath the $\phi\ \eta$ events for the PWA fit. The sideband-subtraction analysis estimates the background to be at the level of 60%. The analysis presents only the fits for the reduced set outlined in table [A.2] here. All spin projections greater than 1 were discarded (from table [A.1]), as they are not expected due to helicity conservation.

Another variable that was accounted for in the analysis, was the effect of choice of the initial starting bin for the PWA fit. The analysis assumes a smooth distribution in the amplitude space for the data and hence uses the final fit results from one bin as the initial starting values for the next neighboring bin fit. Fits were performed where the initial bin to be fit was taken to be from the middle of the distribution (Bin Center = 1.950 MeV). The fit values for the complex amplitude obtained for this bin were then used as the initial

fit parameters for the neighboring bins, cascading towards the edge bins. Other fits were started from the higher mass bin with the fits cascading to the lower mass bins and the other way around. All these fits agreed very well with each other, irrespective of the chosen starting bin for the fit.

Yet another variation that was accounted for in the analysis, was the effect of the starting values for a given PWA fit. Fits were performed where the initial values for all the free parameters were all taken to be 1 and then 0.1. The final fit parameters thus obtained agreed with each other within errors.

Since there were a multitudes of PWA fits performed, only the analysis for a reduced waveset (table[A.2]) is presented in this thesis for reference. The analyses start the fits from the region of the central bins (Bin Center = 1.900 MeV).

Notes: The production amplitudes from the PWA fits all agreed in magnitude within the errors - some of them had their relative signs flipped. Fixing the phase for each of the helicity was important to achieve proper fits; otherwise there was too much freedom in the fit and the fits did not converge. When the simulations were weighed with the production amplitudes from the fits, the best reproduction of the data kinematics was obtained when the analysis had a larger number of waves in the waveset. This is expected due to better description of the data when using larger number of waves to describe it. A sideband subtraction PWA fit using a modified likelihood function to account for the subtraction was also performed, but these fits did not converge. These incomplete results are not presented in the thesis.

The results are ambiguous for most waves, as observed in figure [A.3]. In this PWA presented, a total of '13-3=10' free parameters were used to fit the $\phi\,\eta$ distribution. For each wave, there are 2 free parameters, one real and one imaginary for the complex production amplitude. For each set of waves of a given helicity, the analysis has the freedom to fix the phase of one of the dominant waves. The phase for a given wave is arbitrary but the phase difference between the waves is not. Figure [A.3] represents the fit for the waveset presented in table [A.2] along with a background wave uniform in angular distribution (flat) in the resonance mass frame. The analysis notices the 2 - - wave to be strong and present in many combinations analyzed. This observation when taken along with the yield errors and instability in the fits for other waves does not allow for a robust conclusion. Since these

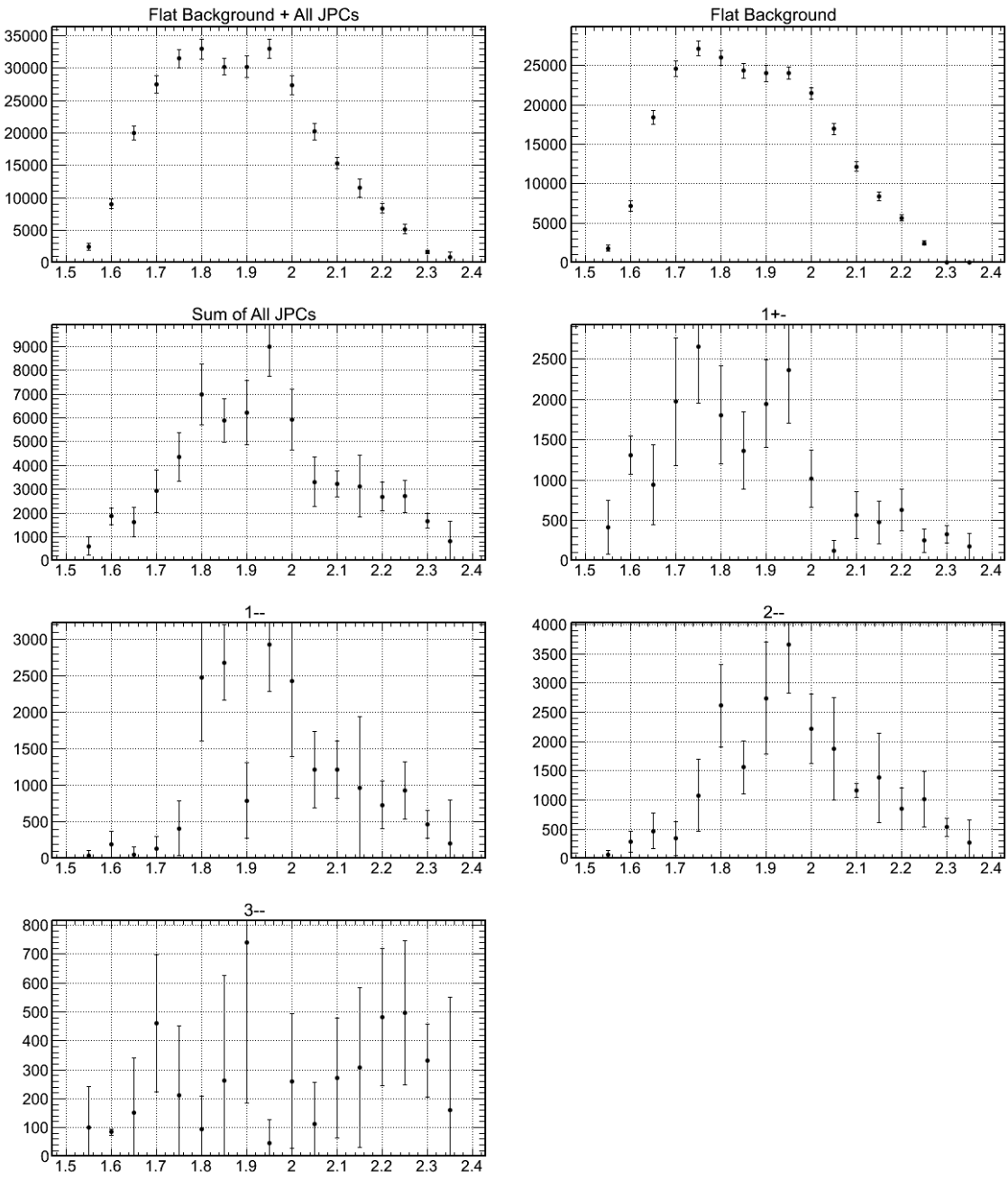

Figure A.3: Flat background distribution and various individual JPC decay distributions summed over their individual waves. The yield presented is acceptance corrected for CLAS using simulations.

Table A.2: Reduced waveset considered to have contributed to the observed ($\phi\,\eta$) invariant mass distribution in our analysis. All Fits are presented for this waveset along with a wave for the flat background added to the fit in the figure [A.3].

Waves of $+^{ve}$ reflectivity
$1+\,-1+\,D$
$1-\,-1+\,P$
$1+\,-1+\,S$
$2-\,-1+\,F$
$2-\,-1+\,P$
$3-\,-1+\,F$

Waves of $-^{ve}$ reflectivity
$1+\,-1-\,D$
$1-\,-1-\,P$
$1+\,-1-\,S$
$2-\,-1-\,F$
$2-\,-1-\,P$
$3-\,-1-\,F$

ambiguities were not resolved for this dataset using the reduced waveset or many of the other wave combinations tested, the results from the partial wave analysis is found to be inconclusive.

BIBLIOGRAPHY

[1] P. Eugenio, C. Salgado, D. Weygand [CLAS Collaboration], Proposal for g12, E-04-005,(2003).

[2] G. Ding *et al.*, [Babar Collaboration], Physics Lett. B **390**, (2007).

[3] T. Barnes, N. Black and P. R. Page, Phys. Rev. D **68**, 054014 (2003) [arXiv:nucl-th/0208072].

[4] S. I. Bityukov *et al.*, Phys. Lett. B 1883 **383**, (1987).

[5] Richard Feynman and Jeffrey Robbins, The Pleasure of Finding Things Out, April, (2005).

[6] H. Fritzsch and M. Gell-Mann, eConf **C720906V2**, 135 (1972) [arXiv:hep-ph/0208010].

[7] M. Gell-Mann, Phys. Rev. **125**, 1067 (1962).

[8] M. Y. Han and Y. Nambu, Phys. Rev. **139**, B1006 (1965).

[9] R. P. Feynman, Phys. Rev. Lett. **24**, 1415 (1969).

[10] J. J. Dudek *et al.*, Phys. Rev. D **83**, 111502(R) (2011).

[11] J. J. Dudek *et al.*, Phys. Rev. D **82**, 034508 (2010).

[12] C. T. H. Davies, Lattice QCD 2007, (2007) [arXiv:hep-ph/0807.1402v1].

[13] R. Gupta, Introduction to lattice qcd, (1998).

[14] H. Yukawa, Proc. Physico-Math. Soc. **17**, Part I (1935).

[15] N. Isgur and J. E. Paton, Phys. Rev. D **31**, 2910 (1985).

[16] T. Barnes, F. E. Close and E. S. Swanson, Phys. Rev. D **52**, 5242 (1995) [arXiv:hep-ph/9501405].

[17] J. Beringer *et al.*, [Particle Data Group], Phys. Rev. D**86**, 010001 (2012).

[18] S. Godfrey and J. Napolitano, Rev. Mod. Phys. **71**, 1411 (1999) [arXiv:hep-ph/9811410].

[19] T. Barnes, Acta Phys. Polon. B **31**, 2545 (2000) [arXiv:hep-ph/0007296].

[20] T. Barnes, [arXiv:nucl-th/0303032].

[21] F. E. Close and P. R. Page, Phys. Rev. D **52**, 1706 (1995) [arXiv:hep-ph/9412301].

[22] A. P. Szczepaniak and M. Swat, Phys. Lett. B **516**, 72 (2001) [arXiv:hep-ph/0105329].

[23] D. Aston *et al.*, [SLAC Collaboration], Phys. Lett. B **231** (1981).

[24] D. Aston *et al.*, [SLAC Collaboration], Phys. Lett. B **573** (1988).

[25] J. M. Link *et al.*, [FOCUS Collaboration], Phys. Lett. B **545**, 50 (2002) [arXiv:hep-ex/0208027].

[26] J. Busenitz *et al.*, Phys. Rev. D **40**, 1 (1989).

[27] B. Aubert *et al.*, [BaBar Collaboration], Phys. Rev. D **77**, 092002 (2008) [arXiv:hep-ex/0710.4451].

[28] B. A. Mecking *et al.*, [CLAS Collaboration], NIM A 503 3, **513** (2003).

[29] Y. C. Chao *et al.*, Journal of Physics: Conference Series, **299** (2011).

[30] Christoph W. Leemann *et al.*, Annu. Rev. Nucl. Part. Sci., 2001 51,**413-50** (2001).

[31] R. Kazimi *et al.*, Proceedings of EPAC 2004, **1512** (2004).

[32] Jefferson lab picture exchange - http://www.jlab.org.

[33] https://www.jlab.org/accelerator-science.

[34] http://hasylab.desy.de/facilities/flash/machine/how_it_works/index_eng.html.

[35] http://legacy.kek.jp/intra-e/topics/2010/MHI013_1stVTresult.html.

[36] http://wwwold.jlab.org/news/OnTarget/2009/2009-05/Story2.html.

[37] Hall Crannell, CLAS NOTE 93-023 (1993).

[38] S. Stepanyan *et al.*, [CLAS Collaboration] NIM A 572, **654** (2007).

[39] D. I. Sober *et al.*, [CLAS Collaboration] NIM A 440, **263** (2001).

[40] http://www.jlab.org/Hall-B/equipment/tagger/tagger.html.

[41] J. Goetz, CLAS g12 analysis note, CLAS NOTE, November, (2012).

[42] J. Goetz, CLAS g12 Thesis, (2010).

[43] Y. G. Sharabian *et al.*, [CLAS Collaboration] NIM A 556, **246** (2006).

[44] M. D. Mesteyar *et al.*, [CLAS Collaboration] NIM A 449, **81** (2000).

[45] G. Adams *et al.*, [CLAS Collaboration] NIM A 465, **414** (2001).

[46] E. S. Smith *et al.*, [CLAS Collaboration] NIM A 432, **265** (1999).

[47] M. Amarian *et al.*, [CLAS Collaboration] NIM A 460, **239** (2001).

[48] E. Pasyuk, CLAS NOTE 2007-016 (2007).

[49] D. Keller, CLAS NOTE 2010-015 (2010).

[50] M. Williams, C. A. Meyer, CLAS NOTE 2003-017 (2003).

[51] J. Ball and E. Pasyuk, CLAS NOTE 2005-002 (2005).

[52] M. Williams, CLAS g11 thesis, (2007).

[53] M. Williams *et al.*, [CLAS Collaboration] Phys. Rev. C **80**, 065208 (2009).

[54] GEANTâĂŤDetector description and simulation tool, CERN Program Library Long Write-up W5013, CERN Geneva,

[55] S. U. Chung *et al.*, Phys. Rev. D **65**, 072001 (2002).

[56] S. U. Chung, Unpublished BNL preprint, BNL-QGS-93-05, September (1999).

[57] S. U. Chung, Unpublished BNL preprint, BNL-76975-2006-IR, July (2008).

[58] S. U. Chung and T. L. Trueman, Phys. Rev. **D11**, 633 (1975).

[59] A. R. Dzierba *et al.*, Phys. Rev. D **73**, 072001 (2006) [arXiv:hep-ex/0510068].

[60] M. Alekseev *et al.*, [COMPASS Collaboration], Phys. Rev. Lett. **104**, 241803 (2010) [arXiv:0910.5842 [hep-ex]].

[61] E. I. Ivanov *et al.*, [E852 Collaboration], Phys. Rev. Lett. **86**, 3977-3980 (2001) [hep-ex/0101058].

[62] J. Kuhn *et al.*, [E852 Collaboration], Phys. Lett. B **595**, 109-117 (2004) [hep-ex/0401004].

[63] J. D. Richman, DOE Research And Development Report, CALT-68-1148, June (1984).

[64] Feldman, Gary J. and Cousins, Robert D., Phys. Rev. D **57**, 3873-3889 (1998)

[65] Laurent Schoeffel, Progress in Particle and Nuclear physics **65**, 9-49 (2010).

BIOGRAPHICAL SKETCH

Mukesh Satyaprakash Saini was born and brought up in the village of Bhayandar, on the outskirts of the city of Bombay, India. He studied at the local school, Our lady of Nazareth high school and traveled to K.C. College for 5 years for his B.Sc. in physics, which he completed in 2002. He obtained his Master of Science in Nuclear Physics from the University of Mumbai in 2004. He left for the distant shores of Florida in 2005, to pursue a Doctoral degree in particle physics at Florida State University. Going forward, he intends to pursue a career that involves teaching, learning, and research.